UNIVERSITAT POLITÈCNICA DE CATALUNYA
BARCELONATECH

Escola d'Enginyeria de Barcelona Est (EEBE)
Departament d'Enginyeria Química

Doctor of Philosophy Dissertation

Development of Scaffolds by Thermally-Induced Phase Separation from Biodegradable Poly(3-hydroxybutyrate-*co*-3-hydroxyvalerate) and Poly(butylene succinate)

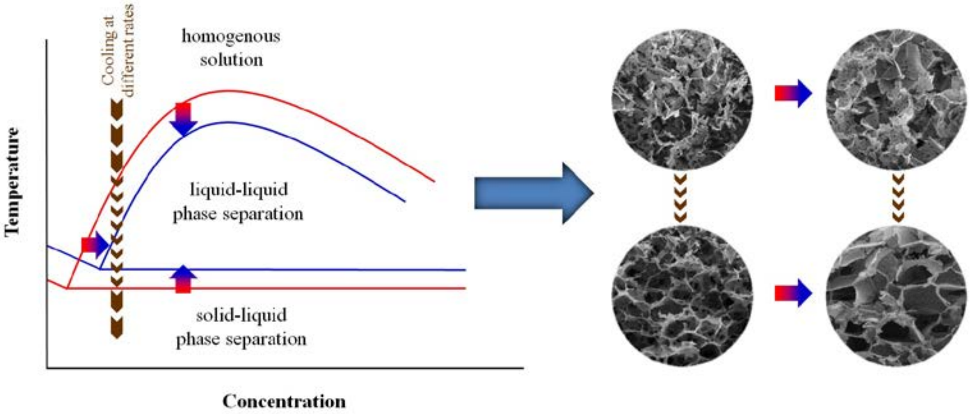

Reza Zeinali

2021

UNIVERSITAT POLITÈCNICA DE CATALUNYA
BARCELONATECH

Escola d'Enginyeria de Barcelona Est (EEBE)
Departament d'Enginyeria Química

Doctor of Philosophy Dissertation

Development of Scaffolds by Thermally-Induced Phase Separation from Biodegradable Poly(3-hydroxybutyrate-*co*-3-hydroxyvalerate) and Poly(butylene succinate)

Presented by

Reza Zeinali

Advisors:

Jordi Puiggalí Bellalta

Luis J. del Valle

Department of Chemical Engineering

Polytechnic University of Catalonia

Barcelona, July 2021

Dedicated to my wonderful family

For all their love and support

Acknowledgements

I take this opportunity to thank my advisor, **Dr. Jordi Puiggalí Bellalta**, for his invaluable guidance and support throughout my PhD period. I am grateful to him for providing me with the opportunity to gain experience in this interesting and challenging area of research. I sincerely appreciate his encouragement and advice that helped me grow, both professionally and personally. I am thankful for his intelligible explications and clarifications that helped me in gaining a better understanding of the basic concepts. Numerous scientific discussions driven by his impressive experience and knowledge inspired me to work independently and think critically. I feel incredibly fortunate to have him as my major advisor.

I would also like to express my deepest gratitude to my associate advisors, **Dr. Luis J. del Valle** for his constant guidance and support during my doctoral research stage. His explicit directions, constructive instructions and insightful comments on experimental studies and laboratory works helped me gain a deeper understanding of the subject and a wider research perspective.

I would like to acknowledge **Dr. Lourdes Franco García** for her technical assistance, especially her companionship and extensive consultations with calorimetric and thermogravimetric analyses and participation in microscopic evaluations.

I would also like to thank our collegiate collaborators from IMEM and PSEP groups, the teaching and administrative staff and my past and present colleagues.

Scientific Publications

1. Zeinali, R.; Khorasani, M.T.; Behnamghader, A.; Atai, M.; Valle, L.; Puiggalí, J. Poly(hydroxybutyrate-*co*-hydroxyvalerate) Porous Matrices from Thermally Induced Phase Separation. *Polymers* **2020**, *12*, 2787.

2. Zeinali, R; del Valle, L.; Torras, J.; Puiggalí, J. Recent Progress on Biodegradable Tissue Engineering Scaffolds Prepared by Thermally-Induced Phase Separation (TIPS). *Int. J. Mol. Sci.* **2021**, *22*, 3504.

3. Zeinali, R; del Valle, L.; Franco, L.; Puiggalí, J. Poly(butylene succinate) Matrices Obtained by Thermally-Induced Phase Separation: Structural Modifications Affect Drug Release. *Molecules*, **2021**. In preparation.

4. Zeinali, R; del Valle, L.; Puiggalí, J. Biobased Terpene Derivatives: Stiff and Biocompatible Compounds to Tune Biodegradability and Properties of Poly(butyelene succinate). Submitted, **2021.** In preparation.

Abstract

Thermally-Induced phase separation (TIPS) is an unsophisticated low-cost technique for preparation of 3D interconnected microporous matrices, suitable for bioapplications such as cell/drug carriers. TIPS process followed by freeze-drying have been used to prepare biodegradable and biocompatible matrices from poly(3-hydroxybutyrate-*co*-3-hydroxyvalerate) (PHBV) containing 5 and 12 wt% of 3-hydroxyvalerate (HV) and poly(butylene succinate) (PBS) polyesters. 1,4 dioxane (DXN) was used as solvent for PHBV copolymers and two different solvents, i.e. DXN and THF were employed for PBS in the TIPS process.

The polymer solutions underwent phase separation by cooling under different temperature gradients. In order to induce phase separation to PHBV solutions, a two-step cooling protocol was applied, that is, a spontaneous multidirectional cooling from ~70 °C to the room temperature, and then a secondary cooling to -5 °C or -25 °C. The cooling protocol applied to PBS-DXN and PBS/THF solutions was a direct multidirectional cooling from ~70 °C to -20 °C or -74 °C, by rapidly transferring the solution-containing molds to the cooling devices. Another cooling system applied only to PBS-DXN system was a uniaxial cooling from ~70 °C to -74 °C or -196 °C, through perimetric isolation of cylindrical glass molds before transferring to the cooling baths. The cloud points of the polymer solutions were determined by turbidimetry method upon a very slow cooling, to predict the locus of binodal curve in the corresponding polymer-solvent phase diagrams.

With regard to PHBV scaffolds, the influence of parameters such as applied temperature gradients and HV molar ratios of the copolymer on TIPS process were studied. Alteration in these parameters gave rise to change in the phase separation mechanism and thus in the morphology and mechanical properties of the scaffolds. Upon high HV content and fast cooling, the solid-liquid phase separation through crystallization of DXN was the controlling mechanism and generated a solid-walled morphology with a great structural continuity. The morphologies ascribed to crystallization of the polymer, mostly with low structural consistency were discernible to a greater extent under slow cooling. An improvement in scaffolds rigidity was observed in low HV and fast cooling conditions, due to the increased polymer crystallinity and the greater structural consistency, respectively. PHBV scaffolds showed a complete biocompatibility towards MDCK and NRK cell adhesion and proliferation in 3D cultures.

In case of PBS scaffolds, the influence of further TIPS process parameters including an extra solvent system (i.e., THF) and additional cooling conditions (in terms of intensity and direction of the temperature gradient) were studied. A one-step TIPS fabrication/drug loading protocol was employed to manufacture microporous matrices and simultaneously to incorporate 5 and 100 wt% of natural curcumin (CUR) and piperine (PIP) drugs into the matrices. For comparison reasons, the neat and drug-loaded PBS films were prepared by solvent casting method and using chloroform. Utilizing DXN and THF solvents, solid-liquid and liquid-liquid phase separation were respectively detected as the main mechanisms responsible for creating the porous structures, while the subregions composed of crystallized PBS were also observed. The applied uniaxial thermal gradient enabled DXN solvent to crystallize along the heat transfer direction and form an oriented microtubular structure. Although the low drug values did not significantly influence the morphology, the high-level drug loading gave rise to the decreased porosity and superficial roughness of the scaffolds. A uniform distribution of prismatic PIP crystals and matrix-integrated CUR aggregation was observed all over the structure. The integration of CUR which was confirmed by the physicochemical analyses attributed to a possible interaction with the PBS matrix, as it also showed a slower release profile compared to PIP. Regarding the greater biocompatibility and also retarded drug release from the dense spherulitic pore walls of microtubular oriented matrices, the TIPS-originated structural orientation could improve cell/drug delivery capability of PBS scaffolds.

As a parallel investigation, the possibility of increasing the biocontent and modifying properties of PBS by blending it with cost-effective biobased polymers was evaluated. Polycarbonate and polyesters having terpene oxide units (e.g., limonene oxide) were studied particularly in terms of physicochemical and thermal properties, degradability and biocompatibility. Although high rigidity and amorphous nature was the main characteristics of these polymers, spherulites were observed upon slow evaporation of polylimonene carbonate from chloroform solution. Crystallization of enantiomeric polylimonene was interesting because only crystallization of racemic polymers had been reported. All the studied polymers exhibited high thermal stability and glass transition temperature as it was expected. Their rigid nature and stiff chain led to insignificant hydrolytic and enzymatic biodegradation, while an accelerated degradation in oxidative media was observed. Nevertheless, apart from their bioresource, their satisfactory biocompatibility and mechanical strength provided some motivation for blending them with the PBS. The blend was biodegradable and biocompatible and was used for fabrication of tissue

engineering scaffolds by TIPS technique. A 30 wt% blend of the copolyester derived from phthalic anhydride and limonene oxide, (i.e, Poly(PA-LO)) with PBS, 1,4 dioxane and different cooling systems were the TIPS parameters. Multidirectional cooling to -20 °C or -74 °C and uniaxial cooling to -74 °C or -196 °C was applied to PBS-Poly(PA-LO)/DXN systems. Porous and interconnective matrices with expecting random and oriented were successfully produced in one-step by TIPS method, with minor effect of the blended polymer on the porosity structure. However, it seemed that the addition of Poly(PA-LO) had restricted the crystallization of PBS from the solution during the TIPS process. Therefore thinner polymer leaves upon multidirectional and lower thermal gradient, and smaller, less planar and less integrated spherolites were formed upon high uniaxial gradient.

Objectives

The main objective of the present investigation is to evaluate/study the capability of TIPS technique for construction of 3D microporous interconnective matrices made of biodegradable and biocompatible polymers for biomedical applications. Specifically, solid-liquid and liquid-liquid phase separation processes are employed to fabricate polymer matrices made of poly(3-hydroxybutyrate-*co*-3-hydroxyvalerate) (PHBV) and polybutylene succinate (PBS) to be used as biosubstrates for cell or drug delivery purposes.

Preparation of various microprorous architectures composed of large regular or elongated pores via solid-liquid phase separation suitable for cell seeding is attractive. Besides, creating small pores (especially in the walls of the larger pores) via liquid-liquid phase separation is beneficial to act as structural interconnectivities, facilitating the transport of nutrients/metabolic waste throughout the scaffold which is crucial to cell viability.

Since the polymers used in this study have a semicrystalline nature, evaluating their potential to be crystallized from the solution during or after the phase separation processes and its corresponding morphological influence seems interesting. Due to importance of biocompatibility in bioapplications, an extensive biocompatibility study is performed for all the materials including pure or blended and all constructs including films and porous matrices, to ensure the safety of the materials and fabrication processes.

The common challenge in TIPS studies, that is, the possibility of controlling the scaffolds characteristics (e.g., morphological and/or mechanical properties) through manipulating TIPS process parameters is another intended target. This will be done by employing different polymer-solvent systems and/or applying different cooling systems in terms of intensity and direction of thermal gradient.

Regarding PHBV scaffolds, providing such a control over the scaffold properties by selecting the copolymers of different 3-hydroxyvalerate content, or by variations in cooling rate is expected. However, In this case, a single solvent system (i.e., 1,4 dioxane) is employed, being expected the induction of solid-liquid phase separation caused by solvent crystallization in the system. The variations in cooling condition in this section is limited to the use of two different cooling baths, while the direction of thermal gradient remains constant (i.e., multidirectional). Thus, the main focus of this part will be evaluating the relationship between the aforementioned process parameters and the scaffold properties.

With respect to PBS scaffolds, although the principal goal is still defined as fabricating the interconnected porous structures by TIPS technique, the survey is extended to further variations in process parameters in terms of solvent system and/or cooling condition. Specifically, in addition to 1,4 dioxane, a THF solvent is also employed to evaluate the possibility of inducing a pure liquid-liquid phase separation in the system. More cooling baths with different temperatures and a uniaxial thermal gradient system are also added to the cooling system variables, which are individually expected to have their own influence on the morphology. Accordingly, by applying both multidirectional and uniaxial temperature gradient, the potential of solid-liquid phase separation to produce isotropic matrices with multidirectional (random) pore architecture and anisotropic ones with unidirectional (oriented) porosity structures is investigated.

Since PBS is the main polymer used in this investigation, developing its bioapplication potential is also considered in the next phase. This includes modification of the polymer properties by blending it with other polymer components, or enhancing the matrix biofunctionality by loading bioactive agents and TIPS-based structural modification to improve the delivery of these agents.

In this regard, curcumin (CUR) and piperine (PIP) natural drugs with proved antioxidant/anti-tumor effects are planned to be incorporated in PBS matrices through a one-step matrix fabrication/drug loading process via TIPS technique. A sustained release of CUR and PIP from the microporous PBS matrices is favored, a feature of crucial importance and the principal objective of drug delivery systems. Hence, a structural modification of PBS devices through TIPS-based porosity orientation by applying a uniaxial cooling system is desired. This will be helpful to have a better understanding of how and how much the structural/morphological features can affect the release rate of bioactive agents. Eventually, the variations in physicochemical properties of drug-loaded and non-loaded matrices are evaluated. Particularly, the possible reaction/binding of the drugs with the polymer component during TIPS preparation method is investigated by analyzing the thermal properties of the scaffolds.

The modification of PBS polymer is performed through increasing its biobased content by blending it with bioresource terpene derivatives with high glass transitions temperature. The physicochemical, thermal, degradation and biocompatibility of pure terpene-derived tablets fabricated by cold pressing is investigated. These characteristics together with mechanical properties of the blended solvent casting films is evaluated and compared with the neat PBS films.

An enhancement in mechanical properties, especially in strength and rigidity is expected as a result of such mixing, a feature of great importance in many biomedical applications.

Incorporation of the terpene-derived materials to the PBS matrices is planned to be performed through a similar one-step fabrication/blending process via TIPS technique. In this case, the TIPS variables will be the manipulation of cooling system in terms of intensity and direction of thermal gradient. Uniaxial and multidirectional thermal gradients in different cooling baths are applied.

Glossary of Acronyms

3D	Three-dimensional
Alg	Alginate
AM	Additive manufacturing
β-TCP	Beta-tricalcium phosphate
BG	Bioactive glass
CaSi	Calcium silicate
CNC	Cellulose nanocrystals
Col	Collagen
Col1	Collagen type 1
CNFs	Carbon nanofibres
CS	Chitosan
DCPD	Dicalcium phosphate dihydrate
DMF	Dimethylformamide
EAB	Ethyl alcohol bath
ECM	Extracellular matrix
EV	Exosome vesicle
FDA	Food and Drug Administration
FESEM	Field emission scanning electron microscope
GEL	Gelatin
GelMA	Gelatin methacryloyl
HAc	Hyaluronic acid
hAD-MSC	Human adipose mesenchymal stem cell
HA	Hydroxyapatite
HFIP	Hexafluoro-2-propanol
HSP	Hansen Solubility Parameters
LCA	Life Cycle Assessment
LD50	Lethal dose
MicroCT	Micro-computed tomography
μFC	Micro-fluorcanasite
MSNs	Mesoporous silica nanoparticles
MWCNT	Multiwalled carbon nanotube
MSCs	Mesenchymal stem cells
NG	Nucleation and growth
NGC	Neural guidance channel
nHA	Nanohydroxyapatite
OA	Oleic acid

PANI	Polyaniline
PBS	Poly(butylene succinate)
PCL	Polycaprolactone
PDA	Polydopamine
PDLLA	Poly(D,L-lactide)
PDLLA-*b*-PBLG	Poly(D,L-lactide)-*b*-poly(γ-benzyl-L-glutamate)
PEG	Polyethylene glycol
PEI	Poly(ethylenimine)
PEEUU	Poly(urethane urea)ester
PGA	Polyglycolide
PGCL	Poly(glycolide-*co*-caprolactone)
PHAA-g-PLLA	Poly(hydroxyalkyl methacrylate)-graft-poly(L-lactide)
PHB	Poly(3-hydroxybutyrate)
PHBV	Poly(3-hydroxybutyrate-*co*-3-hydroxyvalerate)
PLA	Polylactide
PLCL	Poly(lactide-*co*-caprolactone)
PLGA	Poly(lactide-*co*-glycolide)
PLLA	Poly(L-lactide)
PLLGC	Poly(L-lactide-*co*-glycolide-*co*-ε-caprolactone)
PTFE	Polytetrafluoroethylene
Qu	Quercetin
RBMSCs	Rabbit bone mesenchymal stem cells
SA	Salvianic acid
SC-CO_2	Supercritical carbon dioxide
SD	Spinodal decomposition
SEM	Scanning electron microscopy
TCH	Tetracycline hydrochloride
TCP	Tricalcium phosphate
TE	Tissue engineering
THF	Tetrahydrofuran
TIPS	Thermally-induced phase separation
TWB	Thermal water bath
UCST	Upper critical solution temperature

Table of Contents

Chapter 1

Introduction

1.1. Tissue Engineering Scaffolds

Tissue engineering is a multidisciplinary field that combines biology, biochemistry, clinical medicine and materials science. This approach is a quite recently developed alternative to current surgical strategies, which aims to restore, maintain or improve the function of damaged or lost tissues by taking advantage of porous three-dimensional (3D) scaffolds [1-3]. Tissue engineering is based on using biodegradable porous scaffolds integrated with cells or biological molecules for regeneration of tissues or organs [4]. In regenerative medicine, the cell proliferation triangle is defined with its three essential elements including scaffolds, cells and growth factors or other bioactive molecules. Scaffolds represent the conductive capacity inside the triangle, which can be used to carry the cells before in vivo implantation, or only act as a bioactive material attracting the cells on the tissue where they are implanted [5].

In this approach, scaffolds are designed to serve as a temporary artificial extracellular matrix (ECM) to support cell adhesion and also to promote 3D tissue formation. Accordingly, scaffolds should have a suitable surface chemistry as well as highly interconnected porosities with adequate size to be able to mimic the chemical composition, structure and mechanical properties the natural ECM [6,7]. Such scaffolds as *in vivo*-like microenvironments will be able to reproduce the biological and functional entity of natural ECM in order to stimulate the cell-specific responses leading to neo-host tissue formation and subsequently to tissue repair or regeneration [8]. Scaffold characteristics affect different cell processes like adhesion, migration, proliferation and differentiation [9]. Tissue engineering scaffolds with proper and well-regulated interconnected porosities, allow the cells to grow with appropriate physical shapes and assist the vascularization of primary tissues [10,11]. Tissue engineering scaffolds are traditionally made of porous polymer materials to sustain 3D cell growth which is a particular interest in tissue engineering [7]. Biodegradable polymers have extensively been applied for manufacturing tissue engineering scaffolds [12]. The degradability property of the scaffold eliminates the subsequent need for removing the implanted materials or the side effects of remaining foreign materials in the body [13]. The biodegradable polymeric materials must also be biocompatible with tissues. Strictly speaking, they must degrade over a certain period of time after implantation, producing nontoxic by-products which can be either eliminated or metabolized by the body [14,15]. For example, poly(lactic acid) (PLA), a biodegradable thermoplastic crystalline polymer, is broadly used for biomedical applications [16,17].

1.2. Drug Delivery Systems

Drug delivery includes a wide range of techniques used to get therapeutic agents into the human or animal organism. It is an interdisciplinary field aiming to proper administration of bioactive agents in order to enhance the drug therapy and achieve a desired clinical response in the body. The strategies for controlling the drug release from pharmaceutical systems are based on biological, physicochemical and mathematical principles. There are several mechanisms by which the release process of a drug can be controlled in a particular system. These mechanisms are based on a specific application and may act simultaneously or at different stages of the delivery process [18].

The drug release from a polymer matrix is generally controlled by several mechanisms (Figure 1). One mechanism is dependent on diffusion of the active agent from the polymer substrate into the organism and is called diffusion-based controlled release [19]. Diffusion is defined as the mass transfer process of particular molecules of a substance from one part to another part of a system. This process is developed by random molecular motions and is associated with forces such as concentration gradient. The mass transfer is toward reducing the concentration difference through a spontaneous flux of matter, playing an important role in diffusion process at the system/water interface [18]. The diffusion-based controlled release is dependent on the diffusion coefficient, matrix porosity and tortuosity [19].

The polymers used in drug delivery systems controlled by the diffusion process, have a relatively passive function. They act as carriers for the active agent, delaying its release velocity into the targeting site. Nevertheless, polymeric carriers may play a more active function in the drug delivery process [18]. By employing biodegradable polymers for such applications, another possible mechanism based on the erosion of the polymeric carrier must be considered and is called erosion-based controlled release [19]. In this case, the biodegradable polymer carriers undergo erosion when they suffer chemical reactions, leading to the release of the active agent. These systems are favored for implantable or injectable therapies, because they do not need to be retrieved from the organism after the full release of the active agent [18].

Another mechanism is a triggered pathway initiated by changing the environmental conditions such as pH or temperature [20]. It is common for a drug delivery system or device to present more than one mechanism [18].

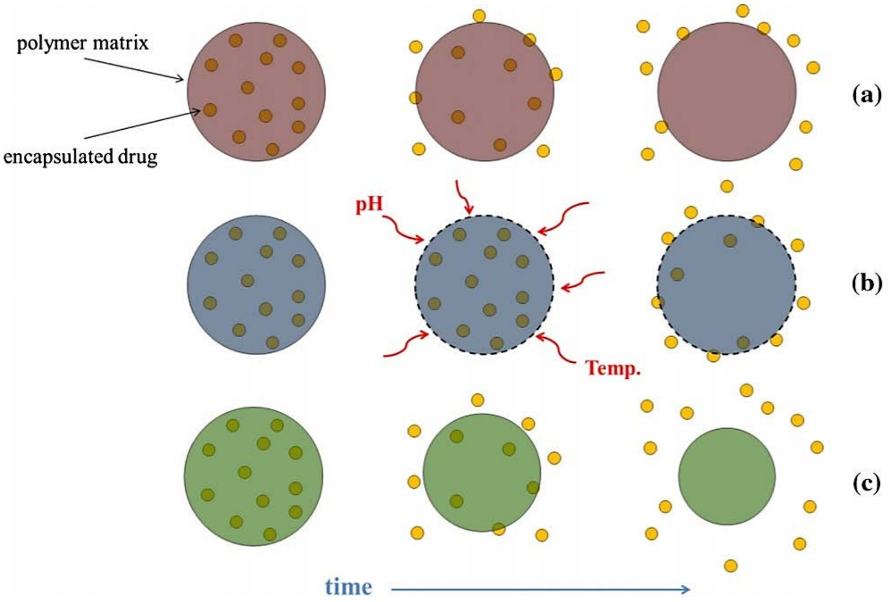

Figure 1. Drug release mechanisms: diffusion-based controlled release (**a**), triggered release (**b**), and erosion-based controlled release (**c**) [19].

1.3. Biodegradable Polymers

Biodegradable polymers attract great interest for biomedical applications. In the last 15 years, a lot of biomaterials have been identified as promising substances for producing different types of matrices. Among them, biodegradable and biocompatible polymers such as PLA, PCL, PGA and their copolymers have attracted significant scientific attention, and most of them have already been approved by the FDA to be used as materials for biomedical applications [21,22]. Due to possessing great design flexibility in synthesis, processing, and modification, these synthetic biodegradable polymers are suitable candidates as matrix materials to develop biodegradable tissue engineering scaffolds [23]. Although all these biopolymers are hydrolytically degradable, the degradation rate may vary from one to another, for example PCL is rather long-lasting. Taking into account the drug delivery systems and tissue engineering matrices are categorized as temporal applications within the organism, the degradation procedure and rate is a matter of great importance [14,15].

The hydrolytic degradation of aliphatic polyesters [24,25] might be due to either surface degradation or en-bloc degradation mechanisms. The surface degradation will occur on condition that the hydrolytic rupture of the polymer chains and the consequent production and diffusion of oligomers and monomers into the environment is faster than the entry of water into the polymer. Thus, the polymer mass will be reduced from the exterior surfaces towards the interior parts throughout the degradation process. Such degradation pattern does not affect the structure of interior parts, meaning that its molecular weight is maintained. The advantage of this type of degradation which is quite predictable can be very useful in applications such as drug delivery systems to control the speed of drug release.

On the contrary, when the water penetrates into the inner parts of the polymer and leads to establishment of hydrolytic reactions and reduction of molecular weight in these parts, en-bloc degradation takes place. In such conditions, if the water diffusion is adequate, the resulting oligomers and monomers will spread in a uniform way throughout the polymer mass and all of the polymer will be equally degraded. In contrast, if the water diffusion is hindered, the acidic products of the degradation process which are able to react with the ester groups will accumulate in the inner parts. Such phenomenon gives rise to a self-catalyzed degradation reaction which degrades the interior parts more quickly than the exterior parts where the diffusion and evacuation of these products are easier. In this situation, the reduction of molecular weight will be faster from the middle to the surface of the polymer mass [24-26].

Continuous efforts have been made to improve the performance characteristics of polymeric materials for bio-application purposes [27]. Among all biodegradable polymers, natural and synthetic aliphatic polyesters are the most broadly investigated ones. They can be classified into different main groups based on their repeating unit type: poly(α-hydroxyacid)s, poly(ω-hydroxyacid)s, poly(3-hydroxyalkanoate)s and poly(alkylene dicarboxylate)s. The first group is usually prepared by ring-opening polymerization while poly(3-hydroxyalkanoate)s are biologically synthesized by microorganisms [27-29].

1.3.1. Poly(hydroxyalkanoate)s

Poly(hydroxyalkanoate)s (PHA)s are natural biodegradable polyesters and biocompatible thermoplastics which are derived from various microorganisms like *Bacillus megaterium*, *Pseudomonas oleovorans*, *Alcaligenes latus*, *Alcaligenes eutrophus*, soil bacteria, estuarine microflora, blue-green algae, and also from genetically modified plants [30]. In recent years, this family of polyesters has received many scientific attention, especially because they can be biotechnologically produced from different microorganism resources [31]. PHAs are a family of lineal biopolyesters made of hydroxyalkanoate (HA) units which are organized in a basic structure formed by bacterial fermentation, and are promising substances for a sustainable future [32]. PHAs stand out as a sustainable alternative materials among the most-produced commercialized biopolymers because by the microorganisms present in the water and soil they can be transformed into water and carbon dioxide in the presence of oxygen, or into methane under anaerobic conditions [33]. Properties like their natural-based origin, biodegradability, biocompatibility, non-toxicity, piezoelectricity and thermoplasticity have made them suitable choices for various industrial and medical applications [31]. The chemical structure of PHAs is very similar to polylactides (PLA)s which are the most common synthetic polymers in biomaterial application, and also similar to the copolymers of PLA with glycolide, PLGA. However, PHAs generally degrade with a lower rate than PLA and PLGA. Due to their appropriate properties, numerous applications of the PHAs in biomedical fields such as in drug delivery and tissue engineering have been reported [34]. In addition, their properties can be easily selected by choosing a suitable PHA, or be modified by blending them, giving many options for material selection based on PHAs for cell or drug delivery purposes [35]. However, by now only two members from the PHA family have commercially been produced, i.e., Poly(3-hydroxybutyrate) (PHB) and poly(3-hydroxybutyrate-*co*-3-hydroxyvalerate) (PHBV) [36]. PHB is a thermoplastic polymer with physical properties similar to some petroleum-derived polymers, showing a high degree of crystallinity, insolubility in water and a relative resistance to hydrolytic degradation [37].

1.3.1.1. Poly(3-hydroxybutyrate-co-3-hydroxyvalerate)

PHBV is less crystalline, more flexible, and thus more processable compared to PHB itself [38]. This copolymer exhibits a complete biodegradation without producing any toxic products. Being derived from biological sources is also considered as its advantage compared to PLGA [34]. Depending on different percentages of 3-hydroxyvalerate (HV) units in the PHBV structure (Figure 2), its mechanical properties (i.e., tensile and compression strength) and chemical properties (i.e., surface energy and hydrolysis rate) can be altered [34]. Although PHBV is a semicrystalline copolymer showing crystallinity in all PHV contents, a wide range of properties depending on its PHV content is observed. The higher HV content in the PHBV structure, the lower melting point and crystallinity [37] and the higher degradation rate in aqueous media is obtained [34].

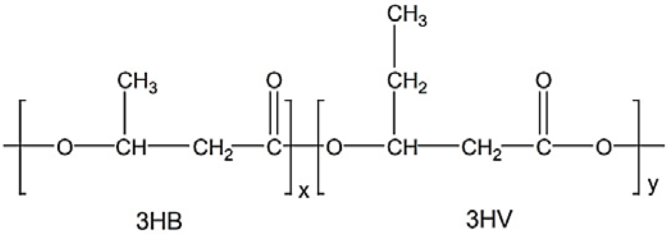

Figure 2. Molecular structure of PHBV, showing HB (x) and HV (y) repeating units [39].

The outstanding properties of PHBV such as absorption capacity, biological origin, low cytotoxicity, piezoelectricity and thermoplasticity, render it as a promising material for a wide range of biomaterial applications, such as absorbable surgical sutures, and medical packaging [40], cardiovascular stents [41], drug release and transport systems [41,42].

Applications of PHBV in the field of tissue engineering include the elaboration of tissue patches, biodegradable implants, biosensors and fabrication of porous scaffolds [2,43,44]. The porous PHBV scaffolds have been found to be suitable substrates for the cell structures. No tissue necrosis, abscess formation, or acute inflammation was observed in the tissues adjusted to the implanted materials [45,46]. Due to its piezoelectric properties, PHBV has the potential to induce the formation of new bone tissue [47]. It has been reported that PHBV is able to sustain the fibroblast cell proliferation rate similar to that observed in the collagen sponges [48].

1.3.2. Poly(alkylene dicarboxylate)s

Poly(alkylene dicarboxylate)s are polyesters with great interest due to their easy synthesis and the potential applications arising from their biodegradability [49]. In general, these polymers are highly crystalline. This feature may improve some of their properties but may hinder their degradation process. In order to obtain materials with tunable properties, efforts have currently been focused on the formation of random copolymers that can be easily synthesized by using mixtures of diols and/or dicarboxylic acids. In this way, the hydrophobicity, crystallinity and degradation rate of poly(alkylene dicarboxylate)s can be controlled [50,51]. Poly(butylene succinate) (PBS) is the most widely used polymer from poly(alkylene dicarboxylate) family, due to its relatively low production cost, good mechanical properties and easy processability [52]. PBS also has other important physical properties such as semicrystalline nature, thermal stability, good gas barrier properties, and a lower melting point which make it a good candidate for preparation of biodegradable products [53,54]. PBS is an aliphatic polyester which is synthesized by polycondensation reaction of petroleum-based aliphatic dicarboxylic acid (i.e., succinic acid) and 1,4-butane diol [55,56]. Generally, the biodegradability of PBS is similar to cellulose and bacterial polyesters like poly(3-hydroxybutyrate-*co*-3-hydroxyvalerate) (PHBV) [57]. The molecular structure of polybutylene succinate has been shown in Figure 3.

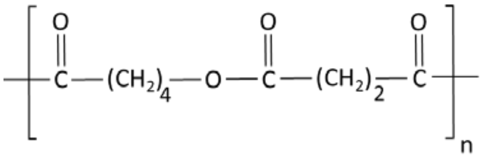

$$-\left[\overset{O}{\overset{\|}{C}} -(CH_2)_4-O-\overset{O}{\overset{\|}{C}}-(CH_2)_2-\overset{O}{\overset{\|}{C}} \right]_n-$$

Figure 3. Molecular structure of polybutylene succinate (PBS). Based on [58].

It must be considered that PBS is derived from succinic acid, which is typically produced in microbes in the metabolic tricarboxylic acid cycle which is used for producing energy. Taking into account this potential, great efforts are being developed to obtain succinic acid in a low-cost way from renewable resources like starch, glucose or cellulose [59]. Synthesize of PBS from renewable resource-based succinic acid reduces its carbon footprint while its total performance is preserved [58]. This also applies to other C4 derivatives like 1,4-butanediol, which is the second monomer used for the synthesis of PBS [59]. Different types of copolymers and blends of PBS have recently been developed for different purposes, for example, to increase biodegradability, decrease costs, increase commercial offer or even modify final properties [52].

1.3.2.1. Poly(butylene succinate)

The majority of studies on PBS and PBS-based copolymers have been focused on synthesis and characterization categories, while the final application of these recently developed systems has received less scientific attention. Although several reports have provided additional data in this respect, conducting more investigations on the bioapplication of PBS-based systems seems inevitable [19].

The studies on application category have mainly been conducted in the field of bone tissue engineering by employing PBS or PBS-based composite scaffolds. In this regard, PBS [60,61], plasma-treated PBS [62,63] and surface hydrolyzed PBS [64] scaffolds have been studied. Composite scaffolds made of PBS/hydroxyapatite (HA) [65,66], PBS/chitosan (CS) [67-70], PBS/fluorapatite (FA) [71], surface hydrolyzed

PBS/tricalcium phosphate (TCP) [72,73] and PBS wollastonite/apatite [74] and also PBS microspheres incorporated in carboxymethyl chitosan scaffolds [75] have recently been developed for bone repair purposes. It has been reported that PBS/C scaffolds could induce the osteogenic differentiation of stem cells [76,77]. PBS–DLA copolymers have also displayed a great potential for cardiac tissue engineering [78,79]. The potential application of PBS-based copolymers and composites in drug delivery systems has been evaluated through the release of molecules from the films [80], micro and nanoparticles [20, 81-83], or scaffolds [84]. With respect to fabrication methods, thin films have mainly been fabricated by compression molding and scaffolds mostly through salt leaching [60,68-70,76,77] and electrospinning [61,64-66,74,79,85] techniques.

In vitro release of ipriflavone (a compound that inhibits bone resorption by maintaining bone density and preventing osteoporosis) was studied in chain-extended PBS scaffolds fabricated by particulate leaching. Two main phases were highlighted from the obtained release profiles: the initial burst phase, attributed to the dissolution of drug aggregates from the scaffold surface, and a sustained release phase indicating a gradual decrease in release rate until a plateau value was achieved. In this case, no effect of the porosity or pore size of the scaffolds was detected, while the high-load efficiency and capacity were observed. Nevertheless, some differences in the release rate with respect to the scaffold structure during the experiment were reported. Specifically, the thickness of inter-cellular walls significantly affected the drug diffusion from the scaffold [60]. Similar results have been obtained related to the release kinetics of indomethacin (a non-steroidal anti-inflammatory drug used in the treatment of soft tissue problems), from poly(butylene succinate)/poly(caprolactone) (PBS/PCL) microcapsules [81], and also related to the release of camptothecin (a natural plant alkaloid with antitumor activity), from poly(ω-pentadecalactone-*co*-butylene succinate) nanoparticles [83].

Mohanraj et al. [82] loaded PBS microcapsules with levodopa (an anti-Parkinson's drug) and reported a higher encapsulation efficiency for smooth microspheres compared to the porous ones. They also observed a higher drug release in simulated cerebrospinal fluid than phosphate buffer, indicating the great importance of the release medium composition in drug release evaluations [82].

In another study, polymeric films made of PBS and multiblock PBS-based copolymers containing ether-linkages (PBS-b-PTES), loaded with fluorescein isothiocyanate (FITC) were prepared by solvent casting. The release of FITC, as a model molecule, was monitored by UV absorbance measurement. All the polymeric films displayed a diffusion-driven release behavior, with a primary burst release within the first 6 h, followed by a sustained release profile. However, different release profiles were observed, due to the different hydrophilicity and chain mobility of these polymer systems. Specifically, PBS as the most hydrophobic polymer, showed the slowest release of FITC, while a faster release caused by higher hydrophilicity was observed in the polymer system containing TES co-monomeric units. The crystal phase was also seemed to have an effect on the burst phase of the release profile, because the crystal lamellae may act as a barrier to FITC molecules and delay the diffusion process. Nevertheless, this effect was no longer observed at longer incubation times, due to the polymer hydrolysis and therefore a possible change in the release mechanism from diffusion-based to erosion-based [80].

Jeger et al. [20], evaluated the release of hydrophobic model drug paclitaxel (PTX) from PBS–DLA nanoparticles and compared it with the drug-loaded nanoparticles made of PLA and PLGA. PTX release was monitored by HPLC and scattering measurements. During the first 12 h of incubation, about 40% of the encapsulated drug was released while after 120 h, only 10% more was released from the nanoparticles. Interestingly, the structure of the nanoparticles was modified by the presence of the model drug, such that the nanoparticles were able to hold a high amount of water in the drug-free media. Nevertheless, the drug encapsulation led to a shrinkage of the nanoparticles, as the water was replaced with the hydrophobic PTX drug. The release profile in this case was also controlled by the drug diffusion and water draining from the polymer matrix [20].

Utilization as antimicrobial biomaterials is another potential application of PBS-based copolymers. In this regard, the antimicrobial activity of PBS/PLA electrospun scaffolds loaded with potassium salt of 5-nitro-8-hydroxyquinoline or 5-chloro-8-quinolinol against *Staphylococcus aureus* has been evaluated. Although the neat PBS/PLA scaffolds did not exhibit any significant antibacterial effect, well-distinguished zones with inhibited growth of bacterial cells were discernible in the drug-loaded samples. This indicates that the drugs could preserve their antimicrobial activity when incorporated in the electrospun matrices [85].

1.4. Biobased Terpene-Derived Polymers

The formation of bio-derived materials is increasingly gaining momentum in the academic area and also in the industrial section. Because of the growing demand for the production of partially to fully bio-derived polymers in a sustainable way, the usage of renewable bio-based monomers is being developed [86]. Although PBS is composed of monomers derived from fossil fuels or bacterial fermentation [87], efforts have been made to increase its bio-based content and also mechanical properties by blending it with natural components [88]. By now, the utilization of terpene oxides as renewable monomers for the preparation of bio-based polymers yet remains limited. Therefore, blending PBS with terpene-derived epoxides such as limonene oxide (LO) or menthene oxide (MO) is considered as an interesting and novel idea. The terpene compounds have frequently been studied as functional monomers for the synthesis of various polymer structures such as polyesters [89-93], polycarbonates [94-98], and polyterpenes [99-102].

Specifically, these monomers can participate in a ring-opening copolymerization in the presence of various aromatic high-rigidity anhydrides to produce bio-based semiaromatic polyesters with high glass transition temperature. Poly(phthalic anhydride-*alt*-limonene oxide), P(PA-LO) is a case of such rigid semiaromatic polyesters with high glass transition temperature up to 135 °C that has recently been synthesized by some researchers [86]. The ring opening polymerization of PA and LO has been illustrated in Figure 4.

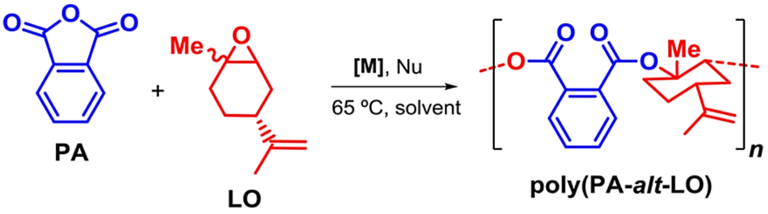

Figure 4. Ring-opening polymerization of PA and LO in the presence of metal-based (Me) epoxide activators (i.e., [M]=Fe or Al) and 4-(dimethylamino)pyridine (DMAP) or bis(triphenylphosphine)iminium chloride (PPNCl) initiators. Nu stands for nucleophile [86].

Another example is the synthesis of bio-based polycarbonates from terpene-base monomers. Poly(limonene)carbonate (PLC) is such a case that can be synthesize by coupling biorenewable-based limonene oxide monomer and carbon dioxide. Peña et al. have recently synthesized altering PLC using *cis*, *trans* or *cis*/*trans* limonene oxide monomers (Figure 5) with binary catalyst systems including mino-triphenolate derived Al complexes combined with suitable nucleophiles.

Pure *cis* limonene oxide could produce 93-96% *trans* PLC, resulting in high stereo-regularity and therefore high molecular weight and glass transition temperature. Specifically, the highest M_n (10.6 Kg/mol) and T_g (112 °C) belonged to 96% *trans* PLC. On the other hand, pure *trans* or *cis*/*trans* mixture of limonene oxide led to the formation of the less *trans* isomeric contribution of PLC, leading to a decrease in its stereo-regularity and thus in its corresponding T_m and T_g [103].

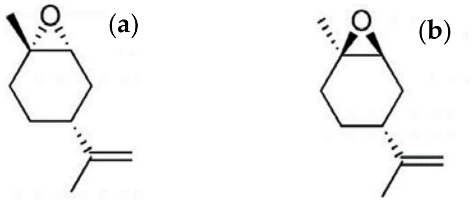

Figure 5. *Trans* (**a**) and *cis* (**b**) isomers of limonene oxide [103].

It is expected that blending PBS polymer with such bio-based terpene derivatives with high glass transitions temperature improves its strength, a feature of a great importance in many biomedical applications. In addition, due to the amorphous nature of these bio-based components, a change in crystallinity and degradation behaviour of the blend is also expected.

1.5. Curcumin and Piperine Natural Drugs

Regarding the promising potential of PBS in the field of drug delivery, it is considered as a suitable candidate to be used as a substrate for sustained release of pharmaceutical and bioactive agents. On the other hand, the usage of herbal medicines or nutraceuticals is expanding rapidly across the world. Most of the world's population rely on herbal medicinal products as a primary source of healthcare and have resorted to using these natural products for the treatment of various health challenges [104]. Curcumin (CUR) and piperine (PIP) are two examples of these natural and herbal-source drugs with anticancer and anti-inflammatory effects. Herein, the capacity of PBS polymer matrices for the controlled release of these drugs have been studied.

Curcumin is a bright yellow substance produced by some plants. It is the principal curcuminoid of turmeric *Curcuma longa*, a member of the ginger family (*Zingiberaceae*) [105]. It has been utilized for a long time for food flavoring and food coloring and also as an ingredient of cosmetic products and as herbal supplement. Curcumin is chemically a diarylheptanoid belonging to the curcuminoids group. This group of materials are natural phenols responsible for turmeric's yellow color. It is a tautomeric compound which exists in organic solvents in an enolic form, as well as in water in a keto form [106]. The chemical structure of curcumin is shown in Figure 6.

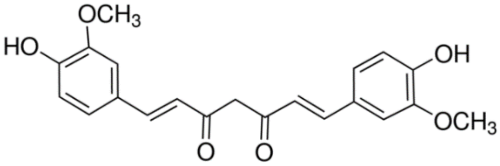

Figure 6. Molecular structure of curcumin [105].

Curcumin has a prolonged usage as a dietary ingredient with known health benefits. Over the last decade, extensive studies has shown that curcumin possesses anticancer activities with a preventive capacity or as a treatment agent against cancers. It exhibits such properties either as a single therapy or as a combination with chemotherapeutic agents. Curcumin also affects multiple steps in the carcinogenic process, which is important to avoid chemoresistance. Chemoresistance is the main problem in cancer chemotherapy which is common in advance staged cancers and is the major cause of cancer-related death. The curcumin function as a chemo-sensitizing agent in combination therapy has also important to overcome chemoresistance [106].

Due to its anti-inflammatory, antioxidant, anticancer and antimicrobial effects [107] curcumin has been recognized as one of the most active therapeutic agent of turmeric [108]. It has been reported that curcumin possess several biological activities which are therapeutically beneficial to cancer treatment. Moreover, it has been revealed that curcumin increases the efficacy of other chemotherapeutic agents and reduce their toxic side effects. Note that such toxic side effects are the major drawback of most chemotherapeutic agents. Curcumin is well known also for its anti-inflammatory activities. The presence of keto form and double bonds in the curcumin structure is believed to be responsible for its anti-inflammatory function [109]. Due to the fact that cancer often develops under chronic inflammatory conditions, curcumin can act as a preventive treatment agent against cancer. Unlike most chemotherapeutic agents which affect a specific process of cancer development, that is, cell growth or apoptosis, curcumin influence various stages of cancer development. Specifically, it affect oncogene activation, cancer cell proliferation, apoptosis evasion, anoikis resistance, and metastasis [106].

Piperine is an alkaloid that can be found in the fruits and also in the roots of *Piper nigrum* and *Piper longum* species of *Piperaceae* family. The presence of alkaloid is responsible for the pungency of black pepper and long pepper. The chemical structure of piperine has been showed in Figure 7.

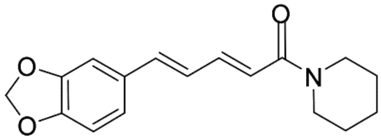

Figure 7. Molecular structure of piperine [110].

This compound represents a variety of phytochemical and pharmacological activities such as antioxidant, anti-inflammatory anticancer, antiviral and hepatoprotective effects [110,111]. Piperine increases the secretion of pancreatic enzymes and bioavailability of many drugs. It prevents oxidative damage and decreases lipid peroxidation due to its anti-inflammatory properties (either alone or in combination with other herbal drugs) can be used for the treatment of rheumatoid arthritis [112].

The anti-tumor activity of piperine was detected when its oral administration could prevent some forms of gastrointestinal cancers [113]. An alcoholic extract of black pepper containing piperine, could act as an effective treatment against lung cancer by altering lipid peroxidation, which leads to the spread of free radical reactions and cellular damage [114].

1.6. Scaffold Fabrication Techniques

Due to the crucial importance of scaffolds in the tissue engineering approach, which is mimicking the structure and the function of ECM, constant efforts are made at scaffold design and development. In spite of recent progress and advances in scaffold fabrication techniques, further improvements are still necessary for processing biomaterials as porous cell carriers with desirable porosity, pore size and structure and outer shape [115]. The desired structure and characteristics of the scaffold can be varied and must be designed according to the application type, the target organ and the seeded cell type. Another factors such as anatomical location, patient age, trauma severity and other pathological conditions must also be considered [116]. A variety of processing technologies have been developed to produce highly porous 3D scaffolds with appropriate pore size and interconnected pore structure. The scaffold fabrication technique must be flexible to design alternatives to meet multiple requirements for these constructs. Some of the current conventional techniques for fabrication of porous scaffolds are thermally induced phase separation (TIPS) [117-119], solvent casting and particulate leaching [120,121], sintering [122,123], gas foaming [124,125], emulsion freeze-drying [126,127], melt-molding [128] and electro-spinning [129,130]. Scaffolds produced by such techniques have a huge number of tissue engineering applications such as bone regeneration. Using the conventional methodologies, scaffolds with a continuous and uninterrupted pore structure can be produced. However, the resulted scaffolds are sometimes lacking in long-range channeling microarchitecture, precision and reproducibility [131,132].

The interior architecture of the scaffolds fabricated by the conventional methods are determined by elements of the processing technique [132]. In other words, the control over the scaffold architecture using these techniques is highly process-driven, and not design-driven [133]. For example in particulate leaching, the internal structure of the scaffold is determined by the embedded salts in the dissolved polymer matrix. Since the salt particles are subsequently leached and leave behind the interior pores, the pore diameters of the scaffolds can be controlled by regulating the salt particle size. However, agglomeration of salt particles during the leaching process can alter the final size and distribution of the pores [131]. In the case of freeze drying, the scaffold internal architecture is controlled by the size and microstructures of the solvent crystals, which in turn, are governed by the freezing rate [134].

Table 1 briefly presents the advantages, limitations and some other specifications of the commonly used scaffold fabrication techniques. The majority of the scaffold fabrication techniques are based on applying heat and/or pressure or an organic solvent to the polymer system. The choice of fabrication technique highly depends on the bulk and surface properties and other requirements for the specific type of tissue [135].

Table 1. Comparison of the scaffold fabrication techniques. Produced based on [116,135-138].

Fabrication Technique	Advantages	Limitations	Other Specifications
Solvent casting/Particulate leaching	1. Easy and low-cost 2. High porosity 3. Control over process 4. Compatible with other techniques	1. Limited control over pore size and distribution 2. Low pore interconnectivity 3. Use of organic solvent 4. Time-consuming	Suitable for thin 3D matrices
Gas foaming	1. No use of organic solvents 2. High porosity 3. Control over process	1. Quite expensive and equipment-needed process 2. low interconnectivity	1. Use of pressure 2. Creating closed-pore structure

	4. Stable processing	3. Limited to certain polymers	
Emulsion freeze drying	1. No use of high temperatures 2. High porosity 3. Control over process and pore size	1. Low pore interconnectivity 2. Use of solvents 3. High energy consumption 4. Time consuming	Use of pressure
Solid freeform fabrication (SFF)	1. Control over process, porosity, pore size and interconnectivity 2. No use of organic solvents 3. High reproducibility	1. Advanced equipment-needed process 2. Micro-scale resolution is not ideal in some SFF techniques	Use of computer-controlled equipment
Electrospinning	1. High surface area to volume ratio 2. High porosity and pore interconnectivity 3. Easy and cost-effective process 4. Control over process 5. Tailorable mechanical properties	1. Difficult to obtain 3D structures (mostly 2D) 2. Limited control over micro-architecture/pore size 3. Low mechanical strength 4. Residual solvent problems 5. Limited to certain polymers 6. Many process variables	1. Use of electric field 2. Special process for fabrication of fibrous structures (in micro/nano scale)
Thermally-induced phase separation (TIPS)	1. Easy and low-cost 2. High porosity and pore interconnectivity 3. Control over process, morphology and pore size 4. Producing 3D matrices with controllable shape 5. Control over structural isotropy 6. Tailorable mechanical properties 7. Compatible with other techniques	1. Use of organic solvent 2. Limited to certain polymers 3. Complex procedure	1. Able to produce random/oriented microporous structures 2. Able to produce fibrous structures (in micro/nano scale)

On the other hand, computer-aided design and solid freeform fabrication (SFF) [133,139] are design-driven techniques and in some cases have been combined with the conventional methods [135,140]. The hybrid techniques allow fabricating scaffolds with hierarchical macro/microporous structures. While micropores are necessary for cell adhesion and growth, macropores permit vessel growth and transport of nutrients and metabolic wastes throughout the matrix [135].

Among the conventional scaffold fabrication techniques, thermally-induced phase separation (TIPS) methodology has received great scientific attentions in recent years. It has been the subject of over 2,000 technical papers published in the past 10 years. One of the most attractive characteristics of the TIPS technique over other conventional methods is its capacity for the formation of an intrinsically interconnected porous network in a single and simple process that is fast, controllable and scalable [7]. The architecture and morphological features of the scaffolds produced by the TIPS technique can be closely controlled by manipulating the process parameters, including the polymer type and concentration, ceramic content, solvent/non-solvent type and ratio, surfactant or porogen addition and quenching temperature, period and rate [141,142].

1.7. Thermally-Induced Phase Separation (TIPS)

Phase separation of polymer solutions has previously been used for preparation of synthetic membranes. There are four main methods for the preparation of polymer matrices through controlled phase separation process [117-119] as follows:

- *Thermally induced phase separation (TIPS)*: This method is based on the phenomenon that the solvent quality usually decreases by decreasing the temperature. When phase separation is induced in the polymer solution, the solvent can subsequently be removed by extraction, evaporation or freeze drying [143].

- *Air-casting of a polymer solution* [144,145]: In this process, the polymer is dissolved in a mixture of a solvent and a nonsolvent with high and low volatility, respectively. Since the solubility of the polymer decreases during the evaporation of the solvent, the phase separation can occur.

- *Precipitation from the vapor phase*: In this method the phase separation is induced in the polymer solution through penetration of nonsolvent vapor in the solution.

- *Immersion precipitation*: The polymer solution is cast as a thin film or is extruded through a die, and then is immersed in a nonsolvent bath. Since the good solvent in the polymer solution is exchanged for nonsolvent, the precipitation can takes place.

The difference between the four methods is based on differences in separation mechanisms [143]. While each of these methods has its advantages, thermally-induced phase separation TIPS procedure is perhaps the most versatile and simplest fabrication technique [146]. The TIPS method is suitable for binary mixtures involving a polymer and a solvent, where the latter component is usually referred to as the diluent [116]. In its simplest form, the TIPS process consists of the following steps (Figure 8):

- *Solution preparation*: a homogeneous solution is formed through blending the polymer with a liquid with high boiling point and low molecular weight, as the diluent at an elevated temperature. The initial temperature must be less than the diluent boiling point and typically 25-100 K higher than the melting point or glass transition temperature of the pure polymer. At this initial temperature, the polymer must be stable and the diluent should have low volatility.

- *Phase separation*: the polymer solution is cast into the desired shape and then is cooled at a controlled rate to induce phase separation and solidification of the polymer.

- *Solvent removal*: the diluent is finally removed (typically by solvent sublimation or extraction) to form a microporous structure. In case of removing the solvent by extraction, the extractant must also be removed, which is typically performed through evaporation [146,147].

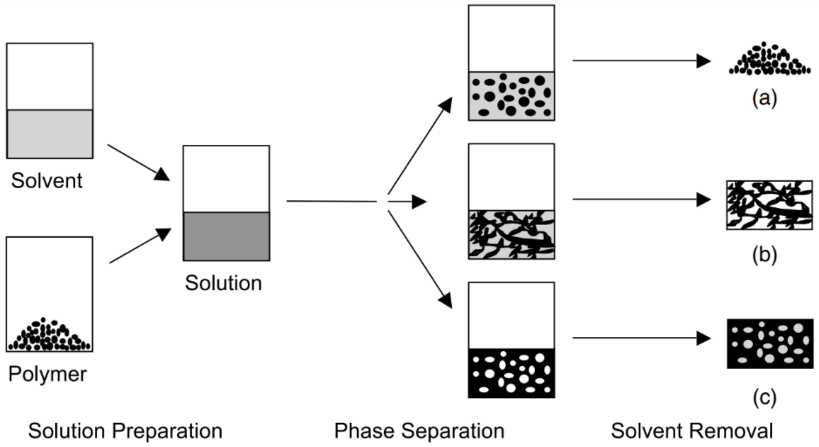

Figure 8: Schematic illustration of phase separation process including three main steps of solution preparation, phase separation and solvent removal. The structures obtained after removing the solvent are: polymer beads (**a**), polymer matrix with a continuous network (**b**) and foam with closed pores (**c**) [148].

The TIPS method at least from one point of view can be distinguished from the familiar nonsolvent-induced phase inversion process. In the TIPS process, the homogeneous solution is converted to a two-phase mixture through removing the thermal energy, not by the slow exchange of solvent with nonsolvent. TIPS method has some important advantages over the other methods. First, the TIPS process is applicable to a broad range of polymers, as polymers with poor solubility could not be used in nonsolvent-induced phase inversion process. Hence, one of the distinct advantages of TIPS is its potential to be applied for semi-crystalline polymers. Second, TIPS technique is capable of producing a variety of microstructures [149-154]. Third, TIPS has also the capability to produce relatively thick isotropic microporous structures suitable for controlled release. Formation of anisotropic microporous structures via TIPS process is also possible if the direction of thermal gradient applied to the solution is controlled [152-154]. Due to the fewer process variables, the TIPS procedure is easier to control than nonsolvent-solvent exchange method [146]. Microporous polymeric matrices can be prepared via solid-liquid or liquid-liquid phase separation mechanisms with subsequent solidification of the polymer [149-151].

1.7.1. TIPS Process Based on Liquid-Liquid Mechanism

Phase separation through liquid-liquid mechanism play an important role in most of the TIPS processes [143]. Liquid-liquid phase separation can take place in the solution systems involving either crystalline or glassy polymers. In a system involving a semicrystalline polymer, the miscibility is the main factor determining the phase separation occurs through liquid-liquid or solid-liquid (through crystallization of the polymer) mechanisms. The miscibility of the system is quantified as the interaction parameter of the semicrystalline polymer-diluent system [155]. If the polymer-diluent interactions are strong (small interaction parameter), the system undergoes solid-liquid phase separation via crystallization of the polymer during cooling. Conversely, when the polymer-diluent interactions are weak (great interaction parameter), the system becomes unstable and liquid-liquid phase separation occurs, showing an upper-critical solution temperature (UCST) behavior. Many semicrystalline polymer-diluent systems at low polymer concentrations undergo liquid-liquid phase separation followed by polymer crystallization, while at high polymer concentrations only solid-liquid phase separation (i.e. polymer crystallization) occurs [147,155].

1.7.1.1. Phase Equilibria in Liquid Polymer Systems

Thermodynamics of polymer solutions were modeled by Flory and Huggins by utilizing a mean field approach:

$$\Delta H_{mix} = k_B T \chi \phi (1-\phi) \tag{1}$$

$$\Delta S_{mix} = -k_B \left[\frac{\phi}{N} \ln \phi + (1-\phi)\ln(1-\phi)\right] \tag{2}$$

Where N is the degree of polymerization, ϕ is the volume fraction of polymer, k_B is the Boltzmann constant, T is absolute temperature, χ is the Flory–Huggins interaction parameter and ΔH_{mix} and ΔS_{mix} represent the enthalpy and entropy of mixing, respectively [156]. On the other hand the relation between the Gibs free energy of mixing and enthalpy and entropy of mixing is:

$$\Delta G_{mix} = \Delta H_{mix} - T\Delta S_{mix} \tag{3}$$

Thus, the former equations can be solved for ΔG_{mix} , as it has been formulated by Flory and Huggins to give:

$$\Delta G_{mix} = k_B T \left[\frac{\phi}{N} \ln \phi + (1-\phi)\ln(1-\phi) + \chi\phi(1-\phi)\right] \tag{4}$$

The miscibility criteria in binary polymer-diluent systems at a fixed temperature T and pressure P, can be expressed in terms of ΔG_{mix} and its second derivatives with respect to polymer volume fraction, ϕ_p, as follows:

$$\Delta G_{mix} < 0 \tag{5}$$

$$(\partial^2 \Delta G_{mix}/\partial \phi_p^2)_{T,P} > 0 \tag{6}$$

If each of two criteria is not met, the solution may separate into two phases which are in equilibrium. The expressed criteria have been illustrated in Figure 9, with three possibilities: immiscibility (Figure 9a) and miscibility (Figure 9c) in the entire composition range, and partial miscibility, i.e., immiscibility within the composition range where second derivative is negative (Figure 9b). These three possibilities can represent three different polymer-diluent systems or one system at three different temperatures [147].

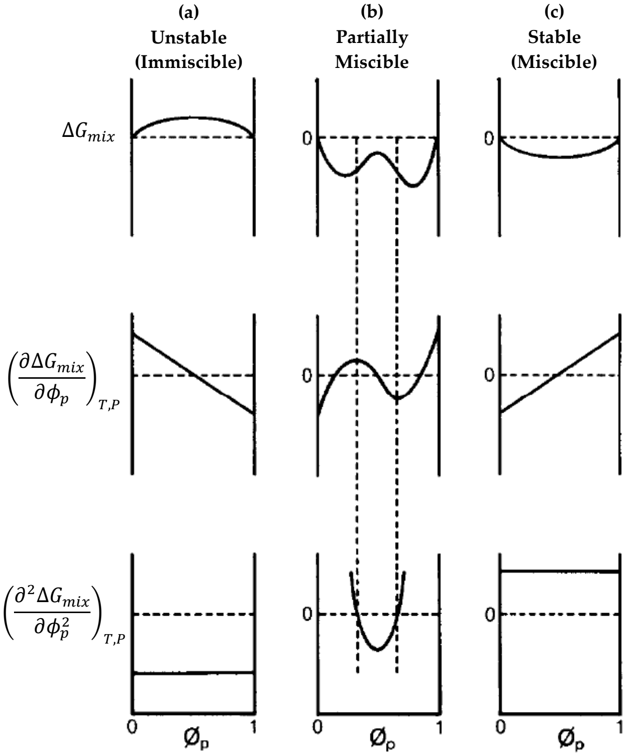

Figure 9. Gibbs free energy of mixing and its first and second derivatives as a function of the volume fraction of polymer, ϕ_p, at a fixed temperature and pressure: immiscibility (**a**), partial miscibility (**b**) and miscibility (**c**) [147].

If a polymer-diluent system is partially miscible, a homogeneous one-phase solution is formed only under certain composition-temperature conditions (Figure 10a). Considering the line represent the fixed temperature of T_2, ΔG_{mix} is negative across the entire composition range, indicating the possibility of being miscible. However, there is an upward bend in the ΔG_{mix}-composition curve between co-tangential points, ϕ'_b and ϕ''_b. In the region where ΔG_{mix} of the homogeneous solution is greater (i.e., less negative) than that of the points ϕ'_b and ϕ''_b the occurrence phase separation can minimize the free energy of the system. Therefore, any initial composition between ϕ'_b and ϕ''_b, separate into two phases with compositions of ϕ'_b and ϕ''_b. Since the two separated phases are in equilibrium, they have the same chemical potential (that is, the derivative of ΔG_{mix} with respect to composition), indicated by a common tangent.

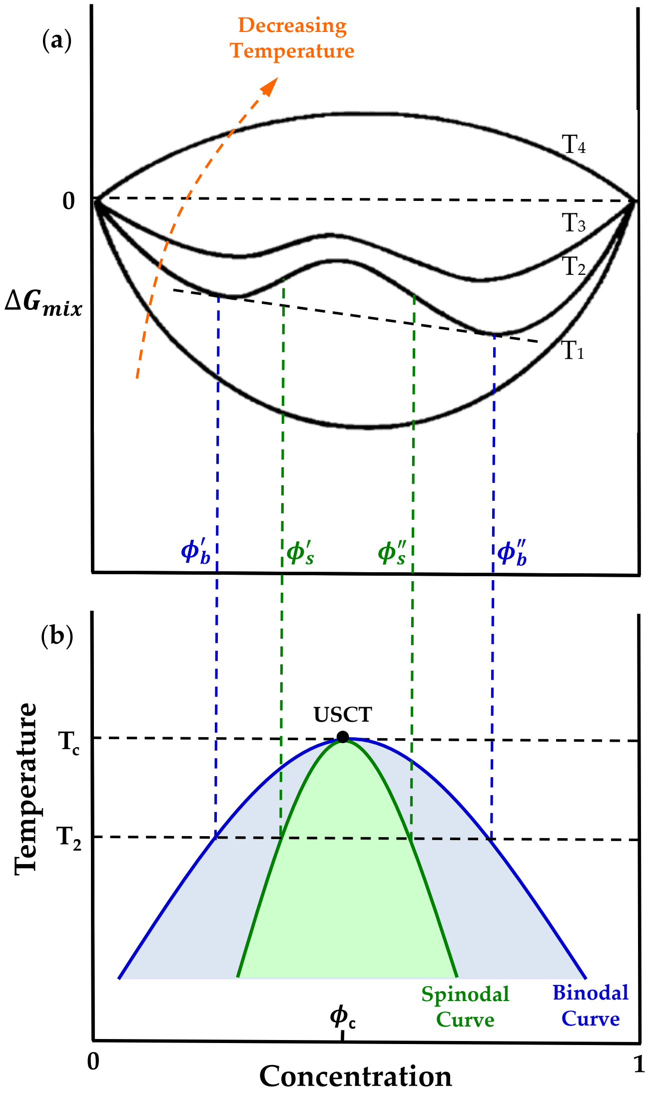

Figure 10. Changes in Gibbs free energy of mixing as a function of volume fraction of polymer at different temperatures ($T_1 > T_2 > T_3 > T_4$), showing miscibility (T_1), partial miscibility (T_2) and (T_3), and immiscibility (T_4) (**a**). Plotting the minimum points (i.e., ϕ_b' and ϕ_b'') and inflection points (i.e., ϕ_s' and ϕ_s'') for each temperature, gives binodal and spinodal curves, respectively (**b**). The inclined dashed-line indicate common tangent (equilibrium phases of equal chemical potential). The arrow shows the effect of temperature for a system with an UCST. Produced based on [147,157,158].

The second derivative of ΔG_{mix} is negative in the composition range between ϕ_s' and ϕ_s'', (i.e., the inflection points) in the ΔG_{mix}-composition curve. This indicates that the system in this composition range is unstable, so in this region there will be a spontaneous phase separation [147]. In this region, all fluctuations in composition lead to a decrease in free energy and trigger a wave of fluctuations within the solution [143]. The second derivative of ΔG_{mix} between the compositions ϕ'_b and ϕ'_s and also between ϕ''_s and ϕ''_b is positive. In these regions, there is no spontaneous phase separation because the system is metastable (i.e., is stable to small fluctuations in concentration). The terms unstable and metastable refer to the solution's ability to resist phase separation. Phase separation in metastable region can take place where there is a large enough fluctuation in concentration that can overcome the energy barrier [147]. The degree of undercooling necessary to induce phase separation through binodal mechanism is very low for polymer solutions [143].

The effect of temperature on a partially miscible system with UCST is observed in Figure 10a. At high temperatures within the entire composition range, there is sufficient thermal energy to achieve a homogenous solution. By decreasing the temperature, thermal energy is removed and the strength of the polymer-diluent interactions decreases. Thus, the polymer and diluent molecules retract each other and phase separation occurs in the composition range between the co-tangential points. If the locus of co-tangential points in Figure 10a is plotted during cooling in the form of a temperature-composition phase diagram, the obtained curve is referred to "binodal curve" [147], which is presented with a blue curve in Figure 10b. The boundary of the liquid-liquid demixing region is usually called the binodal, but the term "cloud point curve" is more appropriate for polydisperse polymers. Compositions located on the binodal curve and connected by a horizontal tie line are in equilibrium (e.g., the compositions ϕ'_b and ϕ''_b which are located on the intersections of binodal curve and the dashed line representing the temperature T_2 in Figure 10b). The ratio of the equilibrium phases with specific composition is determined by the lever rule [143]. In a similar way, if the locus of inflection points is plotted the obtained curve is referred to "spinodal curve" (green curve in Figure 10b).

A schematic phase diagram for a binary polymer-solvent system displaying an UCST has been illustrated in Figure 11, showing the one-phase region (i.e. homogenous solution) and the boundary of liquid-liquid phase separation with the possible structures formed in the different parts of two-phase region. For a polymer solution involving a solvent with lower molecular mass, a strongly asymmetric phase diagram is typical [148]. Binary phase diagrams by illustrating the phase boundaries as a function of temperature and composition, specify which phase transition can takes place in the solution during the TIPS process. An equilibrium phase diagram provides a map for the thermodynamically favored phase transitions. However, the kinetics of phase separation processes determine whether the thermodynamically favored transition will occur or not, and also to what extent the transition will take place [143].

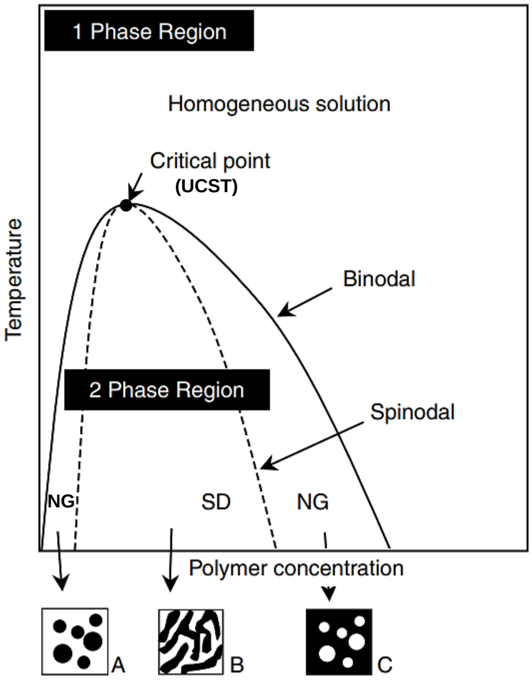

Figure 11. Schematic temperature-composition phase diagram for a polymer-diluent system displaying an upper critical solution temperature (UCST), one-phase region (homogenous solution), binodal (solid-line) and spinodal (dashed-line) curves and liquid-liquid phase separation in the two-phase region through nucleation and growth (NG) or spinodal decomposition (SD) mechanisms. Insets A, B and C illustrate the structure obtained from each region [148].

The binodal curve (the solid curve in Figure 11) separates the homogeneous one-phase liquid region from the heterogeneous two-phase liquid-liquid region (including both unstable and metastable regions) [147,148]. The kinetic barrier against the phase separation in the metastable region, can be overcome through a nucleation event [143]. Thus, two liquid phases in the metastable regions are separated through a nucleation and growth mechanism [148,149]. Specifically, in this regions the system separates by nucleation and growth of the droplets of polymer-rich phase in a surrounding matrix of polymer-lean phase when the polymer concentration is lower than that of the critical point. Conversely, the droplets of polymer-lean phase are formed in a surrounding matrix of polymer-rich phase, at concentrations higher than critical point. The formed droplet in both cases can grow because of the presence of a concentration gradient towards the droplets [143]. For concentrations lower than critical point, the resulting morphology after removing the solvent is composed of solid polymer beads [150] or a powder-like structure, while for concentrations higher than the critical point a foam with a closed-pore structure is formed [148].

The spinodal (the dashed curve in Figure 11) divides the two-phase region into unstable and metastable regions, the former below the spinodal curve and the latter surrounded by the binodal and spinodal curves [147]. Since there is no activation barrier against phase separation in the unstable region, the phase separation occurs spontaneously through spinodal decomposition mechanism [148,149]. In the unstable region, when a wave of concentration fluctuations throughout the solution is triggered, fluctuations with different wave lengths and amplitude develop. The amplitude of the fluctuations will increase because the molecules of both components are moved from the low-concentration to high-concentration regions. The wave length with the highest growth rate results in the formation of most-frequently domain size (Figure 12) [143].

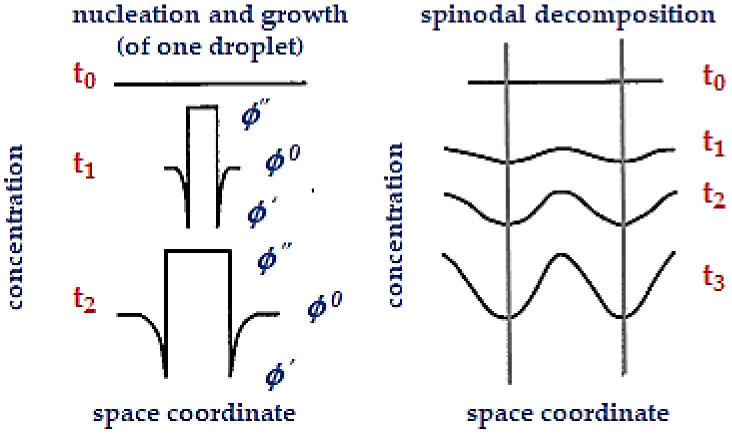

(**a**) (**b**)

Figure 12. A schematic depiction for the nucleation and growth process via binodal mechanism (**a**), and for the concentration fluctuations as a function of time during spinodal decomposition (**b**). ϕ^0 represents the original polymer concentration; $\phi'$and ϕ''represent binodal compositions. t_0-t_3 indicate time, starting from initial time, t_0. The vertical lines represent the wave length of the fluctuation in the composition. Based on [143].

When the fraction of the minor phase is high enough, spinodal decomposition will proceed through the formation of -bicontinuous structures in which both polymer rich-phase and polymer-lean phases are completely interconnected [143,148,151]. After removing the solvent, a polymer matrix with a continuous pore network and fine pores ranging from several to tens of microns is formed. The development dynamics of this fine-scaled structure obtained by spinodal decomposition are expected to be very fast, without enough time to have a control over the experimental condition [148].

The maximum temperature at which a two-phase liquid-liquid mixture can exist is the critical point, at which the binodal and the spinodal curves coincide. This point is unique for each polymer-diluent system and is indicated by the critical temperature, T_c, and critical concentration, ϕ_c, which represent the critical point value [147,160]. In the vicinity of the critical point, the quantity and compositions of the two separated phases become more similar. For monodisperse polymers, this point is located at the maximum point of the binodal curve, but for polydisperse polymers the system becomes more complicated [143]. The critical point also satisfies the following criteria:

$$(\partial^2 \Delta G_{mix}/\partial \phi_p^2)_{T,P} = 0 \qquad \text{(Criterion 1)}$$

$$(\partial^3 \Delta G_{mix}/\partial \phi_p^3)_{T,P} > 0 \qquad \text{(Criterion 2)}$$

$$(\partial^4 \Delta G_{mix}/\partial \phi_p^4)_{T,P} = 0 \qquad \text{(Criterion 3)}$$

The interaction parameter at the critical point, which is known as the critical interaction parameter (χ_c) is also used as a criterion of system miscibility. Both ϕ_c and χ_c are dependent on the size of the polymer and diluent molecules [147,159,160].

Regarding phase diagram, liquid-liquid phase separation through a pure spinodal mechanism can only be achieved in a solution with the concentration of critical point. In all other cases, the metastable area must be passed first. It is important to note that the transition between binodal and spinodal decomposition mechanisms should be regarded as a gradual change and not a sudden change. High cooling rates can be used to prevent phase separation in the metastable area [143]. The Flory-Huggins equation for the polymer-diluent system is:

$$\frac{\Delta G_{mix}}{RT} = \frac{\phi_d}{x_d} \ln \phi_d + \frac{\phi_p}{x_p} \ln \phi_p + \chi \phi_d \phi_p \qquad (7)$$

Where ΔG_{mix} is the Gibbs free energy of mixing per lattice site, ϕ_d and ϕ_p are respectively the volume fraction of the diluent and polymer, x_d and x_p are respectively the number of lattice sites occupied by diluent and polymer molecules, and χ is the Flory-Huggins interaction parameter. The first two terms on the right side of Flory-Huggins equation are always negative, representing the combinatorial entropy. The last term on the right side represents the enthalpy contribution and depending on the sign of χ can be positive or negative [147]. The chi (χ) parameter, reflects the compatibility of the polymer and solvent pair and can be calculated through the Hansen's solubility parameters according to equation (8), as follows:

$$\chi = \frac{V_m}{RT}\left[(\delta_D^{pol} - \delta_D^{sol})^2 + 0.25(\delta_P^{pol} - \delta_P^{sol})^2 + 0.25(\delta_H^{pol} - \delta_H^{sol})^2\right] \qquad (8)$$

Where; δ_D, δ_P, and δ_H are the dispersion, polar, and hydrogen bonding component of Hansen's solubility parameters, respectively [156]. Lower χ values indicate better compatibility between the solution components or improved solubility of polymer in the solvent. According to equation (8), decreasing the solution temperature lead to an increase in the χ value and a UCST behavior.

If χ has a large positive value, ΔG_{mix} becomes positive and thus the liquid–liquid phase separation becomes thermodynamically favorable [161]. The effect of χ on the shape and location of the binodal curve has schematically been shown in Figure 13.

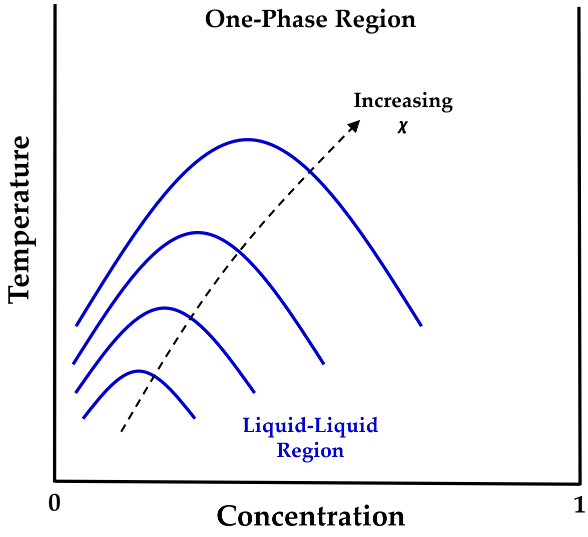

Figure 13. Effect of strength of interaction on shape and location of binodal curve. (Except χ, all variables in Flory-Huggins equation are fixed). Reproduced based on [147,149]

As it is observed, the position of the binodal curve is influenced by the interaction parameter, such that as χ increases, the curve shifts up to higher temperatures and concentrations [162,163]. Specifically, selecting a diluent with lower compatibility with the polymer results in weaker interactions between the solution components (i.e., greater χ). In such condition, the location of binodal curve shifts to higher temperatures at a specific polymer concentration, or to higher polymer concentrations at a specific temperature, and therefore the two-phase liquid region increases in size [147,149].

1.7.2. TIPS Process Based on Solid-Liquid Mechanism (Polymer Crystallization)

A polymer could be able to crystallize when its molecular chain enjoys sufficient regularity. Crystallization of such polymers from the solution depending on concentration can lead to different morphologies from loose precipitates to various types of percolating structures (i.e. interconnected networks of crystallites). Such interconnected networks are one case among several types of solid-like phases that are called "gels" [164,165]. A schematic crystallization curve with the trends toward the formation of different gel morphologies as a function of polymer concentration has been depicted in Figure 14. Chain folded lamellae are usually formed through crystallization of the polymer from low concentrated solutions. The morphology of the lamellae is strongly affected by the polymer characteristics and the crystallization conditions. As it is observed in Figure 14, a suspension of supramolecular architectures of these lamellae is obtained at higher polymer concentrations. Axialites and spherulites are examples of supramolecular structures that can be isolated from gels or solid-liquid phases. The supramolecular organization of the crystals is affected by kinetic aspects of the crystallization [143].

When the polymer crystallinity is decreased, the extent of the supramolecular organization of the lamellae is decreased. Nevertheless, the final morphology of the crystallites also depends on the kinetics of nucleation and growth. When a polymer can crystallize into different crystalline forms, the different crystal stability and nucleation, and growth rates result in a complicated gelation behavior.

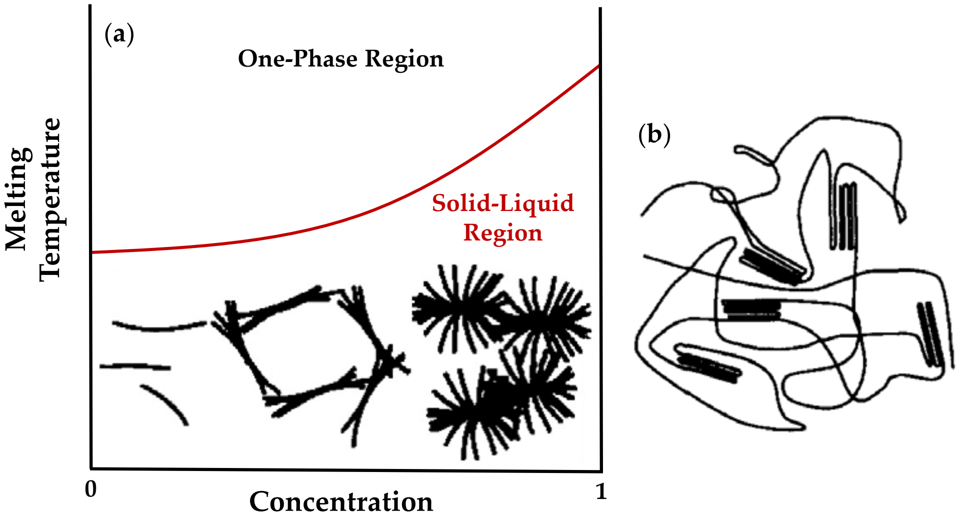

Figure 14. (**a**) Schematic equilibrium phase diagram for solid-liquid transition (polymer crystallization). Crystallization/precipitation of polymer from the solution at very low, low and high polymer concentrations results in the formation of single crystals, lamellar stacks and spherulites, respectively. (**b**) Molecular depiction of a gel formed via polymer crystallization from a dilute solution showing amorphous and crystalline regions. The junctions between the polymer chains are assumed to have a chain folded nature. Modified from [143].

At high enough polymer concentrations, interpenetration and interlocking of crystal agglomerates can lead to the formation of stiff brittle crystalline gels. Almost all crystalline polymers can form these kinds of gels [143,148]. The formation of gels rather than unconnected precipitates can be promoted in several ways, for example by stirring the solution or introducing flow and increasing the polymer concentration or molecular weight [164,165]. The gel may be turbid or transparent depending on the size of the polymer crystallites. Large crystallites and turbid gels are usually formed by using highly crystalline polymers will usually give relatively while transparent gels can be formed by low-crystallinity polymers (like random copolymers). The fringed micelle is postulated to be the crystallization model for very small crystallites [143]. In this model, the junctions are formed by passing the polymer chains through each other, not by chain folded crystallites.

However, properties like heat and temperature of fusion for the gel crystallites of some low-crystallinity polymers are the same as those of the chain folded crystallites precipitated from dilute solutions. Thus, it can be supposed that the junctions in the gels made of such low-crystallinity polymers have been formed by the chain folded crystallites, and not by fringed micelle crystallites [143,166]. A gel molecule with the junctions formed by chain folded crystallites has been sketched in Figure 14b and shows its amorphous and crystalline regions.

1.7.2.1. Phase Equilibria in Semi-Crystalline Polymer Systems

For binary polymer-diluent systems involving a polymeric component which is able to crystallize, the polymer melting/crystallization point can be related to the mixture composition. The melting point of a semi-crystalline polymer is depressed due to the presence of a diluent. The depression magnitude has been formulated by Flory in a semi-empirical way, as follows:

$$\frac{1}{T_m} - \frac{1}{T_m^0} = \frac{RV_u}{\Delta H_\mathrm{u}\, V_d}(\phi_d - \chi\phi_d^2) \tag{9}$$

Where T_m and T_m^0 are the melting temperatures of the semicrystalline polymer in the solution and in the pure form, respectively; V_d is the molar volume of the diluent, V_u is the molar volume of the repeating unit, ΔH_u is the heat of fusion for the repeating unit, ϕ_d is the volume fraction of the diluent, and χ is the Flory-Huggins interaction parameter [161]. The former equation can be solved for T_m to give:

$$T_m = \frac{1}{\frac{RV_u}{\Delta H_\mathrm{u}\, V_d}(\phi_d - \chi\phi_d^2) + \frac{1}{T_m^0}} \tag{10}$$

T_m has been plotted as a function of $\phi_p (= 1 - \phi_d)$ in Figure 15. The line which distinguishes the homogeneous one-phase liquid region at high temperatures from the heterogeneous two-phase solid-liquid region refers to the melting point depression curve [146]. According to Flory's theory, the melting point depression curve for the polymer-solvents system, is mostly determined by the polymer concentration and the heat of fusion of the polymer crystals [143]. When all other variables in equation (10) are constant, smaller ΔH_u value results in larger melting point depression [146]. For a given polymer, the degree of melting point depression is controlled by the diluent volume fraction (ϕ_d) and molar volume (V_d) and also χ parameter [149]. Therefore, all else being equal, the smaller molar volume of diluent with respect to polymer, leads to larger melting point depression [146]. Conclusively, at a given polymer concentration, the depression degree is controlled by the value of χ. Specifically, if χ increases, the melting point increases and the slope of the melting point curve decreases as shown in Figure 15 [147,162].

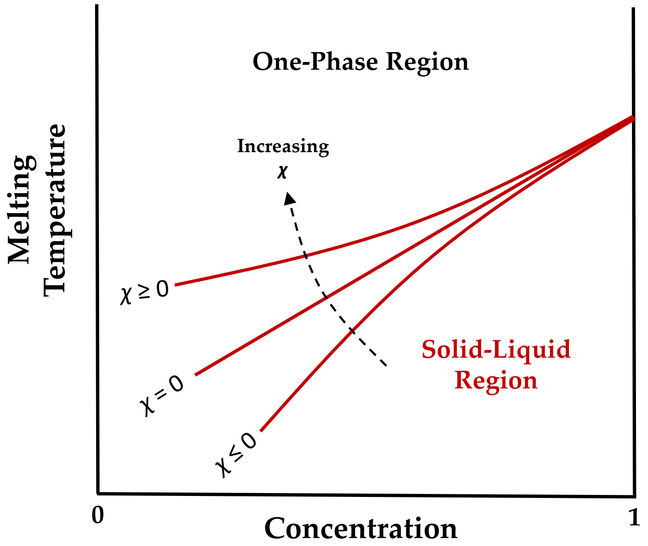

Figure 15. Schematic temperature-composition phase diagram for a binary polymer-diluent system containing a semi-crystalline polymer showing the effect of interaction parameter χ when all other variables in equation (10) are fixed. Reproduced based on [146].

When the strength of interaction decreases (χ increases), the temperature at which the solid-liquid phase separation (i.e., via polymer crystallization) occurs increases. For $\chi \leq 0$, the relationship shows a concave curvature with respect to the horizontal composition axis. For $\chi = 0$, the relationship is linear and for $\chi \geq 0$, a convex curvature is observed [146].

In case of a large positive χ, the plot tends to be stabilized through the formation of a binodal curve at least at low polymer concentrations (Figure 16). In this case, liquid-liquid phase separation followed by solid-liquid phase separation (via solidification of the polymer) is usually observed [146]. Consequently, the phase separation mechanism is changed from pure solid-liquid to liquid-liquid with subsequent polymer crystallization caused by low compatibility/interactions between polymer and solvent pair. If the χ value continues to increase, the monotectic point (which is the intersection of binodal and polymer crystallization curves) shifts to higher temperatures and concentrations and the two-phase liquid-liquid region also expands, as explained before. The changes in phase separation mechanism significantly affect the resulting matrix structure. The effect of interaction parameter, on the shape and position of the combinational phase diagram where all other variables are constant has been depicted in Figure 16 [147]. As it is observed, interaction parameter affect the position of the binodal curve to a higher extent than the polymer crystallization curve. Greater interaction parameter dramatically shift the binodal curve to higher temperatures with respect to the crystallization curve [143].

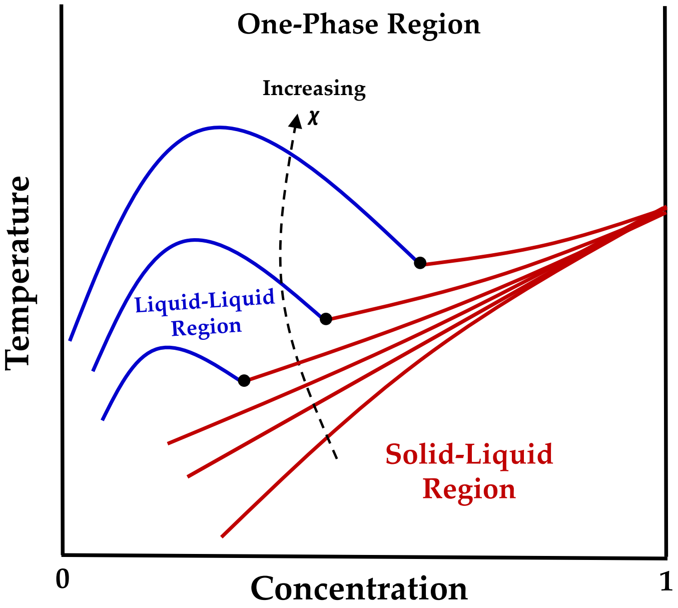

Figure 16. Effect of increase in χ value on the general phase diagram and the location of the monotectic point: Gradual change in phase separation mechanism from pure solid-liquid phase separation (i.e. crystallization of polymer) to a combination of solid-liquid and liquid-liquid phase separations. Reproduced based on [147,151].

1.7.3. Liquid-Liquid Phase Separation and Polymer Crystallization

1.7.3.1. General Phase Diagram

The general phase diagram for a system with weak interactions between the semi-crystalline polymer and diluent has been represented in Figure 17. In such diagrams, the position of the two-phase liquid-liquid region is below the binodal curve and on the left side of the monotectic point, ϕ_m. Below the melting point depression curve on the right side of ϕ_m and also below the horizontal broken line, the two-phase solid-liquid region is located. In these regions, the diluent is not able to dissolve all of the polymer and therefore the polymer crystallizes from the solution [147].

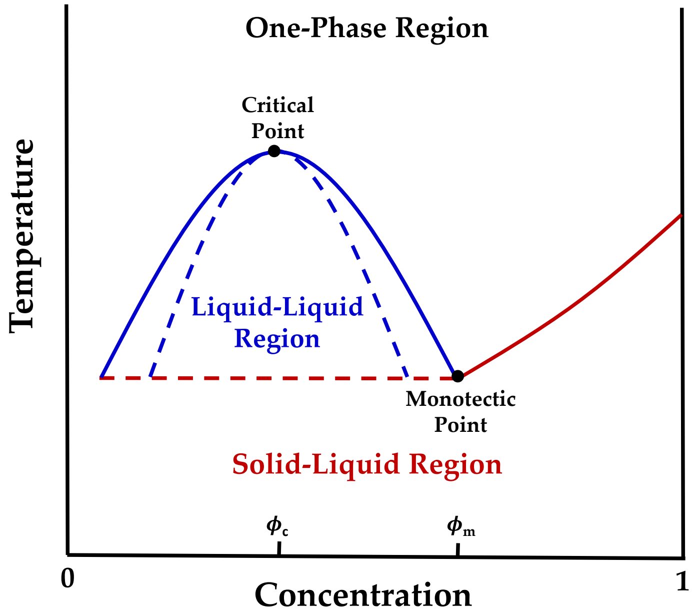

Figure 17. Schematic temperature-composition phase diagram for a system showing phase separation with two mechanisms of liquid-liquid and solid-liquid (i.e., polymer crystallization). Note monotectic point, ϕ_m. Reproduced based on [147,167].

In the areas below the binodal curve, liquid-liquid phase separation will first occur, when the solution passes through the binodal curve and the polymer-rich phase will be able to crystallize when the solution is cooled to a temperature below the monotectic transition temperature. The structure of the phase-separated solution via liquid-liquid mechanism is then stabilized by crystallization of the polymer in the polymer-rich phase. Thus, the final morphology will be largely dependent on liquid-liquid phase separation [143,148]

1.7.3.2. Non-Equilibrium Phase Diagrams

The kinetics play an important role in the competition between liquid-liquid phase separation and polymer crystallization. The thermodynamic background of liquid-liquid phase separation and polymer crystallization combination has previously been described by Burghardt [168]. In this situation, kinetic phenomena are important: generally liquid-liquid phase separation processes proceed rapidly in polymer solutions (even for a small degree of undercooling), while polymer crystallization through nucleation and growth develops slowly [143,148], and is dependent on the cooling rate and on the degree of undercooling. Due to the fast kinetics of liquid-liquid phase separation, it can precede polymer crystallization even when the polymer crystallization is thermodynamically favored [169]. Hence, the distance between the binodal curve and the polymer crystallization curve has great importance. Crystallization of the polymer can control the morphology of porous structure only if its corresponding curve is located at temperatures much higher than that of the binodal. However, when the liquid-liquid phase separation and crystallization curves are somewhat located in the same temperature range, the phase separation process can become very complicated [143]. Such systems has been studied by Önder *et al.* [149-151]. Different transitions can occur depending on the polymer concentration. Liquid-liquid phase separation is favored upon low polymer concentrations and relatively high temperatures, while solid-liquid phase separation is commonly the consequence of the combination of high polymer concentrations and higher temperatures. A polymer solution with a very low concentration is thermodynamically in equilibrium with a crystalline polymer phase at low temperatures (below the monotectic transition). The phase separation in this region is practically controlled by non-equilibrium processes (Figure 18).

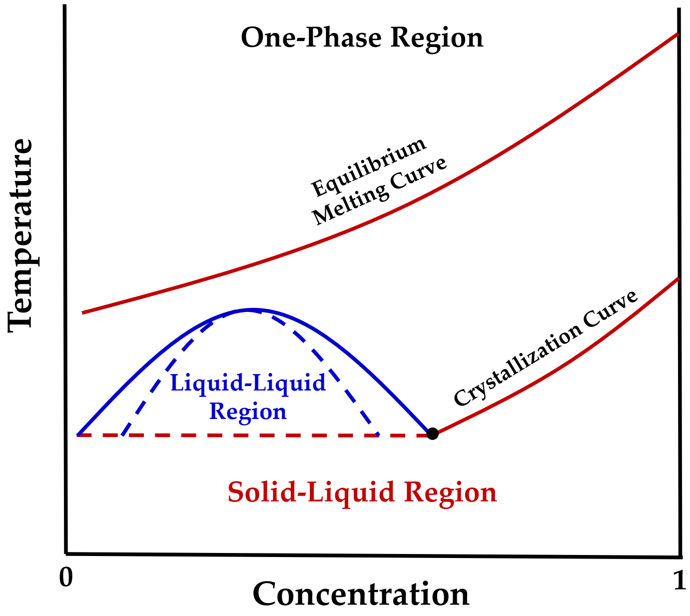

Figure 18. Schematic none-equilibrium phase diagram for a binary polymer-solvent system, showing equilibrium melting/crystallization point depression curve and crystallization curve of the polymer. Reproduced based on [143,170].

In the interpretation of phase diagrams, the melting point depression curve should not be confused with the crystallization curve. Due to the large activation energy needed for the formation of crystalline nuclei and its limited growth rate, the crystallization curve is located at much lower temperatures than the melting curve. The melting curve, that is, the melting temperature as a function of polymer concentration is obtained by reheating the crystallized solution. It can also be qualitatively described by an equilibrium theory, like the Flory theory for the melting point depression of polymeric crystals in the solution [161].

Upon non-equilibrium cooling conditions, the solution is cooled to a temperature below its corresponding equilibrium crystallization temperature while the polymer actually has not been crystallized from the solution yet (that is well-known as supercooling). In this situation, the practical crystallization temperature is less than the equilibrium melting/crystallization temperature [147].

The study of non-equilibrium systems for solutions rapid-crystallizing polymers resulted in a great variety of structures, ranging from crystallized polymer beads to spherulites with cellular or bicontinuous pore structures [149-151,171,172]. On the contrary, the polymer crystallization had less influence on the structure formed by liquid-liquid phase separation for slow-crystallizing polymers [143].

Taking into account that TIPS is practically a non-equilibrium process, the effects of cooling rate on the phase diagram must be considered. A controllable cooling rate in the experimental condition has a relatively slight influence on the liquid-liquid phase separation temperature and the location of the cloud point curve (which is representative of the binodal curve) [147,151]. On the contrary, a significant effect of the cooling rate on the solid-liquid phase separation temperature is observed. Supercooling affects the non-equilibrium phase diagram obtained from experimental conditions in different ways. By increasing the cooling rate (i.e., a higher degree of supercooling), the crystallization temperature of the pure polymer, polymer crystallization curve (i.e., crystallization temperature-concentration curve), and also the solid-liquid line beneath the liquid-liquid region shift to lower temperatures. In addition, the monotectic point, ϕ_m shifts to greater polymer concentrations to a small extent, leading to a possible change in the mechanism of phase separation (liquid-liquid followed by solid-liquid versus pure solid-liquid) in the concentration range near the monotectic point (Figure 19). For example, a polymer solution with a concentration slightly greater than ϕ_m would directly undergo solid-liquid phase separation upon slow cooling while may undergo liquid-liquid phase separation followed by polymer crystallization through fast cooling [147].

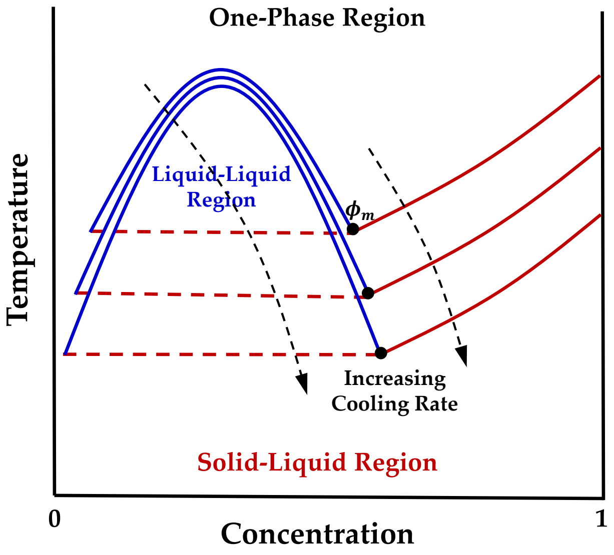

Figure 19. Effect of cooling rate on crystallization temperature-concentration curve, monotectic point and boundaries of liquid-liquid and solid-liquid regions in a non-equilibrium phase diagram. Produced based on [147,151].

1.7.4. TIPS process based on solid-liquid mechanism (solvent crystallization)

A polymer-solvent system in which the solvent crystallization temperature (freezing point) is higher than the liquid-liquid phase separation temperature, can separate by lowering the temperature [148]. In this process which is called solid-liquid phase separation, the solvent is frozen prior to liquid-liquid phase separation during cooling [143]. During solvent crystallization, the polymer is expelled from the solvent crystallization front to the grain boundaries of the solvent crystallite. After removing the solvent, the pore morphology will be similar to the typical geometry of the solvent crystallites. Depending on the applied temperature gradient during the cooling process, the pores may be large and isotropic or highly elongated (i.e. oriented) [143,148]. A schematic phase diagram for a system that undergoes liquid-liquid phase separation followed by solid-liquid phase separation (through crystallization of the solvent) has been illustrated in Figure 20. When the crystallization temperature of the solvent is much lower than the phase separation temperature (for example by using THF, DMF, dioxin/water solvent systems) the liquid-liquid phase separation occurs prior to the solvent freezing [148].

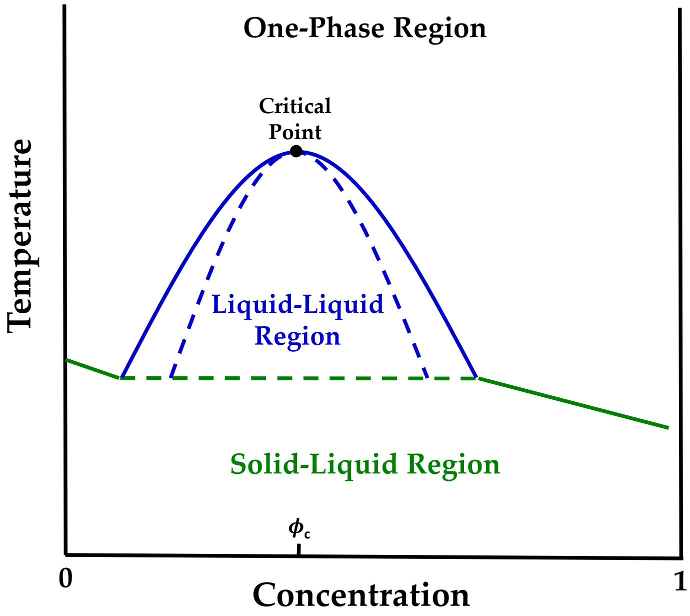

Figure 20. Schematic phase diagram representing a combination of liquid-liquid phase separation and solid-liquid phase separation (i.e., solvent crystallization). Reproduced based on [143,173,174].

In this situation, the microstructure is controlled by the earlier mechanism and there is no considerable influence of solvent crystallization on the morphology. In this case, the solvent freezing is an effective way to stabilize the structure of the phase-separated polymer solution [143]. The fine-scaled "early-stage" structure formed by liquid-liquid phase separation can be "frozen-in" when the solvent freezes [148].

1.8. References

1. Langer, R.; Vacanti, J. Advances in Tissue Engineering. *J. Pediatr. Surg.* **2016**, *51*, 8−12.
2. Hutmacher, D.W. Scaffolds in tissue engineering bone and cartilage. *Biomaterials* **2000**, *21*, 2529–2543.
3. Gregor, A., Filová, E., Novák, M. *et al.* Designing of PLA scaffolds for bone tissue replacement fabricated by ordinary commercial 3D printer. *J. Biol. Eng.* 2017, *11*, 31.
4. Langer, R.; Vacanti, J.P. Tissue engineering. *Science* **1993**, *260*, 920-926.
5. Crane, D.; Everts, P. Platelet rich plasma (PRP) matrix grafts. *Pract. Pain Manag.* **2008**, *8*, 12-26.
6. Chen, S.; He, Z.; Xu, G.; Xiao, X. Fabrication and characterization of modified nanofibrous poly(L-lactic acid) scaffolds by thermally induced phase separation technique and aminolysis for promoting cyctocompatibility. *J. Biomater. Sci., Polym. Ed.* **2016**, *27*, 1058-1068.
7. Martinez Perez, C.; Olivas-Armendariz, I.; Castro-Carmona, J.; Garcia Casillas, P.E. Scaffolds for Tissue Engineering Via Thermally Induced Phase Separation. In *Advances in Regenerative Medicine*; Wislet, S., Ed.; IntechOpen: 2011.
8. Aldana, A.A.; Abraham, G.A. Current advances in electrospun gelatin-based scaffolds for tissue engineering applications. *Int. J. Pharm.* **2017**, *523*, 441-453.
9. Harley, B.A.C.; Kim, H.-D.; Zaman, M.H.; Yannas, I.V.; Lauffenburger, D.A.; Gibson, L.J. Microarchitecture of Three-Dimensional Scaffolds Influences Cell Migration Behavior via Junction Interactions. *Biophys. J.* **2008**, *95*, 4013-4024.
10. Shim, S. B.; Jeong, J. Y.; Kim, J. S.; Yoo, J. C. Evaluation of risk factors for irreparable rotator cuff tear in patients older than age 70 including evaluation of radiologic factors of the shoulder. *J. Shoulder Elbow Surg.* **2018**, *27*, 1932−1938.
11. Shim, S. B.; Jeong, J. Y.; Yum, T. H.; Yoo, J. C. A Comparative Study to Evaluate the Risk Factors for Medium-Sized Rotator Cuff Tear in Patients Younger Than 50 Years of Age. *Arthroscopy* **2018**, *34*, 2971−2979.
12. Hsu, S.-h.; Hung, K.-C.; Chen, C.-W. Biodegradable polymer scaffolds. *J. Mater. Chem. B* **2016**, *4*, 7493-7505.
13. Sultana, N. Scaffolds for tissue engineering. In *Biodegradable Polymer-Based Scaffolds for Bone Tissue Engineering*; Sultana, N., Ed.; Springer Berlin Heidelberg: Berlin, Heidelberg, 2013; pp. 1-17.
14. Patel, H.; Bonde, M.; Srinivasan, G. Biodegradable Polymer Scaffold for Tissue Engineering. *Trends Biomater. Artif. Organs* **2011**, *25*, 20-29.
15. Kroeze, R.J.; Helder, M.N.; Govaert, L.E.; Smit, T.H. Biodegradable Polymers in Bone Tissue Engineering. *Materials* **2009**, *2* (3), 833-856.
16. Nugroho, R.W.N.; Odelius, K.; Höglund, A.; Albertsson, A.-C. Highlighting the Importance of Surface Grafting in Combination with a Layer-by-Layer Approach for Fabricating Advanced 3D Poly(l-lactide) Microsphere Scaffolds. *Chem. of Mater.* **2016**, *28*, 3298-3307.

17. Soares, D.G.; Zhang, Z.; Mohamed, F.; Eyster, T.W.; de Souza Costa, C.A.; Ma, P.X. Simvastatin and nanofibrous poly(l-lactic acid) scaffolds to promote the odontogenic potential of dental pulp cells in an inflammatory environment. *Acta Biomater.* **2018**, *68*, 190-203.
18. Bruschi, M.L. 4- Main mechanisms to control the drug release. In *Strategies to Modify the Drug Release from Pharmaceutical Systems*, Bruschi, M.L., Ed. Woodhead Publishing: 2015; pp. 37-62.
19. Gigli, M.; Fabbri, M.; Lotti, N.; Gamberini, R.; Rimini, B.; Munari, A. Poly(butylene succinate)-based polyesters for biomedical applications: A review. *European Polymer Journal* **2016**, *75*, 431-460.
20. Jäger, A.; Gromadzki, D.; Jäger, E.; Giacomelli, F.C.; Kozlowska, A.; Kobera, L.; Brus, J.; Říhová, B.; El Fray, M.; Ulbrich, K., et al. Novel "soft" biodegradable nanoparticles prepared from aliphatic based monomers as a potential drug delivery system. *Soft Matter* **2012**, *8*, 4343-4354.
21. Davachi, S.M.; Kaffashi, B. Polylactic Acid in Medicine. *Polym.-Plast. Technol. Eng.* **2015**, *54*, 944–967.
22. Ruiz-Hitzky, E.; Fernandes, F. Progress in Bionanocomposites: From green plastics to biomedical applications. *Prog. Polym. Sci.* **2013**, *38*, 1391.
23. Nair, L.S.; Laurencin, C.T. Biodegradable polymers as biomaterials. *Prog. Polym. Sci.* **2007**, *32*, 762-798.
24. Burkersroda, F.v.; Schedl, L.; Göpferich, A. Why degradable polymers undergo surface erosion or bulk erosion. *Biomaterials* **2002**, *23*, 4221-4231.
25. Fuentes, G.; Hernández, Y.; Campos, Y.; López, N.; Rojas-Cervantes, M.; Peón Avés, E.; Almirall, A.; Delgado, J. Composition influence on properties of acrylic composites loaded with synthetic hydroxyapatite. *Lat. Am. Appl. Res.* **2008**, *38*, 105-112.
26. Göpferich, A. Mechanisms of polymer degradation and erosion. *Biomaterials* **1996**, *17*, 103-114.
27. Malafaya, P.B.; Silva, G.A.; Reis, R.L. Natural–origin polymers as carriers and scaffolds for biomolecules and cell delivery in tissue engineering applications. *Adv. Drug. Deliv. Rev.* **2007**, *59*, 207-233.
28. Pouton, C.W.; Akhtar, S. Biosynthetic polyhydroxyalkanoates and their potential in drug delivery. *Adv. Drug. Deliv. Rev.* **1996**, *18*, 133-162.
29. inn, M.; Witholt, B.; Egli, T. Occurrence, synthesis and medical application of bacterial polyhydroxyalkanoate. *Adv. Drug. Deliv. Rev.* **2001**, *53*, 5-21.
30. Chen, G.-Q.; Wu, Q. The application of polyhydroxyalkanoates as tissue engineering materials. *Biomaterials* **2005**, *26*, 6565-6578.
31. Williams, S.F.; Martin, D.P.; Horowitz, D.M.; Peoples, O.P. PHA applications: addressing the price performance issue: I. Tissue engineering. *Int. J. Biol. Macromol.* **1999**, *25*, 111-121.
32. Li, Z.; Yang, J.; Loh, X.J. Polyhydroxyalkanoates: Opening doors for a sustainable future. *NPG Asia Mater.* **2016**, *8*, e265.

33. Khanna, S.; Srivastava, A.K. Recent advances in microbial polyhydroxyalkanoates. *Process Biochem.* **2005**, *40*, 607–619.

34. Fei, B.; Chen, C.; Wu, H.; Peng, S.; Wang, X.; Dong, L. Quantitative FTIR study of PHBV/bisphenol A blends. *Eur. Polym. J.* **2003**, *39*, 1939-1946.

35. Gassner, F.; Owen, A.J. Some properties of poly(3-hydroxybutyrate)–poly(3-hydroxyvalerate) blends. *Polym. Int.* **1996**, *39*, 215-219.

36. Lee, S. Y. Bacterial Polyhydroxyalkanoates. *Biotech. and Bioeng.* **1996**, *49*, 1–14.

37. Sudesh, K.; Abe, H.; Yoi, D. Synthesis, structure and properties of polyhydroxyalkanoates: Biological polyesters. *Prog. Polym. Sci.* **2000**, *25*, 1503–1555.

38. Wang, Y.; Lu, L.; Zheng, Y.; Chen, X. Improvement in hydrophilicity of PHBV films by plasma treatment. *J. Biomed. Mater. Res. A* **2006**, *76A*, 589-595.

39. Pich, A.; Schiemenz, N.; Corten, C.; Adler, H.-J.P. Preparation of poly(3-hydroxybutyrate-co-3-hydroxyvalerate) (PHBV) particles in O/W emulsion. *Polymer* **2006**, *47*, 1912-1920.

40. Wu, J.; Xue, K.; Li, H.; Sun, J.; Liu, K. Improvement of PHBV scaffolds with bioglass for cartilage tissue engineering. *PLOS ONE* **2013**, *8*, e71563.

41. Smith, J.R.; Lamprou, D.A. Polymer coatings for biomedical applications: A review. *Trans. IMF* **2014**, *92*, 9–19.

42. Riekes, M.K.; Junior, L.R.; Pereira, R.N.; Borba, P.A.; Fernandes, D.; Stulzer, H.K. Development and evaluation of poly (3-hydroxybutyrate-co-3-hydroxyvalerate) and polycaprolactone microparticles of nimodipine. *Curr. Pharm. Des.* **2013**, *19*, 7264–7270.

43. Gheibi, A.; Khoshnevisan, K.; Ketabchi, N.; Derakhshan, M.A.; Babadi, A.A. Application of Electrospun Nanofibrous PHBV Scaffold in Neural Graft and Regeneration: A Mini-Review. *Nanomed. Res. J.* **2016**, *1*, 107–111.

44.] Li, W.; Ding, Y.; Rai, R.; Roether, J.A.; Schubert, D.W.; Boccaccini, A.R. Preparation and characterization of PHBV microsphere/45S5 bioactive glass composite scaffolds with vancomycin releasing function. *Mater. Sci. Eng. C* **2014**, *41*, 320–328.

45. Müller, H.-M.; Seebach, D. Poly(hydroxyalkanoates): A Fifth Class of Physiologically Important Organic Biopolymers? *Angew. Chem., Int. Ed. Engl.* **1993**, *32*, 477-502.

46. Gogolewski, S.; Jovanovic, M.; Perren, S.M.; Dillon, J.G.; Hughes, M.K. Tissue response and in vivo degradation of selected polyhydroxyacids: Polylactides (PLA), poly(3-hydroxybutyrate) (PHB), and poly(3-hydroxybutyrate-co-3-hydroxyvalerate) (PHB/VA). *J. Biomed. Mater. Res.* **1993**, *27*, 1135-1148.

47. Hasirci, V.; Tezcaner, A.; Hasirci, N.; Suzer, S. Oxygen Plasma Modification of Poly(3-hydroxybutyrate-co-3-hydroxyvalerate) Film Surfaces for Tissue Engineering Purposes. *J. Appl. Polym. Sci.* **2003**, *87*, 1285–1289.

48. Fukada, E.; Ando, Y. Piezoelectric properties of poly-β-hydroxybutyrate and copolymers of β-hydroxybutyrate and β-hydroxyvalerate. *Int. J. Biol. Macromol.* **1986**, *8*, 361-366.

49. Y. Doi, A. Steinbüchel, *Polyesters II – Properties and Chemical Synthesis*, Wiley-VCH: New York, USA, 2002.

50. Papageorgiou, G.Z.; Bikiaris, D.N. Synthesis, Cocrystallization, and Enzymatic Degradation of Novel Poly(butylene-co-propylene succinate) Copolymers. *Biomacromolecules* **2007**, *8*, 2437-2449.

51. Gan, Z.; Abe, H.; Doi, Y. Crystallization, Melting, and Enzymatic Degradation of Biodegradable Poly(butylene succinate-co-14 mol ethylene succinate) Copolyester. *Biomacromolecules* **2001**, *2*, 313-321.

52. Díaz, A.; Franco, L.; Puiggalí, J. Study on the crystallization of poly(butylene azelate-co-butylene succinate) copolymers. *Thermochim. Acta* **2014**, *575*, 45-54.

53. Qiu, Z.; Ikehara, T.; Nishi, T. Poly(hydroxybutyrate)/poly(butylene succinate) blends: miscibility and nonisothermal crystallization. *Polymer* **2003**, *44*, 2503-2508.

54. Wang, J.; Zheng, L.; Li, C.; Zhu, W.; Zhang, D.; Xiao, Y.; Guan, G. Fully biodegradable blends of poly(butylene succinate) and poly(butylene carbonate): Miscibility, thermal properties, crystallization behavior and mechanical properties. *Polym. Test.* **2012**, *31*, 39-45.

55. Soccio, M.; Lotti, N.; Gigli, M.; Finelli, L.; Gazzano, M.; Munari, A. Reactive blending of poly(butylene succinate) and poly(triethylene succinate): characterization of the copolymers obtained. *Polym. Int.* **2012**, *61*, 1163-1169.

56. Huang, C.-L.; Jiao, L.; Zhang, J.-J.; Zeng, J.-B.; Yang, K.-K.; Wang, Y.-Z. Poly(butylene succinate)-poly(ethylene glycol) multiblock copolymer: Synthesis, structure, properties and shape memory performance. *Polym. Chem.* **2012**, *3*, 800-808.

57. Kim, S.-W.; Lim, J.-C.; Kim, D.-J.; Seo, K.-H. Synthesis and characteristics of biodegradable copolyesters from the transesterification of poly(butylene adipate-co-succinate) and poly(ethylene terephthalate). *J. Appl. Polym. Sci.* **2004**, *92*, 3266-3274.

58. Muthuraj, R.; Misra, M.; Mohanty, A.K. Biodegradable Poly(butylene succinate) and Poly(butylene adipate-co-terephthalate) Blends: Reactive Extrusion and Performance Evaluation. *J. Polym. Environ.* **2014**, *22*, 336-349.

59. Díaz, A.; Franco, L.; Estrany, F.; del Valle, L.J.; Puiggalí, J. Poly(butylene azelate-co-butylene succinate) copolymers: Crystalline morphologies and degradation. *Polym. Degrad. Stab.* **2014**, *99*, 80-91.

60. Hariraksapitak, P.; Suwantong, O.; Pavasant, P.; Supaphol, P. Effectual drug-releasing porous scaffolds from 1,6-diisocyanatohexane-extended poly(1,4-butylene succinate) for bone tissue regeneration. *Polymer* **2008**, *49*, 2678-2685.

61. Sutthiphong, S.; Pavasant, P.; Supaphol, P. Electrospun 1,6-diisocyanatohexane-extended poly(1,4-butylene succinate) fiber mats and their potential for use as bone scaffolds. *Polymer* **2009**, *50*, 1548-1558.

62. Wang, H.; Ji, J.; Zhang, W.; Zhang, Y.; Jiang, J.; Wu, Z.; Pu, S.; Chu, P.K. Biocompatibility and bioactivity of plasma-treated biodegradable poly(butylene succinate). *Acta Biomater.* **2009**, *5*, 279-287.

63. Wang, H.; Ji, J.; Zhang, W.; Wang, W.; Zhang, Y.; Wu, Z.; Zhang, Y.; Chu, P.K. Rat calvaria osteoblast behavior and antibacterial properties of O2 and N2 plasma-implanted biodegradable poly(butylene succinate). *Acta Biomater.* **2010**, *6*, 154-159.

64. Kosorn, W.; Thavornyutikarn, B.; Phumsiri, B.; Uppanan, P.; Meesap, P.; Janvikul, W. Hydrolyzed Poly(Butylene Succinate) Scaffolds Coated with Bioactive Agent. *J. Met. Mater. Miner.* **2010**, *20*, 98-99.
65. Kaewkong, P.; Uppanan, P.; Thavornyutikarn, B.; Kosorn, W.; Janvikul, W. Chondrocyte Growth and Function on HPBS/HA Composite Scaffolds: Static Versus Dynamic Culture. *IPCBEE* **2012**, *43*, 11-14.
66. Uppanan, P.; Meesap, P.; Thavornyutikarn, B.; Kosorn, W.; Janvikul, W. Study on Surface-Hydrolyzed Poly(butylene succinate)/Hydroxyapatite Composite Scaffolds for Cartilage Regeneration. *Adv. Sci. Lett.* **2013**, *19*, 3070-3072.
67. Coutinho, D.F.; Pashkuleva, I.H.; Alves, C.M.; Marques, A.P.; Neves, N.M.; Reis, R.L. The Effect of Chitosan on the In Vitro Biological Performance of Chitosan−Poly(butylene succinate) Blends. *Biomacromolecules* **2008**, *9*, 1139-1145.
68. Costa-Pinto, A.R.; Salgado, A.J.; Correlo, V.M.; Sol, P.; Bhattacharya, M.; Charbord, P.; Reis, R.L.; Neves, N.M. Adhesion, Proliferation, and Osteogenic Differentiation of a Mouse Mesenchymal Stem Cell Line (BMC9) Seeded on Novel Melt-Based Chitosan/Polyester 3D Porous Scaffolds. *Tissue Eng. A* **2008**, *14*, 1049-1057.
69. Oliveira, J.T.; Correlo, V.M.; Sol, P.C.; Costa-Pinto, A.R.; Malafaya, P.B.; Salgado, A.J.; Bhattacharya, M.; Charbord, P.; Neves, N.M.; Reis, R.L. Assessment of the Suitability of Chitosan/PolyButylene Succinate Scaffolds Seeded with Mouse Mesenchymal Progenitor Cells for a Cartilage Tissue Engineering Approach. *Tissue Eng. A* **2008**, *14*, 1651-1661.
70. Alves da Silva, M.L.; Crawford, A.; Mundy, J.M.; Correlo, V.M.; Sol, P.; Bhattacharya, M.; Hatton, P.V.; Reis, R.L.; Neves, N.M. Chitosan/polyester-based scaffolds for cartilage tissue engineering: Assessment of extracellular matrix formation. *Acta Biomater.* **2010**, *6*, 1149-1157.
71. Niu, Y.; Cao, L.; Wei, J.; Ma, Y.; Song, S.; Weng, W.; Li, H.; Liu, C.; Su, J. Development of a bioactive composite of nano fluorapatite and poly(butylene succinate) for bone tissue regeneration. *J. Mater. Chem. B* **2014**, *2*, 1174-1181.
72. Ngamviriyavong, P.; Patntirapong, S.; Janvikul, W.; Arphavasin, S.; Meesap, P.; Singhatanadgit, W. Development of poly(butylene succinate)/calcium phosphate composites for bone engineering. *Compos. Interf.* **2014**, *21*, 431-441.
73. Patntirapong, S.; Singhatanadgit, W.; Meesap, P.; Theerathanagorn, T.; Toso, M.; Janvikul, W. Stem cell adhesion and proliferation on hydrolyzed poly(butylene succinate)/β-tricalcium phosphate composites. *J. Biomed. Mater. Res. A* **2015**, *103*, 658-670.
74. Zhang, D.; Chang, J.; Zeng, Y. Fabrication of fibrous poly(butylene succinate)/wollastonite/apatite composite scaffolds by electrospinning and biomimetic process. *J. Mater. Sci., Mater. Med.* **2008**, *19*, 443-449.
75. Meesap, P.; Uppanan, P.; Thavornyutikarn, B.; Kosorn, W.; Janvikul, W. Surface Hydrolyzed Poly(Butylene Succinate) Microsphere Incorporated Carboxymethylchitosan Scaffolds for Cartilage Tissue Engineering. *J. Met. Mater. Miner.* **2010**, *20*, 107-111.
76. Costa-Pinto, A.R.; Correlo, V.M.; Sol, P.C.; Bhattacharya, M.; Srouji, S.; Livne, E.; Reis, R.L.; Neves, N.M. Chitosan–poly(butylene succinate) scaffolds and human bone marrow

stromal cells induce bone repair in a mouse calvaria model. *J. Tissue Eng. Regen. Med.* **2012**, *6*, 21-28.

77. Costa-Pinto, A.R.; Vargel, I.; Tuzlakoglu, K.; Correlo, V.M.; Sol, P.C.; Faria, S.; Piskin, E.; Reis, R.L.; Neves, N.M. Influence of scaffold composition over in vitro osteogenic differentiation of hBMSCs and in vivo inflammatory response. *J. Biomater. Appl.* **2013**, *28*, 1430-1442.

78. allawi, M.; Rai, R.; R-Gleixner, M.; Roerick, O.; Weyand, M.; Roether, J.A.; Schubert, D.W.; Kozlowska, A.; Fray, M.E.; Merle, B., et al. Poly(glycerol sebacate)/Poly(butylene succinate-dilinoleate) Blends as Candidate Materials for Cardiac Tissue Engineering. *Macromol. Symp.* **2013**, *334*, 57-67.

79. Tallawi, M.; Zebrowski, D.C.; Rai, R.; Roether, J.A.; Schubert, D.W.; El Fray, M.; Engel, F.B.; Aifantis, K.E.; Boccaccini, A.R. Poly(glycerol sebacate)/poly(butylene succinate-dilinoleate) (PGS/PBS–DLA) fibrous scaffolds for cardiac tissue engineering. *Tissue Eng. C Methods* **2014**, *20*, 412-422.

80. Gualandi, C.; Soccio, M.; Saino, E.; Focarete, M.L.; Lotti, N.; Munari, A.; Moroni, L.; Visai, L. Easily synthesized novel biodegradable copolyesters with adjustable properties for biomedical applications. *Soft Matter.* **2012**, *8*, 5466-5476.

81. Park, S.-J.; Lee, Y.-M.; Hong, S.-K. Release behaviors of porous poly(butylene succinate)/poly(ε-caprolactone) microcapsules containing indomethacin. *Colloid. Surface. B* **2006**, *47*, 211-215.

82. Mohanraj, K.; Sethuraman, S.; Krishnan, U.M. Development of poly(butylene succinate) microspheres for delivery of levodopa in the treatment of Parkinson's disease. *J. Biomed. Mater. Res. B* **2013**, *101B*, 840-847.

83. Liu, J.; Jiang, Z.; Zhang, S.; Saltzman, W.M. Poly(ω-pentadecalactone-co-butylene-co-succinate) nanoparticles as biodegradable carriers for camptothecin delivery. *Biomaterials* **2009**, *30*, 5707-5719.

84. Hariraksapitak, P.; Suwantong, O.; Pavasant, P.; Supaphol, P. Effectual drug-releasing porous scaffolds from 1,6-diisocyanatohexane-extended poly(1,4-butylene succinate) for bone tissue regeneration. *Polymer* **2008**, *49*, 2678-2685.

85. Stoyanova, N.; Paneva, D.; Mincheva, R.; Toncheva, A.; Manolova, N.; Dubois, P.; Rashkov, I. Poly(l-lactide) and poly(butylene succinate) immiscible blends: From electrospinning to biologically active materials. *Mater. Sci. Eng. C* **2014**, *41*, 119-126.

86. Peña Carrodeguas, L.; Martín, C.; Kleij, A.W. Semiaromatic Polyesters Derived from Renewable Terpene Oxides with High Glass Transitions. *Macromolecules* **2017**, *50*, 5337-5345.

87. Doug S. *BCC research reports PLS050A.* 2010. Bioplastics: technologies and global markets.

88. Flores, E.D.; Funabashi, M.; Kunioka, M. Mechanical properties and biomass carbon ratios of poly(butylene succinate) composites filled with starch and cellulose filler using furfural as plasticizer. *J. Appl. Polym. Sci.* **2009**, *112*, 3410–3417.

89. Robert, C.; de Montigny, F.; Thomas, C. M. Tandem Synthesis of Alternating Polyesters from Renewable Resources. *Nat. Commun.* **2011**, *2*, 586.

90. Nejad, E. H.; Paoniasari, A.; van Melis, C. G. W.; Koning, C. E.; Duchateau, R. Catalytic Ring-Opening Copolymerization of Limonene Oxide and Phthalic Anhydride: Toward Partially Renewable Polyesters. *Macromolecules* **2013**, *46*, 631−637.

91. Sanford, M. J.; Peñ a Carrodeguas, L.; Van Zee, N. J.; Kleij, A. W.; Coates, G. W. Alternating Copolymerization of Propylene Oxide and Cyclohexene Oxide with Tricyclic Anhydrides: Access to Partially Renewable Aliphatic Polyesters with High Glass Transition Temperatures. *Macromolecules* **2016**, *49*, 6394−6400.

92. Quilter, H. C.; Hutchby, M.; Davidson, M. G.; Jones, M. D. Polymerisation of a Terpene-derived Lactone: a Bio-based Alternative to ε-Caprolactone. *Polym. Chem.* **2017**, *8*, 833−837

93. Van Zee, N. J.; Sanford, M. J.; Coates, G. W. Electronic Effects of Aluminum Complexes in the Copolymerization of Propylene Oxide with Tricyclic Anhydrides: Access to Well-Defined, Funcionalizable Aliphatic Polyesters. *J. Am. Chem. Soc.* **2016**, *138*, 2755−2761.

94. Hauenstein, O.; Agarwal, S.; Greiner, A. Biobased Polycarbonate as Synthetic Toolbox. *Nat. Commun.* **2016**, *7*, 11862.

95. Hauenstein, O.; Reiter, M.; Agarwal, S.; Rieger, B.; Greiner, A. Bio-based Polycarbonate from Limonene Oxide and CO2 with high Molecular Weight, Excellent Thermal Resistance, Hardness and Transparency. *Green Chem.* **2016**, *18*, 760−770.

96. Martín, C.; Kleij, A. W. Terpolymers derived from Limonene Oxide and Carbon Dioxide: Access to Cross-Linked Polycarbonates with Improved Thermal Properties. *Macromolecules* **2016**, *49*, 6285− 6295.

97. Auriemma, F.; De Rosa, C.; Di Caprio, M. R.; Di Girolamo, R.; Ellis, W. C.; Coates, G. W. Stereocomplexed Poly(Limonene Carbonate): A Unique Example of the Cocrystallization of Amorphous Enantiomeric Polymers. *Angew. Chem., Int. Ed.* **2015**, *54*, 1215−1218.

98. Reiter, M.; Vagin, S.; Kronast, A.; Jandl, C.; Rieger, B. A Lewis Acid β-Diiminato-Zinc-Complex as All-rounder for Co- and Terpolymerisation of various Epoxides with Carbon Dioxide. *Chem. Sci.* **2017**, *8*, 1876−1882.

99. Zhao, J.; Schlaad, H. Synthesis of Terpene-Based Polymers. *Adv. Polym. Sci.* **2011**, *253*, 151−190.

100. Firdaus, M.; Montero de Espinosa, L.; Meier, M. A. R. TerpeneBased Renewable Monomers and Polymers via Thiol−Ene Additions. *Macromolecules* **2011**, *44*, 7253−7262.

101. Grau, E.; Mecking, S. Polyterpenes by Ring Opening Metathesis Polymerization of Caryophyllene and Humulene. *Green Chem.* **2013**, *15*, 1112−1115.

102. Wilbon, P. A.; Chu, F.; Tang, C. Progress in Renewable Polymers from Natural Terpenes, Terpenoids, and Rosin. *Macromol. Rapid Commun.* **2013**, *34*, 8−37.

103. Peña Carrodeguas, L.; González-Fabra, J.; Castro-Gómez, F.; Bo, C.; Kleij, A.W. AlIII-Catalysed Formation of Poly(limonene)carbonate: DFT Analysis of the Origin of Stereoregularity. *Chem. Eur. J.* **2015**, *21*, 6115-6122.

104. Ekor, M. The growing use of herbal medicines: issues relating to adverse reactions and challenges in monitoring safety. *Frontiers in Pharmacology* **2014**, *4*.

105. Rai, M.; Pandit, R.; Gaikwad, S.; Yadav, A.; Gade, A. Potential applications of curcumin and curcumin nanoparticles: from traditional therapeutics to modern nanomedicine. *Nanotechnol. Rev.* **2015**, *4*, 161-172.

106. Pongrakananon, V.; Rojanasakul, Y. Anticancer Properties of Curcumin. 2011 In book: Advances in Cancer Therapy Pages 345-368

107. Rajasekaran S. Therapeutic potential of curcumin in gastrointestinal disease.*World J. Gastrointest. Pathophysiol.* **2011**, *2*, 1–14.

108. Anand P, Thomas S, Kunnumakkara A, Sundaram C, Harikumar K, Sung B, Tharakan S, Misra J, Priyadarsini I, Rajasekhran K, Aggarwal B. Biological activities of curcumin and its analogues (Congeners) made by man and mother nature. *Biochem. Pharmacol.* **2008**, *76*, 1590–1611.

109. Patumraj S, Yoysungneon P. Curcumin as a therapeutic agent against cancer. *Asian Biomed.* **2007**, *1*, 239–252.

110. Shityakov, S.; Bigdelian, E.; Hussein, A.A.; Hussain, M.B.; Tripathi, Y.C.; Khan, M.U.; Shariati, M.A. Phytochemical and pharmacological attributes of piperine: A bioactive ingredient of black pepper. *Eur. J. Med. Chem.* **2019**, *176*, 149-161.

111. Tiwari, A.; Mahadik, K.R.; Gabhe, S.Y. Piperine: A comprehensive review of methods of isolation, purification, and biological properties. *Med. Drug Discovery* **2020**, *7*, 100027.

112. Mujumdar, A.M.; Dhuley, J.N.; Deshmukh, V.K.; Raman, P.H.; Naik, S.R. ANTI-INFLAMMATORY ACTIVITY OF PIPERINE. *Jpn. J. Med. Sci. Biol.* **1990**, *43*, 95-100.

113. Tharmalingam, N.; Kim, S.-H.; Park, M.; Woo, H.J.; Kim, H.W.; Yang, J.Y.; Rhee, K.-J.; Kim, J.B. Inhibitory effect of piperine on Helicobacter pylori growth and adhesion to gastric adenocarcinoma cells. *Infect. Agent. Cancer.* **2014**, *9*, 43-43.

114. Ahmad, N.; Fazal, H.; Abbasi, B.H.; Farooq, S.; Ali, M.; Khan, M.A. Biological role of Piper nigrum L. (Black pepper): A review. *Asian Pac. J. Trop. Biomed.* **2012**, *2*, 1945-1953.

115. Tessmar, J.K.V.; Holland, T.A.; Mikos, A.G. Salt Leaching for Polymer Scaffolds: Laboratory-Scale Manufacture of Cell Carriers. In *Scaffolding in Tissue Engineering*; Ma, P.X., Elisseeff, J., Eds.; Taylor & Francis: Boca Raton, FL, USA, 2006; pp. 111-124.

116. Eltom, A.; Zhong, G.; Muhammad, A. Scaffold Techniques and Designs in Tissue Engineering Functions and Purposes: A Review. *Adv. Mater. Sci. Eng.* **2019**, *2019*, 3429527.

117. Huang, Y.X.; Ren, J.; Chen, C.; Ren, T.B.; Zhou, X.Y. Preparation and Properties of Poly(lactide-co-glycolide) (PLGA)/ Nano-Hydroxyapatite (NHA) Scaffolds by Thermally Induced Phase Separation and Rabbit MSCs Culture on Scaffolds. *J. Biomater. Appl.* **2007**, *22*, 409-432.

118. Blaker, J.J.; Knowles, J.C.; Day, R.M. Novel fabrication techniques to produce microspheres by thermally induced phase separation for tissue engineering and drug delivery. *Acta Biomater.* **2008**, *4*, 264-272.

119. Shao, J.; Chen, C.; Wang, Y.; Chen, X.; Du, C. Early stage structural evolution of PLLA porous scaffolds in thermally induced phase separation process and the corresponding biodegradability and biological property. *Polym. Degrad. Stab.* **2012**, *97*, 955-963.

120. Sabir, M.I.; Xu, X.; Li, L. A review on biodegradable polymeric materials for bone tissue engineering applications. *J. Mater. Sci.* **2009**, *44*, 5713-5724.
121. Mehrabanian, M.; Nasr-Esfahani, M. HA/nylon 6,6 porous scaffolds fabricated by salt-leaching/solvent casting technique: effect of nano-sized filler content on scaffold properties. *Int. J. Nanomed.* **2011**, *6*, 1651-1659.
122. Williams, J.M.; Adewunmi, A.; Schek, R.M.; Flanagan, C.L.; Krebsbach, P.H.; Feinberg, S.E.; Hollister, S.J.; Das, S. Bone tissue engineering using polycaprolactone scaffolds fabricated via selective laser sintering. *Biomaterials* **2005**, *26*, 4817-4827.
123. Eshraghi, S.; Das, S. Mechanical and microstructural properties of polycaprolactone scaffolds with one-dimensional, two-dimensional, and three-dimensional orthogonally oriented porous architectures produced by selective laser sintering. *Acta Biomater.* **2010**, *6*, 2467-2476.
124. Ji, C.; Annabi, N.; Hosseinkhani, M.; Sivaloganathan, S.; Dehghani, F. Fabrication of poly-DL-lactide/polyethylene glycol scaffolds using the gas foaming technique. *Acta Biomater.* **2012**, *8*, 570-578.
125. Singh, M.; Sandhu, B.; Scurto, A.; Berkland, C.; Detamore, M.S. Microsphere-based scaffolds for cartilage tissue engineering: Using subcritical CO2 as a sintering agent. *Acta Biomater.* **2010**, *6*, 137-143.
126. Whang, K.; Thomas, C.H.; Healy, K.E.; Nuber, G. A novel method to fabricate bioabsorbable scaffolds. *Polymer* **1995**, *36*, 837-842.
127. Whang, K.; Tsai, D.C.; Nam, E.K.; Aitken, M.; Sprague, S.M.; Patel, P.K.; Healy, K.E. Ectopic bone formation via rhBMP-2 delivery from porous bioabsorbable polymer scaffolds. *J. Biomed. Mater. Res.* **1998**, *42*, 491-499.
128. Cui, Y.; Liu, Y.; Cui, Y.; Jing, X.; Zhang, P.; Chen, X. The nanocomposite scaffold of poly(lactide-co-glycolide) and hydroxyapatite surface-grafted with l-lactic acid oligomer for bone repair. *Acta Biomater.* **2009**, *5*, 2680-2692.
129. Yoshimoto, H.; Shin, Y.M.; Terai, H.; Vacanti, J.P. A biodegradable nanofiber scaffold by electrospinning and its potential for bone tissue engineering. *Biomaterials* **2003**, *24*, 2077-2082.
130. Bhardwaj, N.; Kundu, S.C. Electrospinning: A fascinating fiber fabrication technique. *Biotechnol. Adv.* **2010**, *28*, 325-347.
131. Sachlos, E.; Czernuszka, J. T. Making tissue engineering scaffolds work. Review on the application of solid freeform fabrication technology to the production of tissue engineering scaffolds. *Eur Cell Mater*, **2003**, *5*, 29–40.
132. Kundu, J.; Pati, F.; Shim, J.H.; Cho, D.W. 10 - Rapid prototyping technology for bone regeneration. In *Rapid Prototyping of Biomaterials*; Narayan, R., Ed. Woodhead Publishing: 2014; pp. 254-284.
133. Hutmacher, D.W.; Sittinger, M.; Risbud, M.V. Scaffold-based tissue engineering: rationale for computer-aided design and solid free-form fabrication systems. *Trends Biotechnol.* **2004**, *22*, 354-362.
134. Tabata, Y. Biomaterial technology for tissue engineering applications. *J. R. Soc. Interface*, **2009**, *6*, S311–S324.

135. Liang, Y.; Zheng, X.; Zhai, W.; Sun, T. 3D PLLA/nano-hydroxyapatite scaffolds with hierarchical porous structure fabricated by low-temperature deposition manufacturing. *J. Wuhan Univ. Technol. Mate. Sci. Ed.* **2012**, *27*, 265-269.

136. Akbarzadeh, R.; Yousefi, A.M. Effects of processing parameters in thermally induced phase separation technique on porous architecture of scaffolds for bone tissue engineering. *J. Biomed. Mater. Res. B Appl. Biomater.* **2014**, *102*, 1304–1315.

137. Asadian, M.; Chan, K.V.; Norouzi, M.; Grande, S.; Cools, P.; Morent, R.; De Geyter, N. Fabrication and Plasma Modification of Nanofibrous Tissue Engineering Scaffolds. *Nanomaterials* **2020**, *10*, 119.

138. Shimojo, A.A.M.; Rodrigues, I.C.P.; Perez, A.G.M.; Souto, E.M.B.; Gabriel, L.P.; Webster, T. Scaffolds for Tissue Engineering: A State-of-the-Art Review Concerning Types, Properties, Materials, Processing, and Characterization. In *Racing for the Surface: Antimicrobial and Interface Tissue Engineering*, Li, B., Moriarty, T.F., Webster, T., Xing, M., Eds. Springer International Publishing: Cham, 2020; pp. 647-676.

139. Saito, E.; Liao, E.E.; Hu, W.-W.; Krebsbach, P.H.; Hollister, S.J. Effects of designed PLLA and 50:50 PLGA scaffold architectures on bone formation in vivo. *J. Tissue Eng. Regen. Med.* **2013**, *7*, 99-111.

140. Liu, L.; Xiong, Z.; Yan, Y.; Zhang, R.; Wang, X.; Jin, L. Multinozzle low-temperature deposition system for construction of gradient tissue engineering scaffolds. *J. Biomed. Mater. Res. B Appl. Biomater.* **2009**, *88B*, 254-263.

141. Martina, M.; Hutmacher, D.W. Biodegradable polymers applied in tissue engineering research: A review. *Polym. Int.* **2007**, *56*, 145–157.

142. He, L.; Zuo, Q.; Shi, Y.; Xue, W. Microstructural characteristics and crystallization behaviors of poly(l-lactide) scaffolds by thermally induced phase separation. *J. Appl. Polym. Sci.* **2014**, *131*.

143. van de Witte, P.; Dijkstra, P.J.; van den Berg, J.W.A.; Feijen, J. Phase separation processes in polymer solutions in relation to membrane formation. *J. Membr. Sci.* **1996**, *117*, 1–31.

144. Zeman, L.; Fraser, T. Formation of air-cast cellulose acetate membranes. Part I. Study of macrovoid formation. *J. Membr. Sci.* **1993**, *84*, 93-106.

145. Zeman, L.; Fraser, T. Formation of air-cast cellulose acetate membranes Part II. Kinetics of demixing and microvoid growth. *J. Membr. Sci.* **1994**, *87*, 267-279.

146. Lloyd, D.R.; Kinzer, K.E.; Tseng, H.S. Microporous membrane formation via thermally induced phase separation. I. Solid-liquid phase separation. *J. Membr. Sci.* **1990**, *52*, 239–261.

147. Lloyd, D.R.; Kim, S.S.; Kinzer, K.E. Microporous membrane formation via thermally-induced phase separation. II. Liquid—liquid phase separation. *J. Membr. Sci.* **1991**, *64*, 1–11.

148. Chen, V.J.; Ma, P.X. Polymer phase separation. In *Scaffolding in Tissue Engineering*; Ma, P.X., Elisseeff, J., Eds.; Taylor & Francis: Boca Raton, FL, USA, 2006; pp. 125–137.

149. Önder, Ö.C.; Yilgör, E.; Yilgör, I. Critical parameters controlling the properties of monolithic poly(lactic acid) foams prepared by thermally induced phase separation. *J. Polym. Sci. Part B Polym. Phys.* **2019**, *57*, 98–108.

150. Önder, Ö.C.; Yilgör, E.; Yilgör, I. Fabrication of rigid poly(lactic acid) foams via thermally induced phase separation. *Polymer* **2016**, *107*, 240–248.

151. Önder, Ö.C.; Yilgör, E.; Yilgör, I. Preparation of monolithic polycaprolactone foams with controlled morphology. Polymer 2018, 136, 166–178.

152. Dai, Y.; Shen, T.; Ma, L.; Wang, D.; Gao, C. Regeneration of osteochondral defects in vivo by a cell-free cylindrical poly(lactide-co-glycolide) scaffold with a radially oriented microstructure. *J. Tissue Eng. Regen. Med.* **2018**, *12*, e1647–e1661.

153. Xu, C.; Okpokwasili, C.; Huang, Y.; Shi, X.; Wu, J.; Liao, J.; Tang, L.; Hong, Y. Optimizing Anisotropic Polyurethane Scaffolds to Mechanically Match with Native Myocardium. *ACS Biomater. Sci. Eng.* **2020**, *6*, 2757–2769.

154. Feng, X.; Xu, P.; Shen, T.; Zhang, Y.; Ye, J.; Gao, C. Influence of pore architectures of silk fibroin/collagen composite scaffolds on the regeneration of osteochondral defects in vivo. *J. Mater. Chem. B* **2020**, *8*, 391–405.

155. Kim, S.S.; Lloyd, D.R. Thermodynamics of polymer/diluent systems for thermally induced phase separation: 3. Liquid-liquid phase separation systems. *Polymer* **1992**, *33*, 1047-1057.

156. Hansen, C.; Beerbower, A. Solubility Parameters. In *Kirk-Othmer Encyclopedia of Chemical Technology*, 2nd ed.; Wiley:New York, USA, 1971; Suppl. Vol., pp. 889–910.

157. Bribesh, F.; Madruga, S. Free surface liquid films of binary mixtures. Two-dimensional steady structures at off-critical compositions. *Phys. Fluids* **2016**, *28*.

158. Zhu, J.; Balieu, R.; Wang, H. The use of solubility parameters and free energy theory for phase behaviour of polymer-modified bitumen: a review. *Road Mater. Pavement Des.* **2021**, *22*, 757-778.

159. Sanchez I.C. Polymer phase separation. In *Encyclopedia of Physical Science and Technology*, Meyers A.R., Ed.; Academic Press: New York, USA, 1987, pp. 1-18.

160. Sofokleous, P.; Chin, M.H.W.; Day, R. 5 - Phase-separation technologies for 3D scaffold engineering. In *Functional 3D Tissue Engineering Scaffolds*, Deng, Y., Kuiper, J., Eds. Woodhead Publishing: 2018; pp. 101-126.

161. Flory, P.J. *Principles of Polymer Chemistry*; Cornell University Press: Ithaca, NY, USA, 1953; pp. 541–594.

162. Bulte, A.M.W.; Folkers, B.; Mulder, M.H.V.; Smolders, C.A. Membranes of semicrystalline aliphatic polyamide nylon 4,6: Formation by diffusion-induced phase separation. *J. Appl. Polym. Sci.* **1993**, *50*, 13-26.

163. Gu, M.; Zhang, J.; Wang, X.; Tao, H.; Ge, L. Formation of poly(vinylidene fluoride) (PVDF) membranes via thermally induced phase separation. *Desalination* **2006**, *192*, 160-167.

164. Lemstra, P.J.; van Aerle, N.A.J.M.; Bastiaansen, C.W.M. Chain-Extended Polyethylene. *Polym. J.* **1987**, *19*, 85-98.

165. Zwijnenburg, A.; van Hutten, P.F.; Pennings, A.J.; Chanzy, H.D. Longitudinal growth of polymer crystals from flowing solutions V.: Structure and morphology of fibrillar polyethylene crystals. *Colloid Polym. Sci.* **1978**, *256*, 729-740.

166. Domszy, R.C.; Alamo, R.; Edwards, C.O.; Mandelkern, L. Thermoreversible gelation and crystallization of homopolymers and copolymers. *Macromolecules* **1986**, *19*, 310-325.

167. Matsuyama, H.; Teramoto, M.; Kuwana, M.; Kitamura, Y. Formation of polypropylene particles via thermally induced phase separation. *Polymer* **2000**, *41*, 8673-8679.

168. Burghardt, W.R. Phase diagrams for binary polymer systems exhibiting both crystallization and limited liquid-liquid miscibility. *Macromolecules* **1989**, *22*, 2482-2486.

169. Lee, H.K.; Myerson, A.S.; Levon, K. Nonequilibrium liquid-liquid phase separation in crystallizable polymer solutions. *Macromolecules* **1992**, *25*, 4002-4010.

170. Dechet, M.A.; Goblirsch, A.; Romeis, S.; Zhao, M.; Lanyi, F.J.; Kaschta, J.; Schubert, D.W.; Drummer, D.; Peukert, W.; Schmidt, J. Production of polyamide 11 microparticles for Additive Manufacturing by liquid-liquid phase separation and precipitation. *Chem. Eng. Sci.* **2019**, *197*, 11-25.

171. Park, S.A.; Lee, S.H.; Kim, W.D. Fabrication of porous polycaprolactone/hydroxyapatite (PCL/HA) blend scaffolds using a 3D plotting system for bone tissue engineering. *Bioprocess Biosyst. Eng.* **2011**, *34*, 505-513.

172. Kanno, T.; Uyama, H. Unique leafy morphology of poly(lactic acid) monoliths controlled via novel phase separation technology. *RSC Adv.* **2017**, *7*, 33726–33732.

173. Young, A.T. Polymer-Solvent Phase Separation as a Route to Low Density, Microcellular Plastic Foams. *J. Cell. Plast.* **1987**, *23*, 55-72.

174. Yang, F.; Murugan, R.; Ramakrishna, S.; Wang, X.; Ma, Y.X.; Wang, S. Fabrication of nano-structured porous PLLA scaffold intended for nerve tissue engineering. *Biomaterials* **2004**, *25*, 1891–1900.

Chapter 2

Recent Progress on Biodegradable Tissue Engineering Scaffolds Prepared by Thermally-Induced Phase Separation (TIPS)

Abstract

Porous biodegradable scaffolds provide a physical substrate for cells allowing them to attach, proliferate and guide the formation of new tissues. A variety of techniques have been developed to fabricate tissue engineering (TE) scaffolds, among them the most relevant is the thermally-induced phase separation (TIPS). This technique has been widely used in recent years to fabricate three-dimensional (3D) TE scaffolds. Low production cost, simple experimental procedure and easy processability together with the capability to produce highly porous scaffolds with controllable architecture justify the popularity of TIPS. This paper provides a general overview of the TIPS methodology applied for the preparation of 3D porous TE scaffolds. The recent advances in the fabrication of porous scaffolds through this technique, in terms of technology and material selection, have been reviewed. In addition, how properties can be effectively modified to serve as ideal substrates for specific target cells has been specifically addressed. Additionally, examples are offered with respect to changes of TIPS procedure parameters, the combination of TIPS with other techniques and innovations in polymer or filler selection.

2.1. Introduction

Tissue engineering is a multidisciplinary field that combines biology, biochemistry, clinical medicine and materials science. This approach is a quite recently developed alternative to current surgical strategies, which aims to restore, maintain or improve the function of damaged or lost tissues by taking advantage of porous three-dimensional (3D) scaffolds [1-3]. Tissue engineering is based on using biodegradable porous scaffolds integrated with biological cells or molecules for regeneration of tissues or organs [4]. In regenerative medicine, the cell proliferation triangle is defined with its three essential elements including scaffolds, cells and growth factors or other bioactive molecules. Scaffolds represent the conductive capacity inside the triangle which can be used to carry the cells before in vivo implantation, or only act as a bioactive material attracting the cells on the tissue where they are implanted [5].

Tissue engineering (TE) is a very tested field of biotechnology that has been developed for over two decades [1,2]. TE aims to construct biological substitutes to restore and maintain normal function of injured or diseased tissues by applying the knowledge of biology, cell transplantation, materials science and bioengineering [3]. In this strategy, a biodegradable three-dimensional (3D) porous scaffold integrated with biological cells or molecules is often studied for regeneration of tissues or organs [4].

3D biodegradable polymer scaffolds with a porous structure usually act as temporary template for seeding, adhesion, growth and proliferation of living cells to guide regeneration and formation of new tissues, while the biodegradable polymer matrix is subjected to biodegradation [5,6]. Moreover, the 3D porous architecture of the scaffold can affect cell migration by regulating the transport of oxygen and nutrients [7,8].

Another important application of biodegradable polymeric scaffold is their use as support materials for different drug loadings. Scaffolds can be designed to allow drug release in a sustained and controlled manner over a desired period of time [9,10].

Various synthetic and natural biomaterials have been widely investigated as scaffolding materials in tissue engineering fields [11]. Among them, aliphatic polyesters such as polylactide (PLA) [12–14], polyglycolide (PGA) [15,16], polycaprolactone (PCL) [17,18] and their copolymers like poly(lactide-*co*-glycolide) (PLGA) [19–22], poly(L-lactide-*co*-caprolactone) (PLCL) [23], poly-(glycolide-*co*-caprolactone (PGCL) [24] and poly(L-lactide-*co*-glycolide-*co*-ε-caprolactone)

(PLLGC) [25] have received significant scientific attention due to their good biocompatibility and biodegradability. Furthermore, most of them have been approved by the Food and Drug Administration (FDA) for certain clinical applications [26,27]. Apart from the usage of natural/synthetic polymeric scaffolds in various fields of tissue engineering, a promising strategy is the design and fabrication of binary hybrid/composite matrices consisting of biodegradable polymers and inorganic fillers like hydroxyapatite (HA) [28–33] and tricalcium phosphate (TCP) [1,34,35]. These are ideal for regeneration of bone-like tissues.

Many techniques have been developed to produce porous tissue engineering scaffolds, such as porogen leaching [36,37], emulsion freeze drying [38,39], 3D printing [40], gas foaming [41,42], electrospinning [43–45], thermally-induced phase separation (TIPS) [46,47] and any possible combinations of two of these techniques [48].

Among all the indicated techniques, TIPS is one of the most efficient due to its ease implementation (i.e., expensive specific equipment are not required) and its potential capability to produce scaffolds with tunable properties [49]. Different parameters can be considered to obtain the required properties for each specific application. The most important are the selection of the polymeric system (including composites), polymer concentration, solvent and nonsolvent system (including ratio between them) and cooling rate [50]. Adjusting such parameters, allows for efficient control over the final structure of the scaffold in terms of morphology, average pore size and degree of interconnected pores, which have a significant and very often limiting role in tissue regeneration [48,51]. Additionally, other important features of scaffolds like biodegradability [52] and mechanical properties [46,47] can also be controlled by the TIPS method. Porous scaffolds of tissue engineering can be prepared by TIPS technique without remnant of solvents, so preserving the biocompatibility of the scaffold [50].

The TIPS method has been developed in 1978 to fabricate microporous membranes [53]. In this process, a homogeneous multicomponent system (polymer, solvent, filler, drug, etc.) under defined circumstances becomes thermodynamically unstable, inducing the system to be separated into two distinct phases [54], a polymer-rich and a polymer-lean phase. After solvent removal by extraction, evaporation or sublimation, the polymer-rich phase is converted into the skeleton of a porous scaffold, while the removed solvent is responsible of the final porosity [55,56]. This method allows obtaining polymeric foams with porosity over 95% [57] and pore diameters from ~1 to 100 μm [53]. Numerous innovations in this area, including combination of TIPS with other fabrication techniques such as electrospinning [58,59], porogen leaching [60–62], 3D printing [21,22,63], modification of the solvent removal procedure [14,64] or variations in TIPS parameters [14,21,46,51,64,65] has been reported in literature.

All these advancements have enabled researchers to produce a variety of architectures and pore morphologies in micro/nanometer scale, desirable for specific utilizations. Porous scaffolds with architectures identified as micro/macro-porous [18,22,66], fibrillar (nano/micro-fibrous) [13,18,63,67,68], isotropic (random-pore) [46,51,60,69,70], anisotropic (oriented/aligned-pore or microtubular) [62,64,71–74], bilayered [58,59,75], biphasic [20,75] structures, lamellar platelets, lamellar stacks, axialites, spherulites [14] or a mixture of these structures have recently been produced by TIPS or TIPS-based strategies.

The great variety of 3D porous polymeric scaffolds developed by TIPS allows to satisfy a wide range of tissue engineering applications for regeneration of cartilage [76], bone [17,60,67,73,77,78], osteochondral [62,72,75], dermal [20], cardiovascular [58,71], neural [59,68,79,80] tissues and so on.

In this paper an overview of TIPS technique is provided and includes essential issues like methodology, influence of processing parameters and explanation of the different mechanisms of phase separation. Recent TIPS and TIPS-based technologies and materials used for fabrication of tissue engineering scaffolds have subsequently been reviewed considering structural features, properties and applications of the scaffolds. In the last section, the paper has been centred on tissue engineering scaffolds with special architectures produced through different mechanisms of phase separation and under specific fabrication conditions.

2.2. TIPS technique

2.2.1. Methodology

The TIPS technique is based on decreasing the temperature of a homogenous polymer solution or a homogeneous multicomponent system which has been formed at high temperature. The decrease of the thermal energy is used as a driving force to induce phase separation [50]: upon cooling, the system becomes thermodynamically unstable, being induced to separate into two distinct phases [54]. A polymer-rich and a polymer-lean (solvent-rich) phase with high and low polymer concentrations, respectively. The solvent in the polymer-lean phase is subsequently eliminated by extraction, evaporation or sublimation [81]. After solvent removal, the polymer-lean phase forms porosities and the polymer-rich phase is converted into a porous network characterized by appropriate pore geometry and interconnectivity [55,56,64].

The TIPS process is a function of polymer-solvent affinity and may follow two typical mechanisms (Figure 1) [64], namely liquid-liquid and solid-liquid phase separations. The former occurs before the solvent freezing, and the latter only happens when the solvent has completely been frozen [53]. The specific way of separation can be selected by choosing the TIPS parameters that affect the thermodynamics of the process (e.g., solvent system, polymer type and concentration, cooling temperature or cooling rate) [64]. Solid-liquid phase separation may happen during cooling when there is a good compatibility between the polymer and solvent (e.g., PLA and 1,4-dioxane with Hansen solubility parameters (HSP) of 21.9 $MPa^{1/2}$ and of 20.5 $MPa^{1/2}$, respectively) [64,82] and the solvent has a relatively high freezing point (Figure 1a). For the occurrence of solid–liquid phase separation in such type of system, the solvent crystallization temperature (freezing point) in the solution must be higher than the liquid–liquid phase separation temperature. By lowering the temperature of the polymer solution, the solvent is crystallized, the polymer is expelled from the crystallization front and the system consequently undergoes solid–liquid phase separation [83]. In this process, the structuration of the network is controlled by the crystallization of the solvent part [53]. Specifically, after removing the solvent, the morphology of the resulting foam is characterized by the pores having a geometry like the solvent crystallites [81,84,85]. For example, in the case of PLA solutions in 1,4-dioxane, a porous structure with an average pore size of around 100 microns has been created [53].

When a polymer-solvent system experiences a solid-liquid phase separation, the final structure and pore architecture of the resulting foam widely depends on the used solvent and its crystallization temperature, the phase separation temperature, the polymer concentration and the temperature gradient which has applied to the system [83]. Typically, an organic solvent with quite high freezing point like benzene (5.5 °C) or 1,4-dioxane (11.8 °C) is used for fabrication of synthetic polymer matrices using solid-liquid phase separation process.

By controlling the cooling process, matrices produced by solid-liquid phase separation may have isotropic or anisotropic architectures. Matrices with a randomly-oriented (isotropic) pore structure are formed by transferring quickly the homogeneous solution to a cooling device that allows solvent crystallization and solid-liquid phase separation. Indeed, when the crystallization direction is controlled and a uniaxial temperature gradient is applied to the system (for example by insulating the side walls of the mould that contains the polymer solution, before transferring it to the cooling device) an oriented-pore structure (anisotropic) is achieved.

Liquid–liquid phase separation in a polymer solution may occur during the cooling process, when the polymer-solvent affinity is very weak. Schugens et al. [86] and Nam and Park [87] showed that by adding water to a PLA/1,4-dioxane system, the phase separation mechanism can be changed under cooling. When water, as a poor solvent of PLA (note that its HSP is 47.8 $MPa^{1/2}$), is added to the system, the interactions between the polymer and solvent are lowered. As a result, a liquid–liquid demixing occurred at the temperatures higher than the solvent crystallization temperature.

The Flory–Huggins equation for the polymer-solvent system is shown in Equation (1) [88]:

$$\frac{\Delta G_{mix}}{RT} = \frac{\phi_d}{x_d} \ln \phi_d + \frac{\phi_p}{x_p} \ln \phi_p + \chi \phi_d \phi_p \tag{1}$$

where ΔG_{mix} is the Gibbs free energy of mixing per lattice site, ϕ_d and ϕ_p are the volume fraction of solvent and polymer, x_d and x_p are the number of lattice sites being respectively occupied by the molecules of solvent and polymer, and χ is the Flory–Huggins interaction parameter which is affected by the strength of interactions between polymer and solvent.

The first two terms on the right side of the Flory–Huggins equation represent combinatorial entropy contribution and are always negative, while the third term which represents the enthalpic contribution can be positive or negative (in function of the sign of χ). Weak interactions between polymer and solvent lead to a large and positive value of χ, resulting in a positive ΔG_{mix} that led to a liquid–liquid demixing. By contrast, when the strength of interactions between polymer and solvent is high (small χ), occurrence of liquid–liquid phase separation is more difficult (i.e., lower temperatures are needed). In this situation, the homogenous one-phase region in the phase diagram (Figure 1b) expands, and therefore the binodal curve, which is the boundary of liquid–liquid phase separation, shifts to lower temperatures [89].

In case the solvent crystallization temperature is much lower than the phase separation temperature, the polymer solution undergoes liquid-liquid phase separation upon cooling [83]. Typical phase diagram for a polymer-solvent system, characterized by an upper critical solution temperature (UCST) -critical point- is introduced in Figure 1b [64]. When the temperature is high, the solution is homogenous and in a one-phase region. During cooling, when a homogeneous polymer solution reaches to a temperature-composition point below the binodal curve, a liquid-liquid phase separation occurs, and the system is separated to polymer-rich and polymer-lean phases [83].

According to the thermodynamic pathway (composition, temperature, time), the phase separation can take place with different behaviours [65,87]. The first possible scenario is that demixing occurs below the binodal curve, in a region which is called metastable. In this region solutions are stable with respect to small fluctuations in the composition and there is a kinetic barrier against the phase separation. This kinetic barrier can be overcome by a nucleation process. Hence, the two phases separate through a nucleation and growth (NG) mechanism. This mechanism proceeds by NG of polymer-rich phase in a surrounding matrix of polymer-lean phase, when polymer concentration in the solution is lower than that of the critical point [81]. In this situation a powder-like polymer solid or a bead-like structure is obtained [83,90]. Conversely, NG of polymer–lean droplets in a matrix of polymer rich phase at concentrations higher than critical, results in formation of a foam with closed pores, or a poorly-interconnected polymeric matrix with spherical or pseudo-spherical pores [64,83].

The second scenario which is called spinodal decomposition (SD), can take place when the spinodal curve is crossed for a given polymer concentration under cooling. The region below the spinodal curve is called unstable, where there is no activation barrier against phase separation. Any fluctuations in composition cause free energy to decrease and a wave of fluctuations throughout the solution is triggered. In this region, the system separates into two phases through a well-known SD mechanism, resulting in formation of a bicontinuous and interconnected structure of polymer-rich and polymer-lean phases [81,87,91]. After removing the solvent, a 3D well-interconnected porous network is formed as a result of SD. Generally, the polymeric foams prepared through NG mechanism (metastable region) have relatively large pores while those prepared via SD mechanism (unstable region) have a fine microcellular structure (a network of small interconnected pores) [90,92].

The third possible scenario, which is the most likely one, is a combination of the two previous mechanisms (i.e., NG, and SD mechanisms). This occurs when both curves are crossed upon cooling for a certain polymer concentration. Since liquid-liquid phase separation trough NG is quite slow and through SD is very fast [92], higher cooling rate conditions can be applied to limit or prevent NG mechanism in the metastable region and achieve the fine SD-derived structures [81,89,92,93]. Önder et al., in addition to the cooling rate, by altering other TIPS parameters (i.e., polymer concentration and solvent/nonsolvent ratio) could control the NG/SD-derived morphologies during TIPS process [90]. After the liquid-liquid phase separation through both mechanisms is finished, the resulting structure becomes frozen in a solid state by continuing the cooling process to a temperature below the glass transition or gelation or solvent crystallization temperature in the solution. The next step is the removing of the solvent from the frozen structure to create a polymeric porous network. The conventional method of solvent removal from the phase-separated structures is freeze-drying. This is a long process (i.e., generally takes between three days [39,65,83,87] to one week [94,95]) and, particularly, a high energy-consuming method. Supercritical CO_2 drying technology is an effective alternative for the reduction of the duration and environmental cost of the whole process that is being successfully developed by scientists [96].

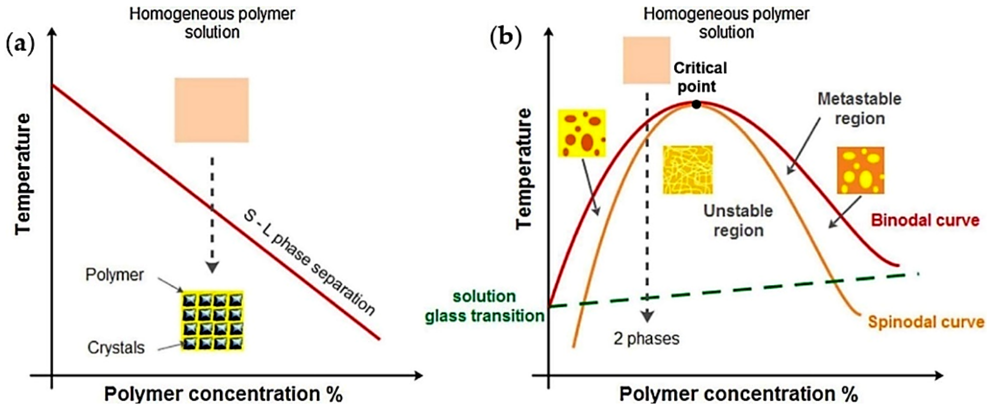

Figure 1. TIPS process in polymer solutions through two main mechanisms: solid-liquid phase separation (**a**), liquid–liquid phase separation (**b**). Reprinted with permission from [64].

Fabrication of porous matrices via solid–liquid and liquid–liquid phase separations, with the use of organic solvents with high freezing points (i.e., 1,4-dioxane or benzene), and others with low freezing points (i.e., tetrahydrofuran (THF), dimethylformamide (DMF) and pyridine) has been reported [84,85,94,97,98]. Recently, the use of ethylene carbonate (EC) as a solvent for preparation of poly(lactide-*co*-glycolide) (PLGA) foams by TIPS method has also been reported [20,99,100]. This solvent with a melting point of 36.4 °C [101] can be supercooled between 0–10 °C before freezing [102,103]. Furthermore, its high miscibility with water allows its fast leaching from the scaffolds [99], and becomes an appropriate selection when rapid process manipulations are required [20]. Considering the lethal dose (LD50) of 1,4- dioxane, THF and EC, which are 4200–5400 $mg \cdot kg^{-1}$, 1650 $mg \cdot kg^{-1}$ and 10400 $mg \cdot kg^{-1}$, respectively, EC represents therefore a proper solvent for clinical applications with relatively low health hazards [99,104–106].

Porous matrices with the morphology consisting of a continuous isotropic structure with pores ranging from several to tens of microns can be easily produced by means of liquid-liquid phase separation [83]. In some cases, a gelation process may happen during liquid-liquid phase separation upon cooling [107,108]. The formed gel is a network of physically crosslinked polymer chains with trapped solvent within the network [109]. This gelation process have also great interest for fabrication of polymer matrices with nanofibrous structures [83]. In semicrystalline polymers, the interlocking of crystal agglomerates may be the mechanism for the formation of gel [109]. When the gel is formed, the solvent is exchanged and the gel is freeze-dried to render a 3D nanofibrous network.

By utilizing a semicrystalline polymer, due to the crystallization potential of the polymer, the solution encounters driving forces for liquid-liquid phase separation and for crystallization of polymer during cooling. This coexistence somewhat complicates the process. Thus, polymer can crystallize if its crystallization temperature is higher than the phase separation temperature, and also if the solution is held long enough at a temperature higher than that of the phase separation. In this case, another type of solid-liquid phase separation –caused by solidification of the polymer- occurs [83]. This type of phase separation in the literature has also been called "solid-liquid phase separation" and, in some cases, "crystallization-induced phase separation".

Depending on the polymer concentration, different morphologies can be obtained as a result of crystallization or precipitation of polymer from the solution. These morphologies vary from loose precipitates (unconnected precipitates) to percolating structures (interconnected networks of crystallites) [81]. Specifically, microarchitectures such as platelet-like structures from quite low concentrated solutions [94] and spherulitic structures from relatively high concentrations have been produced [89,110].

As a representative example, it is interesting to note that a semicrystalline polymer like PLA could render a phase separation via a typical liquid-liquid mechanism or via polymer crystallization. As a matter of fact, there is a competition between these two processes due to both mentioned driving forces. When liquid-liquid phase separation precedes the polymer crystallization upon cooling, phase separation occurs through binodal or SD mechanisms. By contrast, if crystallization of polymer precedes liquid-liquid phase separation, the earlier process (polymer crystallization) becomes thermodynamically favourable when the temperature drops below the crystallization point of the polymer. When enough undercooling is available the polymer crystallizes, and the polymer crystals are formed through NG mechanism [111].

2.2.2. Application of Foams Prepared by TIPS

The TIPS technique has been developed to produce microporous membranes in 1978 [53]. This method has widely been used in non-biomedical fields to prepare synthetic membranes for separation and filtration purposes so far. As recent examples of applications of TIPS for nonmedical applications, the production of nanocomposite-based epoxy resins with favourable electrical, thermal and mechanical properties from polyacrylonitrile aerogel and carbon nanofibres (CNFs) can be mentioned [112]. Epoxy resins, as thermosetting polymers with unique physical, mechanical and chemical resistance, can be used in protective coatings, adhesives, high-performance composites, moulding and electrical applications [113,114].

Employing TIPS technique in the biomedical sector is also habitual, for example to develop drug delivery systems. Specifically, this methodology has been used for preparation of microspheres incorporating pharmaceutical and biological agents [3,115]. It should also to be considered among the biomedical sector applications that TIPS is among the common techniques which are employed to manufacture 3D porous scaffolds for tissue engineering applications [25,73,76,80].

A tissue engineering scaffold is a concept of designed and appropriate replacement material for regeneration of tissues such as bone, cartilage, etc. [116]. The scaffold must fulfil essential requirements such as possessing a 3D porous structure with the pores inside and on the surface to allow cell adhesion, proliferation, and differentiation. Such a pore structure also permits the nutrients and waste materials to be transported throughout the scaffold and also helps to form a mimetic host tissue that lead to the regeneration process [117]. Other requirements are biocompatibility, due to degradation of the materials over time [118], adequate mechanical properties until the target tissue is completely regenerated [119] and, in addition, a simple and sustainable manufacturing process [115].

The TIPS method is an effective conventional technique for the fabrication of tissue engineering scaffolds, as it is able to generate highly porous matrices with an interconnected pore network [84,120]. This technique is also compatible with incorporation of high amounts of filler materials, enjoying the advantages of low production cost and easy processability [121]. Specifically, TIPS allows fabricating polymer foams with porosity over 95% [57], with a wide range of pore diameter ranging from ~1 to 100 μm [53]. Due to the all mentioned potentials, and also to the versatility, ease of operation and the vast range of attainable scaffold morphologies, phase separation-based procedures have proven to be reliable methods for creating 3D porous scaffolds [93,122]. TIPS experimentally allows researchers to control the final structure of the scaffold with respect to morphology, average pore size and degree of interconnection [51]. Specifically, it has been reported that process parameters such as the polymer concentration and crystallinity, the cooling temperature and rate, and also the presence of ceramic powders can be manipulated to be able to have control over the indicated morphologic characteristics [84,123].

Depending on the applied polymer and phase separation conditions, polymer scaffolds in terms of structure can be classified as solid-walled isotropic and anisotropic (e.g., microtubular), fibrous, nanofibrous, and platelet-like structures [84,85,94,97,98]. In addition, the different mechanisms of TIPS techniques, including solid–liquid [84,85,97], liquid–liquid [94,98] and crystallization-induced phase separations [94], have been used for the preparation of different micro- and nano-structured polymer networks.

Porosity is a crucial parameter to be noticed when approaching tissue engineering. Numerous attempts have been reported in the literature aimed to manufacture highly porous scaffolds by different techniques and a great variety of materials. For example, PLA-based scaffolds having 20% of β-TCP have been produced by the salt leaching method [124], and composite sponges made of PLGA, collagen (Col) and apatite particles have been prepared by sintering being reached porosity levels so high as 87% [125]. Although there is no consensus about the optimal values concerning porosity and derived morphology in the literature [8], porosity values higher than 90% are suggested for bone tissue engineering applications [124-127]. This level results in a high cell proliferation, bone ingrowth and osteogenesis [8] as a consequence of the high transport of oxygen and nutrients [128]. TIPS is a technique that without the need of high temperatures (that may affect the polymer matrix or mineral filler properties) allows to prepare scaffolds with porosities higher than 90% [121]. Typical porous architecture produced by the TIPS technique consisted of interconnected pores with a wide range of pore sizes [53], an interesting and desirable feature for tissue regeneration. Thus, larger pores (in tens of microns) allow transport of typical cells and the smaller ones are ideal for perfusion of small molecules such as nutrients and growth factors [129].

Considering the potentiality of TIPS to produce highly porous PCL scaffolds [126], Gandolfi et al. employed this technique to fabricate PCL-based scaffolds loaded with different amounts of calcium silicate (CaSi) and calcium phosphate for bone regeneration. Scaffolds could reach a 95% of open porosity even for a 20 wt% of fillers. The composite scaffolds were not brittle and the inorganic fillers played a reinforcing effect by improving viscoelastic properties. Nucleation of calcium phosphates and apatite on their surface created a bone forming osteoblastic microenvironment [69].

An appropriate bone tissue engineering scaffold allowing cells to grow with appropriate physical shapes and assisting the vascularization of primary tissues, not only needs to have enough porosity, since requires also a well-regulated interconnected pore structure. TIPS is an ideal technique since allows the preparation of 3D scaffolds with adjustable porosity and interconnected pores [130].

Correspondingly, Kozehkonan et al. used TIPS to produce PCL scaffolds with high porosity and pore interconnectivity. As a surface modification to overcome the hydrophobicity of PCL scaffolds, they coated the resulted scaffolds with chitosan (CS), bioactive glass (BG) and nanoparticles of gelatin (GEL). TIPS-obtained PCL scaffolds were highly porous, had variable pore sizes from several to a few hundred microns, and an appropriate pore interconnectivity. The applied surface modification improved the degradation rate and spreading tendency of the cells on the scaffolds. Compared to single or binary coating systems without BG, the proposed ternary system resulted in the highest mechanical strength and a significant improvement in MG-63 cell proliferation [131].

An ideal tissue engineering scaffold to be anatomically adapted must also provide enough mechanical resistance [132]. Montanheiro et al. [74] employed the TIPS technique to produce poly(3-hydroxybutyrate-*co*-3-hydroxyvalerate) (PHBV) scaffolds reinforced with cellulose nanocrystals (CNC). Different levels (1–3 wt%) of nanocrystals were efficiently dispersed by ultrasonication of PHBV/dioxane solutions, and after freezing and freeze-drying steps porous nanocomposite scaffolds were achieved. These scaffolds consisted of oriented pores and unidirectional channels with some regions of random pores. A wide range of pore size distribution was reported: bigger pores in the bulk and smaller ones on the walls which would allow the transport of cells and nutrients. Results revealed that incorporation of CNCs did not affect the morphology but led to a decrease in the porosity of the scaffolds due to changes in the phase separation mechanism. Although they nano-scaled needle-like CNCs were added to the polymer solutions, a dispersion of micron-sized CNC agglomerates was still observed. Therefore, dispersion was not efficient along the whole matrix, especially at higher CNC ratios. However, reinforced scaffolds showed an improvement in the compression modulus and mouse fibroblast cell attachment and proliferation with respect to neat PHBV scaffolds [74].

Taking advantages of structural features of TIPS-obtained scaffolds (i.e., high porosity and interconnective pore structure), and positive biological activities of electrospun GEL nanofibres and taurine, Samadian et al. developed composite scaffolds for bone regeneration. Thus, pre-prepared electrospun GEL nanofibres having different contents of taurine were incorporated to PLA/PCL-based scaffolds. These modifiers were added to a PLA/PCL/dioxane solution and by freezing phase separation was induced. Figure 2 shows the highly porous scaffolds with interconnected porosities that were generated after sublimation of the solvent through freeze-drying. New scaffolds were good candidates for bone regeneration purposes due to their acceptable hydrophilicity, weight loss, mechanical properties, hemo- and cytocompatibility and capability to support bone cell proliferation in vitro and bone regeneration in vivo [133].

In addition to porosity, pore size and structure, biocompatibility of tissue engineering scaffolds must be considered in tissue engineering applications. Presence of organic solvents or inadequate leaching of some porogen agents can affect the biocompatibility of scaffolds. The TIPS process allows fabrication of tissue engineering scaffolds without remaining solvents and, therefore, preserving biocompatibility. Various TIPS-obtained scaffolds with especial characteristics have recently been applied in myocardial, dermal and bone tissue regeneration [20,50,134].

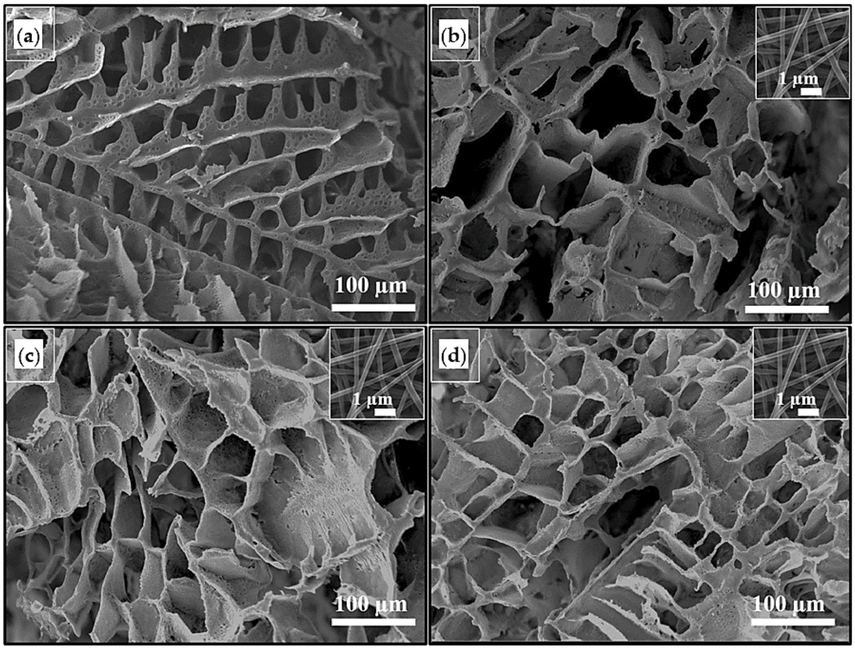

Figure 2. SEM micrograph of the prepared scaffolds. PCL/PLA/GNF (**a**), PCL/PLA/GNF/Tau 0.1% (**b**), PCL/PLA/GNF/Tau 1% (**c**) and PCL/PLA/GNF/Tau 10% (**d**). The insets show SEM micrograph of GNFs. Reprinted with permission from [133].

Employing two different synthetic polyesters (i.e., PCL and a poly(urethane urea)ester (PEUU), Wang et al. prepared biocompatible 3D scaffolds by TIPS for massive rotator cuff tear regeneration. An irregular pore structure was obtained from both polymers using the same parameters. An interconnected structure was obtained, being the largest pores about 40 μm and 80 μm for PCL and PEUU scaffolds, respectively (Figure 3). The PEUU scaffold had an ideal biocompatibility, suitable structural properties and elastic mechanical properties. In addition, it could better support the proliferation and migration of rabbit bone (RBMSCs) in vitro and efficiently induced physical tendon-to-bone interface and tendon regeneration in a rabbit model. Hence, the macroporous PEUU scaffold was suggested as an efficient graft for tissue repairing/regeneration [66].

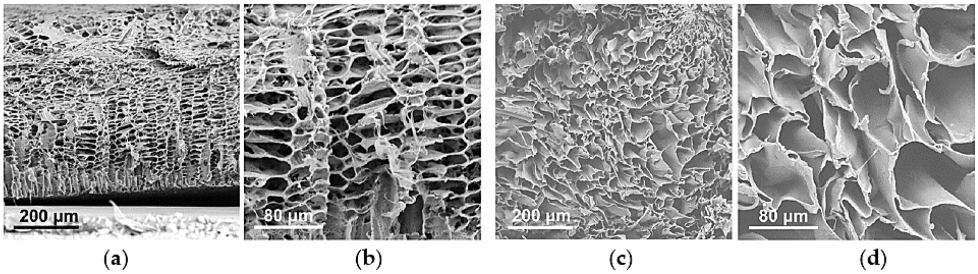

Figure 3. SEM images exhibiting the cross-sectional structure obtained from PCL (**a**,**b**) and PEUU (**c**,**d**) scaffolds prepared using same TIPS experimental conditions (i.e., solvent, polymer concentration, cooling and drying conditions). Reprinted with permission from [66].

2.3. TIPS and TIPS-Based Technologies for Fabrication of Tissue Engineering Scaffolds

2.3.1. Preparation of TE Scaffolds by the TIPS Technique

TIPS is one of the most versatile methodologies to produce scaffolds with a high degree of interconnection and a wide range of pore dimensions via targeted temperature versus time protocols [135,136]. Taking into account this capability of TIPS technique, Lombardo et al. [51] controlled porous structure and pore size of poly(L-lactide) (PLLA) scaffolds to be used as 3D support for in vitro culture of tumour cells and studied the effect of porosity and average pore size on cell adhesion and growth. Different demixing temperatures and times (i.e., in a thermal water bath (TWB) of 20–30 °C/15–30 min) were applied to a ternary mixture of polymer-solvent-nonsolvent (i.e., PLLA-dioxane-water). Then the samples were quenched in an ethyl alcohol bath (EAB) at −20 °C for 10 min. By using/not using a polytetrafluoroethylene (PTFE) insulating shell (COAT/NOCOAT) they tuned the heat transfer during the phase separation and/or quenching process and produced 3D PLLA foams with pore sizes ranging from 25 to 150 μm (Figure 4). Demixing temperatures of 25 °C and 30 °C lay within the binodal region, where phase separation occurs through NG mechanism [135] and resulted in average pore size of 100 μm and 150 μm, respectively [51]. Reduction of time and the demixing temperature (i.e., 20 °C) resulted in structures with average pore sizes from 30 μm to 60 μm. In this condition, the lower cooling rate allowed the system to remain for longer time in the metastable region, giving rise to nuclei growth and thus an increase in pore size.

On the other hand, direct quench from 60 °C to −20 °C led to a highly interconnected structure with very small pores of 25–30 μm, which is in accordance with the structure where phase separation occurs through SD mechanism [93,122]. Specifically, the sudden temperature drop caused that the ternary polymer solution mainly remained in the unstable region where the biphasic system was not generated via NG. The two phases interpenetrated each other, resulting in the formation of a scaffold with highly interconnected microporous structure [93]. The work confirms that TIPS is a suitable manufacturing technique for finely tuning the scaffolds architecture. An average pore size of 40–50 μm was obtained being an optimal value for the growth and proliferation of breast cancer cells. Aggregation of tumour cells could be induced and an irregular tumour mass could be formed in vivo [51].

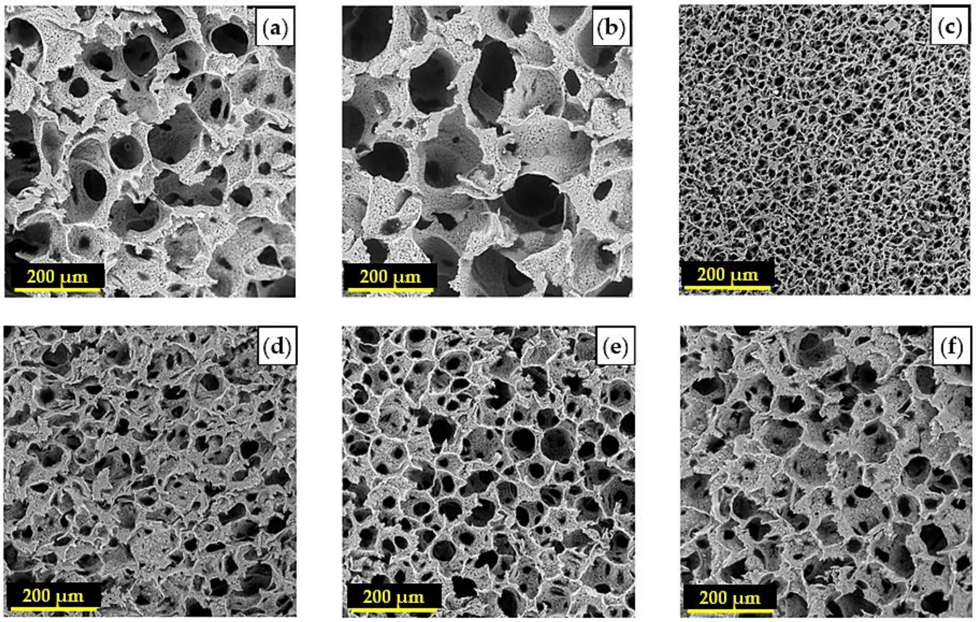

Figure 4. SEM micrographs of PLLA scaffolds obtained by TIPS according to a slow cooling for 30 min and demixing temperatures of 25 °C (**a**) and 30 °C (**b**), and a fast quenching (**c**). The average pore sizes were 100 μm, 150 μm and 25–30 μm, respectively. By keeping the demixing temperature at 20 °C for 15 min and using/not using an insulating PTFE shell (COAT/NOCOAT) in TWB and/or in EAB, (**d**) COAT-NOCOAT; (**e**) NOCOAT-COAT; (**f**) COAT-COAT. The average pore sizes were about 30 μm, 40–50 μm and 60 μm, respectively. Reproduced with permission from [51].

Conoscenti et al. used the ternary solution of PLLA/dioxane/water loaded with various amounts of BG 1393 to produce composite foams via TIPS technique in a single step. They dispersed BG particles in the solution by sonication and applied phase separation by placing the system in a thermal bath (30 °C/75 min) and then freezing it in an EAB. After washing with deionized water and vacuum drying, they produced composite scaffolds and studied their chondrogenesis ability [76]. Functionalization of PLLA with BG1393 took profit of its good processability, low reactivity and the well demonstrated suitability for TIPS processes [137]. Porous PDLLA and BG45S5 composite foams fabricated by TIPS process exhibited anisotropic tubular pore morphology [138], while PLLA/BG1393 composite foams developed a typical TIPS architecture (i.e., highly porous foams with isotropic and an interconnected pore structure in which the morphology was not affected by addition of the BG particles). PLLA/BG1393 scaffolds were considered highly promising for osteochondral articular cartilage repair due to the survival of chondrocytes on the culture period, easy colonization in the inner parts and maintenance of the chondrocyte phenotype [76].

Another advantage of the TIPS technique is the easy incorporation of various desirable materials/agents (depending on the target tissue) to the primary polymer solution. Farzamfar et al. [70] developed PCL/PLA scaffolds containing tetracycline hydrochloride (TCH) antibiotic for bone regeneration. They added different levels of TCH to solutions of PCL/PLA (1:1 *w*/*w*) in 1,4-dioxane and fabricated microporous matrices for local administration of the antibiotic and the evaluation of their bone healing activity. The resulting scaffolds had open microstructures with irregular-shaped pores with diameters around 100 μm and showed antibacterial and osteoinductive properties. The highest in vitro cell proliferation and viability and the highest in vivo bone formation in a rat femoral defect was found in scaffolds having 10 wt% of TCH antibiotic [70].

Although freeze-drying is the most common and the conventional step to remove the organic solvents after the phase separation process, sublimation of the frozen solvent is, relatively, a time- and energy-consuming process. Recently, researchers have paid attention to other effective alternatives to reduce both processing time and energy consumption. Supercritical carbon dioxide (SC-CO_2) drying technology seems to be an excellent alternative but rarely have been studied so far [96] due to its good extraction ability. Reverchon et al. showed that SC-CO_2 extraction of 1,4-dioxane from PLA matrices could reduce the residual solvent below 263 ppm after only 4 h, which is in accordance with the concentration limits of 1,4- dioxane (380 ppm) authorized by the pharmacopeial convention [139].

In this regard, some researchers conducted a parametric study of the TIPS process. Thus, by adjusting polymer concentration and molecular weight, solvent miscibility, and cooling temperature, the phase separation of PLA/1,4-dioxane-water solvent system could be finely controlled and, therefore, the structural and mechanical properties of the resulting scaffolds could be tuned. Specifically, PLA scaffolds were prepared using SC-CO_2 freeze-drying an environmental analysis using the Life Cycle Assessment (LCA) methodology was performed. The combination of TIPS and SC-CO_2 drying effectively reduced the time and energy consumption of the whole process and 50–90% of the environmental impacts, so application at the industrial scale was potentially feasible [64].

2.3.2. *Preparation of TE Scaffolds by Combining TIPS with Other Technologies*

TIPS technique has been combined with other TE scaffolds fabrication methods. These more complex processes allowed to meet special requirements for a specific target tissues, to enhance physiochemical, mechanical or morphological properties or to obtain special architectures like hierarchical, biphasic or bilayered structures. Useful information about the components and the structure of some scaffolds fabricated by such combinations are summarized in Table 1. Combination of TIPS with other common methods have been classified and the fabrication process together with recent achievements in this area have been elaborated in the following sections.

2.3.2.1. Combination of TIPS and Porogen Leaching Technologies

Nowadays, many variations concerning TIPS methodology have been developed by altering process parameters [46,51,65], using different solvents [140] or combining the process with other technologies. One of these variations is focused to increase the pores size of the scaffold by adding porogen particles, which can be removed from the system after freeze-drying in a subsequent leaching step. Sodium chloride [50,140-144] or sugar [145,146] particles are the most common porogens. The increase of pore size through complementing TIPS with the leaching technique led to an improvement in cell proliferation, as for example reported for PLLA scaffolds [146].

Szustakiewicz et al. obtained high-porosity composite scaffolds based on PLLA and HA. Using 1,4-dioxane as solvent, they prepared PLLA solutions loaded with different ratios of synthetic HA powder. After addition of NaCl porogen particles, the samples were frozen and then freeze-dried. Salt leaching was performed by soaking the foams in demineralized water. The composite scaffolds obtained after air and vacuum drying had small pores of up to 50 μm and larger ones up to 400 μm resulting from sublimation of 1,4-dioxane and salt leaching, respectively. The HA content increased PLLA thermal stability and crystallinity (due to nucleation effect of HA). Furthermore, the increase of the HA content increased also the surface hydrophilicity, Young modulus, compression stress of the scaffold and the proliferation rate of pre-osteoblast cells. Although scaffolds were highly porous (i.e., 96–98%), pores collapsed for a 90 wt% of HA. Therefore, a 75 wt% HA content was considered optimum [60].

Table 1. Summary of some scaffolds fabricated recently by combination of TIPS and other techniques.

Polymer System	Filler System	Solvent System	Morphology	Fabrication Technique	Application	Reference
PLLA	HA	Dioxane	Microporous	TIPS + salt leaching	Bone TE	[60]
PLGA		Dioxane	Radially-aligned and random pores [1]	TIPS + salt leaching	Osteochondral	[62]
GEL	Nano-silicate	Ethanol:water (1:1)	Nanofibrous	TIPS + porogen leaching [2]	Bone TE	[61]
GEL/PEEUU [3]	MSN/SA [4]	Water/HFIP [5]	Microporous and nanofibrous [6]	TIPS + electrospinning	Vascular TE	[58]
PCL/Col	CNFs	Dioxane/acetic acid [7]	Microporous and nanofibrous [8]	TIPS + electrospinning	Neural TE	[59]
PLLA/CS	PDA/Qu [9]	Acetic acid	Microfibrous and nanofibrous [10]	TIPS + 3D printing	Bone TE	[63]
PLGA	nHA [11]	Dioxane	Microporous and macroporous [12]	TIPS + 3D printing	Bone TE	[22]
PLGA		EC	Microporous and knitted mesh [13]	TIPS + textile technology	Dermal TE	[20]

[1] Radially-aligned pores were obtained from TIPS, random pores from salt leaching; [2] Paraffin spheres have been used as porogen; [3] Poly(ester-urethane)urea (PEEUU); [4] Mesoporous silica nanoparticles (MSNs) loaded with salvianic acid (SA); [5] Distilled water was used as solvent for Gel/MSN/SA system (in TIPS), hexafluoro-2-propanol (HFIP) for PEEUU (in electrospinning); [6,8] The scaffolds have a bilayered (microporous/nanofibrous) tubular structure; [7] 1,4-dioxane for PCL/CNFs system (in TIPS), acetic acid for PCL and Col (in electrospinning); [9] polydopamine (PDA), quercetin (Qu); [10,12] The scaffolds have a hierarchical structure; [11] nanohydroxyapatite (nHA); [13] The scaffold has a biphasic structure.

A porous scaffolds, as synthetic extracellular matrix (ECM), plays an essential role in bone TE since provides a 3D template for cell adhesion and proliferation and also pro-osteoblastic signals for osteoblastic differentiation [147-150]. Hence, an ideal scaffold for bone tissue engineering must have appropriate mechanical properties, osteoconductivity, and growth factor binding/release capacity for bone formation, to be able to mimic the structure and functions of the native bone matrix [151-154]. Although significant progress has been achieved in developing biomimetic biomaterials in the last few years, still these requirements are not met in most current 3D scaffolds [155-158].

To morphologically and chemically mimic the native bone matrix, Yao et al. have recently prepared GEL nanofibrous scaffolds with defined macropore structures, favourable for osteogenic differentiation of stem cells and bone regeneration by employing the combination of TIPS particle and leaching techniques [159-161]. Functionalization with disk-shaped nanosilicates with high surface to volume ratio were later performed to improve mechanical properties and osteoconductivity. Specifically, paraffin microspheres (150–300 μm) were selected as porogens and added them to GEL/nanosilicate solutions in ethanol/water (50%). Composite scaffolds had similar morphologies to the pure GEL ones; a hierarchical structure with interconnected macroporous and a Col-like nanofibrous microstructure. Interestingly, the GEL-nanosilicate nanofibrous/macroporous scaffolds could better promote osteoblastic differentiation of human mesenchymal stem cells (MSCs) than the pure Col scaffolds [61].

2.3.2.2. Combination of TIPS and Electrospinning

Scaffolds with structural similarity to natural ECM at the nanoscale and optimum porosity to facilitate metabolites diffusion have been prepared as a neural guidance channel (NGC) by a combination of TIPS and electrospinning methods [162,163]. Scaffolds constituted by electrospun fibres are promising for peripheral nerve repair [164,165], and TIPS is a method with potential to yield pore interconnectivity [166,167]. Incorporation of CNFs to such a complex system, can create electrical conductivity which has been shown that can improve regenerative capacity of NGCs [54]. Accordingly, Farzamfar et al. [59] prepared an NGC (Figure 5) by preparing a PCL scaffold incorporating CNFs by TIPS which subsequently shaped it in the form of a conduit. Thread-like pieces from a PCL/Col nanofibrous sheet (made by electrospinning) were then introduced into the conduit lumen at the time of implantation into a sciatic nerve defect in the rat model. Results demonstrated the potential application of this construct for peripheral nerve tissue engineering since no toxicity or immunogenic reactions were detected, while successful nerve regeneration was well supported [59].

Due to their good biocompatibility, natural polymers are regularly used for the preparation of vascular scaffolds [168]. Nevertheless, tensile strength of such scaffolds is much lower than that of the human coronary artery [169-173]. In order to prepare scaffolds with sufficient mechanical properties to be used as vascular graft, Guo et al. fabricated bilayered small diameter tubular scaffold by combining TIPS and electrospinning. As an inner layer, a microporous GEL foam incorporating 10 wt% of salvianic acid (SA) loaded-mesoporous silica nanoparticles (MSNs) was firstly prepared using TIPS technique. SA was used as drug anticoagulant. In order to strengthen the vascular scaffold, electrospun poly(ester-urethane)urea (PEEUU) nanofibres were deposited outside of the inner layer. The final material showed good mechanical properties, a sustained release profile, a good proliferation of endothelial cells and in vitro long-term anticoagulant efficacy. In addition, hyperplasia and thrombosis effects were not detected in the rabbits' carotid arteries [58].

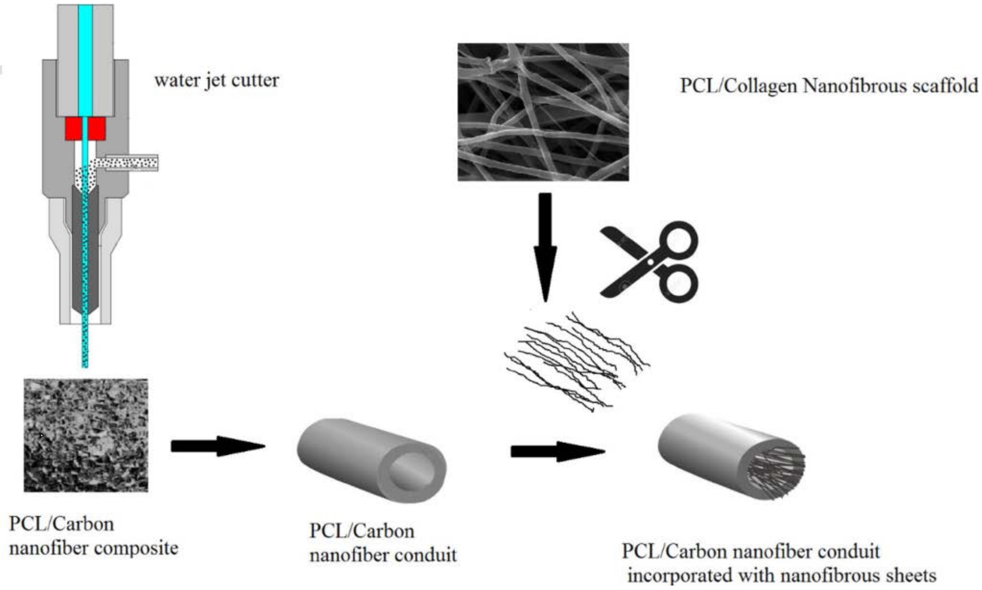

Figure 5. Schematic illustration showing the production process of NGCs. Reproduced with permission from [59].

2.3.2.3. *Combination of TIPS and 3D Printing*

Tissues appropriate for bone regeneration are problematic considering the bone structure, which is a multilevel complex system composed of inorganic and organic components, and the bone formation, which depends on the micro/nano-scale hierarchical structure of ECM [174]. Accordingly, micro/nano-fibre combined scaffolds appear advantageous since can exhibit better cell adhesion and angiogenic potential compared to typical micro-fibre scaffold. Note that an ECM-like nanofibre network has a higher available cell adhesion area and a blood vessel-like structure throughout the formed scaffold [175]. Hence, preparation of multifunctional scaffolds with biomimetic ECM hierarchical structure can be a promising advancement in the treatment of bone defects.

Since TIPS is one of the techniques which are used to construct scaffolds with nano-sized structures [176], combining it with a technique like 3D printing can hopefully overcome the shortcomings of a single technology to get complementary advantages. In this regard, some researchers concluded that 3D-printed PLLA scaffolds having only micro-sized fibres and large-sized pores cannot match the ECM-like hierarchical structures. Therefore, these scaffolds are not particularly conducive to cell adhesion and internal migration that are needed for the formation of high-density vascular networks and bone tissue [177].

However, combination of 3D printing and TIPS technologies can overcome the indicated limitations. Specifically, through TIPS technique, scaffolds consisting of CS nanofibres within 3D printed PLLA microfibres were produced. The resulting hierarchical structure consisted on irregular CS nanofibres, with diameters around 80–600 nm, which were infiltrated into the holes and the surfaces of the PLLA microfibres. These PLLA/CS scaffolds were finally covered with a polydopamine (PDA) layer (PLLA/CS-D) and then functionalized with bioactive quercetin (Qu) (PLLA/CS-D/Qu). The CS nanofibres were not structurally affected by PDA and Qu surface modification (D/Qu) and maintained their original structure. Field emission scanning electron microscope (FESEM) images of unmodified and modified PLLA scaffolds are shown in Figure 6. Incorporation of CS nanofibres, PDA and Qu increased the hydrophilicity and mechanical properties of the neat PLLA scaffold and promoted cell growth and adhesion into the internal pores. Furthermore, an excellent osteogenic activity and anti-inflammatory response conferred an attractive prospect for bone tissue engineering [63].

The necessity of highly-porous networks for cell seeding and tissue growth, complicate the preparation of high-module scaffolds suitable for bone tissue engineering. Some investigators presented the design optimization of PLGA/nanohydroxyapatite (nHA) scaffolds, prepared by TIPS. By applying different experimental parameters including TIPS temperature, PLGA concentration and nHA content, scaffolds with different thickness, density, porosity, and modulus were produced [21]. The possibility of creating macro/microporous architectures was also considered due to the role of macrochannels in transport, and therefore in cell migration and angiogenesis upon in vivo implantation. To this end, extrusion-based additive manufacturing (AM), (i.e., 3D printing) and TIPS techniques were combined.

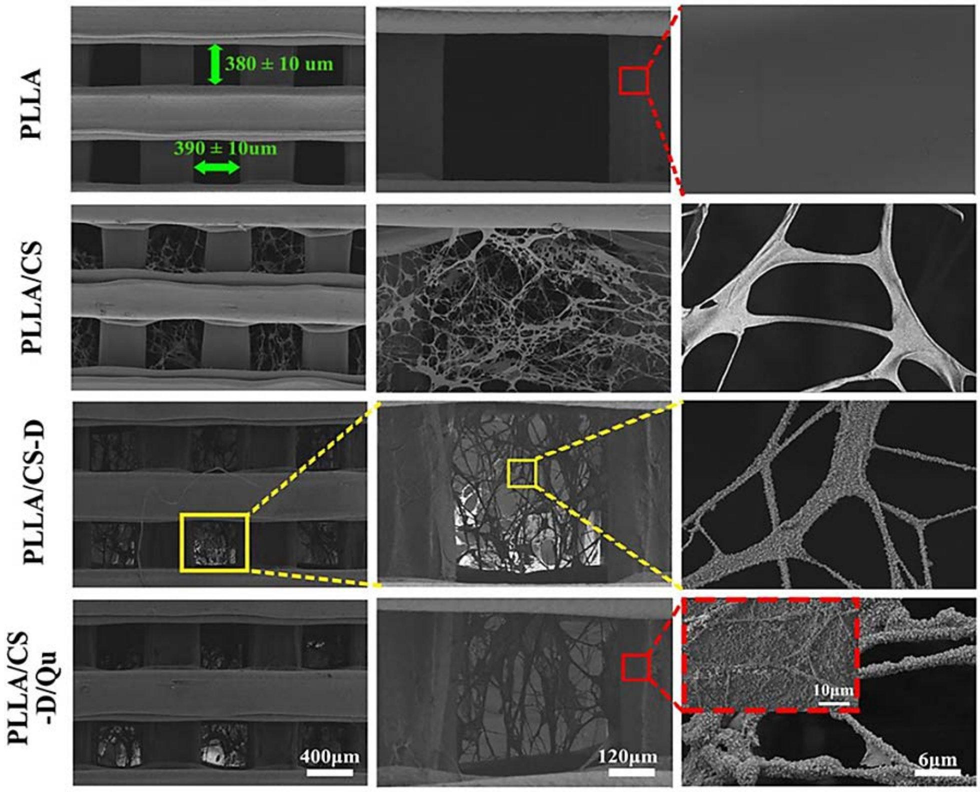

Figure 6. FESEM images of unmodified and modified PLLA scaffolds. The original 3D printed PLLA scaffold had square-like porosity with fibre diameters around 410 ± 18 µm. The transverse distance and the longitudinal distance between two fibres were 390 ± 10 µm and 380 ± 10 µm, respectively. Many particles appeared on the fibre surfaces after successive functionalization with PDA and Qu. Reproduced with permission from [63].

A 3D-plotted strand structure of polyethylene glycol (PEG) was embedded in PLGA/nHA/1,4-dioxane solution and then the system was cooled to get phase separation. In this way a microporous matrix surrounding the PEG macrofibres was obtained after dioxane sublimation. Deionized water extraction of PEG led to the formation of macrochannels [22]. The produced hierarchical PLGA scaffolds with the same procedure had a bimodal pore size distribution (<50 and >300 µm) containing interconnected macrochannels (Figure 7). The orthogonally interconnected channels generated by AM could provide an ideal environment for bone ingrowth, as well as facilitate the transport of oxygen and nutrients. These macro/microporous scaffolds had a potential to act as support materials for in vitro MC3T3-E1 cells growth [120].

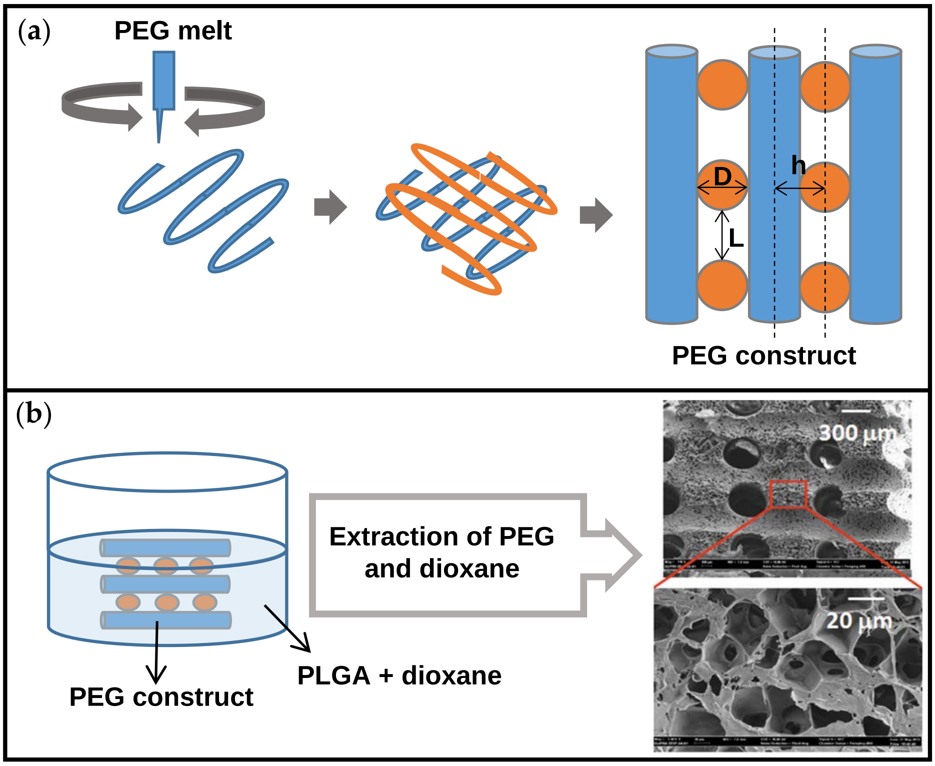

Figure 7. AM bioplotting of PEG constructs and adjustable bioplotting parameters (**a**). Schematics of the fabrication process of a simple PLGA scaffold derived from the previous incorporation of PEG macrofibres (**b**). D,L and h represent strand diameter, pore size and layer thickness, respectively. The successive PEG layers (blue and orange) have perpendicularly been 3D-plotted. Based on [120].

2.3.2.4. Combination of TIPS and Textile Technology

Although textile meshes due to impressive mechanical and manufacturing properties are potential scaffolding materials, both biological and mechanical factors must be considered when designing and manufacturing scaffolds for tissue engineering [20].

Knit mesh structures with tunable tensile properties and compatibility with suturing to adjacent tissues are ideal for dermal tissue repair, but the presence of large void spaces between the fibre bundles complicates the formation of a continuous epithelial cell layer [178,179]. Equipping strong biodegradable textile meshes with a finer secondary structure, which is able to connect fibre bundles and provide a support for cell delivery and growth, is a reliable solution for dermal and other tissue repairing applications [20].

Biphasic scaffolds consisting of PLGA textile knitted meshes embedded in a TIPS-obtained PLGA porous structure have for example been developed. Specifically, PLGA strips were immersed in PLGA/EC solutions and quenched to 4 °C. Phase separation was induced by agitation of the supercooled solution and the solvent was immediately leached in Milli-Q water. Utilizing EC solvent was beneficial since facilitated rapid manipulation and minimized the risk of degradation of PLGA meshes. Integrity and mechanical properties of pre-fabricated textile PLGA meshes was preserved after processing and their tensile strength was unchanged. The microstructure of the resulting biphasic scaffolds consisted of the polymer mesh uniformly encapsulated within an interconnected highly porous TIPS structure with an average pore size of 16.85 ± 3.8 μm (Figure 8) [20].

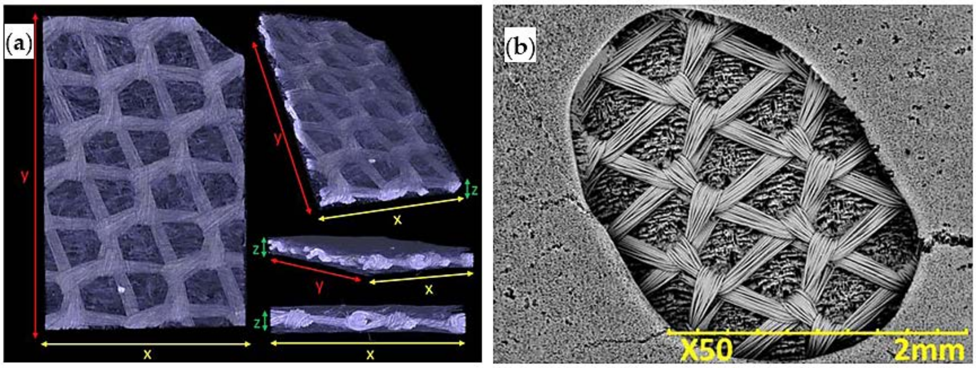

Figure 8. Micro-computed tomography (MicroCT) images of a TIPS-obtained PLGA scaffold incorporating PLGA knitted mesh (**a**) and a SEM image showing the porous TIPS structure and the embedded PLGA mesh through a rare spontaneous bubble (**b**). *X*, *Y* and *Z* are the scaffold dimensions. Reproduced with permission from [20].

2.4. Materials Used in Fabrication of Tissue Engineering Scaffolds by the TIPS Technique

2.4.1. Polymeric (Synthetic, Natural and Blended) Scaffolds

With the rapid progress in the field of tissue engineering, a great variety of scaffolding materials have been developed, being effectively used as biomedical materials in the treatment of tissue defects and the alleviation of the suffering of patients [180,181]. Various scaffolds made of synthetic and natural biomaterials have been broadly investigated and used in tissue engineering fields, opening up the world of organ and tissue regeneration [11]. Since biodegradability is a key factor for a tissue engineering scaffold (because of obviating the need for removing the scaffold when healing occurs) [25], biodegradable polymers have been extensively utilized in the construction of tissue engineering scaffolds [182]. Among them, aliphatic polyesters, such as PLA, PLGA, PCL and PLCL, have been closely studied over past decades, due to properties like biodegradability and biocompatibility [183]. Having such properties, and also good mechanical properties, PLA has been widely used in TIPS technique to fabricate porous scaffolds of tissue engineering [184,185].

Chen et al. synthesized PLLGC terpolyester by melt copolymerization process and then utilized it for preparation of porous scaffolds by TIPS technique. By varying some TIPS processing parameters like polymer concentration (from 2.5 to 15 wt%) and freezing temperature (from 4 to −60 °C) structural and mechanical properties could be controlled. Results showed larger pores and higher porosity, but a lower compressive strength when the polymer concentration was decreased, or the freezing temperature was increased. Furthermore, regular and interconnected pore structures with uniform pore size was achieved, although at high polymer concentration some pores were linear with uneven distribution and inconsistent pore sizes. The decrease in the freezing temperature caused a structural change from an irregular pore distribution to an orientated micro-tubular structure. Changes could be justified considering the crystallization of the employed 1,4-dioxane solvent throughout the phase separation process and the influence of the temperature gradient, which is more significant at lower freezing temperatures [25].

Materials currently employed in tissue engineering are mainly derived from natural polymers and synthetic materials. Natural-based polymers such as alginate (Alg), GEL, gelatin methacryloyl (GelMA), hyaluronic acid (HAc), CS, Col, fibrin, and decellularized ECM, play an important role in the field of biofabrication. Natural polymers generally enjoy considerable advantages in terms of biocompatibility, biodegradability and supporting bioactivity [186]. Additionally, naturally- or biologically-derived materials are also used due to the general lack of synthetic biomaterials responding to physiological stimuli [187].

Col as a kind of ECM proteins plays an important role in supporting cell attachment, migration and proliferation, due to its excellent biocompatibility, biodegradability and low immunogenicity [188]. Due to such properties, it has widely been used to prepare scaffolds for tissue engineering and regenerative medicine [189]. CS is another natural polymer with good properties such as antibacterial action, hemostasis, mechanics and cytocompatibility which has also been used in a variety of biomedical fields including wound healing, drug delivery carriers, surgical thread and tissue engineering [190]. Naturally-based polymers with their improved biocompatibility are notably employed to fabricate tissue engineering scaffolds using phase-separation technologies [91].

Si et al. [79] fabricated for example porous CS/Col scaffolds with controlled degradation behaviour by TIPS. These natural-based blend polymer scaffolds were employed as a potential support matrix for peripheral nerve regeneration. Different polymer solutions with different volume ratios (ranging from 10–90%) of CS and Col in acetic acid, and pure CS and Col solutions as control were processed. Pore size, degradation rate and mechanical properties of the resulting scaffolds could be tuned by changing the ratio of the two components. Thus, the increase in CS content led to a decrease of the mean pore size, liquid uptake and degradation rate, while improved mechanical properties. Morphological evaluations showed fibre-like structure with an interconnected network in pure Col scaffolds and those with low CS content, while this structure gradually disappeared and changed into a cobblestone-like structure when the CS content reached 90% (Figure 9).

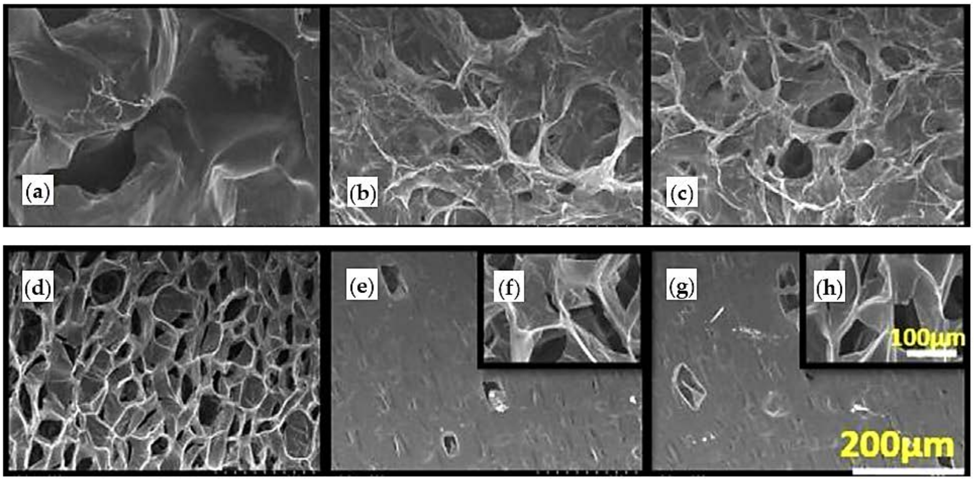

Figure 9. SEM morphologic observations of pure Col (**a**), pure CS (**g**,**h**) and CS/Col scaffolds with wt% ratios of: 10/90 (**b**), 50/50 (**c**), 70/30 (**d**) and 90/10 (**e**,**f**), respectively. All micrographs have the same magnification as well the two insets. Reproduced with permission from [79].

The prepared scaffolds logically showed good cytocompatibility to L929 fibroblasts, lack of toxicity and great capability to promote the attachment, migration and proliferation of Schwann cells. A modulated degradation behaviour without any inflammatory reaction was found when the Col/CS scaffolds were subcutaneously implanted in rabbits, indicating the potential application of these TIPS-obtained and natural-based scaffolds in tissue engineering [79].

Although biomaterials from both synthetic or natural resources are potential candidates for tissue engineering applications, the synthetic ones can be better modified in terms of geometric structure, biocompatibility, porosity and mechanical properties [191]. However, low biodegradation rate, hydrophobicity, and lack of cell recognition sites limit tissue engineering applications of a synthetic biodegradable polymer like PLLA. Thus, blending synthetic polymers with other natural polymers could be an alternative solution [192]. For instance, blending with CS is considered as an efficient approach to obviate some of the indicated drawbacks [193]. Such blending permits taking advantages of both polymers not only as scaffolds for bone [194], cartilage [195] and nerve [196] tissue engineering applications, but also as drug delivery carriers [197].

TIPS appears an advantageous technique since it is highly flexible to blend the polymer-solvent system with other polymers, solvents or inorganic fillers for specific purposes. Salehi et al. employed solid-liquid phase separation to produce porous scaffolds from PLLA and CS. Such blending was aimed to mimic cellular microenvironment and anatomical structure of nerve tissue. The scaffold behaviour and properties were compared with those made from pure PLLA or CS. CS/acetic acid:water (50:50) solution was specifically added to a PLLA/chloroform one, and then solid-liquid phase separation was induced by quenching the mixture to −80 °C (i.e., a lower temperature than the freezing point of both solvents, 63.5 °C and 16 °C for chloroform and acetic acid, respectively). After freeze-drying the resulting scaffolds were soaked in glutaraldehyde to cross-link the CS. The blend scaffolds were highly porous with interconnected porosities and showed proper mechanical properties. In addition, they were more porous and hydrophilic, and had higher degradation rate and lower amounts of free radicals compared to neat PLLA. Furthermore, the blended scaffold could better support human nerve cells than pure PLLA and CS scaffolds, indicating than an effective strategy to prepare promising scaffolds for nerve tissue engineering applications was developed [80].

2.4.2. Composite (Natural/Synthetic Polymer-Ceramic) Scaffolds

Bone is a hard tissue that acts a supporting framework or skeleton of the body and protects organs [198]. Bone tissue regularly heals with minimal scarring, but critical-sized bone defects fail to heal naturally [199,200]. Effective grafting techniques for treating bone defects, i.e., bone autografts and allografts often have problems associated with insufficient bone cell availability, donor site morbidity and bone transplantation failures [201]. Thus, there is a growing need for effective synthetic bone substitute materials [202]. Bone substitutes made of conventional bioceramics, such as HA and beta tricalcium phosphate (β-TCP), have made a significant contribution in orthopedic applications to repair and augment the damaged bone tissues [203-205]. Tissue engineering is an effective therapy for bone defects which utilizes scaffolds, cells and growth factors to fabricate artificial bones to be implanted into patients [206]. Taking into account that natural ECM is a composite consisting of naturally occurring biopolymers (organic) and biological apatite bioceramics (inorganic) with a well-oriented crystalline structure, the important aspect for developing an appropriate bone scaffold is to get a suitable 3D porous composite with the specific characteristics to mimic the ECM [207-209]. Therefore, an effective material selection requires to combine biodegradable polymers able to be biologically degraded and replaced by growing cells and inorganic bioactive particles [210,211]. A practical approach to enhance cell growth and adhesion and also to avoid the implant rejection is to provide the growing cells with supporting materials with both suitable structure and chemical-physical properties [212,213]. Porosity, and a well-regulated interconnected porosity, are crucial factors for designing scaffolds to mimic the bone architecture [5,214]. In contrast with other conventional methods such as salt leaching, gas foaming and freeze drying, TIPS has proven to be capable of developing interconnected microporous structures similar to the bone architecture [215,216].

Collagen type 1 (Col1) and HA are the major constituents of human natural bone tissue and consequently have widely been studied as promising materials for scaffold preparation. Thus, Wang et al. reported the usefulness of porous Col1/nHA scaffolds for restoration of critical-size bone defects [217]. Bioactive molecules like Col1 and CS have also been used as composite components for regeneration of bone tissue [218-222].

Reves et al. recommended pore sizes of 100–800 μm for microparticle-based scaffolds [223], being the recommended porosity to accommodate osteoblasts or osteoprogenitor cells ≥90% [224]. In order to meet such requirements, Rahman et al.

chose TIPS technique as the methodology to develop composite HA/Col/CS scaffolds for restoration of defected maxillofacial mandible bone, using different cross-linkers. Irregular 3D porous microstructures with 3D interconnected fibre microstructure, were obtained, while the pore diameter was ranging from 98 to 204 μm and the porosity reached the recommended porosity of ≥90%. Scaffolds showed desirable blood biocompatibility without cytotoxicity. Scaffolds could also be cross-linked by either irradiation or de-hydrothermal treatment. Final materials were compatible for MSCs attachment and growth, mineralization and supported in vivo new bone formation in rabbit model [225].

Osteochondral tissue is comprised of an articular cartilage region and a subchondral bone region, while a calcified cartilage connects these two microenvironments [226]. Multiphasic scaffolds, in which different layers can model different microenvironments, are the basis of new potential treatment approach. However, the achievement of a stable joining between layers during fabrication remains challenging [75]. Osteochondral tissue regeneration in monophasic scaffolds is lower than multiphasic ones, and due to inadequate mimicking of the native microenvironment they are unable to simultaneously support chondrogenesis and osteogenesis [227,228]. Accordingly, Erickson et al. using TIPS developed multiphasic bilayered scaffolds that were able modelling native osteochondral by combining two distinct scaffolds optimized for cartilage and bone, respectively. Polysaccharide and glycosaminoglyca-based scaffolds were obtained using a mechanical stiffness gradient. Specifically, scaffolds consisted of a CS/HAc layer (as cartilage part) and a Cs/Alg/HA layer with higher stiffness and osteoconductivity (as bone part). The bilayered scaffolds showed seamless gradient transition zone at the interface with increasing stiffness and calcium content resembling that of native osteochondral tissue. Osteogenesis and chondrogenesis were found in the associated layers during a two-week co-culture with chondrocyte-like (or MSCs) and osteoblast-like cells and, importantly, showed the potential of TIPS for fabrication of multilayered scaffolds for osteochondral TE as well as for other complex layered tissues [75].

Binary hybrid materials made of biodegradable and bioresorbable polymers such as PGA, PLLA [229], poly (D,L-lactide) P(DLLA), PCL or their copolymers [230] have been widely studied for bone tissue engineering or regeneration of damaged bone. As polymer fillers, inorganic materials like TCP [1,34,35], HA [28-33], bioglass [231,232] and FeHA (Fe-doped nHA) [233,234] are generally used.

Díaz et al. [12] produced nHA/PLLA composite scaffolds and films using TIPS technique and solvent casting method, respectively. The 10–50 wt% of nHA were added to 2.5 *w*/*v*% PLLA/chloroform solutions and dispersed through ultrasonic stirring. This nanocomposite system was subsequently used for fabrication of such scaffolds and films. Thermal and mechanical properties of prepared composite scaffolds and films during the in vitro degradation period was evaluated and the influence of nHA content on properties and structure was determined. TIPS scaffolds showed a highly porous structure, while films had a dense and non-porous structure. An increase in elastic modulus and yield stress was characteristic for all samples when nHA particles were incorporated, but these parameters decreased faster in the film samples than scaffolds during degradation. Films also degraded more rapidly in a heterogenous way due to an autocatalytic effect caused by more difficult release of acidic degradation products. The improvement of mechanical performance was scarce for high HA contents (i.e., 50 wt%) due to agglomeration effects and the corresponding reduction of the interfacial contact with the polymer matrix [12].

Particle dispersion in the polymeric matrix is a parameter with crucial importance and that must be controlled to obtain homogeneous nanocomposite materials. Achievement of a good dispersion is still one of the main problems when preparing composites through mechanical stirring or ultrasound mixing methods. "In situ synthesis" of nanoparticles within the polymer matrix is an efficient alternative to the conventional mechanical methods of particle dispersion, enabling to overcome the strong agglomeration trend of nanoparticles which leads to form micrometric aggregates. In this method, fillers are directly synthesized in the hosting polymeric matrix, hence, particle aggregation is prevented and dispersion is improved [235]. Interestingly, this synthetic method is particularly compatible with the TIPS technique allowing in addition the fabrication of porous structures [121,236]. Recently, combination of in situ synthesis and TIPS for manufacturing PLA-based nanocomposite scaffolds containing HA and polyaniline (PANI) nanoparticles have been reported [67,77].

In a recent study, Esposti et al. [77] produced nanostructured composite porous scaffolds based on poly(3-hydroxybutyrate) (PHB). Composite suspensions were prepared according to two different methods: The innovative in situ synthesis of HA nanoparticles in PHB/dioxane solution, and the conventional mechanical dispersion of ex situ synthesized HA nanoparticles in the same polymer solution. By applying TIPS to all suspensions in addition to solvent exchange using ethanol and vacuum drying, two groups of porous scaffolds were obtained and compared. In situ synthesis of HA clearly limited the particle aggregation problem and rendered high porosity even at relatively high HA contents (up to 8 wt%), while the scaffolds containing ex situ synthetized HA particles were not porous at high HA contents (Figure 10).

Although both scaffold groups inhibited pre-osteoblast cell adhesion and proliferation, and could promote osteogenesis, the scaffolds loaded with in situ-synthesized HA produced the highest amount of alkaline phosphatase and the typical morphology of the terminal differentiation stages of osteoblasts. These findings justify extending this new TIPS-based fabrication process to other polymeric matrices or inorganic nanoparticles, as a simple and scalable tool for the preparation of high surface area polymer-based composites with tailored properties [77].

Pure PLA still has some deficiencies to be used as a biomaterial in bone tissue engineering. Bone tissue engineering puts a great demand on mechanical properties. However, among all PLA deficiencies for its right application in bone tissue engineering, it should be emphasized its moderate strength makes it an unsuitable choice for bone fixation at the site of loadbearing [237], and also its strong hydrophobicity that is not conducive to cell adsorption and growth [238]. To overcome such problems a filler material like CNC could be helpful, due to its strong hydrophilicity and excellent mechanical properties [239-241]. In a recent approach Luo et al. fabricated PLA-based scaffolds reinforced with CNC by combining in situ polymerization and TIPS technique. In this approach, CNCs were firstly prepared by acid hydrolysis of cellulose fibres and then nanocomposites were obtained through in situ polymerization of lactic acid and CNCs. The resulting nanocomposites were dissolved in a dioxane/water system to apply the typical TIPS process. Final scaffolds showed higher compression modulus, hemocompatibility, protein adsorption in vitro than neat PLA scaffolds. The proposed nanocomposite scaffolds were also promising for bone tissue engineering considering their good mechanical properties, biocompatibility, biomineralization and bioactivity [242].

Polyester-based scaffolds reinforced with multiwalled carbon nanotubes (MWCNTs) have recently been produced by TIPS [19,243,244]. Possessing a wide variety of properties such as electrical, thermal, mechanical and structural, MWCNTs have been reported as proper candidates for biomedical applications [245]. Even presence of small quantities of carbon nanotubes (e.g., <0.5 wt%) in a polymer matrix can lead to a significant increase in mechanical properties. Note that the average Young modulus of native human bone, bioglass and HA are 12–18 GPa, 35 GPa and 95 GPa, respectively, while that of the MWCNTs is between 200 to 1950 GPa [246]. Apart from mechanical properties, choosing CNTs as filler materials was especially due to their magnetic properties, which enable scaffolds to guide the proliferation, differentiation and mineralization of bone cells [247].

Díaz et al. [19] incorporated small amounts of MWCNT fillers into PLGA-based scaffolds. Nanotubes were dispersed in a PLGA-dioxane solution by ultrasonication and the final composite scaffold was obtained by the TIPS method. Ultrasonic dispersion and TIPS technique facilitated the incorporation, dispersion and distribution of CNTs in the polymer matrix. In addition, TIPS allowed a good control over morphology and porosity of the composite scaffolds.

They reported that the addition of small quantities of carbon nanotubes (0.1–0.5 wt%) to PLGA scaffold could modify in vitro degradation, magnetic properties and cytotoxicity of the scaffolds [19]. The effect of higher levels of MWCNTs (i.e., 1–10 wt%) and the incorporation of HA (i.e., 10 wt%) on PCL-based scaffold properties was subsequently evaluated. Samples were obtained by ultrasonic dispersion of MWCNTs and nHA particles in PCL-dioxane solutions followed by TIPS to get porous composite matrices [243]. Despite the excellent properties of CNTs, having other features like high surface area, small diameter and high aspect ratio (>1000) predispose them to form agglomerates when being incorporated as reinforcements into biopolymers, especially in high loading levels [248]. They reported that both mechanical properties and in vitro degradation were clearly modified by adding MWCNTs: up to 5% of MWCNTs the structural arrangement of the scaffolds was positively changed, but higher levels led to agglomeration, an irregular structure and a negative effect on mechanical properties [243]. The decrease of nHA content to 1 wt%, allowed a clear evaluation of the influence of various levels of MWCNTs (1–10 wt%). Although mechanical properties and conductivity of these scaffolds were improved by adding MWCNTs, properties were dependent on the concentration of nanotubes. Thus, PLLA scaffolds with up to 5 wt% of nanotubes had the best properties with very uniform and a well-arranged structure, but at a higher nanotube concentration scaffold properties dropped due to aggregation, indicating that ultra-sonication/TIPS techniques were not suitable for production of composite scaffolds with such high levels of fillers [244].

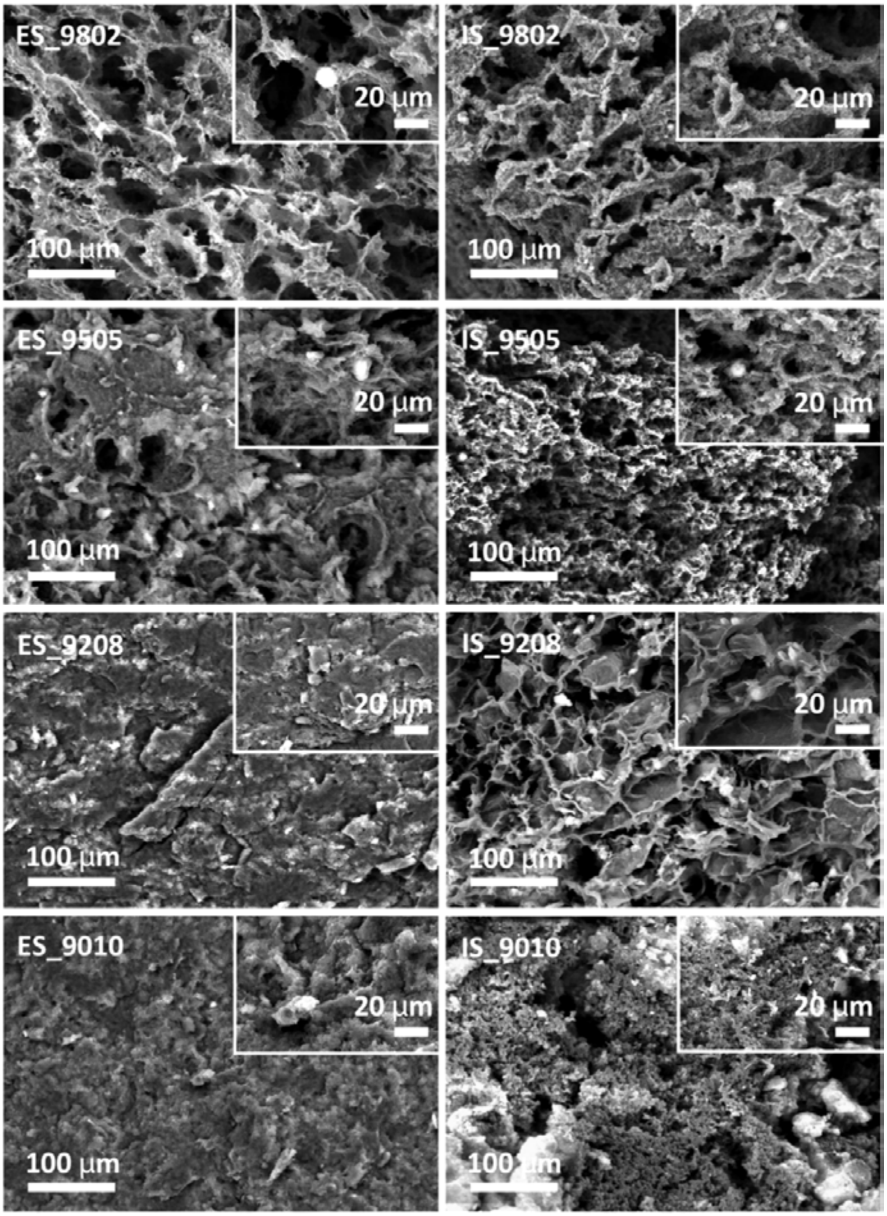

Figure 10. Cross-section SEM micrographs of PHB/HA composite scaffolds. PHB scaffolds containing 2–10 wt% of ex situ- and in situ-synthesized HA nanoparticles have been indicated as (ES9802 to ES9010) and (IS9802 to IS9010), respectively. Insets show higher magnification for each sample. Reprinted with permission from [70].

Gandolfi et al. [121] tried to incorporate different loading levels of dicalcium phosphate dihydrate (DCPD) and/or hydraulic CaSi into PLA-based scaffolds using TIPS. The resulting composite scaffolds were highly porous (i.e., >90%), biocompatible and bioactive. Furthermore, the presence of the added minerals helped to overcome typical PLA disadvantages such as hydrophobicity, release of acid degradation products and reduced cell adhesion and growth [121]. Bone regeneration ability was subsequently improved by enriching these composite scaffolds with exosome vesicles (EVs) that were derived from MSCs and deposited on the scaffold surface. EVs are released from all cell types and are able to modify the activities of target cells by proteins, growth factors, mRNAs, and micro RNAs internalization, facilitating in addition cells communication [249]. Exosome-enriched composite scaffolds, especially those with the highest amount of mineral fillers could properly stimulate osteogenic commitment of human adipose mesenchymal stem cells (hAD-MSCs). Therefore, new scaffolds could be considered to have a promising potential in regenerative bone healing using stem cells [78].

PCL scaffolds containing different ratios of micro-fluorcanasite (μFC) glass-ceramic particulates, as potential bioactive reinforcements, have recently been prepared by TIPS. Chloroform was selected as polymer solvent, ultrasonication was applied to disperse glass-ceramic particulates in the polymer solution, and liquid nitrogen to freeze the samples and induce phase separation. All the produced matrices revealed porous cellular microarchitectures. The interconnected microporous structure was enhanced with high amounts (e.g., 30 wt%) of μFC glass-ceramic particulates, a feature that attributed to a possible nucleating effect of particulates. A tunable biodegradation was also found since the increase of glass-ceramic content resulted in a delayed biodegradation of PCL matrices (i.e., structural integrity was enhanced upon incorporation of crystalline μFC particles). Owing to favourable microporous architecture and tunable degradation, PCL/μFC biocomposite scaffolds appear as potential matrices for bone tissue engineering [17].

Developing innovative ceramic fillers in bioengineering, TiO_2 has been identified as an effective biological material because the presence of surface OH groups induces formation of HA from simulated body fluid (SBF) [250]. However, in vitro toxicity inducing pulmonary inflammatory response has been reported for TiO_2 nanoparticles [251]. Functionalization is probably one of the most effective strategies to prevent this toxicity and enhance the stability of nanofillers in certain polymer matrices [252]. Buzarovska et al. functionalized the surface of TiO_2 nanoparticles with oleic acid (OA) and prepared PLLA nanocomposite scaffolds by means of the TIPS technique. Microporous structures were obtained after homogenizing the nanocomposite PLLA/TiO_2/dioxane suspensions by ultrasonication and applying the typical TIPS process. In terms of morphology, a highly porous and anisotropic architecture with characteristic interconnected and elongated pores (length of 70–150 μm, wall thickness of 7–12 μm) was produced. The pore architecture was not influenced by the incorporation of nanoparticles, but nice and evenly distributed nanoparticles were observed as small white dots. The effect of incorporating functionalized nanoparticles on biodegradability, bioactivity and cytocompatibility was also evaluated. Interestingly, scaffolds were bioactive in supersaturated fluids, but became less degradable in simulated body fluid (SBF) than pure PLLA scaffolds. Adding 5 wt% (with respect to the polymer content) of OA-functionalized TiO_2 nanoparticles enhanced cell viability and proliferation, but the increase to 10 wt% led to worse cell proliferation and higher cytotoxicity [73].

2.5. Architectures Obtained through the Manipulation of the TIPS Process Conditions

Highly porous interconnective network with isotropic or randomly-oriented pore structure can be obtained under different thermodynamic and kinetic conditions of phase separation (e.g., through liquid-liquid and solid-liquid processes) as detailed in the Section 2.2.1. It has also been explained how by altering TIPS parameters the morphology of the resulting foams can be controlled. However, by applying especial conditions in TIPS process (e.g., controlling temperature gradient, crystallization direction during solid-liquid phase separation or gelation temperature during liquid-liquid phase separation) other types of architectures can be achieved. In addition, by employing a semicrystalline polymer when polymer crystallization precedes liquid-liquid phase separation during cooling, new morphologies arising from the crystallization of the polymer matrix can be produced. In the next sections some related advances and recent studies focused on producing such structures are reviewed.

2.5.1. Nanofibrous Structures Prepared by Liquid-Liquid Phase Separation

ECM is the ideal 3D template for cell adhesion, proliferation and differentiation and is the reservoir for many growth factors [253,254]. Most components of natural ECM are organized in vivo according to a nano-scale fibrillar construction [13]. Nanofibrous ultrastructure of native ECM provides topological cues for specific cellular behaviour and, therefore, this complex architecture could be a good pattern for design and fabrication of bio-scaffolds [68].

Several techniques have recently been investigated so far to prepare 3D nanofibrous scaffolds, including electrospinning [255-258], self-assembly [259], thermally-induced phase separation (TIPS) combined the porogen leaching technique [61] and 3D printing [260]. The current techniques for producing biomimetic nanofibrous scaffolds have some limitations, for instance, a significant challenge for most 3D printers is to print nanofibrous structures in a well-controlled manner that demand very long processing time and high-end and expensive instruments. These limitations drove investigators to develop an innovative and facile technique for this purpose [18]. TIPS has been favoured by many researchers due to its convenient operation and simple equipment [14,18,22,46]. TIPS is a fabrication method that does not need any specific device for extrusion or non-woven procedures. Besides, to simplify the scaffold fabrication, other processes such as in situ crosslinking and synthesis can be combined with the TIPS [236,261].

Liquid–liquid phase separation followed by nucleation and crystallization growth in the polymer-rich phase is an optimal procedure for the formation of nanofibers [262]. An alternative approach to form artificial 3D nanofibrous structures [263], is to microcrystallize a semi-crystalline polymer like PLLA through TIPS [264]. Using synthetic copolymers, Ma et al. developed nanofibrous scaffolds (50–500 nm) based on poly(hydroxyalkyl methacrylate)-*graft*-poly(L-lactide) (PHAA-g-PLLA) through TIPS [265,266]. In another attempt to produce an ECM-mimicking nanofibrous scaffold, Zhang et al. synthesized poly(D,L-lactide)-*b*-poly(γ-benzyl-L-glutamate) (PDLLA-*b*-PBLG), which underwent nanofibrous self-assembly by α-helix formation of the PBLG segment during controlled TIPS process (Figure 11). The derived scaffold showed a higher degradation rate, nanofibre size and porosity than scaffolds derived from neat PBLG. In addition, new scaffolds were highly cytocompatible and conducive to cell adhesion and proliferation. Due to facilitating neuron-like differentiation of seeded neural stem cells, this nanofibrous scaffold showed a great potential for neural tissue engineering [68].

Recently, some researchers showed the possibility of producing microspheres-aggregated 3D porous scaffold by employing phase-separation and self-assembly processes without using any porogen agent or particular equipment [267-269]. Although their approach was intriguing, the resulting scaffold was lacking in some important properties for potential application in bone tissue engineering, for example the structure was not tunable and had low mechanical properties. In order to overcome these problems, Yao et al. [18] used the TIPS technique and, without the use of porogen agents, fabricated porous microspheres-aggregated PCL scaffolds with macropores, micropores, and nanofibrous-like structures that were suitable for bone tissue engineering. Dioxane:water (9:1) was selected as the solvent-nonsolvent system.

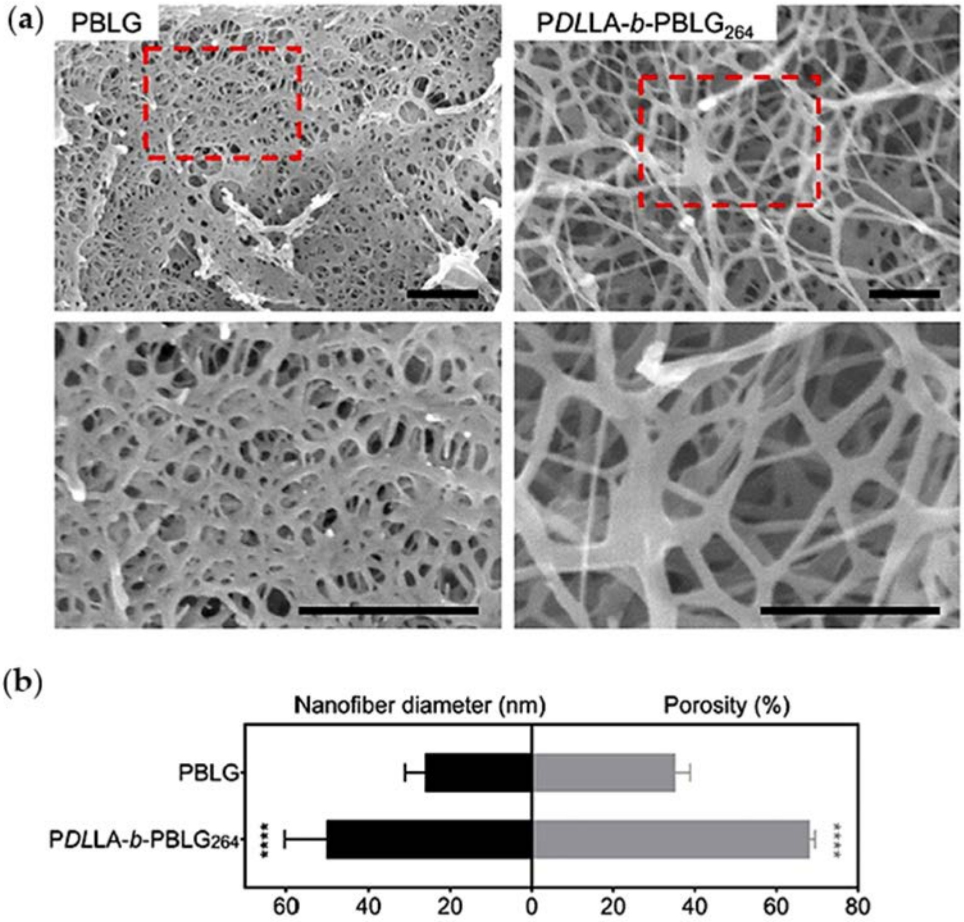

Figure 11. (**a**) SEM images of PBLG and PDLLA-*b*-PBLG 3D-scaffolds. Scale bars = 500 nm. (**b**) Quantification of nanofibre diameter and porosity in PBLG and PDLLA-b-PBLG scaffolds. **** $p < 0.0001$, n = 20 and 3 for nanofibre diameter and porosity analyses, respectively. Reproduced with permission from [68].

Phase separation occurred by lowering temperature up to 273 K, and a nanofibrous structure was formed. In this case, a nonsolvent-induced phase separation also occurred throughout cooling. In addition, dioxane with the crystallization point of 288.8 K solidified during cooling, resulting in formation of a macro-porous structure upon the solvent evaporation. A spherulitic structure was also reported, which possibly could be ascribed to the growth of PCL spherocrystals during the TIPS process. Porosity, pore size, and mechanical properties of the scaffolds could in addition be controlled by a simple change of PCL concentration (Figure 12). High surface area of these constructs improved bioactivity, allowed a sustained release of multiple osteoinductive drugs, and showed high mechanical properties and an improved BMP2-induced osteogenic differentiation [18].

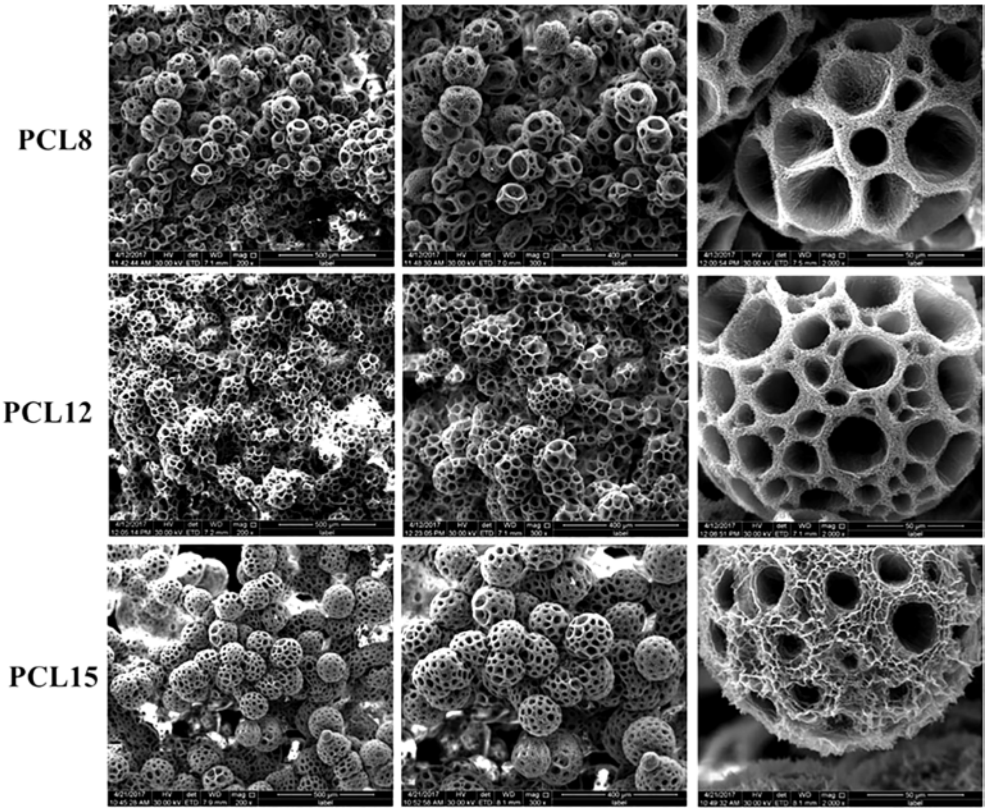

Figure 12. SEM images of PCL scaffolds obtained from 8, 12 and 15 *w/v*% of PCL in 1,4-dioxane/water (9:1) mixture, designated respectively as (PCL8), (PCL12) and (PCL15). Reprinted with permission from [18].

Chen et al. [67] also made an interesting attempt to develop PLA nanofibrous matrices incorporating PANI nanostructures by combining in-situ polymerization and TIPS technique (Figure 13). The logic behind choosing conductive PANI was to overcome some PLA deficiencies like lack of chemical reactivity and biological inertness, which limit its scaffolding application when specific cell-material interactions are needed [270,271]. In-situ polymerization of conductive PANI nanoparticles in a PLA/THF solution followed by TIPS led to a 3D nanofibrous matrix (Figure 14) with interesting properties.

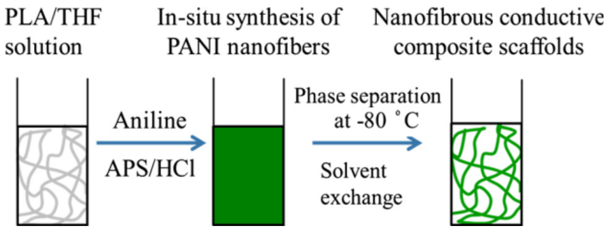

Figure 13. Schematic illustration of the process used for fabrication of conductive nanofibrous PLA scaffolds. Reproduced with permission from [67].

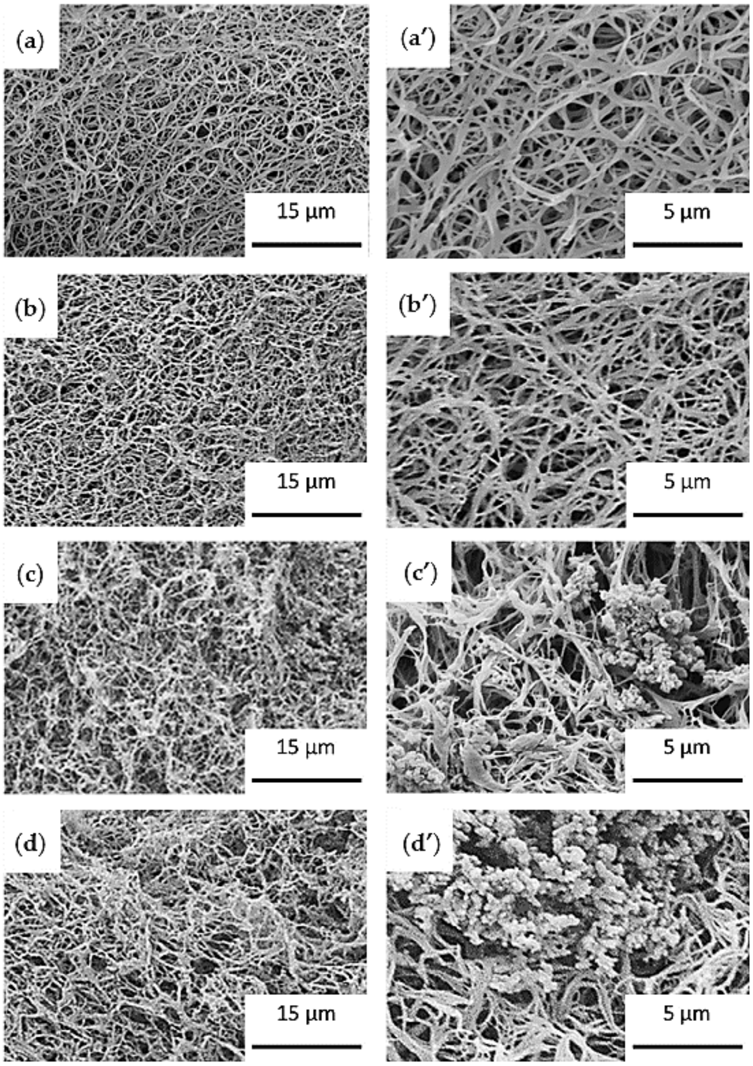

Figure 14. SEM micrographs of nanofibrous conductive scaffolds based on PLA and different PANI contents: 0 (**a**,**a′**), 15 (**b**,**b′**), 10 (**c**,**c′**) and 15 (**d**,**d′**). Reproduced with permission from [67].

Specifically, conductivity and electrochemical properties were evaluated for different PANI contents. Nanofibrous scaffolds with a moderate content of PANI significantly promoted osteogenic differentiation of bone marrow derived MSCs and were highly promising biomaterials for bone tissue regeneration [67].

Another interesting work concerning functionalization has been proposed by Guo et al. where an aminolysis process have been combined with TIPS to obtain PLLA nanofibrous scaffolds modified with poly(ethylenimine) (PEI). The ammonolytic agent, (i.e., PEI dispersed in dioxane) was dropwise added into PLLA/dioxane solutions to perform a typical TIPS process. The aminolysis reaction led to covalent bonds between amino groups of PEI and the ester groups of PLLA. Experimental conditions (i.e., polymer and modifier concentration, aminonolysis time and gelation temperature) affected the formation tendency, morphology of nanofibres and scaffold properties. Optimized conditions rendered a homogenous nanofibrous structure with high hydrophilicity, appropriate mechanical properties, high capacity to favour osteoblast proliferation and a great bone-bioactivity (i.e., apatite formation) [13].

2.5.2. Anisotropic Structures Prepared by Solid-Liquid Phase Separation

Physiological and mechanical properties of many tissues, such as tendon, nerve, blood vessel, bone, ligament, spinal cord and cartilage, are closely associated with their oriented structure [272]. Accordingly, the scaffolds used in tissue engineering and regenerative medicine can be prepared with an oriented-pore structure to better mimic these environments in vivo and guide the spatial cell organization during the tissue formation process as well as facilitating cell proliferation, migration and differentiation [273,274]. As an example, structure anisotropy is important for an ideal cardiac patch to mimic the morphologies of the native myocardium according to the alignment of elongated cardiomyocytes. Such anisotropic structure also allows the biodegradable patch to mechanically match the native myocardium. Mechanical mismatch between the biodegradable cardiac patch and the native myocardium may cause abnormal cardiac functions resulting in implantation failure [275,276]. Table 2 provides a summary of anisotropic/oriented scaffolds being recently fabricated by TIPS technique. Current relevant investigations and advances have been elaborated subsequently.

To simulate the anisotropic architecture of native heart muscle, Xu et al. [71], by employing the TIPS technique, fabricated a series of anisotropic scaffolds made of biodegradable polyurethane to be used as cardiac patch.

Table 2. Summarized information of some scaffolds fabricated recently by the TIPS technique.

Polymer System	Solvent System	Structure	Fabrication Technique	Porosity	Application	Reference
PLLA [1]	1,4-dioxane	Anisotropic pores	TIPS	~91–92%	Bone TE	[73]
polyurethane	DMSO	Anisotropic pores	TIPS (controlled heat direction)	~93–97%	Cardiac patch	[71]
PLLGC	1,4-dioxane	Oriented microtubular	TIPS	~73–85%	TE	[25]
SF [2]/Col	water/acetic acid [3]	radially/axially- aligned pores	TIPS (temperature gradient-guided)	~85%	Osteochondral	[72]
PHBV [4]	1,4-dioxane	Oriented pores, unidirectional channels	TIPS	~41–77%	TE	[74]
PEUU	DMSO	Oriented connected macropores	TIPS		Rotator cuff repair	[66]
PLLA	1,4-dioxane [5]	Anisotropic pores, (~parallelepiped)	TIPS (solid-liquid phase separation)	~75–95%	TE	[64]
PLGA	1,4-dioxane	Radially-aligned pores	TIPS (uniaxial temperature gradient)	~91%	Osteochondral	[62]

[1] The solution incorporated TiO_2 nanoparticles functionalized with OA; [2] silk fibroin (SF); [3] Water as solvent for SF, acetic acid for Col; [4] The solution incorporated CNCs; [5] In case of dioxane/water as solvent, the microstructure was controlled by liquid-liquid phase separation and an anisotropic structure was not observed.

The synthetic polyurethanes with 5, 8 and 10 *w*/*v*% concentrations were dissolved in DMSO while a thermal-resistance wrap was employed to control crystallization in a uniaxial direction during the TIPS process (Figure 15).

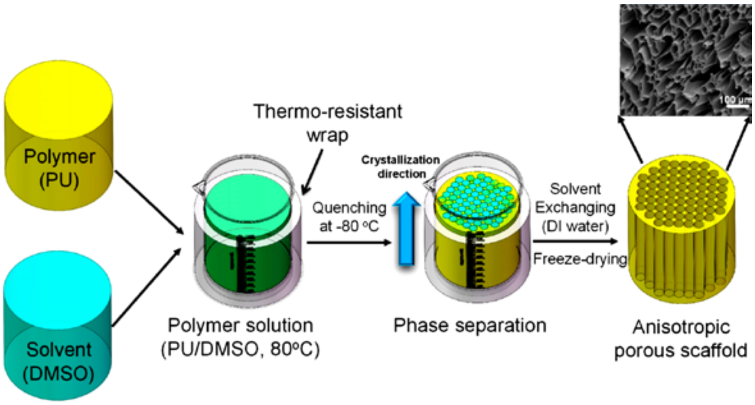

Figure 15. TIPS process for fabrication of anisotropic polyurethane porous scaffolds. Polyurethane was dissolved in DMSO at 80 °C and then directly quenched to −80 °C. The solvent crystallized in the uniaxial direction, was exchanged in deionized (DI) water and then lyophilized to produce anisotropic porous. Reprinted with permission from [71].

After solvent exchange with deionized water and freeze-drying, anisotropic scaffolds with the pores oriented along the crystallization direction were obtained. Honeycomb-like and aligned pore structures were observed in the transversal and longitudinal directions, respectively (Figure 16).

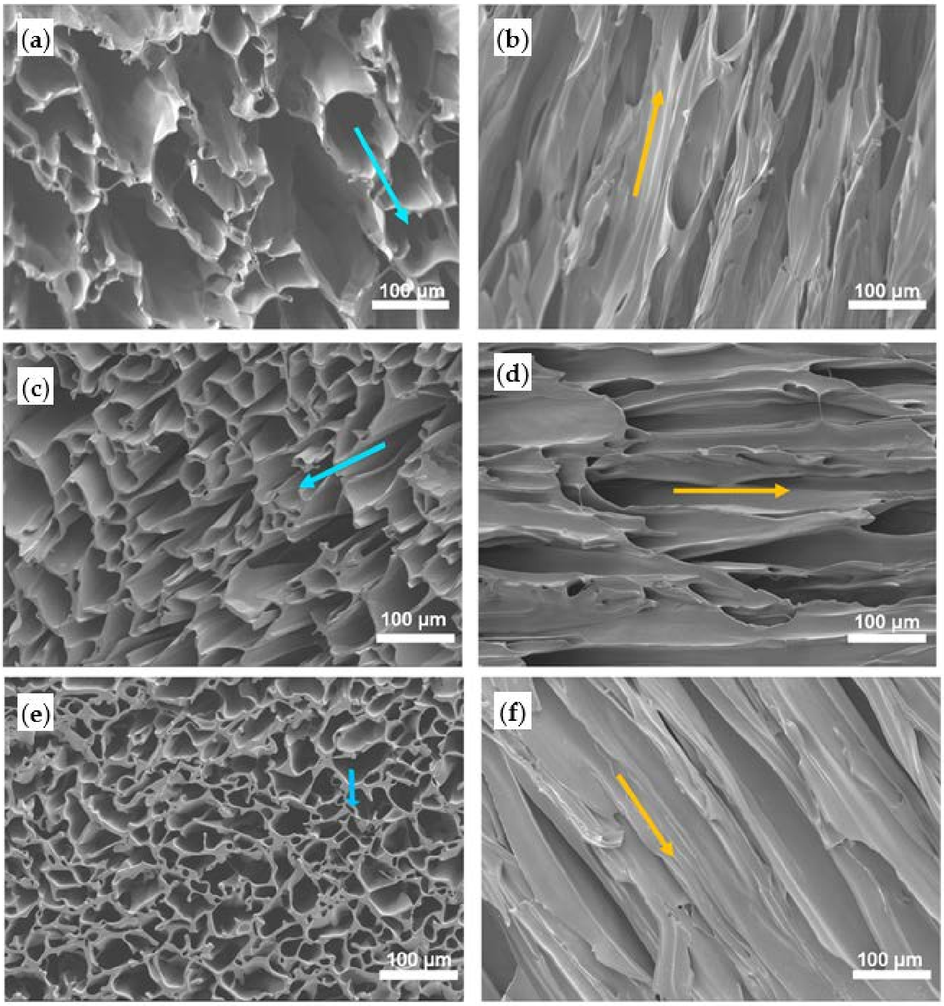

Figure 16. SEM micrographs of anisotropic porous polyurethane scaffolds prepared at −80 °C quenching temperature, from 5 (**a**,**b**), 8 (**c**,**d**) and 10 (**e**,**f**) w/*v*% solutions. Micrographs correspond to transversal (**a**,**c**,**e**) and longitudinal (**b**,**d**,**f**) views are indicated by blue and yellow arrows, respectively. Reprinted with permission from [71].

The average pore sizes and porosities of the scaffolds decreased with increasing the polymer concentration (i.e., from 91 µm and 96% to 51 µm and 90%, for the scaffolds prepared from 5 and 10 *w*/*v*% polymer solutions, respectively). Mechanical properties of the anisotropic scaffolds were also optimized by altering polyurethane types and concentrations to match properties of the native human myocardium. The prepared biohybrid scaffolds were subsequently combined with decellularized and digested porcine myocardium-derived extracellular ECM to improve biocompatibility without affecting mechanical properties. The biohybrid scaffolds had morphologies similar to the acellular porcine myocardial matrix with good tissue compatibility and a minimal immune system response when they were subcutaneously implanted in rats [71].

Scaffolds with an oriented porous architecture can significantly promote cell infiltration and bioactive interflow between neo-host tissues [62,72]. Different examples can be found about in situ regeneration of osteochondral defects. Thus, by controlling the temperature gradient in radial or longitudinal directions throughout TIPS process, bioactive scaffolds with radially- or axially-aligned pore architectures have been developed to enhance in vitro/vivo cell migration and infiltration and promote tissue regeneration [274, 277,278].

Recently, Dai et al. [62] have fabricated PLGA scaffolds with a radially-aligned structure through unidirectional cooling of polymer solutions in the radial direction for in vivo regeneration of osteochondral defects. By adding PLGA/dioxane solution into a polyethylene tube with a thermo-insulating sponge attached to the bottom of that (to prevent heat exchange from the axis direction), and by placing the tube in the central hole of a pre-cooled copper mould as a cooling bath, the cooling direction could be controlled and therefore the crystallization of dioxane along the radial direction. After lyophilization, a highly porous (>90%) cylindrical scaffold with radially-oriented microtubular pores perpendicular to the axial direction of the scaffold was obtained (Figure 17). This construct enabled deep migration of bone marrow stem cells and could induce regular cell and ECMs alignment. It was also reported a simultaneous formation of cartilage and subchondral bone layers integrated with each other, while the smooth neo-tissues were well-integrated with the surrounding host tissues. Regeneration results were demonstrated to be much better than those found using PLGA scaffolds with random pores after the same implantation period, indicating the oriented-pore PLGA scaffold is a promising material for osteochondral regeneration [62]. Using natural resource polymers, Chen et al. also produced Col scaffolds with a radially-oriented pore structure, which could further improve the migration of bone marrow stem cells and regeneration of osteochondral defects compared to randomly-oriented scaffolds [279].

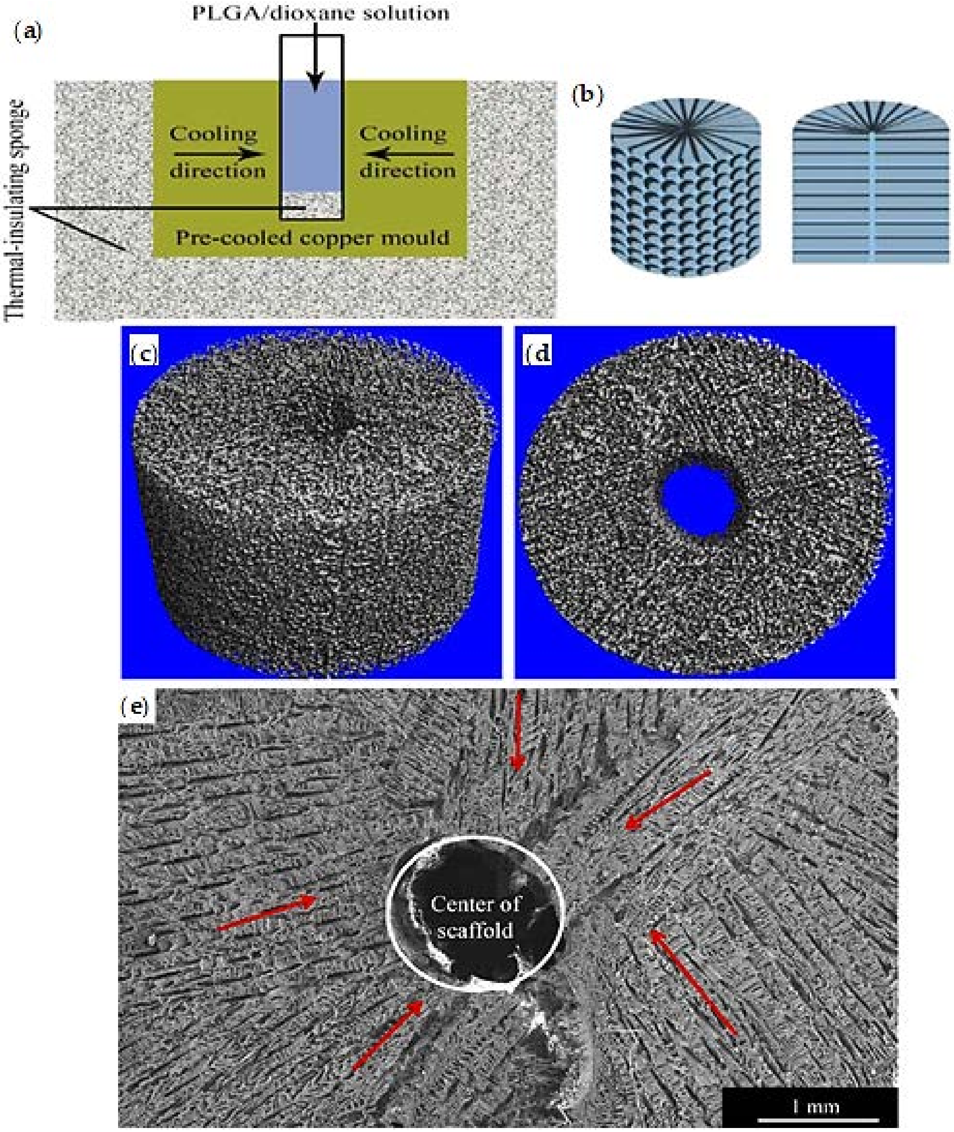

Figure 17. Schematic illustration of fabrication process (**a**) and the anticipated architecture (**b**) of radially-oriented PLGA scaffold through unidirectional cooling. Micro-CT topology evaluation; isometric (**c**) and top view (**d**) and SEM top view image (**e**) of the PLGA scaffold. The direction of oriented microtubules is shown by red arrows. Reprinted with permission from [62].

ECM-mimetic scaffolds based on silk fibroin (SF) and Col with different pore structures, including random pores, radially-aligned and axially-aligned pores were recently prepared by Feng et al. [72] using temperature gradient-guided TIPS. The effect of pore architecture on cell migration in the regeneration process of osteochondral defects was evaluated. To produce axially-aligned scaffolds they mounted a polyethylene tube containing the mixture solution of SF/water and Col/acetic acid into the holes of a larger PTFE mould placed between two pre-cooled aluminum moulds. Radially-aligned scaffolds were obtained following a procedure similar to that reported by Dai et al. [62], but using in this case they used a pre-cooled aluminum mould as a cooling bath (Figure 18). The obtained porous scaffolds had structural and mechanical anisotropy, porosity of about 85%, proper elastic modulus, and could support cellular in vitro and in vivo activities [72]. In vivo cell migration and infiltration was clearly improved in the cross-sectional direction (for the radially-aligned scaffolds) and in the vertical-sectional direction (for the axially-aligned ones) (Figure 19).

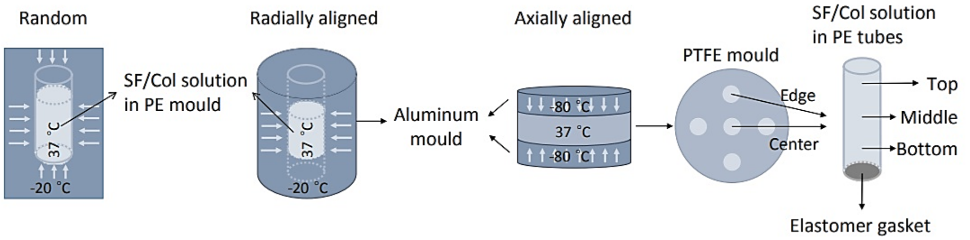

Figure 18. Schematic illustration of mould structures used for preparation of random, radially-aligned and axially-aligned SF/Col composite scaffolds. For fabricating the axially-aligned scaffold, polyethylene (PE) moulds containing the mixed solution was mounted into the holes of a larger PTFE mould, placed between two precooled (−80 °C) aluminum moulds to ensure an axially-aligned heat transfer. The white arrows indicate cooling directions. Reprinted with permission from [72].

Although a satisfactory regeneration of osteochondral tissue with hyaline cartilage formation was observed in both aligned scaffold groups, the regeneration was faster in the radially-aligned scaffold group. Formation of hybrid cartilage (hyaline/fibrocartilage) was reported for the randomly oriented porous structure. Finally, the aligned SF/Col scaffolds, especially the radially-aligned ones, provided a promising alternative for regeneration of osteochondral defects, with a considerable potential to be translated into medical devices [72].

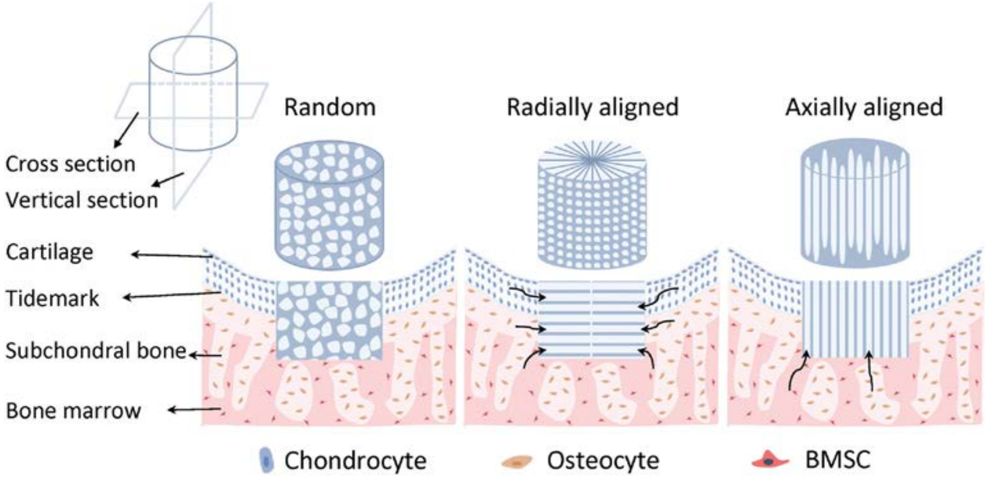

Figure 19. Schematic illustration of SF/Col composite scaffolds structures with random, radially-aligned and axially-aligned pores, and the implantation mechanism into osteochondral defects in vivo. Curvilinear arrows show how the radially-aligned and axially-aligned structures facilitate endogenous cell migration. Reprinted with permission from [72].

2.5.3. Crystalline Structures Prepared by Crystallization-Induced Phase Separation

When, due to thermodynamic conditions, a semicrystalline polymer-solvent system involves driving forces for liquid-liquid phase separation and crystallization of the polymer, the major factor determining which mechanism occurs is the strength of polymer-solvent interactions. In case of strong interactions (small differences between interaction parameters), the solution undergoes solid-liquid phase separation via crystallization of polymer during cooling. When the interactions are weak (great differences between interaction parameter), the polymer concentration determines the mechanism. Lloyd et al. reported that at high polymer concentration (e.g., higher than 59 wt% in case of isotactic polypropylene/n,n-bis (2-hydroxyethyl) tallowamine system) solid-liquid phase separation occurs (i.e., polymer crystalizes) and controls the morphology of the foam. At lower polymer concentrations (e.g., lower than 59 wt% in the above-mentioned system) liquid-liquid phase separation occurs and subsequently polymer crystalizes and stabilizes the phase separated structure. In the latter case, liquid-liquid phase separation controls the morphology [89].

Although a concentrated polymer solution has been used to fabricate various foams and monoliths for applications like membrane formation, generally low-concentrated solutions are used for preparing TE scaffolds (to achieve high porosity). Accordingly, individual utilization of solid-liquid phase separation (via polymer crystallization) as the main mechanism for fabrication of TE scaffolds does not occur very often. Nevertheless, crystallization of the polymer is occasionally observed when solid-liquid (caused by solvent crystallization) and liquid-liquid phase separations have been employed for fabrication of TE scaffolds. In such conditions crystallization of the polymer stabilizes the phase-separated structure and sometimes its corresponding morphological trace is observed throughout the microstructure of phase-separated regions [46].

Kinetic is another factor that may limit crystallization of the polymer during the TIPS process, even if it is thermodynamically favoured. The kinetic of phase separation process determines whether or not, and also to what extent the thermodynamically favoured mechanism occurs [81]. Since TIPS is a non-equilibrium process, the effects of the practical cooling rates on the equilibrium phase diagram must be considered [89]. Cooling the system in the experimental conditions of TIPS permits supercooling, and the crystallization of polymer shifts to lower temperatures than its equilibrium crystallization point. Conversely, the cooling rate has a minor effect on the location binodal curve (liquid-liquid phase separation temperature and the degree of undercooling required for inducing rapid binodal decomposition is very low [81,89]).

Önder et al. [90], by providing different experimental conditions for crystallization of polymer during liquid-liquid phase separation and the gelation process, prepared PLA foams by TIPS followed by solvent exchange and vacuum drying. Various ratios (84/16 to 90/10) of THF/water (solvent/nonsolvent) system were used. Phase separation was induced by cooling the PLA solutions (6–10 wt%) to three different temperatures (i.e., 24, 4 and −20 °C). The resultant PLA gels were subjected to solvent exchange (with ethanol) and then to vacuum-drying to achieve the porous, rigid and highly crystalline micro- and nano-structures. The porosity (between 85.1 and 92.8%), pore size (25–400 μm), morphology and mechanical properties of these rigid PLA foams was controlled by tuning the TIPS process parameters (i.e., polymer concentration, THF/water ratio and quenching temperature). The decrease of the water ratio in the binary solvent/nonsolvent system led to a gradual morphological change from homogeneous microcellular structures to microporous bead-like ones with smaller pore size (Figure 20a–d) and also to an increased crystallinity of the PLA foams. Upon cooling, the system first passed through the metastable region (NG mechanism) and then reached the unstable region (SD mechanism). The decreasing of water content in the solvent/nonsolvent system raised the power of the solvent system and the boundary of liquid-liquid phase separation (binodal curve) shifted to a lower temperature. Accordingly, the system will stay longer in the metastable region and shorter in the unstable region. In such a condition, the polymer had enough time to crystallize through NG mechanism and formed to a greater extent the bead-like morphology (arising from NG of polymer crystals at relatively low concentrations) than the fine cellular morphology (arising from SD mechanism). This effect was more significant upon slower cooling (i.e., higher quenching temperature) (Figure 20e,f) [90].

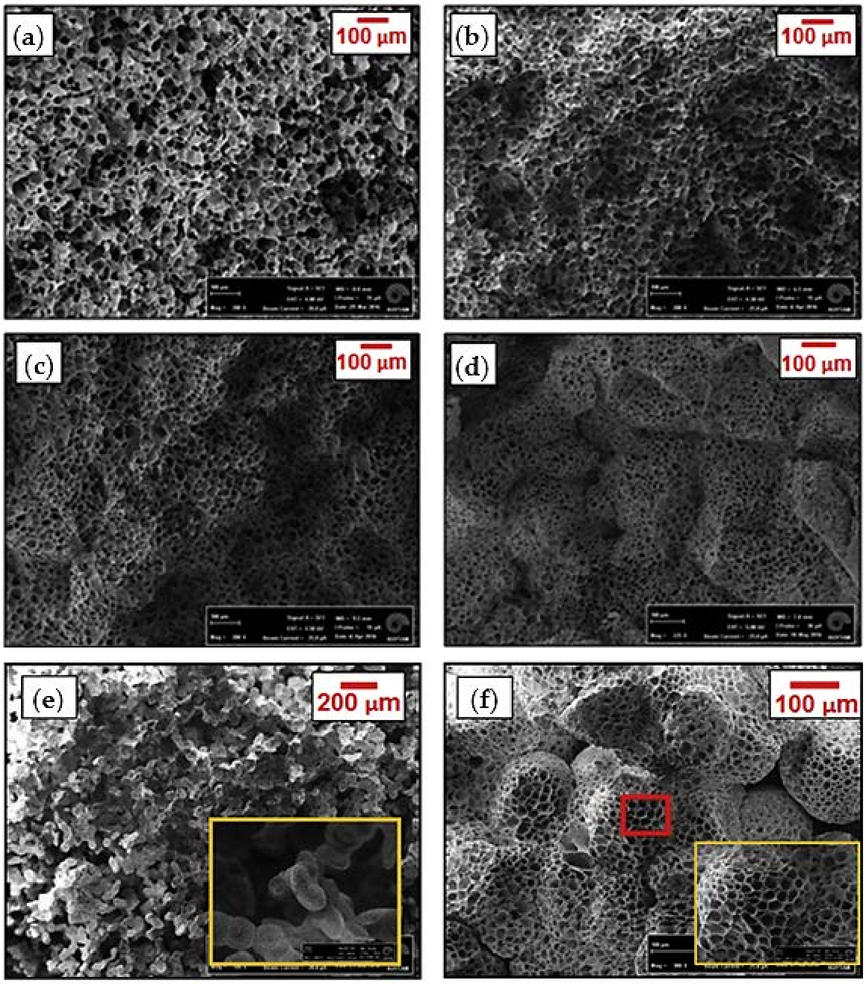

Figure 20. Cross-sectional SEM images of PLA foams prepared from a 8 wt% (**a**–**e**) and 10 wt% (**f**) PLA solution quenched to −20 °C (**a**–**d**), 24 °C (**e**) and 4 °C (**f**), and using a THF/water ratio of: (84/16) (**a**,**e**,**f**), (86/14) (**b**), (88/12) (**c**) and (90/10) (*w*/*w*) (**d**). Reprinted with permission from [90].

In another recent study, Onder et al. [14] have developed PLA foams with various architectures and morphologies from various ratios of THF/methanol (solvent/nonsolvent) after inducing phase separation/gelation by quenching. Resultant gels were stabilized by exchanging the solvent system with ethanol and porous scaffolds were obtained after quenching and supercritical CO_2 drying. Crystallinity, porosity, pore size and structure could be controlled by altering two TIPS processing parameter (i.e., polymer concentration from 8 to 22 wt%) and solvent system quality (i.e., solvent/nonsolvent ratio from 56/44 to 82/18) (Figure 21).

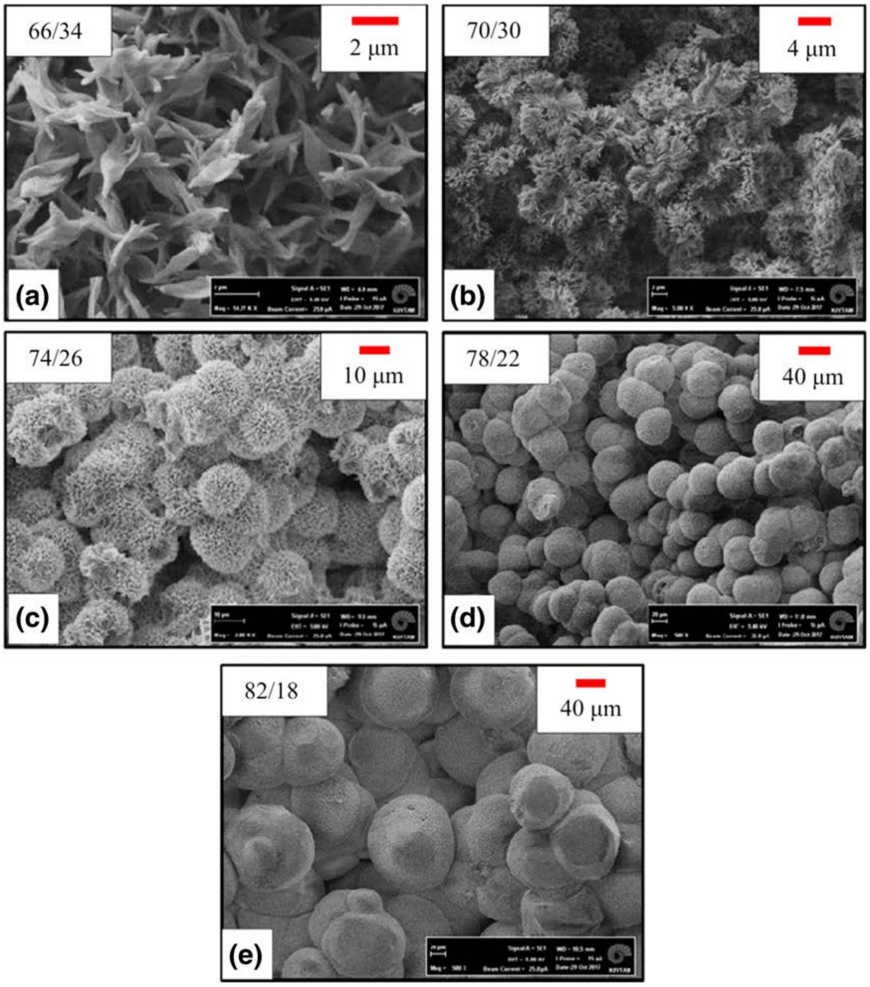

Figure 21. Change in the morphologies of PLA foams obtained through polymer crystallization mechanism as a function of THF/methanol ratio from 66/34 to 82/18 (**a**-**e**), at 18 wt% polymer concentration. Reprinted with permission from [14].

The different architectures arisen from polymer crystallization or from SD mechanism during the TIPS process. Higher crystallinity of PLA foams with the orthorhombic α-form crystal structure was reported at lower polymer concentrations and higher THF solvent contents. In such conditions, various crystalline morphologies like thin lamellar platelets, lamellar stacks, axialites and spherulites were observed. High methanol nonsolvent contents led always to interconnected 3D polymer networks arising from SD mechanism. A decrease in average pore size and the porosity of the 3D polymer foams was also reported at higher PLA concentrations [14].

PLA monoliths are suitable to be used in several fields, such as tissue engineering, drug delivery and filtration technology. These monoliths have been produced using TIPS methods based on binary solvent systems of THF-water [90] and 1,4-dioxane-water [280]. Monoliths showed relatively large pores (25–400 μm) and short-range micron-scale frameworks (10–30 μm), respectively. PLA monoliths have also recently been developed by Kanno and Uyama [281] using a novel TIPS technology. A ternary system including 1,4-dioxane, water and 2-butanone was used as good solvent, non-solvent and midsolvent of PLA, respectively. Using this ternary system, the phase separation process was efficiently controlled and leaf-like morphologies with frameworks in a wide-range scale (i.e., from micron to nano) were produced (Figure 22).

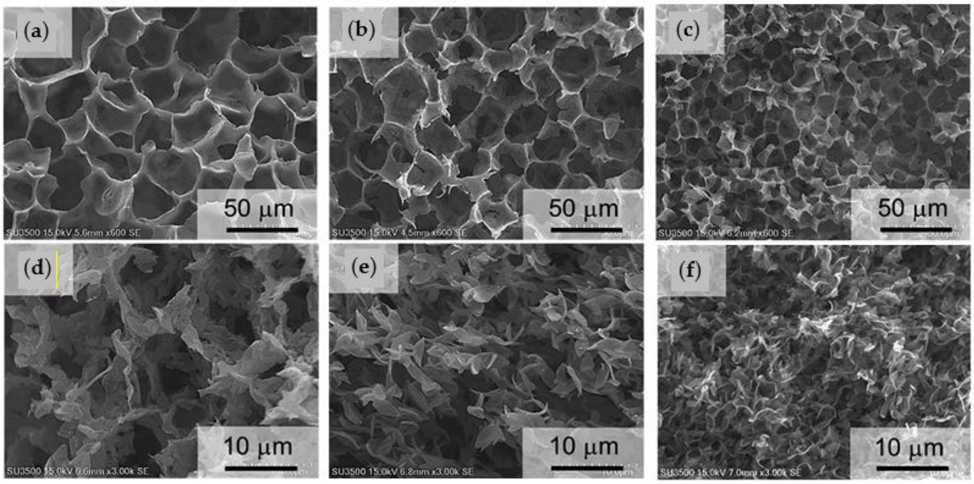

Figure 22. SEM images of PLLA monoliths obtained from different ratios of 1,4-dioxane/2-butanone/water: (**a**) 85/0/15, (**b**) 65/20/15, (**c**) 45/40/15, (**d**) 25/60/15, (**e**) 20/70/10, (**f**) 15/80/5. Reprinted with permission from [282].

By modifying only the solvent ratios a precise control on the morphology and foam characteristics could be achieved. As a result, monoliths with a pore size of 1.1–28.6 μm, skeletal size of 200–2500 nm and porosity around 90–93% were obtained. The novelty of this investigation was the addition of a midsolvent (e.g., 2-butanone), which in addition was able to promote a slow TIPS process and provide sufficient time for PLLA to crystallize (i.e., final crystallinity could be increased from 45 to 66.5%). In such condition, a transition from wall-like morphologies (arising from liquid-liquid phase separation) to interconnected leaf-like structure (obtained via crystallization of the polymer) was also observed [281].

2.6. Conclusions

Porous biodegradable scaffolds play a critical role in tissue engineering. Scaffolds, by mimicking the native ECM, provide physical bio-templates for cells, allowing them to attach, proliferate and guide the formation of new tissues. TIPS is one of the scaffold fabrication methodologies with a great potential for production of highly porous scaffolds with a wide range of pore size/architecture and a proper structural interconnectivity. These characteristics, together with a simple, low-cost and tunable fabrication process, which allows the scientist to incorporate various fillers and/or bioactive agents, have made it a popular method for fabricating polymeric and composite scaffolds. The process enables the generation of a variety of structures with different properties being desirable for regeneration of tissues using specific target cells. Although TIPS is a conventional method for preparing tissue engineering scaffolds, researchers have successfully innovated new approaches in terms of biomaterial selection and variations on the processing parameters, being enhanced its capability and versatility. Herein we reviewed the latest innovations and the recent advancements in scaffolds fabricated by the TIPS technique from the viewpoint of methodology, materials selection and structural features. Owing to the outstanding potentials and promising achievements of this method in producing tissue engineering scaffolds, conducting more investigations and up-to-date surveys in this field seems inevitable.

2.7. References

1. Martina, M.; Hutmacher, D.W. Biodegradable polymers applied in tissue engineering research: A review. *Polym. Int.* **2007**, *56*, 145–157.
2. Bacakova, L.; Zarubova, J.; Travnickova, M.; Musilkova, J.; Pajorova, J.; Slepicka, P.; Kasalkova, N.S.; Svorcik, V.; Kolska, Z.; Motarjemi, H.; et al. Stem cells: Their source, potency and use in regenerative therapies with focus on adipose-derived stem cells—A review. *Biotechnol. Adv.* **2018**, *36*, 1111–1126.
3. Hutmacher, D.W. Scaffolds in tissue engineering bone and cartilage. *Biomaterials* **2000**, *21*, 2529–2543.
4. Hollister, S.J. Porous scaffold design for tissue engineering. *Nat. Mater.* **2005**, *4*, 518–524.
5. Armentano, I.; Dottori, M.; Fortunati, E.; Mattioli, S.; Kenny, J.M. Biodegradable polymer matrix nanocomposites for tissue engineering: A review. *Polym. Degrad. Stab.* **2010**, *95*, 2126–2146.
6. Armentano, I.; Bitinis, N.; Fortunati, E.; Mattioli, S.; Rescignano, N.; Verdejo, R.; Lopez-Manchado, M.A.; Kenny, J.M. Multifunctional nanostructured PLA materials for packaging and tissue engineering. *Prog. Polym. Sci.* **2013**, *38*, 1720–1747.
7. Zeltinger, J.; Sherwood, J.K.; Graham, D.A.; Müeller, R.; Griffith, L.G. Effect of pore size and void fraction on cellular adhesion, proliferation, and matrix deposition. *Tissue Eng.* **2001**, *7*, 557–572.
8. Karageorgiou, V.; Kaplan, D. Porosity of 3D biomaterial scaffolds and osteogenesis. *Biomaterials* **2005**, *26*, 5474–5491.
9. Pellis, A.; Silvestrini, L.; Scaini, D.; Coburn, J.M.; Gardossi, L.; Kaplan, D.L.; Herrero Acero, E.; Guebitz, G.M. Enzyme-catalyzed functionalization of poly(L-lactic acid) for drug delivery applications. *Process. Biochem.* **2017**, *59*, 77–83.
10. Dorati, R.; DeTrizio, A.; Modena, T.; Conti, B.; Benazzo, F.; Gastaldi, G.; Genta, I. Biodegradable Scaffolds for Bone Regeneration Combined with Drug-Delivery Systems in Osteomyelitis Therapy. *Pharmaceuticals* **2017**, *10*, 96.
11. Biomaterials: Silk gland mimic spins strong fibres. *Nature* **2017**, *541*, 137.
12. Díaz, E.; Molpeceres, A.L.; Sandonis, I.; Puerto, I. PLLA/nHA Composite Films and Scaffolds for Medical Implants: In Vitro Degradation, Thermal and Mechanical Properties. *J. Inorg. Organomet. Polym. Mater.* **2019**, *29*, 121–131.
13. Guo, R.; Chen, S.; Xiao, X. Fabrication and characterization of poly (ethylenimine) modified poly (l-lactic acid) nanofibrous scaffolds. *J. Biomater. Sci. Polym. Ed.* **2019**, *30*, 1523–1541.
14. Onder, O.C.; Yilgor, E.; Yilgor, I. Critical parameters controlling the properties of monolithic poly(lactic acid) foams prepared by thermally induced phase separation. *J. Polym. Sci. Part B Polym. Phys.* **2019**, *57*, 98–108.
15. Bernardini, G.; Chellini, F.; Frediani, B.; Spreafico, A.; Santucci, A. Human platelet releasates combined with polyglycolic acid scaffold promote chondrocyte differentiation and phenotypic maintenance. *J. Biosci.* **2015**, *40*, 61–69.

16. Ding, J.; Chen, B.; Lv, T.; Liu, X.; Fu, X.; Wang, Q.; Yan, L.; Kang, N.; Cao, Y.; Xiao, R. Bone Marrow Mesenchymal Stem Cell-Based Engineered Cartilage Ameliorates Polyglycolic Acid/Polylactic Acid Scaffold-Induced Inflammation Through M2 Polarization of Macrophages in a Pig Model. *Stem Cells Transl. Med.* **2016**, *5*, 1079–1089.

17. Kumawat, V.S.; Ghosh, S.B.; Bandyopadhyay-Ghosh, S. Microporous biocomposite scaffolds with tunable degradation and interconnected microarchitecture-A synergistic integration of bioactive chain silicate glass-ceramic and poly(ε-caprolactone). *Polym. Degrad. Stab.* **2019**, *165*, 20–26.

18. Yao, Q.; Liu, Y.; Pan, Y.; Miszuk, J.M.; Sun, H. One-pot porogen free method fabricated porous microsphere-aggregated 3D PCL scaffolds for bone tissue engineering. *J. Biomed. Mater. Res. B Appl. Biomater.* **2020**, *108*, 2699–2710.

19. Díaz, E.; Puerto, I.; Sandonis, I.; Ribeiro, S.; Lanceros-Mendez, S. Hydrolytic degradation and cytotoxicity of poly(lactic-co-glycolic acid)/multiwalled carbon nanotubes for bone regeneration. *J. Appl. Polym. Sci.* **2020**, *137*, 48439.

20. McKenna, E.; Klein, T.J.; Doran, M.R.; Futrega, K. Integration of an ultra-strong poly(lactic-co-glycolic acid) (PLGA) knitted mesh into a thermally induced phase separation (TIPS) PLGA porous structure to yield a thin biphasic scaffold suitable for dermal tissue engineering. *Biofabrication* **2019**, *12*, 015015.

21. Liu, J.; Zhang, J.; James, P.F.; Yousefi, A.-M. I-Optimal design of poly(lactic-co-glycolic) acid/hydroxyapatite three-dimensional scaffolds produced by thermally induced phase separation. *Polym. Eng. Sci.* **2019**, *59*, 1146–1157.

22. Yousefi, A.-M.; Liu, J.; Sheppard, R.; Koo, S.; Silverstein, J.; Zhang, J.; James, P.F. I-Optimal Design of Hierarchical 3D Scaffolds Produced by Combining Additive Manufacturing and Thermally Induced Phase Separation. *ACS Appl. Bio Mater.* **2019**, *2*, 685–696.

23. He, Y.; Liu, W.; Guan, L.; Chen, J.; Duan, L.; Jia, Z.; Huang, J.; Li, W.; Liu, J.; Xiong, J.; et al. A 3D-Printed PLCL Scaffold Coated with Collagen Type I and Its Biocompatibility. *BioMed Res. Int.* **2018**, *2018*, 5147156.

24. Piao, H.; Kwon, J.-S.; Piao, S.; Sohn, J.-H.; Lee, Y.-S.; Bae, J.-W.; Hwang, K.-K.; Kim, D.-W.; Jeon, O.; Kim, B.-S.; et al. Effects of cardiac patches engineered with bone marrow-derived mononuclear cells and PGCL scaffolds in a rat myocardial infarction model. *Biomaterials* **2007**, *28*, 641–649.

25. Chen, P.; Zhou, Z.; Liu, W.; Zhao, Y.; Huang, T.; Li, X.; Duan, J.; Fang, J. Preparation and Characterization of Poly(L-lactide-co-glycolide-co-ε-caprolactone) Scaffolds by Thermally Induced Phase Separation. *J. Macromol. Sci. B* **2020**, *59*, 427–439.

26. Davachi, S.M.; Kaffashi, B. Polylactic Acid in Medicine. *Polym.-Plast. Technol. Eng.* **2015**, *54*, 944–967.

27. Ruiz-Hitzky, E.; Fernandes, F. Progress in Bionanocomposites: From green plastics to biomedical applications. *Prog. Polym. Sci.* **2013**, *38*, 1391.

28. Nie, L.; Chen, D.; Yang, Q.; Zou, P.; Feng, S.; Hu, H.; Suo, J. Hydroxyapatite/poly-l-lactide nanocomposites coating improves the adherence and proliferation of human bone mesenchymal stem cells on porous biphasic calcium phosphate scaffolds. *Mater. Lett.* **2013**, *92*, 25–28.

29. Roeder, R.K.; Converse, G.L.; Kane, R.J.; Yue, W. Hydroxyapatite-reinforced polymer biocomposites for synthetic bone substitutes. *JOM* **2008**, *60*, 38–45.

30. Wilberforce, S.I.J.; Finlayson, C.E.; Best, S.M.; Cameron, R.E. The influence of hydroxyapatite (HA) microparticles (m) and nanoparticles (n) on the thermal and dynamic mechanical properties of poly-l-lactide. *Polymer* **2011**, *52*, 2883–2890.

31. Davachi, S.M.; Kaffashi, B.; Torabinejad, B.; Zamanian, A.; Seyfi, J.; Hejazi, I. Investigating thermal, mechanical and rheological properties of novel antibacterial hybrid nanocomposites based on PLLA/triclosan/nano-hydroxyapatite. *Polymer* **2016**, *90*, 232–241.

32. Pietrasik, J.; Szustakiewicz, K.; Zaborski, M.; Haberko, K. Hydroxyapatite: An Environmentally Friendly Filler for Elastomers. *Mol. Cryst. Liq. Cryst.* **2008**, *483*, 172–178.

33. Hickey, D.J.; Ercan, B.; Sun, L.; Webster, T.J. Adding MgO nanoparticles to hydroxyapatite-PLLA nanocomposites for improved bone tissue engineering applications. *Acta Biomater.* **2015**, *14*, 175–184.

34. Marques, C.F.; Olhero, S.; Abrantes, J.C.C.; Marote, A.; Ferreira, S.; Vieira, S.I.; Ferreira, J.M.F. Biocompatibility and antimicrobial activity of biphasic calcium phosphate powders doped with metal ions for regenerative medicine. *Ceram. Int.* **2017**, *43*, 15719–15728.

35. Zhang, F.; Chang, J.; Lu, J.; Ning, C. Surface modification of beta-tricalcium phosphate scaffolds with topological nanoapatite coatings. *Mater. Sci. Eng. C* **2008**, *28*, 1330–1339.

36. Zhang, Q.; Zhou, Z.; Peng, C.; Huang, T.; Liu, W.; Liu, Q.; Zhou, H.; Wang, W.; Yan, H. Preparation and Properties of Novel Maleated Poly (D, L-lactide-co-glycolide) Porous Scaffolds for Tissue Engineering. *J. Macromol. Sci. Part B Phys.* **2017**, *56*, 505–515.

37. Duan, J.; Zhou, Z.; Huang, T.; Liu, W.; Zhao, Y.; Wu, W.; Li, X.; Fang, J. Biocompatibility properties of composite scaffolds based on 1,4-butanediamine modified poly(lactide-co-glycolide) and nanobioceramics. *Int. J. Polym. Anal. Charact.* **2019**, *24*, 428–438.

38. Whang, K.; Thomas, C.H.; Healy, K.E.; Nuber, G. A novel method to fabricate bioabsorbable scaffolds. *Polymer* **1995**, *36*, 837–842.

39. Sultana, N.; Wang, M. Fabrication of HA/PHBV composite scaffolds through the emulsion freezing/freeze-drying process and characterisation of the scaffolds. *J. Mater. Sci. Mater. Med.* **2008**, *19*, 2555–2561.

40. An, J.; Teoh, J.E.M.; Suntornnond, R.; Chua, C.K. Design and 3D Printing of Scaffolds and Tissues. *Engineering* **2015**, *1*, 261–268.

41. Ji, C.; Annabi, N.; Hosseinkhani, M.; Sivaloganathan, S.; Dehghani, F. Fabrication of poly-DL-lactide/polyethylene glycol scaffolds using the gas foaming technique. *Acta Biomater.* **2012**, *8*, 570–578.

42. Dehghani, F.; Annabi, N. Engineering porous scaffolds using gas-based techniques. *Curr. Opin. Biotechnol.* **2011**, *22*, 661–666.

43. del Valle, L.; Franco, L.; Katsarava, R.; Puiggalí, J. Electrospun biodegradable polymers loaded with bactericide agents. *AIMS Mol. Sci.* **2016**, *3*, 52–87.

44. Llorens, E.; Armelin, E.; Pérez-Madrigal, M.; del Valle, L.; Alemán, C.; Puiggalí, J. Nanomembranes and Nanofibers from Biodegradable Conducting Polymers. *Polymers* **2013**, *5*, 1115–1157.

45. del Valle, L.; Camps, R.; Díaz, A.; Franco, L.; Rodriguez-Galan, A.; Puiggalí, J. Electrospinning of polylactide and polycaprolactone mixtures for preparation of materials with tunable drug release properties. *J. Polym. Res.* **2011**, *18*, 1903–1917.

46. Zeinali, R.; Khorasani, M.T.; Behnamghader, A.; Atai, M.; Valle, L.; Puiggalí, J. Poly(hydroxybutyrate-*co*-hydroxyvalerate) Porous Matrices from Thermally Induced Phase Separation. *Polymers* **2020**, *12*, 2787.

47. Molladavoodi, S.; Gorbet, M.; Medley, J.; Ju Kwon, H. Investigation of microstructure, mechanical properties and cellular viability of poly(L-lactic acid) tissue engineering scaffolds prepared by different thermally induced phase separation protocols. *J. Mech. Behav. Biomed. Mater.* **2013**, *17*, 186–197.

48. Flaibani, M.; Elvassore, N. Gas anti-solvent precipitation assisted salt leaching for generation of micro- and nano-porous wall in bio-polymeric 3D scaffolds. *Mater. Sci. Eng. C* **2012**, *32*, 1632–1639.

49. Carfì Pavia, F.; Palumbo, F.S.; La Carrubba, V.; Bongiovì, F.; Brucato, V.; Pitarresi, G.; Giammona, G. Modulation of physical and biological properties of a composite PLLA and polyaspartamide derivative obtained via thermally induced phase separation (TIPS) technique. *Mater. Sci. Eng. C* **2016**, *67*, 561–569.

50. Akbarzadeh, R.; Yousefi, A.M. Effects of processing parameters in thermally induced phase separation technique on porous architecture of scaffolds for bone tissue engineering. *J. Biomed. Mater. Res. B Appl. Biomater.* **2014**, *102*, 1304–1315.

51. Lombardo, M.E.; Carfì Pavia, F.; Vitrano, I.; Ghersi, G.; Brucato, V.; Rosei, F.; La Carrubba, V. PLLA scaffolds with controlled architecture as potential microenvironment for in vitro tumor model. *Tissue Cell* **2019**, *58*, 33–41.

52. La Carrubba, V.; Pavia, F.C.; Brucato, V.; Piccarolo, S. PLLA/PLA scaffolds prepared via Thermally Induced Phase Separation (TIPS): Tuning of properties and biodegradability. *Int. J. Mater. Form.* **2008**, *1*, 619–622.

53. Schugens, C.; Maquet, V.; Grandfils, C.; Jerome, R.; Teyssie, P. Biodegradable and macroporous polylactide implants for cell transplantation: 1. Preparation of macroporous polylactide supports by solid-liquid phase separation. *Polymer* **1996**, *37*, 1027–1038.

54. Salehi, M.; Naseri-Nosar, M.; Ebrahimi-Barough, S.; Nourani, M.; Khojasteh, A.; Hamidieh, A.A.; Amani, A.; Farzamfar, S.; Ai, J. Sciatic nerve regeneration by transplantation of Schwann cells via erythropoietin controlled-releasing polylactic acid/multiwalled carbon nanotubes/gelatin nanofibrils neural guidance conduit. *J. Biomed. Mater. Res. B Appl. Biomater.* **2018**, *106*, 1463–1476.

55. Kasoju, N.; Kubies, D.; Sedlačík, T.; Janoušková, O.; Koubková, J.; Kumorek, M.M.; Rypáček, F. Polymer scaffolds with no skin-effect for tissue engineering applications fabricated by thermally induced phase separation. *Biomed. Mater.* **2016**, *11*, 015002.

56. Langford, C.R.; Cameron, N.R. Materials for Tissue Engineering and 3D Cell Culture. In *Bio-Inspired Polymers*; Bruns, N., Kilbinger, A.F.M., Eds.; The Royal Society of Chemistry: 2017; pp. 460–489.
57. Lou, T.; Wang, X.; Yan, X.; Miao, Y.; Long, Y.-Z.; Yin, H.-L.; Sun, B.; Song, G. Fabrication and biocompatibility of poly(l-lactic acid) and chitosan composite scaffolds with hierarchical microstructures. *Mater. Sci. Eng. C* **2016**, *64*, 341–345.
58. Guo, X.; Zhu, J.; Zhang, H.; You, Z.; Morsi, Y.; Mo, X.; Zhu, T. Facile preparation of a controlled-release tubular scaffold for blood vessel implantation. *J. Colloid Interface Sci.* **2019**, *539*, 351–360.
59. Farzamfar, S.; Salehi, M.; Tavangar, S.M.; Verdi, J.; Mansouri, K.; Ai, A.; Malekshahi, Z.V.; Ai, J. A novel polycaprolactone/carbon nanofiber composite as a conductive neural guidance channel: An in vitro and in vivo study. *Prog. Biomater.* **2019**, *8*, 239–248.
60. Szustakiewicz, K.; Gazińska, M.; Kryszak, B.; Grzymajło, M.; Pigłowski, J.; Wiglusz, R.J.; Okamoto, M. The influence of hydroxyapatite content on properties of poly(L-lactide)/hydroxyapatite porous scaffolds obtained using thermal induced phase separation technique. *Eur. Polym. J.* **2019**, *113*, 313–320.
61. Yao, Q.; Fuglsby, K.E.; Zheng, X.; Sun, H. Nanoclay-functionalized 3D nanofibrous scaffolds promote bone regeneration. *J. Mater. Chem. B* **2020**, *8*, 3842–3851.
62. Dai, Y.; Shen, T.; Ma, L.; Wang, D.; Gao, C. Regeneration of osteochondral defects in vivo by a cell-free cylindrical poly(lactide-co-glycolide) scaffold with a radially oriented microstructure. *J. Tissue Eng. Regen. Med.* **2018**, *12*, e1647–e1661.
63. Zhu, L.; Chen, S.; Liu, K.; Wen, W.; Lu, L.; Ding, S.; Zhou, C.; Luo, B. 3D poly (L-lactide)/chitosan micro/nano fibrous scaffolds functionalized with quercetin-polydopamine for enhanced osteogenic and anti-inflammatory activities. *Chem. Eng. J.* **2020**, *391*, 123524.
64. Gay, S.; Lefebvre, G.; Bonnin, M.; Nottelet, B.; Boury, F.; Gibaud, A.; Calvignac, B. PLA scaffolds production from Thermally Induced Phase Separation: Effect of process parameters and development of an environmentally improved route assisted by supercritical carbon dioxide. *J. Supercrit. Fluids* **2018**, *136*, 123–135.
65. Chen, J.-S.; Tu, S.-L.; Tsay, R.-Y. A morphological study of porous polylactide scaffolds prepared by thermally induced phase separation. *J. Taiwan. Inst. Chem. Eng.* **2010**, *41*, 229–238.
66. Wang, L.; Kang, Y.; Chen, S.; Mo, X.; Jiang, J.; Yan, X.; Zhu, T.; Zhao, J. Macroporous 3D Scaffold with Self-Fitting Capability for Effectively Repairing Massive Rotator Cuff Tear. *ACS Biomater. Sci. Eng.* **2020**, doi:10.1021/acsbiomaterials.0c00193.
67. Chen, J.; Yu, M.; Guo, B.; Ma, P.X.; Yin, Z. Conductive nanofibrous composite scaffolds based on in-situ formed polyaniline nanoparticle and polylactide for bone regeneration. *J. Colloid Interface Sci.* **2018**, *514*, 517–527.
68. Zhang, C.; Dong, P.; Bai, Y.; Quan, D. Nanofibrous polyester-polypeptide block copolymer scaffolds with high porosity and controlled degradation promote cell adhesion, proliferation and differentiation. *Eur. Polym. J.* **2020**, *130*, 109647.

69. Gandolfi, M.G.; Zamparini, F.; Degli Esposti, M.; Chiellini, F.; Fava, F.; Fabbri, P.; Taddei, P.; Prati, C. Highly porous polycaprolactone scaffolds doped with calcium silicate and dicalcium phosphate dihydrate designed for bone regeneration. *Mater. Sci. Eng. C* **2019**, *102*, 341–361.

70. Farzamfar, S.; Naseri-Nosar, M.; Sahrapeyma, H.; Ehterami, A.; Goodarzi, A.; Rahmati, M.; Ahmadi Lakalayeh, G.; Ghorbani, S.; Vaez, A.; Salehi, M. Tetracycline hydrochloride-containing poly (ε-caprolactone)/poly lactic acid scaffold for bone tissue engineering application: In vitro and in vivo study. *Int. J. Polym. Mater. Polym. Biomater.* **2019**, *68*, 472–479.

71. Xu, C.; Okpokwasili, C.; Huang, Y.; Shi, X.; Wu, J.; Liao, J.; Tang, L.; Hong, Y. Optimizing Anisotropic Polyurethane Scaffolds to Mechanically Match with Native Myocardium. *ACS Biomater. Sci. Eng.* **2020**, *6*, 2757–2769.

72. Feng, X.; Xu, P.; Shen, T.; Zhang, Y.; Ye, J.; Gao, C. Influence of pore architectures of silk fibroin/collagen composite scaffolds on the regeneration of osteochondral defects in vivo. *J. Mater. Chem. B* **2020**, *8*, 391–405.

73. Bužarovska, A.; Dinescu, S.; Chitoiu, L.; Costache, M. Porous poly(L-lactic acid) nanocomposite scaffolds with functionalized TiO_2 nanoparticles: Properties, cytocompatibility and drug release capability. *J. Mater. Sci.* **2018**, *53*, 11151–11166.

74. Montanheiro, T.L.d.A.; Montagna, L.S.; Patrulea, V.; Jordan, O.; Borchard, G.; Lobato, G.M.M.; Catalani, L.H.; Lemes, A.P. Evaluation of cellulose nanocrystal addition on morphology, compression modulus and cytotoxicity of poly(3-hydroxybutyrate-co-3-hydroxyvalerate) scaffolds. *J. Mater. Sci.* **2019**, *54*, 7198–7210.

75. Erickson, A.E.; Sun, J.; Lan Levengood, S.K.; Swanson, S.; Chang, F.-C.; Tsao, C.T.; Zhang, M. Chitosan-based composite bilayer scaffold as an in vitro osteochondral defect regeneration model. *Biomed. Microdevices* **2019**, *21*, 34.

76. Conoscenti, G.; Carfì Pavia, F.; Ongaro, A.; Brucato, V.; Goegele, C.; Schwarz, S.; Boccaccini, A.R.; Stoelzel, K.; La Carrubba, V.; Schulze-Tanzil, G. Human nasoseptal chondrocytes maintain their differentiated phenotype on PLLA scaffolds produced by thermally induced phase separation and supplemented with bioactive glass 1393. *Connect. Tissue Res.* **2019**, *60*, 344–357.

77. Degli Esposti, M.; Chiellini, F.; Bondioli, F.; Morselli, D.; Fabbri, P. Highly porous PHB-based bioactive scaffolds for bone tissue engineering by in situ synthesis of hydroxyapatite. *Mater. Sci. Eng. C* **2019**, *100*, 286–296.

78. Gandolfi, M.G.; Gardin, C.; Zamparini, F.; Ferroni, L.; Esposti, M.D.; Parchi, G.; Ercan, B.; Manzoli, L.; Fava, F.; Fabbri, P.; et al. Mineral-Doped Poly(L-lactide) Acid Scaffolds Enriched with Exosomes Improve Osteogenic Commitment of Human Adipose-Derived Mesenchymal Stem Cells. *Nanomaterials* **2020**, *10*, 432.

79. Si, J.; Yang, Y.; Xing, X.; Yang, F.; Shan, P. Controlled degradable chitosan/collagen composite scaffolds for application in nerve tissue regeneration. *Polym. Degrad. Stab.* **2019**, *166*, 73–85.

80. Salehi, M.; Farzamfar, S.; Bozorgzadeh, S.; Bastami, F. Fabrication of Poly(L-Lactic Acid)/Chitosan Scaffolds by Solid-Liquid Phase Separation Method for Nerve Tissue

Engineering: An In Vitro Study on Human Neuroblasts. *J. Craniofac. Surg.* **2019**, *30*, 784–789.

81. van de Witte, P.; Dijkstra, P.J.; van den Berg, J.W.A.; Feijen, J. Phase separation processes in polymer solutions in relation to membrane formation. *J. Membr. Sci.* **1996**, *117*, 1–31.
82. Auras, R.; Lim, L.-T.; Selke, S.; Tsuji, H. *Poly(Lactic Acid): Synthesis, Structures, Properties, Processing, and Applications*; John Wiley & Sons: Hoboken, NJ, USA, 2010.
83. Chen, V.J.; Ma, P.X. Polymer phase separation. In *Scaffolding in Tissue Engineering*; Ma, P.X., Elisseeff, J., Eds.; Taylor & Francis: Boca Raton, FL, USA, 2006; pp. 125–137.
84. Zhang, R.; Ma, P.X. Poly(α-hydroxyl acids)/hydroxyapatite porous composites for bone-tissue engineering. I. Preparation and morphology. *J. Biomed. Mater. Res.* **1999**, *44*, 446–455.
85. Ma, P.X.; Zhang, R. Microtubular architecture of biodegradable polymer scaffolds. *J. Biomed. Mater. Res.* **2001**, *56*, 469–477.
86. Schugens, C.; Maquet, V.; Grandfils, C.; Jerome, R.; Teyssie, P. Polylactide macroporous biodegradable implants for cell transplantation. II. Preparation of polylactide foams by liquid-liquid phase separation. *J. Biomed. Mater. Res.* **1996**, *30*, 449–461.
87. Nam, Y.S.; Park, T.G. Biodegradable polymeric microcellular foams by modified thermally induced phase separation method. *Biomaterials* **1999**, *20*, 1783–1790.
88. Flory, P.J. *Principles of Polymer Chemistry*; Cornell University Press: Ithaca, NY, USA, 1953; pp. 541–594.
89. Lloyd, D.R.; Kim, S.S.; Kinzer, K.E. Microporous membrane formation via thermally-induced phase separation. II. Liquid—liquid phase separation. *J. Membr. Sci.* **1991**, *64*, 1–11.
90. Önder, Ö.C.; Yilgör, E.; Yilgör, I. Fabrication of rigid poly(lactic acid) foams via thermally induced phase separation. *Polymer* **2016**, *107*, 240–248.
91. Martinez Perez, C.; Olivas-Armendariz, I.; Castro-Carmona, J.; Garcia Casillas, P.E. Scaffolds for Tissue Engineering Via Thermally Induced Phase Separation. In *Advances in Regenerative Medicine*; Wislet, S., Ed.; IntechOpen: 2011.
92. Conoscenti, G.; Carrubba, V.; Brucato, V. A Versatile Technique to Produce Porous Polymeric Scaffolds: The Thermally Induced Phase Separation (TIPS) Method. *Arch. Chem. Res.* **2017**, *1*, 1–3.
93. Pavia, F.C.; La Carrubba, V.; Piccarolo, S.; Brucato, V. Polymeric scaffolds prepared via thermally induced phase separation: Tuning of structure and morphology. *J. Biomed. Mater. Res. A* **2008**, *86A*, 459–466.
94. Ma, P.X.; Zhang, R. Synthetic nano-scale fibrous extracellular matrix. *J. Biomed. Mater. Res.* **1999**, *46*, 60–72.
95. He, L.; Zhang, Y.; Zeng, X.; Quan, D.; Liao, S.; Zeng, Y.; Lu, J.; Ramakrishna, S. Fabrication and characterization of poly(l-lactic acid) 3D nanofibrous scaffolds with controlled architecture by liquid–liquid phase separation from a ternary polymer–solvent system. *Polymer* **2009**, *50*, 4128–4138.

96. Salerno, A.; Domingo, C. Making microporous nanometre-scale fibrous PLA aerogels with clean and reliable supercritical CO2 based approaches. *Microporous Mesoporous Mater.* **2014**, *184*, 162–168.

97. Ma, P.X.; Zhang, R.; Xiao, G.; Franceschi, R. Engineering new bone tissue in vitro on highly porous poly(α-hydroxyl acids)/hydroxyapatite composite scaffolds. *J. Biomed. Mater. Res.* **2001**, *54*, 284–293.

98. Yang, F.; Murugan, R.; Wang, X.; Ma, Y.; Wang, S. Fabrication of nano-structured porous PLLA scaffold intended for nerve tissue engineering. *Biomaterials* **2004**, *25*, 1891–1900.

99. Cao, Y.; Croll, T.; O'Connor, A.; Stevens, G.; Cooper-White, J. Systematic selection of solvents for the fabrication of 3D combined macro- and microporous polymeric scaffolds for soft tissue engineering. *J. Biomater. Sci. Polym. Ed.* **2006**, *17*, 369–402.

100. Vaquette, C.; Cooper-White, J. A simple method for fabricating 3-D multilayered composite scaffolds. *Acta Biomater.* **2013**, *91*, 4599–4608.

101. Iwahashi, M.; Nozaki, T.; Kamaya, K.; Taguchi, K.; Fujita, M.; Kasahara, Y.; Minami, H.; Matsuzawa, H.; Nakamura, S.; Harada, K.; et al. Phase behavior of binary mixtures composed of ethylene carbonate and various organic solvents. *J. Chem. Thermodyn.* **2011**, *43*, 80–87.

102. Kenar, J.A. Latent heat characteristics of biobased oleochemical carbonates as potential phase change materials. *Sol. Energy Mater. Sol. Cells* **2010**, *94*, 1697–1703.

103. Bonner, O.D.; Kim, S.-J.; Torres, A.L. Comparison of the osmotic and activity coefficients of some solutes in structured solvents. *J. Phys. Chem.* **1969**, *73*, 1968–1974.

104. Stickney, J.; Carlson-Lynch, H. Dioxane, 1,4. In *Encyclopedia of Toxicology*, 3rd ed.; Wexler, P., Ed.; Academic Press: Oxford, UK, 2014; pp. 186–189.

105. Parod, R.J. Tetrahydrofuran. In *Encyclopedia of Toxicology*, 3rd ed.; Wexler, P., Ed.; Academic Press: Oxford, UK, 2014; pp. 505–508.

106. Ethylene Carbonate, ECHA. Availabe online: https://echa.europa.eu/registration-dossier/-/registered-dossier/14909/7/3/1 (accessed on 4 January 2021).

107. Hile, D.D.; Amirpour, M.L.; Akgerman, A.; Pishko, M.V. Active growth factor delivery from poly(d,l-lactide-co-glycolide) foams prepared in supercritical CO2. *J. Control. Release* **2000**, *66*, 177–185.

108. Sodian, R.; Sperling, J.S.; Martin, D.P.; Egozy, A.; Stock, U.; Mayer, J.E.; Vacanti, J.P. Technical Report: Fabrication of a Trileaflet Heart Valve Scaffold from a Polyhydroxyalkanoate Biopolyester for Use in Tissue Engineering. *Tissue Eng.* **2000**, *6*, 183–188.

109. Koegler, W.S.; Patrick, C.; Cima, M.J.; Griffith, L.G. Carbon dioxide extraction of residual chloroform from biodegradable polymers. *J. Biomed. Mater. Res.* **2002**, *63*, 567–576.

110. Lloyd, D.R.; Kinzer, K.E.; Tseng, H.S. Microporous membrane formation via thermally induced phase separation. I. Solid-liquid phase separation. *J. Membr. Sci.* **1990**, *52*, 239–261.

111. Povh, N.P.; Marques, M.O.M.; Meireles, M.A.A. Supercritical CO2 extraction of essential oil and oleoresin from chamomile (Chamomilla recutita [L.] Rauschert). *J. Supercrit. Fluids* **2001**, *21*, 245–256.

112. Dourani, A.; Haghgoo, M.; Hamadanian, M. Multi-walled carbon nanotube and carbon nanofiber/ polyacrylonitrile aerogel scaffolds for enhanced epoxy resins. *Compos. B Eng.* **2019**, *176*, 107299.

113. Aradhana, R.; Mohanty, S.; Nayak, S.K. High performance epoxy nanocomposite adhesive: Effect of nanofillers on adhesive strength, curing and degradation kinetics. *Int. J. Adhes. Adhes.* **2018**, *84*, 238–249.

114. Wang, Y.; Chen, S.; Chen, X.; Lu, Y.; Miao, M.; Zhang, D. Controllability of epoxy equivalent weight and performance of hyperbranched epoxy resins. *Compos. B Eng.* **2019**, *160*, 615–625.

115. Hutmacher, D. Scaffold design and fabrication technologies for engineering tissues—State of the art and future perspectives. *J. Biomater. Sci. Polym. Ed.* **2001**, *12*, 107–124.

116. Elsayed, Y.; Lekakou, C. Designing and modeling pore size distribution in tissue scaffolds. In *Characterisation and Design of Tissue Scaffolds*; Tomlins, P., Ed.; Woodhead Publishing: 2016; pp. 23–43.

117. Lee, J.; Cuddihy, M.; Kotov, N. Three-Dimensional Cell Culture Matrices: State of the Art. *Tissue Eng. Part B Rev.* **2008**, *14*, 61–86.

118. Liu, Y.; Lim, J.; Teoh, S.-H. Review: Development of clinically relevant scaffolds for vascularised bone tissue engineering. *Biotechnol. Adv.* **2013**, *31*, 688–705.

119. O'Brien, F.J. Biomaterials & scaffolds for tissue engineering. *Mater. Today* **2011**, *14*, 88–95.

120. Akbarzadeh, R.; Minton, J.A.; Janney, C.S.; Smith, T.A.; James, P.F.; Yousefi, A.-M. Hierarchical polymeric scaffolds support the growth of MC3T3-E1 cells. *J. Mater. Sci. Mater. Med.* **2015**, *26*, 116–127.

121. Gandolfi, M.G.; Zamparini, F.; Degli Esposti, M.; Chiellini, F.; Aparicio, C.; Fava, F.; Fabbri, P.; Taddei, P.; Prati, C. Polylactic acid-based porous scaffolds doped with calcium silicate and dicalcium phosphate dihydrate designed for biomedical application. *Mater. Sci. Eng. C* **2018**, *82*, 163–181.

122. Mannella, G.A.; Carfì Pavia, F.; La Carrubba, V.; Brucato, V. Phase separation of polymer blends in solution: A case study. *Eur. Polym. J.* **2016**, *79*, 176–186.

123. Wang, X.-D.; Shou, J.; Wong, P.; French, D.; Gao, W.-Q. Notch1-expressing cells are indispensable for prostatic branching morphogenesis during development and re-growth following castration and androgen replacement. *J. Biol. Chem.* **2004**, *279*, 24733–24744.

124. Roy, T.D.; Simon, J.L.; Ricci, J.L.; Rekow, E.D.; Thompson, V.P.; Parsons, J.R. Performance of degradable composite bone repair products made via three-dimensional fabrication techniques. *J. Biomed. Mater. Res. A* **2003**, *66A*, 283-291.

125. Chen, G.; Ushida, T.; Tateishi, T. Poly(DL-lactic-co-glycolic acid) sponge hybridized with collagen microsponges and deposited apatite particulates. *J. Biomed. Mater. Res.* **2001**, *57*, 8–14.

126. Fabbri, P.; Cannillo, V.; Sola, A.; Dorigato, A.; Chiellini, F. Highly porous polycaprolactone-45S5 Bioglass® scaffolds for bone tissue engineering. *Compos. Sci. Technol.* **2010**, *70*, 1869–1878.

127. Amini, A.R.; Adams, D.J.; Laurencin, C.T.; Nukavarapu, S.P. Optimally Porous and Biomechanically Compatible Scaffolds for Large-Area Bone Regeneration. *Tissue Eng. Part A* **2012**, *18*, 1376–1388.

128. Feng, B.; Jinkang, Z.; Zhen, W.; Jianxi, L.; Jiang, C.; Jian, L.; Guolin, M.; Xin, D. The effect of pore size on tissue ingrowth and neovascularization in porous bioceramics of controlled architecture in vivo. *Biomed. Mater.* **2011**, *6*, 015007.

129. Liang, D.; Hsiao, B.; Chu, B. Functional Electrospun Nanofibrous Scaffolds for Biomedical Applications. *Adv. Drug Del. Rev.* **2008**, *59*, 1392–1412.

130. Biswas, D.; Tran, P.; Tallon, C.; O'Connor, A. Combining mechanical foaming and thermally induced phase separation to generate chitosan scaffolds for soft tissue engineering. *J. Biomater. Sci. Polym. Ed.* **2016**, *28*, 1–31.

131. Kozehkonan, G.S.; Salehi, M.; Farzamfar, S.; Ghanbari, H.; Adabi, M.; Amani, A. Preparation and characterization of PCL polymeric scaffolds coated with chitosan/ bioactive glass/gelatin nanoparticles using the tips methodology for bone tissue engineering. *Nanomed. J.* **2019**, *6*, 311–320.

132. Hermida, E.; Ruiz, I.; Baldessari, A.; Kreimann, E.; Cabrini, R.; Juvenal, G.; Hermida, G.; Fungueiro, M. Biodegradation and Histological Response of PHBV Porous Scaffolds. In Proceedings of the 2nd Workshop on Artificial Organs, Biomaterials and Tissue Engineering, Mar del Plata, Argentina, 28–30 September 2011; p. A9.

133. Samadian, H.; Farzamfar, S.; Vaez, A.; Ehterami, A.; Bit, A.; Alam, M.; Goodarzi, A.; Darya, G.; Salehi, M. A tailored polylactic acid/polycaprolactone biodegradable and bioactive 3D porous scaffold containing gelatin nanofibers and Taurine for bone regeneration. *Sci. Rep.* **2020**, *10*, 13366.

134. Fang, Y.; Zhang, T.; Zhang, L.; Gong, W.; Sun, W. Biomimetic design and fabrication of scaffolds integrating oriented micro-pores with branched channel networks for myocardial tissue engineering. *Biofabrication* **2019**, *11*, 035004.

135. Conoscenti, G.; Schneider, T.; Stoelzel, K.; Carfì Pavia, F.; Brucato, V.; Goegele, C.; La Carrubba, V.; Schulze-Tanzil, G. PLLA scaffolds produced by thermally induced phase separation (TIPS) allow human chondrocyte growth and extracellular matrix formation dependent on pore size. *Mater. Sci. Eng. C* **2017**, *80*, 449–459.

136. Rigogliuso, S.; Pavia, F.C.; Brucato, V.; Carrubba, V.L.; Favia, P.; Intranuovo, F.; Gristina, R.; Ghersi, G. Use of Modified 3D Scaffolds to Improve Cell Adhesion and Drive Desired Cell Responses. *Chem. Eng. Trans.* **2012**, *27*, 415–420.

137. Conoscenti, G.; Carfì Pavia, F.; Ciraldo, F.E.; Liverani, L.; Brucato, V.; La Carrubba, V.; Boccaccini, A.R. In vitro degradation and bioactivity of composite poly-l-lactic (PLLA)/bioactive glass (BG) scaffolds: Comparison of 45S5 and 1393BG compositions. *J. Mater. Sci.* **2018**, *53*, 2362–2374.

138. Boccaccini, A.R.; Notingher, I.; Maquet, V.; Jérôme, R. Bioresorbable and bioactive composite materials based on polylactide foams filled with and coated by Bioglass® particles for tissue engineering applications. *J. Mater. Sci. Mater. Med.* **2003**, *14*, 443–450.

139. Reverchon, E.; Cardea, S.; Rapuano, C. A new supercritical fluid-based process to produce scaffolds for tissue replacement. *J. Supercrit. Fluids* **2008**, *45*, 365–373.

140. Yin, G.; Zhao, D.; Zhang, L.; Ren, Y.; Ji, S.; Tang, H.; Zhou, Z.; Li, Q. Highly porous 3D PLLA materials composed of nanosheets, fibrous nanosheets, or nanofibrous networks: Preparation and the potential application in oil–water separation. *Chem. Eng. J.* **2016**, *302*, 1–11.

141. Razak, S.I.A.; Sharif, N.F.A.; Rahman, W.A.W.A. Biodegradable polymers and their bone applications: A review. *Int. J. Basic Appl. Sci.* **2012**, *12*, 31–49.

142. Murphy, W.; Dennis, R.; Kileny, J.; Mooney, D. Salt Fusion: An Approach to Improve Pore Interconnectivity within Tissue Engineering Scaffolds. *Tissue Eng.* **2002**, *8*, 43–52.

143. El-Kady, A.M.; Rizk, R.A.; Abd El-Hady, B.M.; Shafaa, M.W.; Ahmed, M.M. Characterization, and antibacterial properties of novel silver releasing nanocomposite scaffolds fabricated by the gas foaming/salt-leaching technique. *J. Genet. Eng. Biotechnol.* **2012**, *10*, 229–238.

144. Le Bolay, N.; Santran, V.; Dechambre, G.; Combes, C.; Drouet, C.; Lamure, A.; Rey, C. Production, by co-grinding in a media mill, of porous biodegradable polylactic acid–apatite composite materials for bone tissue engineering. *Powder Technol.* **2009**, *190*, 89–94.

145. Wei, G.; Ma, P.X. Macroporous and nanofibrous polymer scaffolds and polymer/bone-like apatite composite scaffolds generated by sugar spheres. *J. Biomed. Mater. Res. A* **2006**, *78A*, 306–315.

146. Ge, M.; Xue, L.; Nie, T.; Ma, H.; Zhang, J. The precision structural regulation of PLLA porous scaffold and its influence on the proliferation and differentiation of MC3T3-E1 cells. *J. Biomater. Sci. Polym. Ed.* **2016**, *27*, 1685–1697.

147. Li, L.; Zhou, G.; Wang, Y.; Yang, G.; Ding, S.; Zhou, S. Controlled dual delivery of BMP-2 and dexamethasone by nanoparticle-embedded electrospun nanofibers for the efficient repair of critical-sized rat calvarial defect. *Biomaterials* **2015**, *37*, 218–229.

148. Cho, H.-j.; Perikamana, S.K.M.; Lee, J.-h.; Lee, J.; Lee, K.-M.; Shin, C.S.; Shin, H. Effective immobilization of BMP-2 mediated by polydopamine coating on biodegradable nanofibers for enhanced in vivo bone formation. *ACS Appl. Mater. Interfaces* **2014**, *6*, 11225–11235.

149. Hou, Y.; Xie, W.; Achazi, K.; Cuellar-Camacho, J.L.; Melzig, M.F.; Chen, W.; Haag, R. Injectable degradable PVA microgels prepared by microfluidic technology for controlled osteogenic differentiation of mesenchymal stem cells. *Acta Biomater.* **2018**, *77*, 28–37.

150. Zhou, Q.; Ren, X.; Bischoff, D.; Weisgerber, D.W.; Yamaguchi, D.T.; Miller, T.A.; Harley, B.A.C.; Lee, J.C. Nonmineralized and Mineralized Collagen Scaffolds Induce Differential Osteogenic Signaling Pathways in Human Mesenchymal Stem Cells. *Adv. Healthc. Mater.* **2017**, *6*, 1700641.

151. Cao, H.; Kuboyama, N. A biodegradable porous composite scaffold of PGA/beta-TCP for bone tissue engineering. *Bone* **2010**, *46*, 386–395.

152. Bose, S.; Roy, M.; Bandyopadhyay, A. Recent advances in bone tissue engineering scaffolds. *Trends Biotechnol.* **2012**, *30*, 546–554.

153. Polo-Corrales, L.; Latorre-Esteves, M.; Ramirez-Vick, J. Scaffold Design for Bone Regeneration. *J. Nanosci. Nanotechnol.* **2014**, *14*, 15–56.

154. Wang, J.; Valmikinathan, C.M.; Liu, W.; Laurencin, C.T.; Yu, X. Spiral-structured, nanofibrous, 3D scaffolds for bone tissue engineering. *J. Biomed. Mater. Res. A* **2010**, *93*, 753–762.

155. Li, J.J.; Ebied, M.; Xu, J.; Zreiqat, H. Current Approaches to Bone Tissue Engineering: The Interface between Biology and Engineering. *Adv. Healthc. Mater.* **2018**, *7*, 1701061.

156. Smith, B.D.; Grande, D.A. The current state of scaffolds for musculoskeletal regenerative applications. *Nat. Rev. Rheumatol.* **2015**, *11*, 213–222.

157. Zhang, Y.S.; Yue, K.; Aleman, J.; Moghaddam, K.M.; Bakht, S.M.; Yang, J.; Jia, W.; Dell'Erba, V.; Assawes, P.; Shin, S.R.; et al. 3D Bioprinting for Tissue and Organ Fabrication. *Ann. Biomed. Eng.* **2017**, *45*, 148–163.

158. Li, Y.; Xiao, Y.; Liu, C. The Horizon of Materiobiology: A Perspective on Material-Guided Cell Behaviors and Tissue Engineering. *Chem. Rev.* **2017**, *117*, 4376–4421.

159. Yao, Q.; Sandhurst, E.S.; Liu, Y.; Sun, H. BBP-functionalized biomimetic nanofibrous scaffolds can capture BMP2 and promote osteogenic differentiation. *J. Mater. Chem. B* **2017**, *5*, 5196–5205.

160. Yao, Q.; Liu, Y.; Tao, J.; Baumgarten, K.M.; Sun, H. Hypoxia-Mimicking Nanofibrous Scaffolds Promote Endogenous Bone Regeneration. *ACS Appl. Mater. Interfaces* **2016**, *8*, 32450–32459.

161. Yao, Q.; Liu, Y.; Selvaratnam, B.; Koodali, R.T.; Sun, H. Mesoporous silicate nanoparticles/3D nanofibrous scaffold-mediated dual-drug delivery for bone tissue engineering. *J. Control. Release* **2018**, *279*, 69–78.

162. Lannutti, J.; Reneker, D.; Ma, T.; Tomasko, D.; Farson, D. Electrospinning for tissue engineering scaffolds. *Mater. Sci. Eng. C* **2007**, *27*, 504–509.

163. Keane, T.J.; Badylak, S.F. Biomaterials for tissue engineering applications. *Semin. Pediatr. Surg.* **2014**, *23*, 112–118.

164. Prabhakaran, M.; Venugopal, J.; Chan, C. Surface modified electrospun nanofibrous scaffolds for nerve tissue engineering. *Nanotechnology* **2008**, *19*, 455102.

165. Wang, H.B.; Mullins, M.E.; Cregg, J.M.; Hurtado, A.; Oudega, M.; Trombley, M.T.; Gilbert, R.J. Creation of highly aligned electrospun poly-L-lactic acid fibers for nerve regeneration applications. *J. Neural Eng.* **2009**, *6*, 016001.

166. Dong, Z. Electrospinning and Characterization of Composite Membranes for Biomedical Applications. Ph.D. Thesis, University of Rochester, Rochester, NY, USA, 2015.

167. Salehi, M.; Naseri Nosar, M.; Amani, A.; Azami, M.; Tavakol, S.; Ghanbari, H. Preparation of Pure PLLA, Pure Chitosan, and PLLA/Chitosan Blend Porous Tissue Engineering Scaffolds by Thermally Induced Phase Separation Method and Evaluation of the Corresponding Mechanical and Biological Properties. *Int. J. Polym. Mater. Polym. Biomater.* **2015**, *64*, 675–682.

168. Han, F.; Jia, X.; Dai, D.; Yang, X.; Zhao, J.; Zhao, Y.; Fan, Y.; Yuan, X. Performance of a multilayered small-diameter vascular scaffold dual-loaded with VEGF and PDGF. *Biomaterials* **2013**, *34*, 7302–7313.

169. McKenna, K.A.; Hinds, M.T.; Sarao, R.C.; Wu, P.-C.; Maslen, C.L.; Glanville, R.W.; Babcock, D.; Gregory, K.W. Mechanical property characterization of electrospun recombinant human tropoelastin for vascular graft biomaterials. *Acta Biomater.* **2012**, *8*, 225–233.

170. Tillman, B.W.; Yazdani, S.K.; Lee, S.J.; Geary, R.L.; Atala, A.; Yoo, J.J. The in vivo stability of electrospun polycaprolactone-collagen scaffolds in vascular reconstruction. *Biomaterials* **2009**, *30*, 583–588.

171. Martins, A.F.; Facchi, S.P.; da Câmara, P.C.F.; Camargo, S.E.A.; Camargo, C.H.R.; Popat, K.C.; Kipper, M.J. Novel poly(ε-caprolactone)/amino-functionalized tannin electrospun membranes as scaffolds for tissue engineering. *J. Colloid Interface Sci.* **2018**, *525*, 21–30.

172. Pezzoli, D.; Di Paolo, J.; Kumra, H.; Fois, G.; Candiani, G.; Reinhardt, D.P.; Mantovani, D. Fibronectin promotes elastin deposition, elasticity and mechanical strength in cellularised collagen-based scaffolds. *Biomaterials* **2018**, *180*, 130–142.

173. Kreutz, R.P.; Schmeisser, G.; Maatman, B.; Schaffter, A.; Sinha, A.; von der Lohe, E.; Breall, J.A. Fibrin clot strength measured by thrombelastography and outcomes after percutaneous coronary intervention. *Thromb. Haemost.* **2017**, *117*, 426–428.

174. Gong, T.; Xie, J.; Liao, J.; Zhang, T.; Lin, S.; Lin, Y. Nanomaterials and bone regeneration. *Bone Res.* **2015**, *3*, 15029.

175. Santos, M.I.; Tuzlakoglu, K.; Fuchs, S.; Gomes, M.E.; Peters, K.; Unger, R.E.; Piskin, E.; Reis, R.L.; Kirkpatrick, C.J. Endothelial cell colonization and angiogenic potential of combined nano- and micro-fibrous scaffolds for bone tissue engineering. *Biomaterials* **2008**, *29*, 4306–4313.

176. Porter, J.R.; Ruckh, T.T.; Popat, K.C. Bone tissue engineering: A review in bone biomimetics and drug delivery strategies. *Biotechnol. Prog.* **2009**, *25*, 1539–1560.

177. Chen, S.; Zhu, L.; Wen, W.; Lu, L.; Zhou, C.; Luo, B. Fabrication and Evaluation of 3D Printed Poly(l-lactide) Scaffold Functionalized with Quercetin-Polydopamine for Bone Tissue Engineering. *ACS Biomater. Sci. Eng.* **2019**, *5*, 2506–2518.

178. McMillan, J.; Akiyama, M.; Tanaka, M.; Yamamoto, S.; Goto, M.; Abe, R.; Sawamura, D.; Shimomura, M.; Shimizu, H. Small-Diameter Porous Poly (ε-Caprolactone) Films Enhance Adhesion and Growth of Human Cultured Epidermal Keratinocyte and Dermal Fibroblast Cells. *Tissue Eng.* **2007**, *13*, 789–798.

179. Salem, A.K.; Stevens, R.; Pearson, R.G.; Davies, M.C.; Tendler, S.J.B.; Roberts, C.J.; Williams, P.M.; Shakesheff, K.M. Interactions of 3T3 fibroblasts and endothelial cells with defined pore features. *J. Biomed. Mater. Res.* **2002**, *61*, 212–217.

180. Wang, M.O.; Vorwald, C.E.; Dreher, M.L.; Mott, E.J.; Cheng, M.-H.; Cinar, A.; Mehdizadeh, H.; Somo, S.; Dean, D.; Brey, E.M.; et al. Evaluating 3D-Printed Biomaterials as Scaffolds for Vascularized Bone Tissue Engineering. *Adv. Mater.* **2015**, *27*, 138–144.

181. Tian, H.; Tang, Z.; Zhuang, X.; Chen, X.; Jing, X. Biodegradable synthetic polymers: Preparation, functionalization and biomedical application. *Prog. Polym. Sci.* **2012**, *37*, 237–280.

182. Hsu, S.-h.; Hung, K.-C.; Chen, C.-W. Biodegradable polymer scaffolds. *J. Mater. Chem. B* **2016**, *4*, 7493–7505.
183. Gumede, T.P.; Luyt, A.S.; Müller, A. Review on PCL, PBS, and PCL/PBS blends containing carbon nanotubes. *Express Polym. Lett.* **2018**, *12*, 505–529.
184. Xie, M.; Wang, L.; Guo, B.; Wang, Z.; Chen, Y.E.; Ma, P.X. Ductile electroactive biodegradable hyperbranched polylactide copolymers enhancing myoblast differentiation. *Biomaterials* **2015**, *71*, 158–167.
185. Zhao, J.; Zhao, X.; Guo, B.; Ma, P.X. Multifunctional Interpenetrating Polymer Network Hydrogels Based on Methacrylated Alginate for the Delivery of Small Molecule Drugs and Sustained Release of Protein. *Biomacromolecules* **2014**, *15*, 3246–3252.
186. Bao, G. Biofabrication in Tissue Engineering. In *Racing for the Surface*; Moriarty, T., Webster, T., Xing, M., Eds.; Springer, Cham, Switzerland, 2020; pp. 289–312.
187. Kowalski, P.S.; Bhattacharya, C.; Afewerki, S.; Langer, R. Smart Biomaterials: Recent Advances and Future Directions. *ACS Biomater. Sci. Eng.* **2018**, *4*, 3809–3817.
188. Murphy, C.M.; Haugh, M.G.; O'Brien, F.J. The effect of mean pore size on cell attachment, proliferation and migration in collagen–glycosaminoglycan scaffolds for bone tissue engineering. *Biomaterials* **2010**, *31*, 461–466.
189. Pawelec, K.M.; Best, S.M.; Cameron, R.E. Collagen: A network for regenerative medicine. *J. Mater. Chem. B* **2016**, *4*, 6484–6496.
190. LogithKumar, R.; KeshavNarayan, A.; Dhivya, S.; Chawla, A.; Saravanan, S.; Selvamurugan, N. A review of chitosan and its derivatives in bone tissue engineering. *Carbohydr. Polym.* **2016**, *151*, 172–188.
191. Lutolf, M.P.; Hubbell, J.A. Synthetic biomaterials as instructive extracellular microenvironments for morphogenesis in tissue engineering. *Nat. Biotechnol.* **2005**, *23*, 47–55.
192. Jiang, T.; Abdel-Fattah, W.I.; Laurencin, C.T. In vitro evaluation of chitosan/poly(lactic acid-glycolic acid) sintered microsphere scaffolds for bone tissue engineering. *Biomaterials* **2006**, *27*, 4894–4903.
193. Nguyen, T.T.T.; Chung, O.H.; Park, J.S. Coaxial electrospun poly(lactic acid)/chitosan (core/shell) composite nanofibers and their antibacterial activity. *Carbohydr. Polym.* **2011**, *86*, 1799–1806.
194. Xu, T.; Yang, H.; Yang, D.; Yu, Z.-Z. Polylactic Acid Nanofiber Scaffold Decorated with Chitosan Islandlike Topography for Bone Tissue Engineering. *ACS Appl. Mater. Interfaces* **2017**, *9*, 21094–21104.
195. Mallick, S.P.; Pal, K.; Rastogi, A.; Srivastava, P. Evaluation of poly(L-lactide) and chitosan composite scaffolds for cartilage tissue regeneration. *Des. Monomers Polym.* **2016**, *19*, 271–282.
196. Ruiter, G.; Malessy, M.; Yaszemski, M.; Windebank, A.; Spinner, R. Designing ideal conduits for peripheral nerve repair. *Neurosurg. Focus* **2009**, *26*, E5.
197. Prabaharan, M.; Rodriguez-Perez, M.A.; de Saja, J.A.; Mano, J.F. Preparation and characterization of poly(L-lactic acid)-chitosan hybrid scaffolds with drug release capability. *J. Biomed. Mater. Res. B Appl. Biomater.* **2007**, *81B*, 427–434.

198. Liu, M.; Yang, Y.; Zhu, T.; Liu, Z. Chemical modification of single-walled carbon nanotubes with peroxytrifluoroacetic acid. *Carbon* **2005**, *43*, 1470–1478.

199. Einhorn, T.A.; Lee, C.A. Bone Regeneration: New Findings and Potential Clinical Applications. *J. Am. Acad. Orthop. Surg.* **2001**, *9*, 157–165.

200. Keramaris, N.C.; Calori, G.M.; Nikolaou, V.S.; Schemitsch, E.H.; Giannoudis, P.V. Fracture vascularity and bone healing: A systematic review of the role of VEGF. *Injury* **2008**, *39*, S45–S57.

201. Gómez-Barrena, E.; Rosset, P.; Lozano, D.; Stanovici, J.; Ermthaller, C.; Gerbhard, F. Bone fracture healing: Cell therapy in delayed unions and nonunions. *Bone* **2015**, *70*, 93–101.

202. Winkler, T.; Sass, F.A.; Duda, G.N.; Schmidt-Bleek, K. A review of biomaterials in bone defect healing, remaining shortcomings and future opportunities for bone tissue engineering. *Bone Jt. Res.* **2018**, *7*, 232–243.

203. Kokubo, T.; Kim, H.-M.; Kawashita, M. Novel bioactive materials with different mechanical properties. *Biomaterials* **2003**, *24*, 2161–2175.

204. Kalita, S.J.; Bhardwaj, A.; Bhatt, H.A. Nanocrystalline calcium phosphate ceramics in biomedical engineering. *Mater. Sci. Eng. C* **2007**, *27*, 441–449.

205. Navarro, M.; Michiardi, A.; Castaño, O.; Planell, J.A. Biomaterials in orthopaedics. *J. R. Soc. Interface* **2008**, *5*, 1137–1158.

206. Black, C.R.M.; Goriainov, V.; Gibbs, D.; Kanczler, J.; Tare, R.S.; Oreffo, R.O.C. Bone Tissue Engineering. *Curr. Mol. Biol. Rep.* **2015**, *1*, 132–140.

207. Kokubo, T. *Bioceramics and Their Clinical Applications*, 1st ed.; Elsevier: Amsterdam, The Netherlands, 2008.

208. Kim, H.-W.; Knowles, J.C.; Kim, H.-E. Hydroxyapatite/poly(ε-caprolactone) composite coatings on hydroxyapatite porous bone scaffold for drug delivery. *Biomaterials* **2004**, *25*, 1279–1287.

209. Sharma, C.; Dinda, A.K.; Potdar, P.D.; Chou, C.-F.; Mishra, N.C. Fabrication and characterization of novel nano-biocomposite scaffold of chitosan–gelatin–alginate–hydroxyapatite for bone tissue engineering. *Mater. Sci. Eng. C* **2016**, *64*, 416–427.

210. Allo, B.A.; Costa, D.O.; Dixon, S.J.; Mequanint, K.; Rizkalla, A.S. Bioactive and Biodegradable Nanocomposites and Hybrid Biomaterials for Bone Regeneration. *J. Funct. Biomater.* **2012**, *3*, 432–463.

211. Goreham, R.V.; Mierczynska, A.; Smith, L.E.; Sedev, R.; Vasilev, K. Small surface nanotopography encourages fibroblast and osteoblast cell adhesion. *RSC Adv.* **2013**, *3*, 10309–10317.

212. Health and Nutrition. In *Statistical Abstract of the United States*; US Census Bureau: Washington, DC, USA, 2006.

213. Brydone, A.; Meek, D.; Maclaine, S. Bone grafting, orthopaedic biomaterials, and the clinical need of bone engineering. *Proc. Inst. Mech. Eng. Part H* **2010**, *224*, 1329–1343.

214. Gao, C.; Peng, S.; Feng, P.; Shuai, C. Bone biomaterials and interactions with stem cells. *Bone. Res.* **2017**, *5*, 17059.

215. Liu, X.; Ma, P.X. Phase separation, pore structure, and properties of nanofibrous gelatin scaffolds. *Biomaterials* **2009**, *30*, 4094–4103.

216. Wei, G.; Ma, P.X. Structure and properties of nano-hydroxyapatite/polymer composite scaffolds for bone tissue engineering. *Biomaterials* **2004**, *25*, 4749–4757.

217. Wang, X.; Wu, X.; Xing, H.; Zhang, G.; Shi, Q.; E, L.; Liu, N.; Yang, T.; Wang, D.; Qi, F.; et al. Porous Nanohydroxyapatite/Collagen Scaffolds Loading Insulin PLGA Particles for Restoration of Critical Size Bone Defect. *ACS Appl. Mater. Interfaces* **2017**, *9*, 11380–11391.

218. Wang, X.; Xing, H.; Zhang, G.; Wu, X.; Zou, X.; Feng, L.; Wang, D.; Li, M.; Zhao, J.; Du, J.; et al. Restoration of a Critical Mandibular Bone Defect Using Human Alveolar Bone-Derived Stem Cells and Porous Nano-HA/Collagen/PLA Scaffold. *Stem Cells Int.* **2016**, *2016*, 8741641.

219. Croisier, F.; Jérôme, C. Chitosan-based biomaterials for tissue engineering. *Eur. Polym. J.* **2013**, *49*, 780–792.

220. Maji, K.; Dasgupta, S.; Pramanik, K.; Bissoyi, A. Preparation and Evaluation of Gelatin-Chitosan-Nanobioglass 3D Porous Scaffold for Bone Tissue Engineering. *Int. J. Biomater.* **2016**, *2016*, 9825659.

221. Tong, S.; Xu, D.-P.; Liu, Z.-M.; Du, Y.; Wang, X.-K. Synthesis of and in vitro and in vivo evaluation of a novel TGF-β1-SF-CS three-dimensional scaffold for bone tissue engineering. *Int. J. Mol. Med.* **2016**, *38*, 367–380.

222. Tong, S.; Xu, D.-p.; Liu, Z.-m.; Du, Y.; Wang, X.-k. Synthesis of the New-Type Vascular Endothelial Growth Factor–Silk Fibroin–Chitosan Three-Dimensional Scaffolds for Bone Tissue Engineering and In Vitro Evaluation. *J. Craniofac. Surg.* **2016**, *27*, 509–515.

223. Reves, B.T.; Bumgardner, J.D.; Cole, J.A.; Yang, Y.; Haggard, W.O. Lyophilization to improve drug delivery for chitosan-calcium phosphate bone scaffold construct: A preliminary investigation. *J. Biomed. Mater. Res. B Appl. Biomater.* **2009**, *90B*, 1–10.

224. Sabir, M.I.; Xu, X.; Li, L. A review on biodegradable polymeric materials for bone tissue engineering applications. *J. Mater. Sci.* **2009**, *44*, 5713–5724.

225. Rahman, M.S.; Rana, M.; Spitzhorn, L.-S.; Akhtar, N.; Hasan, M.; Choudhury, N.; Fehm, T.; Czernuszka, J.; Adjaye, J.; Asaduzzaman, S. Fabrication of biocompatible porous scaffolds based on hydroxyapatite/collagen/chitosan composite for restoration of defected maxillofacial mandible bone. *Prog. Biomater.* **2019**, *8*, 137–154.

226. Hunziker, E.B. Articular cartilage repair: Basic science and clinical progress. A review of the current status and prospects. *Osteoarthr. Cartil.* **2002**, *10*, 432–463.

227. Seo, S.-J.; Mahapatra, C.; Singh, R.K.; Knowles, J.C.; Kim, H.-W. Strategies for osteochondral repair: Focus on scaffolds. *J. Tissue Eng.* **2014**, *5*, 2041731414541850.

228. Singh, Y.P.; Moses, J.C.; Bhunia, B.K.; Nandi, S.K.; Mandal, B.B. Hierarchically structured seamless silk scaffolds for osteochondral interface tissue engineering. *J. Mater. Chem. B* **2018**, *6*, 5671–5688.

229. Slepicka, P.; Kasalkova, N.S.; Siegel, J.; Kolska, Z.; Bacakova, L.; Svorcik, V. Nano-structured and functionalized surfaces for cytocompatibility improvement and bactericidal action. *Biotechnol. Adv.* **2015**, *33*, 1120–1129.

230. Wu, S.; Liu, X.; Yeung, K.W.K.; Liu, C.; Yang, X. Biomimetic porous scaffolds for bone tissue engineering. *Mater. Sci. Eng. R. Rep.* **2014**, *80*, 1–36.

231. Krishnan, V.; Lakshmi, T. Bioglass: A novel biocompatible innovation. *J. Adv. Pharm. Technol. Res.* **2013**, *4*, 78–83.

232. Jones, J.R.; Brauer, D.S.; Hupa, L.; Greenspan, D.C. Bioglass and Bioactive Glasses and Their Impact on Healthcare. *Int. J. Appl. Glass Sci.* **2016**, *7*, 423–434.

233. Morsi, M.A.; Hezma, A.E.M. Effect of iron doped hydroxyapatite nanoparticles on the structural, morphological, mechanical and magnetic properties of polylactic acid polymer. *J. Mater. Res. Technol.* **2019**, *8*, 2098–2106.

234. Gloria, A.; Russo, T.; D'Amora, U.; Zeppetelli, S.; D'Alessandro, T.; Sandri, M.; Bañobre-López, M.; Piñeiro-Redondo, Y.; Uhlarz, M.; Tampieri, A.; et al. Magnetic poly(ε-caprolactone)/iron-doped hydroxyapatite nanocomposite substrates for advanced bone tissue engineering. *J. R. Soc. Interface* **2013**, *10*, 20120833.

235. Morselli, D.; Bondioli, F.; Sangermano, M.; Messori, M. Epoxy networks reinforced with TiO2 generated by nonhydrolytic sol–gel process: A comparison between in situ and ex situ syntheses to obtain filled polymers. *Polym. Eng. Sci.* **2015**, *55*, 1689–1697.

236. Liang, H.-Q.; Wu, Q.-Y.; Wan, L.-S.; Huang, X.-J.; Xu, Z.-K. Thermally induced phase separation followed by in situ sol–gel process: A novel method for PVDF/SiO2 hybrid membranes. *J. Membr. Sci.* **2014**, *465*, 56–67.

237. Rokkanen, P.U.; Böstman, O.; Hirvensalo, E.; Mäkelä, E.A.; Partio, E.K.; Pätiälä, H.; Vainionpää, S.; Kimmo, V.; Törmälä, P. Bioabsorbable fixation in orthopaedic surgery and traumatology. *Biomaterials* **2000**, *21*, 2607–2613.

238. Stevens, M.M. Biomaterials for bone tissue engineering. *Mater. Today* **2008**, *11*, 18–25.

239. Yin, Y.; Zhao, L.; Jiang, X.; Wang, H.; Gao, W. Poly(lactic acid)-based biocomposites reinforced with modified cellulose nanocrystals. *Cellulose* **2017**, *24*, 4773–4784.

240. Zhou, C.; Shi, Q.; Guo, W.; Terrell, L.; Qureshi, A.T.; Hayes, D.J.; Wu, Q. Electrospun Bio-Nanocomposite Scaffolds for Bone Tissue Engineering by Cellulose Nanocrystals Reinforcing Maleic Anhydride Grafted PLA. *ACS Appl. Mater. Interfaces* **2013**, *5*, 3847–3854.

241. Meesorn, W.; Shirole, A.; Vanhecke, D.; de Espinosa, L.M.; Weder, C. A Simple and Versatile Strategy To Improve the Mechanical Properties of Polymer Nanocomposites with Cellulose Nanocrystals. *Macromolecules* **2017**, *50*, 2364–2374.

242. Luo, W.; Cheng, L.; Yuan, C.; Wu, Z.; Yuan, G.; Hou, M.; Chen, J.Y.; Luo, C.; Li, W. Preparation, characterization and evaluation of cellulose nanocrystal/poly(lactic acid) in situ nanocomposite scaffolds for tissue engineering. *Int. J. Biol. Macromol.* **2019**, *134*, 469–479.

243. Díaz, E.; Aresti, J.; León, J. Evaluation of physicochemical and mechanical properties with the in vitro degradation of PCL/nHA/MWCNT composite scaffolds. *J. Reinf. Plast. Compos.* **2020**, 0731684420943304.

244. Díaz, E.; Martín, J.; León, J. Carbon nanotube reinforced poly(l-lactide) scaffolds: In vitro degradation, conductivity, mechanical and thermal properties. *Compos. Interfaces* **2020**, 1–15.

245. Iijima, S. Helical microtubules of graphitic carbon. *Nature* **1991**, *354*, 56–58.

246. Perkins, B.L.; Naderi, N. Carbon Nanostructures in Bone Tissue Engineering. *Open Orthop. J.* **2016**, *10*, 877–899.

247. Pei, B.; Wang, W.; Dunne, N.; Li, X. Applications of Carbon Nanotubes in Bone Tissue Regeneration and Engineering: Superiority, Concerns, Current Advancements, and Prospects. *Nanomaterials* **2019**, *9*, 1501.

248. Ma, P.-C.; Siddiqui, N.A.; Marom, G.; Kim, J.-K. Dispersion and functionalization of carbon nanotubes for polymer-based nanocomposites: A review. *Compos. Part A Appl. Sci. Manuf.* **2010**, *41*, 1345–1367.

249. Conlan, R.S.; Pisano, S.; Oliveira, M.I.; Ferrari, M.; Mendes Pinto, I. Exosomes as Reconfigurable Therapeutic Systems. *Trends Mol. Med.* **2017**, *23*, 636–650.

250. Uchida, M.; Kim, H.-M.; Kokubo, T.; Fujibayashi, S.; Nakamura, T. Structural dependence of apatite formation on titania gels in a simulated body fluid. *J. Biomed. Mater. Res., A* **2003**, *64A*, 164-170.

251. Oberdörster, G. Pulmonary effects of inhaled ultrafine particles. *Int. Arch. Occup. Environ. Health* **2000**, *74*, 1–8.

252. Treccani, L.; Yvonne Klein, T.; Meder, F.; Pardun, K.; Rezwan, K. Functionalized ceramics for biomedical, biotechnological and environmental applications. *Acta Biomater.* **2013**, *9*, 7115–7150.

253. Alford, A.I.; Kozloff, K.M.; Hankenson, K.D. Extracellular matrix networks in bone remodeling. *Int. J. Biochem. Cell Biol.* **2015**, *65*, 20–31.

254. Gaffney, L.; Wrona, E.A.; Freytes, D.O. Potential Synergistic Effects of Stem Cells and Extracellular Matrix Scaffolds. *ACS Biomater. Sci. Eng.* **2018**, *4*, 1208–1222.

255. Lin, W.; Chen, M.; Qu, T.; Li, J.; Man, Y. Three-dimensional electrospun nanofibrous scaffolds for bone tissue engineering. *J. Biomed. Mater. Res. B Appl. Biomater.* **2020**, *108*, 1311–1321.

256. Llorens, E.; Ibañez, H.; del Valle, L.J.; Puiggalí, J. Biocompatibility and drug release behavior of scaffolds prepared by coaxial electrospinning of poly(butylene succinate) and polyethylene glycol. *Mater. Sci. Eng. C* **2015**, *49*, 472–484.

257. Llorens, E.; Calderón, S.; del Valle, L.J.; Puiggalí, J. Polybiguanide (PHMB) loaded in PLA scaffolds displaying high hydrophobic, biocompatibility and antibacterial properties. *Mater. Sci. Eng. C* **2015**, *50*, 74–84.

258. Llorens, E.; del Valle, L.J.; Ferrán, R.; Rodríguez-Galán, A.; Puiggalí, J. Scaffolds with tuneable hydrophilicity from electrospun microfibers of polylactide and poly(ethylene glycol) mixtures: Morphology, drug release behavior, and biocompatibility. *J. Polym. Res.* **2014**, *21*, 360.

259. Yao, T.; Wieringa, P.A.; Chen, H.; Amit, C.; Samal, P.; Giselbrecht, S.; Baker, M.B.; Moroni, L. Fabrication of a self-assembled honeycomb nanofibrous scaffold to guide endothelial morphogenesis. *Biofabrication* **2020**, *12*, 045001.

260. Prasopthum, A.; Shakesheff, K.M.; Yang, J. Direct three-dimensional printing of polymeric scaffolds with nanofibrous topography. *Biofabrication* **2018**, *10*, 025002.

261. Liu, X.; Chen, W.; Gustafson, C.T.; Miller Ii, A.L.; Waletzki, B.E.; Yaszemski, M.J.; Lu, L. Tunable tissue scaffolds fabricated by in situ crosslink in phase separation system. *RSC Adv.* **2015**, *5*, 100824–100833.

262. Ma, C.; Liu, X. Formation of Nanofibrous Matrices, Three-Dimensional Scaffolds, and Microspheres: From Theory to Practice. *Tissue. Eng. Part C Methods* **2016**, *23*, 50–59.

263. Wade, R.J.; Burdick, J.A. Advances in nanofibrous scaffolds for biomedical applications: From electrospinning to self-assembly. *Nano Today* **2014**, *9*, 722–742.

264. Zeng, C.-g.; Xiong, Y.; Xie, G.; Dong, P.; Quan, D. Fabrication and Evaluation of PLLA Multichannel Conduits with Nanofibrous Microstructure for the Differentiation of NSCs In Vitro. *Tissue Eng. Part A* **2013**, *20*, 1038–1048.

265. Liu, X.; Ma, P.X. The nanofibrous architecture of poly(l-lactic acid)-based functional copolymers. *Biomaterials* **2010**, *31*, 259–269.

266. Zhang, Z.; Gupte, M.J.; Jin, X.; Ma, P.X. Injectable Peptide Decorated Functional Nanofibrous Hollow Microspheres to Direct Stem Cell Differentiation and Tissue Regeneration. *Adv. Funct. Mater.* **2015**, *25*, 350–360.

267. Du, Y.; Chen, X.; Hag Koh, Y.; Lei, B. Facilely fabricating PCL nanofibrous scaffolds with hierarchical pore structure for tissue engineering. *Mater. Lett.* **2014**, *122*, 62–65.

268. Liu, S.; He, Z.; Xu, G.; Xiao, X. Fabrication of polycaprolactone nanofibrous scaffolds by facile phase separation approach. *Mater. Sci. Eng. C* **2014**, *44*, 201–208.

269. Wang, M.; Ma, L.; Li, D.; Jiang, P.; Gao, C. Preparation of polycaprolactone microspheres-aggregated scaffold with ultra big pores and fuzzy sphere surface by a one-step phase separation method. *J. Biomed. Mater. Res. A* **2013**, *101*, 3219–3227.

270. Yang, X.B.; Roach, H.I.; Clarke, N.M.P.; Howdle, S.M.; Quirk, R.; Shakesheff, K.M.; Oreffo, R.O.C. Human osteoprogenitor growth and differentiation on synthetic biodegradable structures after surface modification. *Bone* **2001**, *29*, 523–531.

271. Matsui, T.; Arima, Y.; Takemoto, N.; Iwata, H. Cell patterning on polylactic acid through surface-tethered oligonucleotides. *Acta Biomater.* **2015**, *13*, 32–41.

272. Fu, Q.; Rahaman, M.N.; Bal, B.S.; Brown, R.F. Preparation and in vitro evaluation of bioactive glass (13–93) scaffolds with oriented microstructures for repair and regeneration of load-bearing bones. *J. Biomed. Mater. Res. Part A* **2010**, *93A*, 1380–1390.

273. Li, L.; Zhao, M.; Li, J.; Zuo, Y.; Zou, Q.; Li, Y. Preparation and cell infiltration of lotus-type porous nano-hydroxyapatite/polyurethane scaffold for bone tissue regeneration. *Mater. Lett.* **2015**, *149*, 25–28.

274. Shen, H.; Niu, Y.; Hu, X.; Yang, F.; Wang, S.; Wu, D. A biomimetic 3D microtubule-orientated poly(lactide-co-glycolide) scaffold with interconnected pores for tissue engineering. *J. Mater. Chem. B* **2015**, *3*, 4417–4425.

275. Lakshmanan, R.; Krishnan, U.M.; Sethuraman, S. Living cardiac patch: The elixir for cardiac regeneration. *Expert Opin. Biol. Ther.* **2012**, *12*, 1623–1640.

276. Xu, B.; Li, Y.; Fang, X.; Thouas, G.A.; Cook, W.D.; Newgreen, D.F.; Chen, Q. Mechanically tissue-like elastomeric polymers and their potential as a vehicle to deliver functional cardiomyocytes. *J. Mech. Behav. Biomed. Mater.* **2013**, *28*, 354–365.

277. Jia, S.; Liu, L.; Pan, W.; Meng, G.; Duan, C.; Zhang, L.; Xiong, Z.; Liu, J. Oriented cartilage extracellular matrix-derived scaffold for cartilage tissue engineering. *J. Biosci. Bioeng.* **2012**, *113*, 647–653.

278. Zhang, Y.; Yang, F.; Liu, K.; Shen, H.; Zhu, Y.; Zhang, W.; Liu, W.; Wang, S.; Cao, Y.; Zhou, G. The impact of PLGA scaffold orientation on in vitro cartilage regeneration. *Biomaterials* **2012**, *33*, 2926–2935.

279. Chen, P.; Tao, J.; Zhu, S.; Cai, Y.; Mao, Q.; Yu, D.; Dai, J.; Ouyang, H. Radially oriented collagen scaffold with SDF-1 promotes osteochondral repair by facilitating cell homing. *Biomaterials* **2015**, *39*, 114–123.

280. Tanaka, T.; Lloyd, D.R. Formation of poly(l-lactic acid) microfiltration membranes via thermally induced phase separation. *J. Membr. Sci.* **2004**, *238*, 65–73.

281. Kanno, T.; Uyama, H. Unique leafy morphology of poly(lactic acid) monoliths controlled via novel phase separation technology. *RSC Adv.* **2017**, *7*, 33726–33732.

Chapter 3

Poly(hydroxybutyrate-*co*-hydroxyvalerate) Porous Matrices from Thermally-Induced Phase Separation

Abstract

Thermally-induced phase separation followed by freeze drying has been used to prepare biodegradable and biocompatible scaffolds with interconnected 3D microporous structures from poly(hydroxybutyrate-*co*-hydroxyvalerate) (PHBV) copolymers containing 5 and 12 wt% of 3-hydroxyvalerate (HV). Solutions of PHBV in 1,4-dioxane, underwent phase separation by cooling under two different thermal gradients (at −25 °C and −5 °C). The cloud point and crystallization temperature of the polymer solutions were determined by turbidimetry and differential scanning calorimetry, respectively. Parameters affecting the phase separation mechanism such as variation of both the cooling process and the composition of the PHBV copolymer were investigated. Afterwards, the influence of these variables on the morphology of the porous structure and the final mechanical properties (i.e., rigidity and damping) was evaluated via scanning electron microscopy and dynamic mechanical thermal analysis, respectively. While the morphology of the scaffolds was considerably affected by polymer crystallization upon a slow cooling rate, the effect of solvent crystallization was more evident at either high hydroxyvalerate content (i.e., 12 wt% of HV) or high cooling rate. The decrease in the HV content gave rise to scaffolds with greater stiffness because of their higher degree of crystallinity, being also noticeable the greater consistency of the structure attained when the cooling rate was higher. Scaffolds were fully biocompatible supports for cell adhesion and proliferation in 3D cultures and show potential application as a tool for tissue regeneration.

3.1. Introduction

Numerous applications of natural-origin polymers in the biomedical field (e.g., drug and cell carriers) are focusing the attention of researchers [1]. Polyhydroxyalkanoates (PHAs) are a large sub-branch of natural polyesters that can be extracted from bacteria or genetically modified plants. The poly(3-hydroxybutyrate) (PHB) homopolymer and the poly(3-hydroxybutyrate-*co*-3-hydroxyvalerate) (PHBV) copolymer are the members of the PHAs family with the highest applications. The main problem of PHB concerns to its high brittleness and crystallinity and therefore copolymers incorporating small percentages of 3-hydroxyvalerate (HV) units (i.e., PHBV copolymers) are being commercialized since they can also be easily produced by bacteria (e.g., *Escherichia coli*, *Paracoccus denitrificans*, *Ralstonia eutropha*) as storage products.

Due to properties such as biocompatibility, biodegradability, non-toxicity, and piezoelectricity, the use of PHBV copolymers in a variety of medical fields including surgical sutures, wound dressings, controlled release, and tissue engineering has been reported [2–6]. Chemical and mechanical properties of PHBV copolymers can logically be controlled in function of the HV content. Despite relatively high crystallinity levels can be achieved at various HV ratios, it is obvious that the increase of the comonomer HV content lead to polymers with lower degrees of crystallinity and melting temperatures. In addition, besides exhibiting full degradability in aqueous environments and producing non-toxic by-products, the degradation rate of copolymers can be tuned by varying the HV content [7–9].

The thermally-induced phase separation (TIPS) technique has extensively been used in non-biomedical fields for fabricating synthetic membranes. Applications in the biomedical sector are also habitual as for example for the development of drug delivery systems. Specifically, the methodology has been employed to prepare microspheres incorporating pharmaceutical and biological agents [10,11]. Today, TIPS is a common technique to fabricate porous scaffolds for tissue engineering applications [12–15]. This method is based upon thermodynamic demixing of a homogeneous polymer solution into polymer-rich and polymer-lean (solvent-rich) phases [16]. The solvent in the polymer-lean phase can subsequently be eliminated by extraction, evaporation, or sublimation [17], leaving behind a highly porous polymer network [18,19]. TIPS experimentally allows controlling the final structure of the scaffold in terms of morphology, average pore size and degree of interconnection [20]. The final structure and pore morphology of the phase-separated polymer matrices are greatly dependent on the combination of the selected polymer and solvent system, the polymer concentration, the phase-separation temperature and the temperature gradient applied to the polymer solution [21].

Various biodegradable polymers have been considered to fabricate three-dimensional scaffolds through the TIPS technique and investigated for tissue regeneration applications [22]. In this regard, the application of the phase separation method for scaffolding purposes has been reported for several biodegradable polyesters, especially polylactide (PLA) and poly(lactide-*co*-glycolide) (PLGA). Depending on the polymer system and phase separation conditions, these 3D polyester scaffolds can structurally be classified as solid-walled isotropic and anisotropic (like microtubular), fibrous, nanofibrous, and platelet-like architectures [23–27]. Moreover, the different types of TIPS techniques—i.e., solid–liquid [23–25], liquid–liquid [26,27], and crystallization-induced phase separations [27]—have been used for creating different micro- and nano-structured polymer constructs. Organic solvents with high freezing points like 1,4 dioxane or benzene and others with low freezing points like THF, DMF, and pyridine have successfully been used to fabricate scaffolds by solid–liquid and liquid–liquid phase separations, respectively [23–27].

The phase separation procedure has also been applied to different scaffolding materials based on polyhydroxyalkanoates. Thus, the fabrication of nanofibrous and microtubular architectures have mainly been reported for systems based on PHB, poly(3-hydroxybutyrate-*co*-3-hydroxyhexanoate) (PHBHx) and poly(3-hydroxybutyrate-*co*-4-hydroxybutyrate) (P(3HB-4HB)) [28,29]. Nevertheless, the fabrication of phase-separated porous scaffolds made of PHBV copolymers, has received less attention. Furthermore, scarce studies can be found evaluating TIPS-obtained PHBV scaffolds in terms of pore morphology and paying attention to the copolymer properties and the phase separation conditions.

In the present study, the potential of PHBV copolymers and TIPS technique to develop interconnected 3D networks with solid-wall and platelet-like structures has been appraised. We have specifically addressed how altering the quenching temperatures and copolymer characteristics have a considerable effect on the phase separation process and the scaffold properties. The disparities observed in the morphological features and mechanical properties of resulting scaffolds were discussed with respect to thermodynamic and kinetic conditions of phase separation.

1,4-dioxane is used as a solvent for a variety of practical applications and can be found for example at minimum levels in cosmetics and personal care products. Some toxicologic effects of dioxane have been recognized, being consequently a potential health concern that received the attention of FDA. Despite no specific law requirements have been formulated, manufacturers have been encouraged to remove dioxane from technological processes [30]. Therefore, we have paid also special attention, through biocompatibility tests, to ensure a complete solvent removal in the final processed scaffolds.

3.2. Materials and Methods

3.2.1. Materials and Scaffold Preparation

Poly(3-hydroxybutyrate-*co*-3-hydroxyvalerate)s containing 5 and 12 molar percentages of 3-hydroxyvalerate were purchased from Sigma-Aldrich (St. Louis, MO, USA) and were used for fabrication of polymeric scaffolds. The molecular weights of PHBV(5%HV) and PHBV(12%HV) were 320 kDa and 240 kDa and their corresponding melting points were 165 °C and 161 °C, respectively. 1,4-dioxane was used as solvent and was supplied by Acros Organics ((Morris Plains, NJ, USA), with linear formula of $C_4H_8O_2$, molecular weight of 88.11 g/mol, density of 1.033 g/mL, melting point of 12 °C, and purity of 99.5%. The polymers and the solvent were used without further purification.

For preparing polymeric foams, the corresponding polymer solutions were cooled until phase separation occurred. Subsequently, porous structures were achieved after removing the solvent. Specifically, both PHBV(5%HV) and PHBV(12%HV) copolymers were dissolved at a concentration of 2% (*w*/*v*) in 1,4-dioxane by heating and stirring. When the temperature reached about 70 °C, a clear homogenous polymer solution was attained. The solutions (0.4 mL) were poured into a cylinder-shaped glass container with a diameter of 14 mm and height of 40 mm and then sealed. The samples first were cooled spontaneously to the room temperature and then immediately incorporated to the corresponding cooling devices preset on −5 °C or −25 °C. In this process, phase separation occurred during cooling. Note that this process occurred under two different thermal gradients, that is, from room temperature to −5 °C and −25 °C. Afterwards, samples were kept at rest for 24 h at the selected final temperature. Finally, the samples were lyophilized (Gamma 2-16 LSC, Martin Christ, Osterode am Harz, Germany) for 40 h. The resulting porous scaffolds were dried in a vacuum oven at room temperature to reach a constant weight.

3.2.2. Cloud Point and Cooling Rate Determination and DSC Analysis of Polymer Solutions

The cloud point of polymer solutions was evaluated by visual turbidimetry. In order to predict the location of binodal curve at relatively low concentrations of the PHBV-dioxane phase diagram, the cloud points of 1–10% (*w*/*v*) solutions were determined. The solutions were poured into transparent sealed glass containers and then transferred to a refrigerated incubator to reach equilibrium conditions through a controllable slow cooling. The incubator was preset at 35 °C and programmed to be cooled at a rate of 0.033 °C/min (i.e., 1 °C each 30 min). The temperature at which the clear solution became turbid was recognized as the cloud point. At least three independent turbidimetric assays per sample were performed, being the results averaged and the standard deviations obtained.

Cooling rate of the different polymer solutions was determined using a digital thermometer ((ESCORT 20 T/C, EIC, Taipei, Taiwan) inserted into the center of the tube containing the respective solutions. The thermometer was connected to the computer and plotted the cooling diagrams (temperature versus time) while the samples were cooling from room temperature to −5 °C or −25 °C. Cooling rates were determined from the slopes of the corresponding curves. In fact, three experiments were performed for each condition and the values of the resulting slopes averaged and taken as the cooling rates to be considered in the subsequent differential scanning calorimetry (DSC) analyses. In this way, cooling rates of 2 °C/min and 6 °C/min were obtained, when solutions were cooled from room temperature to −5 °C and −25 °C, respectively. The prepared samples are summarized in Table 1, with abbreviations according to the HV content and the cooling rates.

Table 1. Sample designation

Sample	**Cooling rate (°C/min)**	**Abbreviation**
Pure dioxane	2	DXN-R2
Pure dioxane	6	DXN-R6
PHBV(5%HV)-dioxane	2	HBV5-R2
PHBV(5%HV)-dioxane	6	HBV5-R6
PHBV(12%HV)-dioxane	2	HBV12-R2
PHBV(12%HV)-dioxane	6	HBV12-R6

In the next step, a differential scanning calorimeter ((200 F3, NETZSCH DSC, Selb, Germany) was used to evaluate the crystallization behavior of pure solvent and the polymer solutions. The DSC analyses were carried out by cooling from +40 °C to −50

°C at rates of 2 °C/min and 6 °C/min. The temperature, at which an exothermic peak appeared throughout cooling, was taken into account as the solvent crystallization temperature.

3.2.3. SEM and DMTA Analyses of Polymer Scaffolds

A scanning electron microscope (SEM) (VEGA II, TESCAN, Brno, Czech Republic) was used to study the porous structure of PHBV scaffolds. The microstructural features were evaluated from the outer surface and the transverse cross-section of the scaffolds. These cross-sections were obtained by soaking the scaffolds in liquid nitrogen for 2 h before to split them in two parts. Prior to microscopy, the samples were sputter-coated with a thin layer of gold by using a Mitec K950 Sputter Coater (Quorum Technologies Ltd., Ashford, UK).

A dynamic mechanical thermal analyzer (DMTA) (TRITEC DMA 2000, DMA-TRITON, Lincolnshire, UK) was used to estimate the viscoelastic behavior of PHBV scaffolds under dynamic loading conditions (ASTM E1640-04). Polymeric scaffolds (2 cm × 0.7 cm × 0.2 cm) were subjected to cyclic tensile strains of 0.008 mm with frequency of 1 Hz, while temperature was increased from −50 °C to 180 °C at a rate of 5 °C/min. The stress response of samples was recorded via in-phase modulus (E'), lag modulus (E''), and loss tangent (E''/E') versus temperature.

3.2.4. Assays of Cell Adhesion and Proliferation

MDCK cells (with epithelial-like morphology and derived from Madin–Darby Canine Kidney, ATCC) and NRK cells (with epithelial-like morphology and derived from the kidney of the *Rattus norvegicus*, ATCC) were employed. Both cell lines grow adherently, and were cultured in Dulbecco's modified Eagle's medium (DMEM with 4500 mg/L of glucose, 110 mg/L of sodium pyruvate and 2 mM of l-glutamine) supplemented with 10% fetal bovine serum (FBS), 50 U/mL penicillin, 50 mg/mL streptomycin, and l-glutamine 2 mM at 37 °C in a 10% humidified atmosphere of 5% CO_2 and 95% air. Culture media were changed every two days. For sub-culture, cell monolayers were rinsed with PBS and detached by incubating them with 0.25% trypsin/EDTA for 2–5 min at 37 °C. The incubation was stopped by resuspending in 5 mL of fresh medium and the cell concentration was determined by counting with Neubauer camera and using 4% trypan blue as dye vital.

HBV5 and HBV12 scaffolds were cut off into pieces of 1 × 1 cm^2. These samples were placed in tissue culture plates of 24-wells and fixed to bottom plate with a small drop of silicone (Silbione® Med Adh 4300 RTV, Bluestar Silicones France SAS, Lyon, France), sterilized by exposed to UV light for 15 min. 100 μL containing 5 × 10^4 cells/well to assess cell adhesion, and 2 × 10^4 cells/well for the cell proliferation assay were seeded in each well and incubated for 60 min to allow cell attachment to the material surface. Then, 1 mL of culture medium was added to each well. Quantification of viable cells was performed after 24 h and 7 days to evaluate the cellular adhesion and proliferation, respectively. The control was performed by cell culture on the plate without any material.

The percentage of cells adhered and proliferated was determined through the MTT (3-(4,5-dimethylthiazol-2-yl)-2,5-diphenyltetrazolium bromide) assay [31]. After 24 h or 7 days, 50 μL of MTT (3 mg/mL) were added to each well in the plates and incubated for 4 h. After that, samples were washed twice with PBS and the specimens deposited in a new plate. 1 mL of dimethyl sulfoxide (DMSO) was subsequently added and the absorbance was measured at 570 nm in a microplate reader (Biochrom EZ-Read 400, Cambridge, UK) after 15 min of gentle stirring. Three replicas were evaluated and the corresponding values were averaged and graphically represented. The statistical analysis was performed by one-way ANOVA to compare the average values of all groups; Tukey-test was then applied to determine a statistically significant difference between two studied groups. The tests were performed with a confidence level of 95% ($p < 0.05$).

Samples were fixed overnight with 2.5% formaldehyde in PBS at 4 °C, and then washed five times with PBS to obtain images showing the morphology of cells coming from adhesion and proliferation assays. Samples were also stained to get fluorescence microscopy images. Specifically, actin was labeled with green-fluorescent Alexa Fluor Atto-488 phalloidin dye, and the nucleus was labeled with DAPI (4′,6-diamidino-2-phenylindole). Then, samples were observed using a confocal laser scanning microscope (LSM 900 Zeiss, Oberkochen, Germany), images were taken with a camera controlled by ZEN 2.6 software (blue edition) (Carl-Zeiss Microscopy GmbH, Jena, Germany).

3.3. Results

3.3.1. DSC Testing of Polymer Solutions

DSC results (Figure 1a,b) revealed that crystallization temperature of 1,4-dioxane (T_c of solvent) in the polymer solutions was higher than the pure solvent at the two assayed cooling rates (i.e., 2 °C/min and 6 °C/min).

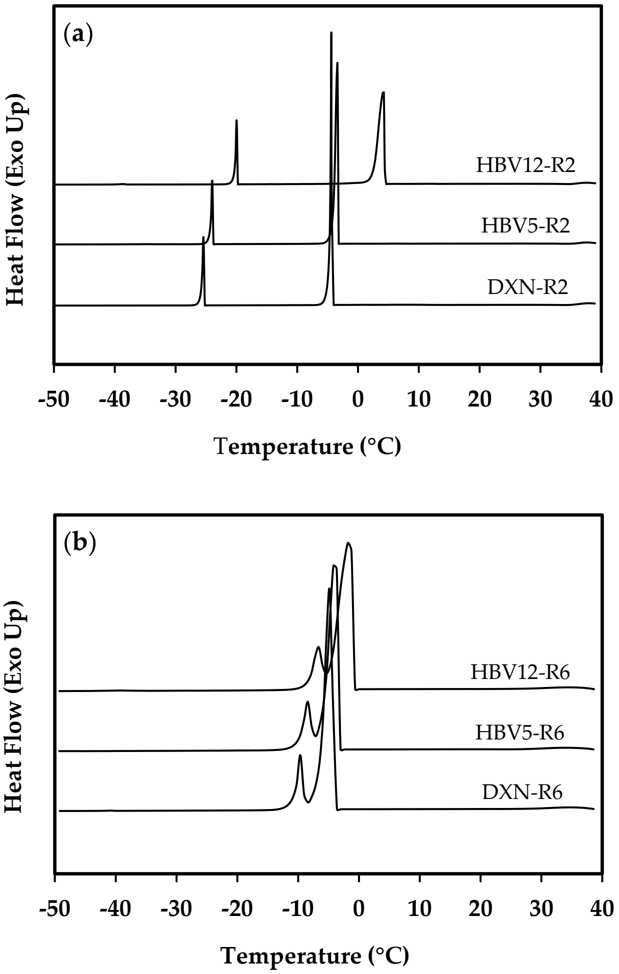

Figure 1. Exothermic peaks observed in the DSC cooling traces of the pure solvent and the two studied copolymer solution samples. Scans were performed at rates of 2 °C/min (**a**) and 6 °C/min (**b**).

Additionally, it was observed that the crystallization temperature of 1,4-dioxane was higher at both cooling rates when the copolymer was enriched in HV units (i.e., PHBV(12%HV) solutions gave rise to a higher solvent crystallization temperature than PHBV(5%HV) solutions). DSC cooling runs showed large exothermic peaks associated with the crystallization of 1,4-dioxane, and small peaks related to the well-known reversible phase transition of 1,4-dioxane from its monoclinic phase I to the monoclinic phase II [32].

Neither the large nor the small peaks observed in each cooling trace of the studied polymer solutions could be attributed to a crystallization of the polymer. Note that pure 1,4 dioxane exhibited both mentioned peaks at the same temperature range. According to the values of 1,4 dioxane crystallization temperature in the samples (i.e., −4.3 °C and −4.6 °C for DXN-R2 and DXN-R6; −3.4 °C and −3.9 °C for HBV5-R2 and HBV5-R6; 1.8 °C and −1.5 °C for HBV12-R2 and HBV12-R6), a decrease in T_c of solvent was detected for all the samples without exception, when a higher cooling rate was applied, a feature that was more significant for the copolymer enriched in HV units.

3.3.2. *Cloud Point of Polymer Solutions*

Cloud point is a temperature at which a clear polymer solution becomes turbid during cooling because of the liquid–liquid phase separation [26]. The boundary of the liquid–liquid demixing region in the polymer-solvent phase diagram is usually named binodal curve, but the term "cloud point curve" is more appropriate for polydisperse polymers [17]. Figure 2 shows the variation of the cloud point as a function of polymer concentration for the binary systems of PHBV(5%HV)-1,4 dioxane and PHBV(12%HV)-1,4 dioxane.

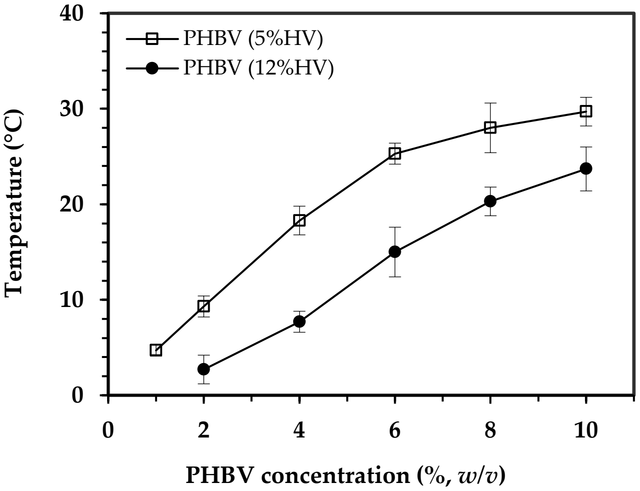

Figure 2. Cloud point curves at relatively low concentrations of PHBV(5%HV)-dioxane and PHBV(12%HV)-dioxane solutions.

According to the experimental cloud point curves, a higher cloud point was observed as the polymer concentration increased (at the evaluated concentration range). Additionally, the temperature at which the solution became cloudy decreased with the increase in HV content in the copolymer. Specifically, the cloud point of 2% (*w*/*v*) solutions of PHBV(5%HV) and PHBV(12%HV), which were used for fabrication of the scaffolds, was 9.3 ± 1.1 °C and 2.7 ± 1.5 °C, respectively. Any trace of cloudy state was not seen in the 1% (*w*/*v*) solution of the PHBV (12%HV) before being frozen. Gelation was also observed to occur before to achieve a cloudy state when concentrated solutions (e.g., higher than 2% (*w*/*v*)) were slowly cooled, especially for the copolymer with lower HV content.

3.3.3. Morphology of Porous Scaffolds

Scanning electron micrographs of split cross-sections (Figure 3) showed that the scaffolds tended to form large pores of around 100 microns with well differentiated walls when underwent phase separation at the higher cooling rate. It is interesting to note that upon the slower cooling condition, platelet-like structures were mainly distinguished. This structure was also observed to a greater extent in the PHBV(5%HV) copolymer. Some areas representing platelet-like morphology have been indicated by dashed-line circles in Figure 4.

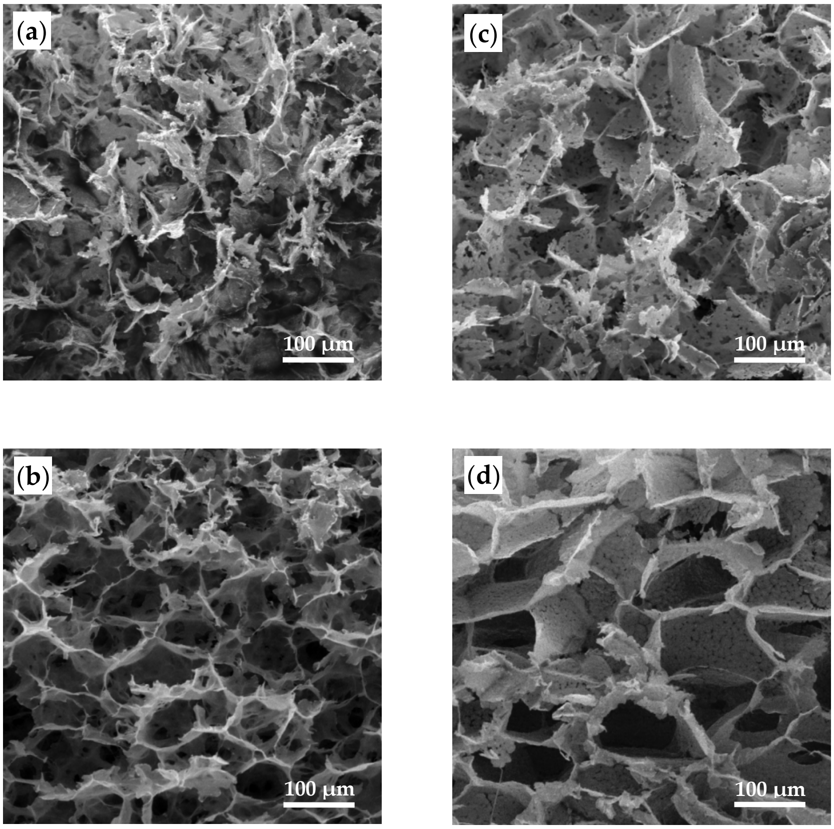

Figure 3. Scanning electron micrographs of cross-sections of PHBV scaffolds: (**a**) HBV5-R2, (**b**) HBV5-R6, (**c**) HBV12-R2, and (**d**) HBV12-R6.

Micrographs demonstrated that scaffolds had a three-dimensional porous structure and that the larger pores were further obtained from the scaffolds derived from the copolymer having the higher HV content. Specifically, PHBV(12%HV) scaffolds prepared at the higher cooling rate appear ideal considering the pore sizes, the homogeneous structure and the reduced platelet-like regions.

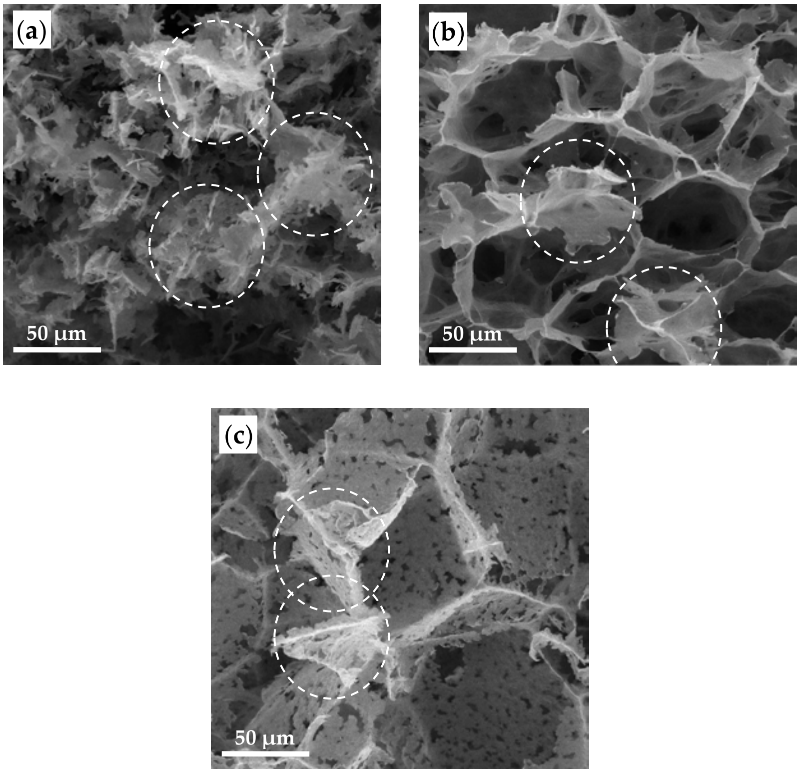

Figure 4. Scanning electron micrographs of cross-sections of PHBV scaffolds: (**a**) HBV5-R2, (**b**) HBV5-R6, (**c**) HBV12-R2. Dashed-line circles present areas detected as platelet-like structures.

The tendency towards forming more large pores and reducing platelet-like morphologies were intensified in the surface image micrographs (Figure 5). Images showed again that the HBV12-R6 sample was the more uniform one. The presence of small orifices in the pore walls ranging from several to tens of micron in size were discernible in both cross-section and surface micrographs, being considered as interconnectivities of the structure.

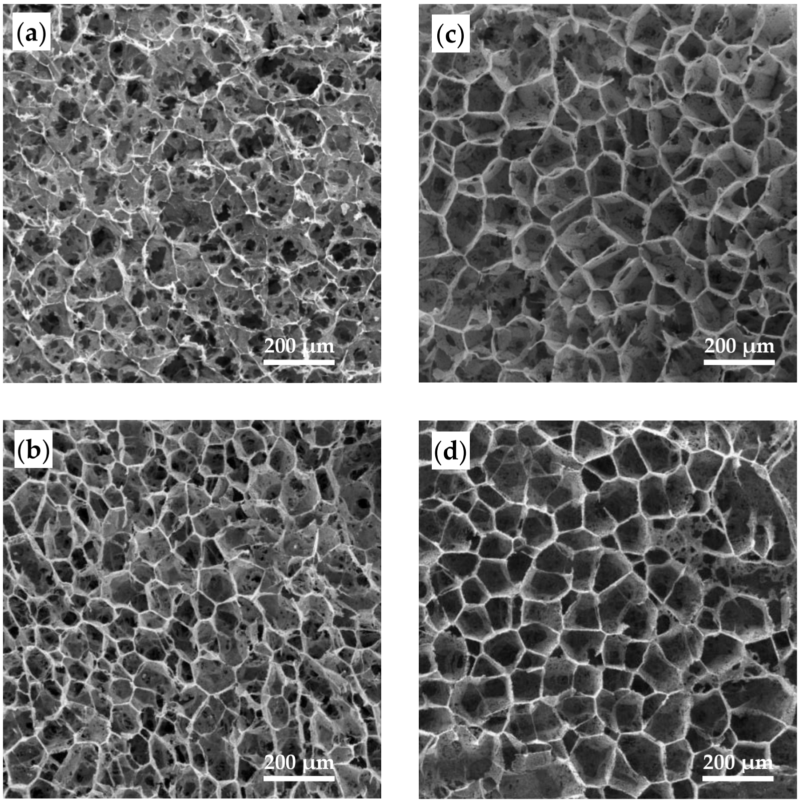

Figure 5. Scanning electron micrographs of the surface of PHBV scaffolds: (**a**) HBV5-R2, (**b**) HBV5-R6, (**c**) HBV12-R2, and (**d**) HBV12-R6.

3.3.4. DMTA Analysis of Polymer Scaffolds

DMTA results revealed that mechanical properties of resulting scaffolds were influenced by the selected cooling rate and logically by the HV molar content of the copolymer, even for the small increase from 5 wt% to 12 wt% (Figure 6).

An increase of the loss modulus (E'') and especially of the storage modulus (E') was observed when solutions were cooled at the highest rate. Therefore, the E''/E' ratio (i.e., loss tangent or tan δ) decreased. A similar effect was roughly observed when the HV content was lower. In summary, the locus of storage modulus curve shifted to the higher values and that of the loss tangent curve to lower values either by increase in cooling rate or decrease in HV contents. The dramatic decrease in the modulus at temperatures around 160 °C is associated with the melting point of the polymer, in accordance with supplier's specifications.

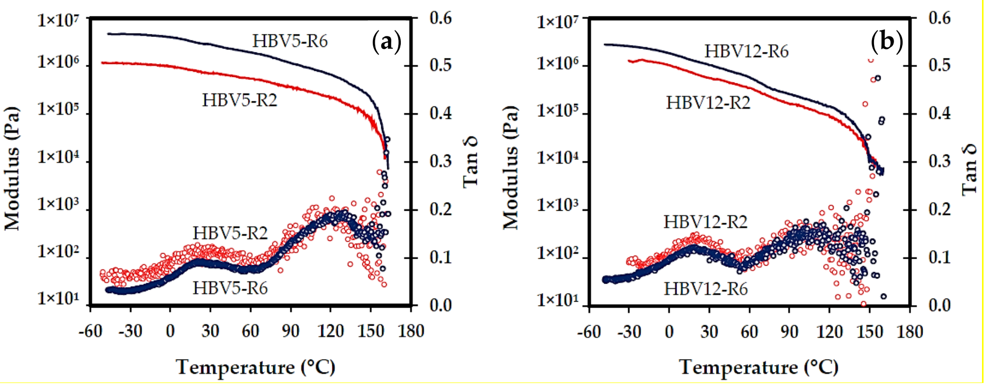

Figure 6. Effect of cooling rate (red and blue symbols/lines correspond to rates of 2 °C/min and 6 °C/min, respectively) on storage modulus (solid-line curves) and loss tangent (circle-marker curves) of PHBV scaffolds containing 5 wt% (**a**) and 12 wt% (**b**) of HV units.

3.3.5. Biocompatibility Assays for Scaffolds Prepared by TIPS from 1,4-Dioxane

HBV5 and HBV12 samples were evaluated as appropriate scaffolds to support cell adhesion and proliferation. Thus, epithelial-like MDCK and NRK cells were seeded in direct contact with the prepared scaffolds (Figure 7). Cell adhesion was determined after 24 h as an early event of the cell growth in the scaffolds, while cell proliferation was determined after 7 days to demonstrate that cell growth and colonization were effective in the prepared scaffolds.

Images of fluorescence microscopy gave evidences of the cell adhesion (Figure 7a,b) and of the formation of a cell monolayer onto all the scaffold samples (Figure 7c,d). In the cell adhesion assay, cells appeared spread onto the surface of the scaffolds and the porous structure was maintained as evidenced by the dark and deep zones. In the cell proliferation assay, there was a clear increase of the number of cells grown on the surface of the sample. Micrographs showed that MDCK and NRK cells grew normally to contact each other and formed a cell monolayer by clusters and stackings, being drawn to the profile of the pores in the scaffold. Cells had a smaller size after proliferation due to its density increase, and the porous scaffold structure was maintained as deduced from the dark and deep zones. In this way, the prepared scaffolds had a sufficiently large pore size to not restrict the entry of cells into the scaffolds. The sponge-like morphology of these scaffolds (Figure 5) is compatible with the excellent biocompatibility demonstrated in both cell adhesion and proliferation assays. Results confirmed that the studied scaffolds had a great potential for applications focused on tissue regeneration and remodeling.

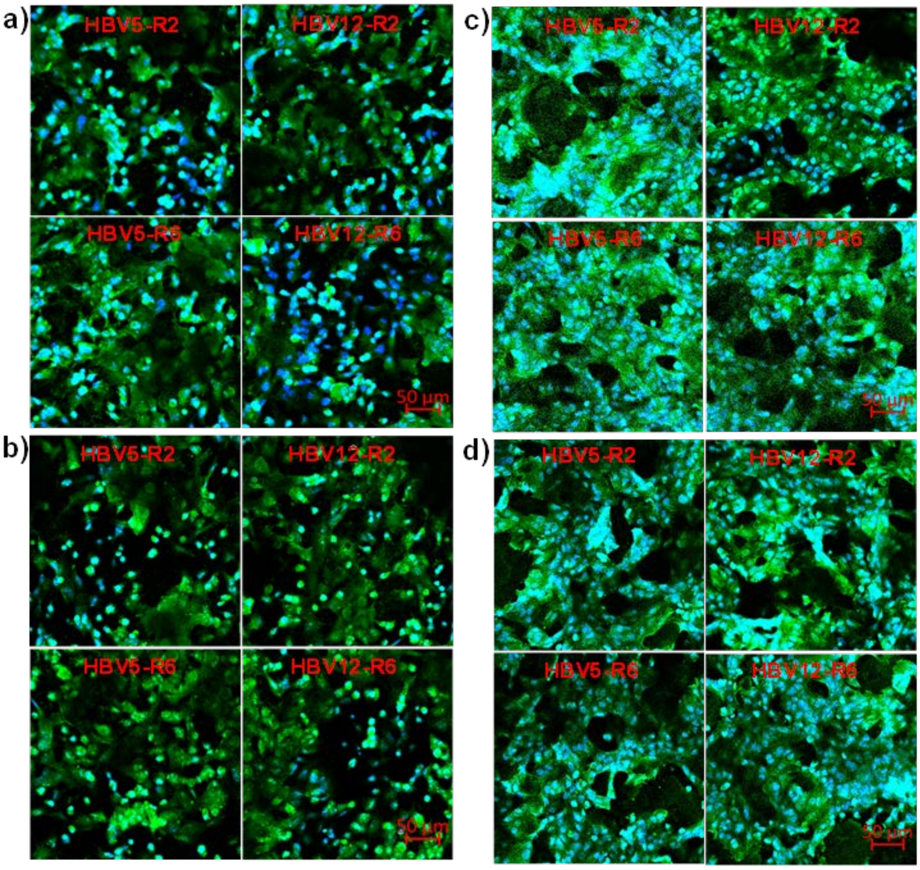

Figure 7. Fluorescence micrographs of NRK (**a** and **c**) and MDCK (**b** and **d**) epithelial cells after performing adhesion (**a**,**b**) and proliferation (**c**,**d**) assays onto HBV5 and HBV12 scaffolds obtained from 1,4-dioxane solutions cooled at rates of 2 and 6 °C/min. The green color is the actin marked with phalloidin and the blue color is the nucleus marked with DAPI.

Quantitative data of cell adhesion and proliferation are shown in Figure 8a,b, respectively. The cell viability was determined considering the ratio between the number of cells grown in the scaffold and on the control (well of the culture plate), respectively.

Results indicated that cell adhesion was quantitatively similar in the prepared scaffolds and the control. Only HBV5-R2 and HBV12-R6 samples showed a significant reduction in the number of adhered MDCK cells, with values around 80% of cell viability. However, the samples HBV12-R2 with MDCK cells and HBV5-R6 with NRK cells were not significantly different despite having average values around 80% viability due to the greater dispersion of data as evidenced by their respective standard deviations (Figure 8a). Regarding cell proliferation, which is a more consistent experiment because it corresponds to a period of 7 days, it was observed that the MDCK cells showed similar growth percentages as the control, while the NRK cells in the HBV5 samples showed a significant growth reduction. However, the measured values are close to 80% of viability (Figure 8b), which can cause us to consider that differences may be caused by uncontrolled experimental factors.

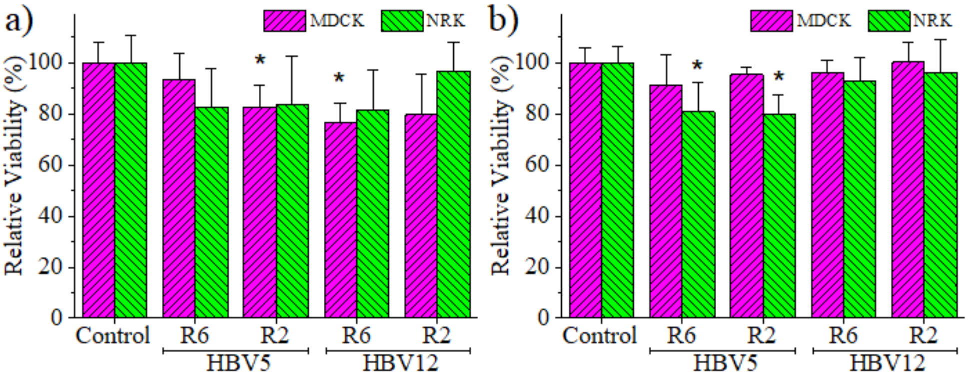

Figure 8. Cell viability of NRK and MDCK epithelial cells for adhesion (**a**) and proliferation (**b**) assays in the HBV5 and HBV12 scaffolds obtained from 1,4-dioxane solutions cooled at rates of 2 and 6 °C/min. * $p < 0.05$ vs. control.

In this sense, it should be indicated that volume of scaffolds should be taken into account instead of surface (1 cm × 1 cm square samples were analyzed) since the scaffold galleries allow cell entry and colonization inside the scaffold. These considerations are supported by the morphological evidence of fluorescence microscopy for both adhesion and proliferation assays (Figure 7). Therefore, results allow us to indicate that HBV5 and HBV12 scaffolds obtained from the 1,4-dioxane solutions at both 2 and 6 °C/min cooling rates are suitable and biocompatible supports for cell adhesion and proliferation in 3D cultures, and show potential interest for tissue regeneration applications.

3.4. Discussion

3.4.1. Solvent Crystallization Temperature

Since TIPS is a non-equilibrium process, the effects of the cooling rate on the phase diagram must be regarded [33]. Based on DSC results, higher cooling rates led to a slight reduction of solvent T_c in all samples. Increasing the cooling rate allows getting a higher supercooling. Namely, the solution can be cooled to a temperature below its equilibrium crystallization temperature, avoiding crystallization of the solvent from the solution [34].

As it was reported before, the crystallization temperature of 1,4-dioxane in the polymer solutions was higher than pure 1,4-dioxane, meaning that the presence of PHBV has provoked the earlier crystallization of 1,4-dioxane during cooling. Crystallization of 1,4-dioxane took place according to a typical mechanism consisting on nucleation and growth steps [23,35]. It could be assumed that crystallization temperature of the solvent becomes higher (anticipation of crystallization during cooling) when the nucleation process is facilitated. Therefore, the incorporation of poly(3-hydroxybutyrate-*co*-3-hydroxyvalerate) in 1,4-dioxane may favor the formation of nuclei.

Note that there are hydroxyl and carboxyl functional groups on both ends of a PHBV chain and two exposed oxygen atoms in the molecular structure of 1,4 dioxane. Interactions between these functional groups and the oxygen lone pair electrons of dioxane are not negligible [36]. In fact, it should be expected that hydrogen bonds were established between 1,4-dioxane and the molecular chains [37]. In this way, the hydrogen bonded molecules of solvent and polymer should have a restricted movement and displacement at the site of binding [38]. These solvent molecules with finite mobility might serve as preferential nucleation sites and facilitate the solvent crystallization.

PHBV(12%HV)-dioxane solutions showed higher T_c of solvent than PHBV(5%HV)-dioxane solutions. Two points may justify this observation: Its lower molecular weight and its lower crystallinity. On one hand, it seems that the increase of functional groups (i.e., terminal groups) should increase the interactions with the solvent. On the other hand, diffusion of the solvent molecules should be easier when the copolymer becomes less crystalline. Therefore, the capability to form hydrogen bonding interactions becomes increased due to the higher accessibility of hydroxyl and carboxyl groups to the solvent molecules. This crystallization behavior is significantly enhanced upon slow cooling, where enough time is available for the molecules to trigger proper interaction sites during the crystallization process.

3.4.2. Cloud Point of Polymer Solutions

At experimentally controllable cooling rates, a minor effect of the cooling rate on the liquid–liquid phase separation temperature and the location of the cloud point curve has been reported [39]. Therefore, only a slow cooling (i.e., a constant rate of 1 °C per 30 min) was applied to reach the equilibrium conditions for the cloud point determination [26]. Logically, the cloud point temperature decreased as the HV content in the copolymer increased.

The Flory–Huggins equation for the polymer-solvent system is [40]

$$\frac{\Delta G_{mix}}{RT} = \frac{\phi_d}{x_d} ln\, \phi_d + \frac{\phi_p}{x_p} ln\, \phi_p + \chi \phi_d \phi_p \tag{1}$$

where ΔG_{mix} is the Gibbs free energy of mixing per lattice site, ϕ_d and ϕ_p are the volume fraction of solvent and polymer, x_d and x_p are the number of lattice sites occupied by solvent and polymer molecules, respectively. χ is the Flory-Huggins interaction parameter which is affected by the strength of polymer–solvent interactions. The first two terms on the right side of the Flory–Huggins equation are always negative and represent combinatorial entropy contribution and the third term can be positive or negative (depending on the sign of χ) and represents the enthalpic contribution. Weak polymer–solvent interactions give rise to a large and positive value of χ, leading to a positive ΔG_{mix} and consequently liquid–liquid demixing happens. On condition that the strength of interactions between polymer and solvent is high (small χ), it is more difficult to attain the liquid–liquid phase separation conditions (i.e., a lower temperature is needed). In this situation, the homogenous one-phase region in the phase diagram (Figure 9) expands, and so the boundary of liquid–liquid phase separation (binodal curve) shifts to lower temperatures [33].

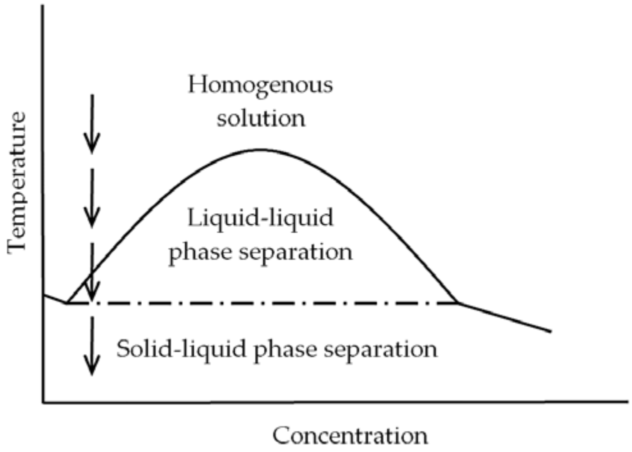

Figure 9. Typical phase diagram for a polymer-solvent system showing the regions of liquid–liquid and solid–liquid phase separation. Arrows schematically indicate the phase separation evolution during cooling for an initial solution with a low (i.e., close to 2%) polymer concentration.

Accordingly, the lower cloud point of PHBV (12%HV) solution is speculated to be the result of its stronger interactions with 1,4-dioxane, compared to the other copolymer. As it was elaborated in the previous section, the lower molecular weight and crystallinity of PHBV (12%HV) results in an increased number of interactions with 1,4-dioxane.

3.4.3. Phase Separation Mechanisms

TIPS can be divided into two major types of separation processes: liquid–liquid and solid–liquid phase separations. The former may occur prior to the solvent freezing, and the latter is only observed when the solvent has been completely frozen [41]. In the case where the solvent crystallization temperature in the solution is higher than the liquid–liquid phase separation temperature, the solid–liquid phase separation occurs during the cooling process [21]. After removing the solvent, the polymeric foam is characterized by pores having a similar geometry of solvent crystallites [17,23,25], namely a pore size of around 100 microns remains [41].

The liquid–liquid phase separation takes place, if the solvent crystallization temperature is much lower than the phase separation temperature. Morphologically, this type of phase separation produces a continuous isotropic structure with pores ranging from several to tens of microns. On condition that the solution involves a semicrystalline polymer, it will encounter driving forces for both liquid–liquid phase separation and polymer crystallization, due to the crystallization potential of the polymer. A crystallization-induced phase separation (another type of solid–liquid phase separation) can occur in this situation, if the polymer crystallization temperature is higher than the phase separation temperature and the solution is held long enough at a temperature above the phase separation temperature [21].

Depending on the polymer concentration, the crystallization or precipitation of polymer from the solution can lead to different morphologies varying from loose precipitates (i.e., unconnected precipitates) to percolating structures (i.e., interconnected networks of crystallites) [17]. In this regard, various microstructures such as platelet-like structures from relatively low concentrations [27] and spherulitic structures from relatively concentrated solutions have been reported [33,34].

A typical phase diagram for the polymer–solvent binary system, corresponding to thermodynamically favored phase transitions of this study is depicted in Figure 9. The concentration used for fabricating the polymeric foams is schematically showed by a sequence of arrows orientated towards lower temperatures. Upon cooling, the solution crosses the binodal curve (solid curve), undergoing liquid–liquid phase separation by nucleation and growth or spinodal decomposition mechanism. As cooling continues and the temperature falls below the solvent crystallization temperature (dashed horizontal line), the solution subsequently experiences the solid–liquid phase separation [21,26].

Regarding the roughly adjacent temperatures measured for the cloud point and solvent crystallization in the solutions, a limited period of time is expected between these two-phase separation types when cooling. Depending on cooling rates and HV contents, the solutions underwent solid–liquid phase separation immediately or in slightly delayed manner after the liquid–liquid demixing, resulting in relatively different morphologies and mechanical properties. Materials with relatively different morphologies and mechanical properties are consequently derived according to the phase separation process.

Considering the PHBV melting temperature of about 160 °C, it can be deduced that PHBV is crystallized from the solution at temperatures higher than the range that we studied in the DSC experiments. Due to existence of a driving force for the crystallization of the polymer at relatively elevated temperatures, this phenomenon is thermodynamically favored until the binodal curve is reached by the solution throughout cooling. Nevertheless, the crystallization-induced phase separation is significantly dependent on the kinetic conditions that have been elaborated in the next section. The gelation observed via slow cooling at relatively high temperatures (above the liquid–liquid phase separation temperature—cloud point) can be attributed to polymer crystallization [27].

Although it is not possible to determine the exact contribution of these three phase separation types in this study, the qualitative changes in their corresponding microstructures (caused by changing the cooling rate and HV contents) is discernible in the SEM micrographs (Figures 3 and 5).

3.4.4. Phase Separation and Morphology Relationship

Scaffold morphologies obtained at different cooling rates can be well explained by analyzing the phase separation process. It should be noted that an increase in the cooling rate results in a rapid temperature decrease from that associated with the binodal curve to that corresponding to the solvent crystallization horizontal line. In other words, the time at which the system remains in the liquid–liquid separation region becomes minimum (Figure 9). On the other hand, higher cooling rate led to a slight decrease in the solvent crystallization temperature and therefore causes an insignificant enlargement of the indicated temperature interval (binodal-solvent crystallization).

Large pores of around 100 microns are usually observed at higher cooling rate in contrast with the great number of small pores (i.e., several microns) that are observed at lower cooling rate. As a consequence, it can be morphologically inferred that crystallization of the solvent bypass the liquid–liquid phase separation under the higher cooling rate conditions used in this study. Similarly, Zhang and Ma showed that when polymer solutions (with several different solvent systems) were cooled fast enough and to a temperature low enough, the solid–liquid phase separation occurred, because there was not enough time for the liquid–liquid phase separation to take place [23].

The prominent effect of the cooling rate on the morphology of the studied system corresponds to the reduction of platelet-like morphologies ascribed to the polymer crystallization. Despite the fact that, above the binodal curve, polymer crystallization is thermodynamically favored during cooling, the kinetics of phase separation specifies that whether the thermodynamically favored transition happens or not, and also to what extent the transition occurs [17].

Since nucleation and growth of polymer crystals from the solution is a slow process [17], it may not happen or happen deficiently upon rapid cooling. In this regard, it has been reported that high cooling rates avoid the nucleation and growth of polymer crystals, being also indicated that platelet-like structures increased with the annealing time at room temperature [27].

The both mentioned morphological effects caused by increase in the cooling rate, especially the reduction of platelet-like zones were clearly observed by comparison of cross-section images (Figure 3) and surface images (Figure 5) for each sample. The observed differences may be due to an unwanted temperature gradient from the surface to the center of the samples during cooling, resulting in different local cooling rates.

From the copolymer type viewpoint, in PHBV (12%HV), the distance between binodal curve and solvent crystallization line decreased in three ways. Firstly, the locus of binodal curve and the intersection point of binodal curve and solvent crystallization line shifted to the right. As it was previously described, the 1% (*w*/*v*) solution of PHBV(12%HV) unlike the same concentrated solution of PHBV(5%HV), was frozen before being cloudy, meaning that the former sample has only crossed the solvent crystallization line at the left side of the intersection point. Secondly, solvent crystallization temperature in the solutions became higher. Thirdly, the locus of binodal curve shifted to lower temperatures. Getting smaller the mentioned temperature interval in the phase diagram, the liquid–liquid demixing and the solvent crystallization almost occur simultaneously in PHBV(12%HV)-dioxane solution.

This situation results in leaving little room for growth of the polymer-lean droplets formed by liquid–liquid phase separation. Hence, most of the pores arising from these droplets might not grow properly to reach tens of microns in size; instead, they remain in the form of small orifices of several microns trapped throughout walls of larger pores (Figure 3c,d). Additionally, the solutions roughly tended to form structures dominated by large pores of around 100 microns pertaining to solid–liquid phase separation (particularly at higher cooling rates).

Regarding the obtained morphologies of split cross-sections (Figure 3), it can be concluded that the highest contribution of solid–liquid phase separation and therefore the highest number of large pores are related to sample HBV12-R6, and the lowest one to sample HBV5-R2. The latter sample also possessed the highest contribution of crystallization-induced phase separation and its corresponding morphology. The sample HBV12-R2 exhibited a platelet-like structure along with the small pores of around 5 microns. Furthermore, the sample HBV5-R6 obviously shows a variety of structures comprising the large pores, the small pores which have grown up to 10–20 microns and also the platelet-like regions, ascribed to three mentioned types of phase separation. Conclusively, crystallization of the polymer seems to be the premier mechanism under slower cooling conditions, while the crystallization of the solvent was the prominent mechanism for samples having the highest HV content.

3.4.5. Structural Characteristics and DMTA Results

According to DMTA results, increase in cooling rate and decrease in HV content of PHBV samples resulted in higher storage modulus and lower loss tangent, which are indicative of scaffold rigidity and damping, respectively (Figure 6). Strictly speaking, viscoelastic behavior of scaffolds is characterized by a higher strength and a lower viscose contribution under the higher cooling rate and lower HV content conditions. The better mechanical properties of the copolymer with lower HV content could be further attributed to its higher crystallinity.

On the other hand, upon slower cooling, the regions having morphologies arising from the polymer crystallization increased. These regions are made up of platelets of polymer rich phase (formed by nucleation and growth of polymer crystals through slow cooling) suspended in a matrix of polymer-lean phase [21]. The regions, which are formed by crystallization of the polymer from dilute solutions, have been characterized by insufficient structural consistency and mechanical properties [27,34].

For example, when PLLA crystallized slow enough from a 5 wt% solution, a loose connection between the platelets was reported by Ma and Zhang [27]. Therefore, weak mechanical properties were justified for the platelet-like structured matrices. Lloyd et al. also produced leafy architectures with structural consistency, when HDPE crystallized from 15–50 wt% solutions, while no structural integrity was reported at concentrations below 15 wt% [34]. Regarding the concentration of the solutions used for fabricating the scaffolds in this study (2% *w*/*v*), a poor structural connection and therefore a mechanical weakness should be expected for the platelet-like regions. Since the amount of these regions is increased by slower cooling, a decrease in the mechanical performance is expected at the lower cooling rate condition as it is confirmed by DMTA results.

On the other hand, the lower HV molar ratio raised crystallinity of PHBV, and so, enhanced mechanical properties can be attributed to this reality. The increase in the storage modulus caused by the decrease in the HV contents is clearly more significant in the rubbery region with respect to the glassy region. It can be postulated that the increase in density and crystallinity led to a high restriction of the segmental motion of the polymer chains in the rubbery region, while a lower influence was derived in the glassy region characterized by limited molecular vibrations.

3.4.6. Biocompatibility of Porous PHBV Scaffolds

Current tissue engineering strategies focus on the reconstruction and regeneration of damaged tissues. The use of porous scaffold biomaterials becomes an interesting issue in reparative medicine. To restore the functionality of a tissue, the presence of a biodegradable scaffold can be essential as an extracellular matrix for cell colonization, migration, growth, and differentiation, until the tissues are restored or regenerated completely. Great attention has been paid to the PHBV bioplastic due to its potential biomedical applications. In this sense, our current work with porous PHBV substrates could be pioneering in demonstrating the good capacity of these substrates to promote adhesion and proliferation of epithelial cells. Our results showed that porous PHBV scaffolds allow the adhesion of a high percentage of epithelial cells (e.g., equal to or greater than 80%). However, our proliferation results at 7 days also indicated that HBV5 scaffolds supported a scarcely lower proliferation of NRK cells, a feature that could be related to the high crystallinity and stiffness of this material. Fortunately, MDCK cells showed an excellent growth on these porous matrices. In vitro tests appear therefore indicative but not conclusive, being required evidence from in vivo tests to improve conclusions about biocompatibility.

The results obtained in this work are sustained for a wide literature data about the excellent biocompatibility of PHBV. Several techniques for the PHBV scaffold fabrication have been developed in the last decades: polymerization in solution, leaching, electrospinning, and 3D printing [42]. PHBV matrices have been developed for both hard [43] and soft [44] tissue engineering applications, e.g., bone and skin, respectively. In particular, epithelial-like cells such as UMR-106 osteoblast maintain their phenotypic characteristics in PHBV matrices [45]. Furthermore, in similar applications for skin engineering, the fiber matrices based on PHBV and obtained by electrospinning demonstrated that human skin fibroblasts (CRL 2072) were able to adhere and colonize these new substrates [44]. Different PHB organogels and scaffolds with complex hierarchical structure and covering a wide range of length scales have been prepared by TIPS and showed an excellent cell viability using the human keratinocyte cell line (HaCaT) [46]. Finally, our results contribute to the suggestion of the great application of PHBV in tissue engineering.

3.5. Conclusions

The principal aim of this work was the study of process-properties relationship for poly(hydroxybutyrate-*co*-hydroxyvalerate) scaffolds fabricated by thermally induced phase separation. Due to presence of different driving forces for polymer and solvent crystallization and also liquid–liquid demixing, the phase separation process became relatively complicated. Thus, it was hard to consider a distinctive mechanism, being responsible for generating the different microporous structures. Variables corresponding to the fabrication process (i.e., cooling rate applied to the polymer solution) and material selection (i.e., PHBV with different HV molar ratios) strongly affected the phase separation process and led to different microporous structures and mechanical properties of the resulted scaffolds. Strictly speaking, more regions having the morphology associated with crystallization of the polymer were conspicuously detected upon slower cooling. These regions of relatively poor structural continuity were assumed to be the reason of the observed decrease in rigidity of the scaffolds. Besides, a tendency towards forming the typical morphology related to a solid–liquid phase separation was also observed in either higher cooling rate or higher HV content. Eventually, a high degree of crystallinity was recognized as the cause for the higher rigidity of the scaffolds having lower HV content. Finally, in-vitro cytocompatibility studies confirmed that these sponges-like scaffolds were nontoxic toward MDCK and NRK cells, and had a suitable porosity to cell adhesion and growth. Our data demonstrated that these biocompatible scaffolds with interconnected 3D networks are a promising to applications focused on tissue regeneration and remodeling.

3.6. References

1. Malafaya, P.B.; Silva G. A.; Reis, R.L. Natural–origin polymers as carriers and scaffolds for biomolecules and cell delivery in tissue engineering applications. *Adv. Drug. Deliv. Rev.* **2007**, *59*, 207–233.
2. Pouton, C.W.; Akhtar, S. Biosynthetic polyhydroxyalkanoates and their potential in drug delivery. *Adv. Drug. Deliv. Rev.* **1996**, *18*, 133–162.
3. Zinna, M.; Witholt, B.; Egli, T. Occurrence, synthesis and medical application of bacterial polyhydroxyalkanoate. *Adv. Drug. Deliv. Rev.* **2001**, *53*, 5–21.
4. Chen, G.Q.; Wu, Q. The application of polyhydroxyalkanoates as tissue engineering materials. *Biomaterials* **2005**, *26*, 6565–6578.
5. Lee, S.Y. Bacterial Polyhydroxyalkanoates. *Biotech. Bioeng.* **1996**, *49*, 1–14.
6. Williams, S.F.; Martin, D.P.; Horowitz, D.M.; Peoples, O.P. PHA applications: addressing the price performance issue I. Tissue engineering. *Int. J. Biol. Macromol.* **1999**, *25*, 111–121.
7. Fei, B.; Chen, C.; Wu, H.; Peng, S.; Wang, X.; Dong, L. Quantitative FTIR study of PHBV/bisphenol A blends. *Eur. Polym. J.* **2003**, *39*, 1939–1946.
8. Gassner, F.; Owen, A.J. Some properties of poly(3-hydroxybutyrate-*co*-3-hydroxyvalerate) blends. *Polym. Int.* **1996**, *39*, 215–219.
9. Sudesh, K.; Abe, H.; Doi, Y. Synthesis, structure and properties of polyhydroxyalkanoates: biological polyesters. *Prog. Polym. Sci.* **2000**, *25*, 1503–1555.
10. Hutmacher, D.W. Scaffolds in tissue engineering bone and cartilage. *Biomaterials* **2000**, *21*, 2529–2543.
11. Hutmacher, D.W. Scaffold design and fabrication technologies for engineering tissues-state of the art and future perspectives. *J. Biomater. Sci. Polymer Edn.* **2001**, *12*, 107–124.
12. Buzarovska A.; Dinescu S.; Chitoiu L.; Costache M. Porous poly(L-lactic acid) nanocomposite scaffolds with functionalized TiO_2 nanoparticles: properties, cytocompatibility and drug release capability. *J. Mater. Sci.* **2018**, *53*, 11151–11166.
13. Conoscenti G.; Carfì Pavia F.; Ongaro A.; Brucato V.; Goegele C.; Schwarz S.; Boccaccini A.R.; Stoelzel K.; La Carrubba V.; Schulze-Tanzil G. Human nasoseptal chondrocytes maintain their differentiated phenotype on PLLA scaffolds produced by thermally induced phase separation and supplemented with bioactive glass 1393. *Connect. Tissue. Res.* **2019,** *60*, 344–357.
14. Salehi M.; Farzamfar S.; Bozorgzadeh S.; Bastami F. Fabrication of poly(L-Lactic Acid)/chitosan scaffolds by solid–liquid phase separation method for nerve tissue engineering: An in-vitro study on human neuroblasts. *J. Craniofac. Surg.* **2019**, *30*, 784–789.
15. Chen P.; Zhou Z.; Liu W.; Zhao Y.; Huang T.; Li X.; Duan J.; Fang J. Preparation and characterization of poly(L-lactide-co-glycolide-co-ε-caprolactone) scaffolds by thermally induced phase separation. *J. Macromol. Sci. B* **2020**, *59*, 1–13.
16. Gaikwad, V.V.; Patil, A.B.; Gaikwad, M.V. Scaffolds for drug delivery in tissue engineering. *Int. J. Pharm. Sci. Nanotech.* **2008**, *1*, 113–122.

17. Van de Witte, P.; Dijkstra, P.J.; van den Berg, J.W.A.; Feijen, J. Phase separation processes in polymer solution in relation to membrane formation. *J. Membr. Sci.* **1996**, *117*, 1–31.
18. Puppi, D.; Chiellini, F.; Piras, A.M.; Chiellini, E. Polymeric materials for bone and cartilage repair. *Prog. Polym. Sci.* **2010**, *35*, 403–440.
19. Mikos, A.G.; Temenoff, J.S. Formation of highly porous biodegradable scaffolds for tissue engineering. *E. J. Biotech.* **2000**, *3*, 1–6.
20. Lombardo, M.E.; Pavia, F.C.; Vitrano, I.; Ghersi, G.; Brucato, V.; Rosei, F.; La Carrubba, V. PLLA scaffolds with controlled architecture as potential microenvironment for in vitro tumor model. *Tissue Cell* **2019**, *58*, 33–41.
21. Chen, V.J.; Ma, P.X. Polymer phase separation. In *Scaffolding in Tissue Engineering*; Williams, C.G., Elisseeff, J.H., Eds.; Taylor & Francis: Boca Raton, FL, USA, 2006; pp. 125–137.
22. Wei, G.; Ma, P.X. Nanostructured biomaterials for regeneration. *Adv. Funct. Mater.* **2008**, *18*, 3568–3582.
23. Zhang, R.; Ma, P.X. Poly(α-hydroxyl acids)/hydroxyapatite porous composites for bone-tissue engineering. I. Preparation and morphology. *J. Biomed. Mater. Res.* **1999**, *44*, 446–455.
24. Ma, P.X.; Zhang, R.; Xiao, G.; Franceschi, R. Engineering new bone tissue *in vitro* on highly porous poly(α-hydroxyl acids)/hydroxyapatite composite scaffolds. *J. Biomed. Mater. Res.* **2001**, *54*, 284–293.
25. Ma, P.X.; Zhang, R. Microtubular architecture of biodegradable polymer scaffolds. *J. Biomed. Mater. Res.* **2001**, *56*, 469–477.
26. Yang, F.; Murugan, R.; Ramakrishna, S.; Wang, X.; Ma, Y.X.; Wang, S. Fabrication of nano-structured porous PLLA scaffold intended for nerve tissue engineering. *Biomaterials* **2004**, *25*, 1891–1900.
27. Ma, P.X.; Zhang R. Synthetic nano-scale fibrous extracellular matrix. *J. Biomed. Mater. Res.* **1999**, *46*, 60–72.
28. Li, X.T.; Zhang, Y.; Chen, G.Q. Nanofibrous polyhydroxyalkanoate matrices as cell growth supporting materials. *Biomaterials* **2008**, *29*, 3720–3728.
29. Cheng, S.T.; Chen, Z.F.; Chen, G.Q. The expression of cross-linked elastin by rabbit blood vessel smooth muscle cells cultured in polyhydroxyalkanoate scaffolds. *Biomaterials* **2008**, *29*, 4187–4194.
30. Paye, M.; Barel, A.O.; Maibach, H.I. *Handbook of cosmetic science and technology*, CRC Press Taylor & Francis Group: Boca Raton, FL, USA, 2006.
31. del Valle, L.J.; Roca, D.; Franco. L.; Puiggalí, J.; Rodríguez-Galán, A. Preparation and release study of ibuprofen-loaded porous matrices of a biodegradable poly(ester amide) derived from L-alanine units. *J. Appl. Polym. Sci*. **2011**, *122*, 1953–1967.
32. Buschmann, J.; Muller, E.; Luger, P. X-ray structure analysis of 1,4-dioxane, phase I at 279 K and phase II at 153 K. *Acta. Cryst.* **1986**, *42*, 873–876.

33. Lloyd, D.R.; Kim, S.S.; Kinzer, K.E. Microporous membrane formation via thermally induced phase separation. II. Liquid-liquid phase separation. *J. Membr. Sci.* **1991**, *64*, 1–11.
34. Lloyd, D.R. Microporous membrane formation via thermally induced phase separation. I. Solid-liquid phase separation. *J. Membr. Sci.* **1990**, *52*, 239–261.
35. Di Martino, P.; Censi, R.; Malaj, L.; Capsoni, D.; Massarotti, V.; Martelli, S. Influence of solvent and crystallization method on the crystal habit of metronidazole. *Cryst. Res. Technol.* **2007**, *42*, 8, 800–806.
36. Rajala, G.E.; Crossley, J. Association of the butyl alcohols and n-decanol. *Can. J. Chem.* **1971**, *49*, 3617–3622.
37. Nangia, A.; Desiraju, G.R. Pseudopolymorphism: occurrences of hydrogen bonding organic solvents in molecular crystals. *Chem. Commun.* **1999**, *7*, 605–606.
38. Ishii, D.; Tatsumi, D.; Matsumoto, T. Effect of solvent exchange on the supramolecular structure, the molecular mobility and the dissolution behavior of cellulose in LiCl/DMAc. *Carb. Res.* **2008**, *343*, 919–928.
39. Koningsveld, R.; Staverman, A.J. Liquid-liquid phase separation in multi-component polymer solutions. IV. Coexistence curve. *Kolloid-Z. Z. Polym.* **1967**, *218*, 114–124.
40. Flory, P.J. *Principles of Polymer Chemistry*; Cornell University Press: Ithaca, NY, USA, 1953; Chapter 13.
41. Schugens, C.H.; Maquet, V.; Grandfils, C.; Jerome, R.; Teyssie, P.H. Biodegradable and macroporous polylactide implants for cell transplantation: 1. Preparation of macroporous polylactide supports by solid-liquid phase separation. *Polymer* **1996**, *37*, 1027–1038.
42. Rivera-Briso, A.I.; Serrano-Aroca, A. Poly(3-hydroxybutyrate-co-3-hydroxyvalerate): Enhancement strategies for advanced applications. *Polymers* **2018**, *10*, 732.
43. Sombatmankhong, K.; Sanchavanakit, N.; Pavasant, P.; Supaphol, P. Bone scaffolds from electrospun fiber mats of poly(3-hydroxybutyrate), poly(3-hydroxybutyrateco-3-hydroxyvalerate) and their blend. *Polymer* **2007**, *48*, 1419–1427.
44. Kuppan, P.; Vasanthan, K.S.; Sundaramurthi, D.; Krishnan, U.M.; Sethuraman, S. Development of poly(3-hydroxybutyrate-co-3-hydroxyvalerate) fibers for skin tissue engineering: Effects of topography, mechanical, and chemical stimuli. *Biomacromolecules* **2011**, *12*, 3156–3165.
45. Liu, H.; Raghavan, D.; Stubbs, J. Evaluation of the biological responses of osteoblast-like UMR-106 cells to the engineered porous PHBV matrix. *J. Biomed. Mater. Res.* **2007**, *81A*, 669–677.
46. Kang, J.; Hwang, J.-Y.; Huh, M.; Yun, S. Porous poly(3-hydroxybutyrate) scaffolds prepared by non-solvent-induced phase separation for tissue engineering. *Macromol. Res.* **2020**, *28*, 835–843.

Chapter 4

Poly(Butylene Succinate) Matrices Obtained by Thermally-Induced Phase Separation: Structural Modifications Affect Drug Release

Abstract

Biodegradable and biocompatible poly(butylene succinate) (PBS) scaffolds with 3D interconnected microporous structures have been prepared by thermally-induced phase separation (TIPS). 5 and 100 wt% of curcumin (CUR) and piperine (PIP) as natural anticancer and anti-inflammatory drugs were incorporated into the 2.5% (*w*/*v*) polymer solutions during the one-step fabrication protocol. Alterations in TIPS process parameters such as solvent system (1,4 dioxane or THF) and cooling condition (employing -20, -74 and -196 °C cooling baths and also multidirectional or uniaxial cooling system) affected the phase separation process and the scaffolds properties. The morphological and physicochemical properties of the scaffolds were evaluated to interpret the drug release profile and biocompatibility results. Microporous structures arisen from solid-liquid and liquid-liquid phase separation mechanisms having crystallized PBS substructures were generally obtained by utilizing DXN and THF solvents, respectively. Controlling the crystallization of DXN in a uniaxial direction, resulted in the formation of microtubular scaffolds with oriented porosities. Although the low-content drug loading did not have a considerable morphological effect, incorporation of high drug contents decreased the porosity level of the scaffolds. A homogenous distribution of well-developed prismatic PIP crystals and rounded CUR agglomerates integrated into the PBS matrix was observed. The integration of CUR was confirmed by physicochemical evaluations because of a possible interaction with the polymer matrix during the phase separation process. The release of PIP was generally faster because of its lower affinity with the polymer matrix and higher solubility in the DMEM aqueous medium. The scaffolds with uniaxially-oriented porosities displayed a greater sustained release of the drugs (i.e., only 50-60% after 170 h) due to the restricted drug diffusion through their dense planar spherulitic pore walls. Such scaffolds also exhibited greater biocompatibility, indicating the positive influence of structural orientation on the properties of TIPS-obtained matrices as cell/drug carriers.

4.1. Introduction

Scaffold materials to be employed for tissue engineering applications must meet certain physical and biological criteria. In terms of physical properties, an ideal scaffold should have a three-dimensional well-connected macroporous structure to accommodate cells and to facilitate cell migration, proliferation, and differentiation, thereby ensuring functional neotissue formation. Consequently, scaffolds with high porosity and interconnected pores generally favor tissue regeneration [1,2]. Moreover, the 3D porous architecture of the scaffold can affect cell migration by regulating the transport of their use as support materials for different drug loadings. Scaffolds can be designed to permit the release of drugs in a sustained and controlled manner over a desired period of time [3,4].

Thermally induced phase separation (TIPS) is an easy and economic technique that can provide suitable porous scaffolds for tissue engineering applications, although it seems also interesting to render new systems for drug delivery and even has been employed in non-medical fields, as for example synthetic membranes [5-7]. The method is based upon thermodynamic demixing of a homogeneous polymer solution into polymer-rich and polymer-poor phases [8]. The solvent in the polymer-lean phase (as well as that incorporated in the polymer rich phase) can subsequently be eliminated by extraction, evaporation or sublimation [9], leaving behind a highly porous polymer network [10,11]. The final structure and pore morphology of the phase-separated polymer matrices are greatly dependent on the polymer and solvent used, the polymer concentration, the phase-separation temperature and the temperature gradient applied to the polymer solution [12]. In this process, the polymer-solvent system can experience a solid-liquid or a liquid-liquid phase separation [13]. In the first case, the final structure and pore architecture of the resulting foam widely depends on the used solvent and its crystallization temperature together with the usual parameters previously indicated [12]. Typically, an organic solvent with quite high freezing point like 1,4 dioxane (11.8 °C) is used for fabrication of such synthetic polymer matrices. In addition, by controlling the cooling process, matrices may have isotropic or anisotropic pore architectures [13-15]. Specifically, depending on the capability to apply a uniaxial temperature gradient an anisotropic oriented-pore structure could be derived [15,16]. Liquid–liquid phase separation in a polymer solution may occur during the cooling process when the polymer-solvent affinity is very weak and the demixing takes place at higher temperatures than the solvent crystallization temperature [17].

Porous 3D scaffolds have been prepared using various fabrication techniques from biodegradable polymers, mainly polyesters such as poly(lactide) (PLA), poly(glycolide) (PGA), their copolymers (PLGA), and polycaprolactone (PCL) [18,19]. These synthetic materials have been demonstrated to be biocompatible and able to degrade into non-toxic components according to a controllable *in vivo* degradation rate [20].

Scaffolds from PLA [21,22], PLGA [23,24] and PCL [25,26] biodegradable polymers have also been fabricated by TIPS techniques and widely investigated for tissue regeneration applications. Poly(alkylene dicarboxylate)s constitute a different family of biodegradable polyesters with high potential, but probably less studied than those polyesters derived from lactones and lactides [27]. Poly(butylene succinate) (PBS), a polymer supplied by Showa High Polymers as Bionolle,™ is currently the most commonly employed poly(alkylene dicarboxylate) due to its relatively low production cost, good thermal and mechanical properties and easy processability [28,29].

PBS and PBS-based copolymers have been studied for tissue engineering applications mostly in the form of films [30-33], scaffolds from salt leaching [34-36], electrospinning [37-40] or extrusion [41]. In addition, preparation of PBS microspheres [42] and nanocarriers [43,44] for drug delivery has also been reported. Both *in vitro* and *in vivo* biocompatibility of PBS have been demonstrated with the use of different cell lines [30]. Applications of PBS based materials and composites have been proposed in different kind of tissues, which can vary for example from a soft myocardial tissue to a hard bone tissue. Nevertheless, PBS is still not commercialized for biomedical applications since further research involving clinical trials seems necessary as well as the Food and Drug Administration approval for uses in biomedicine, which has not yet been received.

Concerning non biomedical applications, it should be indicated that microporous membranes of PBS have been prepared from PBS–chloroform solutions via TIPS using a coagulation bath of methanol. These PBS membranes appeared interesting to be employed as a prefilter for bioseparation processes [45]. PBS membranes have also been prepared by TIPS using 1,1,2,2-tetrachloroethane as a solvent and non-solvents such as methanol, methanol/isopropanol or isopropanol [46].

In the present study, the potential of TIPS technique as a one-step process for fabrication and drug incorporation into PBS matrices has been appraised. The effect of alterations in fabrication parameters on the thermodynamics and kinetics of TIPS process, the phase separation mechanism and therefore on the architecture and morphological features of the scaffolds is elaborated. New TIPS-based scaffolds are evaluated as delivery systems for curcumin (CUR) and piperine (PIP) as natural drugs with antitumor activity and different physical properties (e.g., hydrophilicity). Furthermore, curcumin, as a phenolic compound, displays an antioxidant and bactericide characteristics. We will finally address how important properties for bio-applications like drug release and biocompatibility can be modified by appropriate selection of fabrication parameters, specifically the intensity and direction of thermal gradient.

4.2. Experimental

4.2.1. Materials

Polybutylene succinate (PBS) is a commercial product, Bionolle® 1001 MD, supplied by Showa Denko K.K. (Germany). This polymer has a melt flow index of 1.6 g/10 min, measured at 190 °C under a load of 2.16 Kg according to ASTM-D1238.

CUR and PIP were purchased from Sigma-Aldrich (Spain). 1,4-Dioxane (DXN) and Tetrahydrofuran (THF) solvents were also purchased from Sigma-Aldrich, and used as received it.

Madin-Darby Canine Kidney (MDCK) and Normal Rat Kidney (NRK) cells were selected as epithelial-like cells. Both lines were obtained from ATCC (USA). MTT reagent (3-(4,5-dimethylthiazol-2-yl)-2,5-diphenyl-2H-tetrazolium bromide) was purchased from Sigma-Aldrich (Spain).

4.2.2. Determination of Cloud Point

The cloud point of polymer solutions was evaluated by visual turbidimetry as described elsewhere [14]. In brief, in order to predict the location of binodal curve in the vicinity of the concentration used for fabrication of scaffolds (i.e. 2.5% (*w/v*)) in the PBS-dioxane and PBS-THF phase diagrams, the cloud points of 2.5, 5 and 7.5% (*w/v*) solutions were determined. The solutions were poured into transparent sealed glass containers and then were slowly cooled in a silicon bath at an average rate of 0.4 °C/min. The temperature at which the clear solution became turbid was determined as the cloud point of the polymer solutions. At least three independent turbidimetric assays per sample were performed for each material and the results were averaged and the standard deviations determined.

4.2.3. Optical Microscopy

Optical micrographs were taken with a Zeiss Axioskop 40 Pol light polarizing microscope equipped with a Zeiss AxiosCam MRC5 digital camera. Temperature was controlled with a Linkam system having a THMS 600 heating and freezing stage connected to an LNP 94 liquid nitrogen cooling system. Drops of the different polymer solutions were placed between a slide and the cover slide and observed in bright field.

4.2.4. Scaffold Preparation

Phase separation was induced to selected polymer solutions by decreasing the temperature and then the porous structures were formed after solvent removal. Primarily, PBS was dissolved at concentrations of 2.5% (*w*/*v*) in DXN or THF by heating under stirring the solvent/polymer mixture in closed and sealed containers (i.e., up to about 75 °C for both DXN and THF solutions). The solutions were poured into a cylinder-shaped glass container with a diameter of 14 mm and height of 40 mm and then sealed. Samples were immediately incorporated to the corresponding cooling devices pre-set on -20 °C (freezer), -74 °C (freezer) and -196 °C (liquid nitrogen, LN_2). In this process, phase separation through solid-liquid and/or liquid-liquid phase separation mechanisms could occur during cooling. Cooling process was performed under different thermal gradients, that is, from a relatively high temperature at which the solution is still clear and homogenous to the temperature of the selected bath. Glass containers were immersed in the selected baths to apply a multidirectional temperature gradient (random cooling) or by contacting only their bottom surface with the cooling device (by inserting the containers into a central hole of a polystyrene mold in order to prevent the heat transfer through the side walls) for getting a uniaxial temperature gradient (oriented cooling). After remaining for 24 hours or 30 min in the -20/-74 °C or LN_2 cooling baths, the samples were freeze-dried for a 120 h period using a Virtis® 6201-3120 lyophilizer (Gardiner, NY, USA). The resulting porous scaffolds were then dried in a vacuum oven at room temperature to reach a constant weight.

4.2.5. Scaffold Characterization

SEM characterization. The porous morphologies of the scaffolds were examined with scanning electron microscopy (SEM) (Focus IonBeam Zeiss Neon 40 instrument, Carl Zeiss, Germany) at 5 kV, and controlling by Smart Tiff software (Carl Zeiss SMT Ltd., Germany). The samples were cut by a razor blade or fractured after being frozen in liquid nitrogen for several minutes and then were coated with carbon for 700 s using a sputter coater (Mitec K950 Sputter Coater, England).

FTIR. Infrared absorption spectra were recorded in the 4000-500 cm^{-1} range with a Fourier transform spectrometer (FTIR 4100, Jasco, Japan), using a MKII Golden Gate attenuated total reflection (ATR) accessory (Specac, England).

DSC and TGA. Calorimetric data were obtained by differential scanning calorimetry (DSC) with a TA Instruments (USA) Q100 series equipped with a refrigeration cooling system (RCS). Experiments were conducted under a flow of dry nitrogen, using indium as a calibrant and a sample weight of approximately 5 mg. Heating and cooling runs were carried out at a rate of 10 °C/min. Thermal degradation was studied at a heating rate of 20 °C/min with around 5 mg samples in a Q50 thermogravimetric analyzer (TGA) of TA Instruments (USA) and under a flow of dry nitrogen. Test temperatures ranged from 50 to 600 °C.

Contact angles: Contact angles (CA) were determined at room temperature with sessile drops using an OCA-15 plus Contact Angle Microscope (Dataphysics, USA) and SCA20 software. Contact angle values of the right and left sides of distilled water drops were measured and averaged. Measurements were performed 10 s after the drop (0.5 μL) was deposited on the sample surface. All CA data were an average of six measurements on different surface locations.

XRD. X-ray powder diffraction patterns were obtained with a PANanalytical X'Pert diffractometer with Cu Kα radiation (λ=0.1542 nm) and a Silicon monocrystalline sample holder. Deconvolution of WAXD peaks was performed using the PeakFit 4.0 program.

4.2.6. Determination of the Loaded Drugs in the Scaffolds

CUR or PIP drugs were loaded by dissolving them, together with the PBS polymer, in the selected solvent (i.e., DXN) before inducing the TIPS process. Drug/PBS theoretical ratios were chosen to get samples with 5 and 100 wt% of CUR or PIP. Quantification of the charged drug was performed by dissolving the matrix in a small volume of chloroform, and a subsequent extraction with phosphate buffer saline (SS)/ethanol (EtOH) mixture (3:7 *v*/*v* ratio). Absorbance measurements at 343 nm (PIP) and 430 nm (CUR) were taken using a Shimadzu UV-3600 (Japan) spectrophotometer. Drug concentrations were determined by means of the corresponding calibration curves. Each measurement was performed in triplicate.

4.2.7. Release Experiments

Controlled release measurements were made with pieces weighting around 13 mg that were cut from the corresponding freeze-dried scaffolds loaded with CUR or PIP. Each sample was incubated at 37 °C in an orbital shaker at 120 rpm in a 50 mL tube filled with 40 mL of the release medium for 1 week. Specifically, a Dulbecco's modified Eagle's medium (DMEM with 4500 mg/L of glucose, 110 mg/L of sodium pyruvate and 2 mM of L-glutamine) supplemented with 10% fetal bovine serum (FBS) was employed. At predetermined time intervals, 1 mL was withdrawn from the release medium. The release volume was kept constant by addition of fresh medium. Finally, samples were dissolved in 600 µL of chloroform and extracted with SS/EtOH (3:7 *v/v* ratio) to recover the occluded drug. Drug concentrations were evaluated by UV spectroscopy as previously indicated. All drug release experiments were carried out using three replicates and the results were averaged (mean ± SD).

4.2.8. Cell Adhesion and Proliferation Studies

Both MDCK and NRK cell lines grow adherently, and were cultured in DMEM with 10% FBS, 50 U/mL penicillin and 50 mg/mL streptomycin at 37 °C in a 10% humidified atmosphere of 5% CO_2 and 95% air. Culture media were changed every two days. For sub-culture, cell monolayers were rinsed with PBS buffer and detached by incubating them with 0.25% trypsin/EDTA for 2-5 min at 37 °C. The incubation was stopped by resuspending in 5 mL of fresh medium and the cell concentration was determined by counting with Neubauer camera and using 4% trypan blue as dye vital.

Drug-loaded/unloaded PBS scaffolds were cut off into pieces of 1 cm x 1 cm. These samples were placed in tissue culture plates of 24-wells and fixed to bottom plate with a small drop of silicone (Silbione® Med Adh 4300 RTV, Bluestar Silicones France SAS, Lyon, France), sterilized by exposition to UV light for 15 min. 100 µL containing $5x10^4$ cells to assess cell adhesion, and $2x10^4$ cells for the cell proliferation assay were seeded in each well and incubated for 60 minutes to allow cell attachment to the material surface. Then, 1 mL of culture medium was added to each well. Quantification of viable cells was performed after 24 h and 7 days to evaluate the cellular adhesion and proliferation, respectively. The control was performed by cell culture on the plate without any material.

The percentage of cells adhered or proliferated was quantified through the MTT (3-(4,5-dimethylthiazol-2-yl)-2,5-diphenyltetrazolium bromide) assay [46]. After 24 h or 7 days, 50 µL of MTT (3 mg/mL) were added to each well in the plates and incubated for 4h. After that, samples were washed twice with PBS and the specimens deposited in a new plate. 1 mL of dimethyl sulfoxide (DMSO) was subsequently added and the absorbance was measured at 570 nm in a microplate reader (Biochrom EZ-Read 400) after 15 min of gentle stirring.

4.2.9. Statistical Analysis

Three replicas were evaluated, and the corresponding values were averaged and graphically represented. The statistical analysis was performed by one-way ANOVA to compare the average values of all groups, Tukey-test was then applied to determine a statistically significant difference between two studied groups. The tests were performed with a confidence level of 95% ($p < 0.05$) (Origin Pro Software, USA).

4.3. Results and Discussion

4.3.1. Morphology of PBS scaffolds prepared by TIPS

TIPS is a simple technique that allows preparing highly porous polymeric/composite scaffolds with structural interconnectivity suitable for tissue engineering applications. Due to the deep influence of parameters like solvent/polymer pair, cooling rate and condition on the TIPS mechanism and obtained architecture [17], such parameters must be carefully considered to yield scaffolds with desired morphologies.

Present work demonstrates that PBS becomes a biodegradable polymer that can be easily processed by TIPS, being possible to get a wide variety of morphologies by an appropriate selection of the solvent and control of the cooling process. In this way, solid-liquid and liquid-liquid phase separation were successfully performed using DXN and THF solvents, respectively, while oriented and random pore distributions could be achieved using uniaxial or multidirectional temperature gradients. Selected solvents were able to dissolve PBS at temperatures around 70-75 °C, which was slightly higher than the boiling point of THF (i.e. 66 °C) and lower than that of DXN (i.e., 101 °C). The use of sealed tubes made possible to dissolve the polymer in the boiling THF.

Scarce information about the solubility parameters of PBS can be found in the literature. Although the solubility parameter of 20.3 $MPa^{1/2}$ has been reported for PBS [47], the concept of Hansen´s three-dimensional solubility parameters is often used to estimate the miscibility or compatibility [48]. An estimation with group contribution method based on three-dimensional data [49] can be done, as reported by Valerio et al. [50]. According to equation (1):

$$\delta_T^2 = \delta_D^2 + \delta_P^2 + \delta_H^2 \tag{1}$$

Where δ_D, δ_P and δ_H are dispersive, polar and hydrogen bonding components of the Hansen's total solubility parameter (δ_T), respectively.

Accordingly, the total solubility parameter for PBS, DXN and THF can be estimated as 20.71, 20.47 and 19.46 $MPa^{1/2}$, respectively (being respectively 19.0, 1.8 and 7.4 $MPa^{1/2}$ the δ_D, δ_P and δ_H contributions for DXN and 16.8, 5.7 and 8.0 $MPa^{1/2}$ for THF [51]). The estimated δ for DXN is totally in accordance with the experimentally reported value of 20.5 $MPa^{1/2}$ [13] and clearly closer to the PBS value, compared to THF. Therefore, a different phase separation behavior could be expected when cooling the respective homogeneous solutions as verified in the next sections.

Cloud point is a temperature at which the liquid–liquid phase separation happens in the polymer solution during cooling. As a result, the clear polymer solution becomes turbid [52]. Although the boundary of the liquid–liquid demixing region in the polymer-solvent phase diagram is usually named binodal curve, the more appropriate term for polydisperse polymers is "cloud point curve" [9]. Figure 1 shows the variation in the cloud point as a function of polymer concentration for the two studied binary systems of PBS-DXN and PBS-THF.

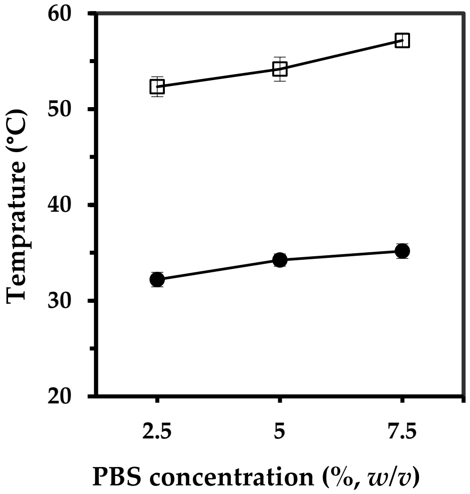

Figure 1. Cloud point determination of PBS-DXN (full circle symbols) and PBS-THF (empty square symbols) solutions with 2.5, 5 and 7.5% (*w*/*v*) concentrations.

According to the experimental cloud point curves, a higher temperature was observed as the polymer concentration increased (at the evaluated concentration range, i.e. 2.5-7,5% (*w*/*v*)). Additionally, the location of the cloud point curve for PBS-THF solutions is at higher temperatures than that determined for PBS-DXN solutions. Results mean that liquid-liquid demixing for the former solutions occurs at higher temperatures compared with the later. These observations are logically in accordance with the indicated analysis of the Hansen Solubility Parameters (HSP) that pointed out a higher compatibility between PBS-DXN pair compared with PBS-THF.

In this situation, the homogenous one-phase region in the polymer-solvent phase diagram expands, and therefore the boundary of liquid–liquid phase separation (binodal curve) shifts to lower temperatures [1]. Accordingly, the lower cloud point of PBS-DXN solution is speculated to be the result of its stronger polymer-solvent interactions. Specifically, the average cloud points of 2.5, 5 and 7.5% (*w*/*v*) solutions of PBS-DXN are 32, 34 and 35 °C, while in case of THF the temperatures increased to 52, 54 and 57 °C, respectively.

Separation of phases was also evaluated through optical microscopy observations during controlled cooling rates. Drops were placed between two cover slides at an initial temperature at which a homogeneous solution was obtained. Measurements were performed at different cooling rates (i.e., 5 and 10 °C/min and also according to the slow natural/spontaneous cooling from 60 °C to the room temperature) for the solutions with different PBS concentrations (i.e., 2.5, 5 and 7.5 wt%). Results were in agreement with the previous cloud point determination but allowed us a direct observation of morphologies (Figure 2).

The development of polymer-rich phase drops was clear in the experiments performed in DXN as well as the crystallization of the solvent at temperatures below the DXN freezing point (11.8 °C). This temperature was dependent on the cooling rate and the polymer concentration. It should be pointed out that PBS was able to crystallize as spherulites/leafy structures in the drops (i.e., polymer beads), especially at slower cooling rates. Logically the solvent rendered randomly-oriented crystals when temperature lower than DXN crystallization was achieved.

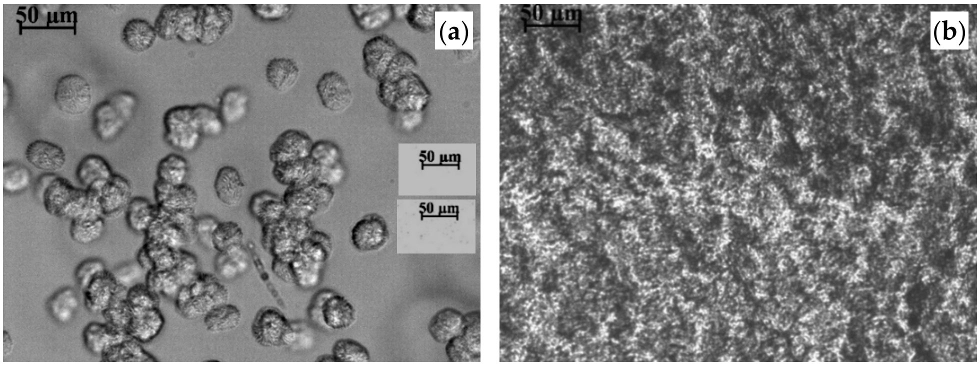

Figure 2. Optical micrographs taken during cooling of a 7.5% (*w*/*v*) PBS-DXN solution from an initial temperature of 60 °C: (**a**) Crystallization of PBS in the phase-separated drops and formation of leafy-structured polymer beads at around 30 °C during a slow natural cooling process. Insets correspond to 32 °C (up) and 30.5 °C (down). Note that separation of phases started at this temperature as a typical nucleation and growth mechanism. (**b**) Structure observed at -25 °C after cooling at the rate of 5 °C/min, displaying advancement of liquid-liquid phase separation through spinodal decomposition mechanism, followed by crystallization of DXN.

4.3.2. Scaffolds from Solid-Liquid Phase Separation with Random Pore Distribution

The rapid cooling of PBS-DXN solution allowed inducing the solid-liquid phase separation and the solidification of the solvent. The application of a multidirectional/random temperature gradient rendered isotropic solvent crystals, which after the long freeze-drying process led to randomly/oriented pores. The homogeneous solution attained at 75 °C became cloudy when temperature reached around 32, 34 and 35°C depending on the polymer concentration. These temperatures were relatively close but higher than those corresponding to the solidification of DXN. Crystallization of liquid DXN results in the formation of solid monoclinic phase I, which can undergo a solid-state transformation to monoclinic phase II at lower temperatures [53].

Regarding the roughly adjacent cloud point and DXN crystallization temperature, a limited period of time is expected between liquid-liquid and solid-liquid phase separations upon cooling. Therefore, at high cooling rates, the solution may directly undergo a solid–liquid phase separation (i.e., when the horizontal line corresponding to the solvent crystallization temperature is reached), due to the limited time for the hypothetical liquid–liquid demixing that should occur below the binodal curve (Figure 3). Thus, solid-liquid phase separation practically controls the resulting morphology at high cooling rates. The solvent forms large crystals through 3D nucleation and growth and subsequently macropores of around 70-90 microns (Figures 4a and 4b) after the sublimation process.

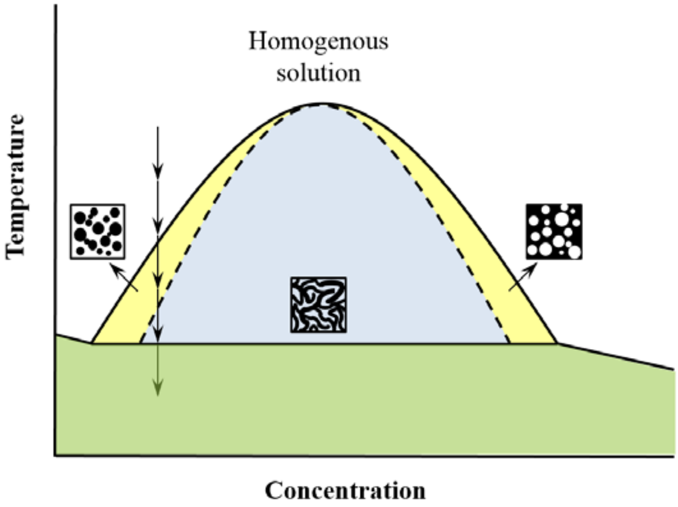

Figure 3. A schematic binary phase diagram for a polymer-solvent system that undergoes liquid-liquid phase separation followed by solid-liquid phase separation, showing one phase region (homogenous solution), liquid-liquid phase separation regions (yellow and blue, that is metastable and unstable regions with NG and SD mechanisms, respectively) and solid-liquid phase separation region (green, region with crystallized/frozen solvent). Solid-line and dashed-line curves represent binodal and spinodal curves (the boundaries of metastable and unstable regions), respectively. Arrows schematically indicate the phase separation evolution during cooling for an initial solution with a relatively low polymer concentration used for the fabrication of porous scaffolds in this study. Insets indicate the typical morphology obtained from each region, arisen from the corresponding mechanism (i.e. NG or SD mechanisms).

Due to the fact that liquid-liquid phase separation through spinodal decomposition (SD) mechanism is also a fast process [54], it could took place to some extent during the fast cooling (i.e., before or during solvent crystallization). In such cases that the occurrence of different phase separation mechanisms is thermodynamically possible, the kinetics of these mechanisms determine whether or not the thermodynamically favoured mechanism happens or not, or to what extent the transition occurs [9]. The liquid-liquid phase separation takes place through SD mechanism in the unstable region (Figure 3), producing a bicontinuous pattern of interconnected polymer-reach and -lean phases [12], that form a network of small interconnected pores after solvent removal [54]. This phenomenon produce a minor but important effect on the morphology. Small pores (several microns) are expected to be formed in the walls of the macropores after sublimation, being therefore enhanced the interconnectivity of the scaffold structure.

The fabrication conditions using DXN solvent and -20 and -74 °C cooling baths allow the partial occurrence of liquid-liquid phase separation and also polymer crystallization slightly before or during the solvent crystallization (as their corresponding morphological influence is discernible in the final structure). But as it will be discussed later, the effect of such phenomena can be disregarded when a rapid quenching in LN_2 is applied for fabricating oriented-pore scaffolds.

The slower cooling condition logically gives a greater opportunity for the slower mechanisms to occur and affect the final morphology. The nucleation and growth (NG) mechanism occurs slowly below the binodal curve and in the metastable region [54] producing a bead-like structure [9,55] that arises from the polymer-rich droplets formed in a liquid matrix of the polymer-lean phase [12].

These structures are clearly observed to a greater extent in the scaffolds prepared through slow cooling (i.e., using -20 °C bath, Figures 4c and 4d) than fast cooling (i.e., using -74 °C bath, Figures 4a and 4b). The very slow NG mechanism of polymer crystals [12] could take place before or during the solvent crystallization, significantly upon slower cooling. The leafy structure showed at high magnification (e.g., see the inset of Figure 4c) is characterized by randomly oriented and connected polymer leaves. Taking into account the dimensions, these polymer leaves are speculated to be stacked lamellae that have developed a significant curvature [56]. Interestingly, an unwanted temperature gradient may provide a slower cooling condition in the inner part (centre) of the scaffolds compared to their surface. This gradient results in the formation of both mentioned NG-derived morphologies (i.e., bead-like and leafy structures arise from liquid-liquid phase separation and crystallization of the polymer, respectively) to a higher extent in the bulk than in the surface of the scaffolds (Figures 4a and 4c). Conversely, macropores should be better outlined and dominant in the surface of the scaffolds (Figure 4b and 4d). A similar trend was also observed in the surface and the bulk of poly(hydroxybutyrate-*co*-hydroxyvalerate) scaffolds prepared previously by TIPS technique [14].

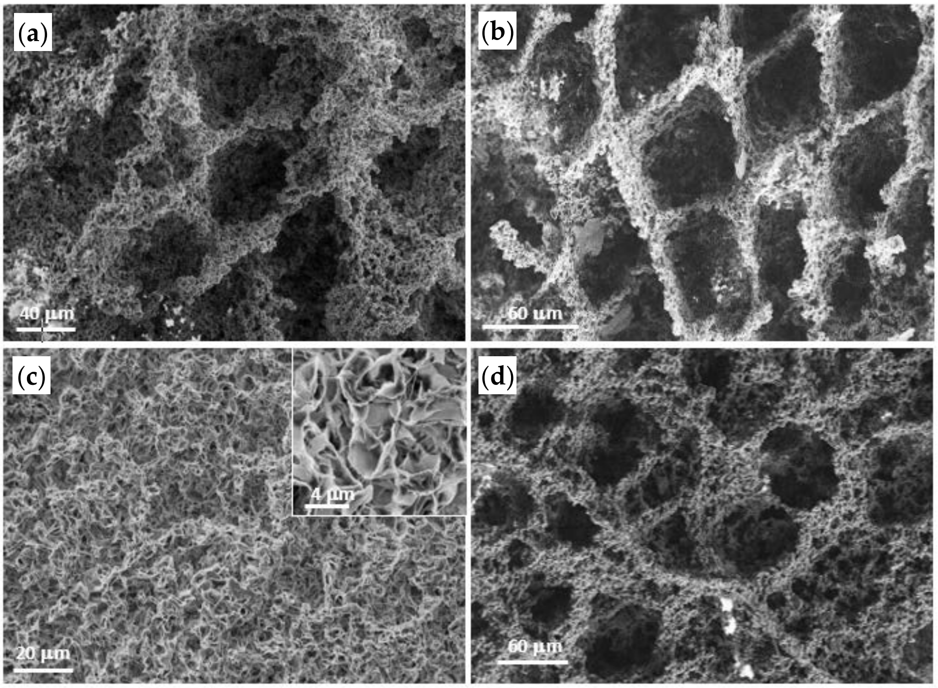

Figure 4. SEM micrographs showing the cross-sections (**a**,**c**) and the top surface (**b**,**d**) of porous PBS scaffolds prepared through solid-liquid phase separation using 1,4 dioxane and applying a random temperature gradient in baths at -74 °C (**a**,**b**) or at -20 °C (**c**,**d**).

Crystallization of PBS during the scaffold preparation is clearly demonstrated through X-ray diffraction patterns and the DSC heating runs (Figure 5). Thus, X-ray diffraction patterns of prepared scaffolds (Figure 5a) indicate that PBS crystallized according to its monoclinic α form, which is typically obtained under quiescent conditions. This structure is defined by a $P2_1/n$ space group and a unit cell containing two molecular chains and having dimensions of a = 0.523 nm, b = 0.912 nm, c (fiber axis) = 1.090 nm, and b = 123.9° (Ihn et al. 1995). Stronger peaks correspond to the (020), (021), (110) and (111) reflections at 0.459, 0.413, 0.398 and 0.313 nm. An amorphous halo centered at 0.439 nm is clearly observed, being possible to infer from deconvolution a crystalline degree between 58% and 69%. Logically, crystallinity decreased as the bath temperature did.

DSC heating runs showed two melting peaks indicative of a lamellar reordering process where thinner lamellae melted and crystallized into thicker crystals as has been reported for PBS. Melting enthalpy clearly decreased when the bath temperature did (i.e., from 108.7 J/g to 76.9 J/g for PBS scaffolds coming from baths at -20 °C and -74 °C, respectively, see Table 1). The low temperature melting peak is related to stable thin lamellar crystals that no experience the reordering process during the heating scan. Note that this population of stable lamellae disappears when the sample is quickly crystallized (i.e., when the LN2 bath was employed).

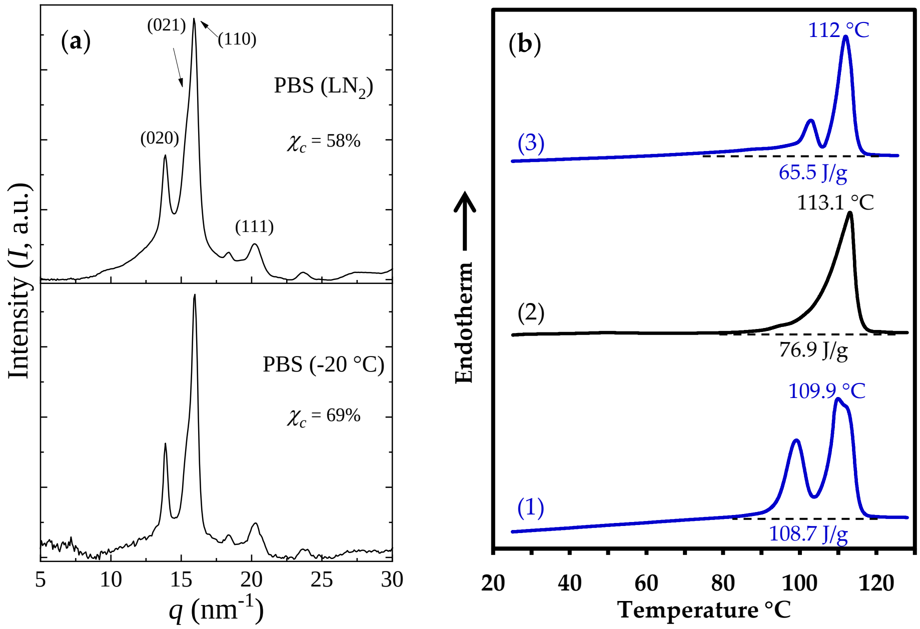

Figure 5. (**a**) X-ray diffraction pattern from PBS scaffolds prepared using LN2 and -20 °C cooling devices. (**b**) DSC heating runs of PBS scaffolds prepared at -20 °C (1) and -196 °C (2) quenching temperatures. The scan 2nd heating run of a melted scaffold (cooled at 10 °C/min) prepared is also shown for comparative purposes (3).

4.3.3. Scaffolds from Solid-liquid Phase Separation with Oriented Pore Distribution

The very fast cooling condition, that is, quenching the clear solution to -196 °C, give rise to prevention of the thermodynamically favoured process (i.e. liquid-liquid phase separation) in the limited temperature range between the binodal curve and solvent crystallization. In this situation a pure solid-liquid phase separation-derived structure is attainable, while crystallization of the polymer may occur later and stabilize the phase-separated structure.

By reaching the solvent crystallization temperature during cooling (horizontal line in Figure 3), the DXN solvent crystallizes and the polymer is expelled from the solvent crystallization front. This solid-liquid phase separation rapidly develop throughout the solution and all the solvent crystallizes. Insulating the perimeter walls of the solution-containing cylindrical glass vial with a polystyrene wrapping mould (except the bottom of the vial), effectively prevent the radial heat transfer and only permit the solvent crystallization progress towards the axial direction. The application of such uniaxial temperature gradient rendered anisotropic solvent crystals, which after the long freeze-drying process led to tubular oriented pores (Figure 6). It is worth to remark the large dimension of DXN crystals and the clearly different morphology of PBS walls

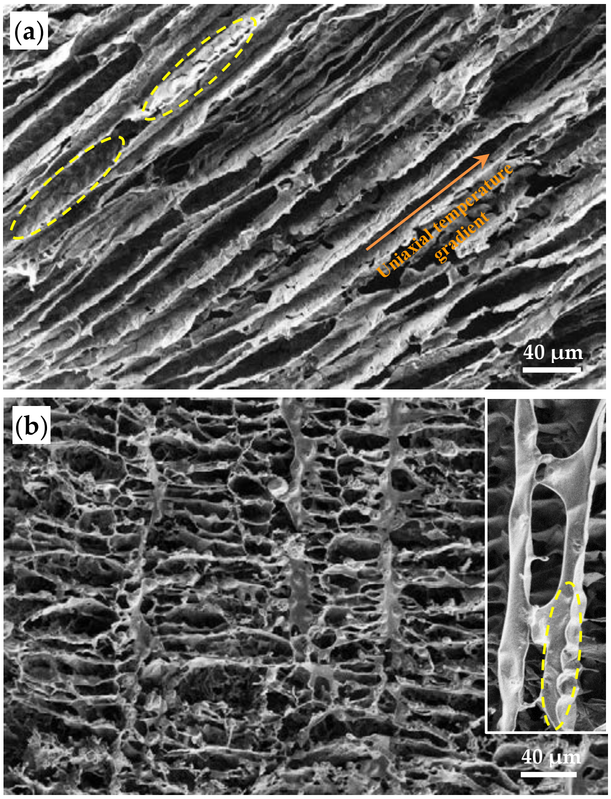

Figure 6. SEM micrographs showing cross-section (**a**) and top surface (**b**) of porous PBS scaffolds prepared through solid-liquid phase separation using DXN, and applying a uniaxial temperature gradient in LN_2. Yellow ellipsoids in (**a**) indicates crystalline structures in the PBS films forming the pore walls. The inset of (**b**) shows the PBS concave films developed on the top surface.

Figure 6a shows the cross-section of the scaffold prepared using a uniaxial thermal gradient in LN_2 cooling device. A relatively uniform distribution of tubular pores with lengths that can reach 500 μm and diameters around 20-40 μm is characteristic. Figure 6b shows that in the surface of this scaffold which is asymmetric and corresponds to ellipsoids with major and minor axes around 40 and 20 µm at maximum. This ladder-like morphology is typically observed on the surface or transversal cross-section (i,e., top view) of the oriented-pore scaffolds, prepared by applying the same longitudinal cooling direction [57,58]. This ladder-like morphology includes repeating units of channels and partitioning walls which are parallel and perpendicular to the temperature gradient (i.e. solidification direction), respectively [57].

By using the uniaxial cooling system and -74 °C bath (Figure 7), the both tubular structure formed in the cross-section and the ladder-like morphologies formed in the surface are less organized than those formed in LN_2 bath. It is logical because under lower thermal gradient the DXN crystals to a limited extent will be able to grow in other directions other than the uniaxial one.

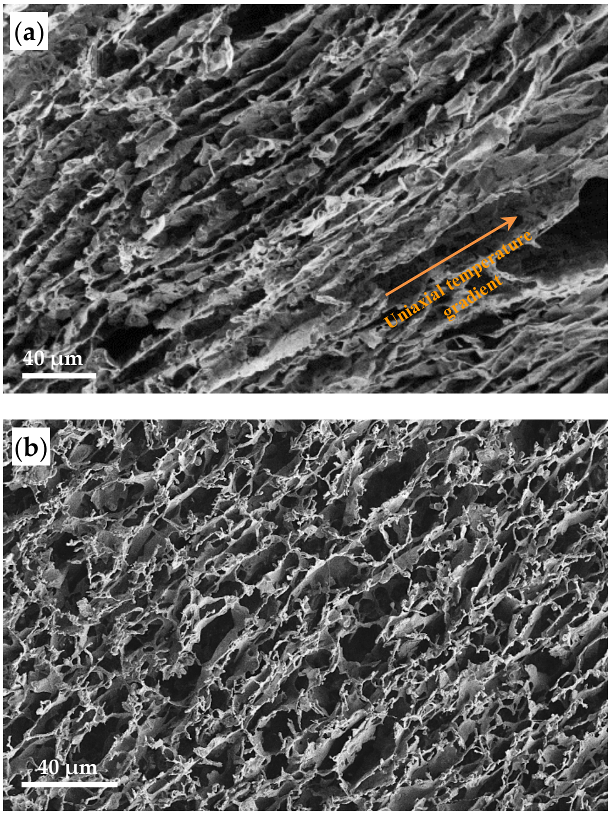

Figure 7. SEM micrographs showing cross-section (**a**) and top surface (**b**) of porous PBS scaffolds prepared through solid-liquid phase separation using DXN, and applying a uniaxial temperature gradient in a -74 °C bath.

Considering the morphology of the oriented pore walls, it seems that under the anisotropic conditions, crystallization of PBS in the concentrated phase took place after the development of DXN crystals (at least under the high temperature gradient caused by LN_2 bath). This striking feature can be envisaged in the texture of thin polymer walls of the oriented-pore scaffolds prepared in LN_2 cooling bath. This texture is indicative of a supramolecular spherulitic structure, which is visible even at the low magnification (see yellow ellipsoids in Figure 6a). This feature is also noticeable in the surface image of these scaffolds, where the small flat and narrow polymer films in the pore walls have such spherulitic texture (inset of Figure 6b).

High magnification micrographs of the polymer walls revealed a clear spherulitic texture (Figure 8). Thus, bidimensional spherulites with diameters of 20-30 μm and less than 3 μm thick grew from well-defined nuclei and developed a ringed texture having a regular spacing close to 2 μm between consecutive rings. A final nucleation density around 0.01 nuclei/μm^2 was also determined.

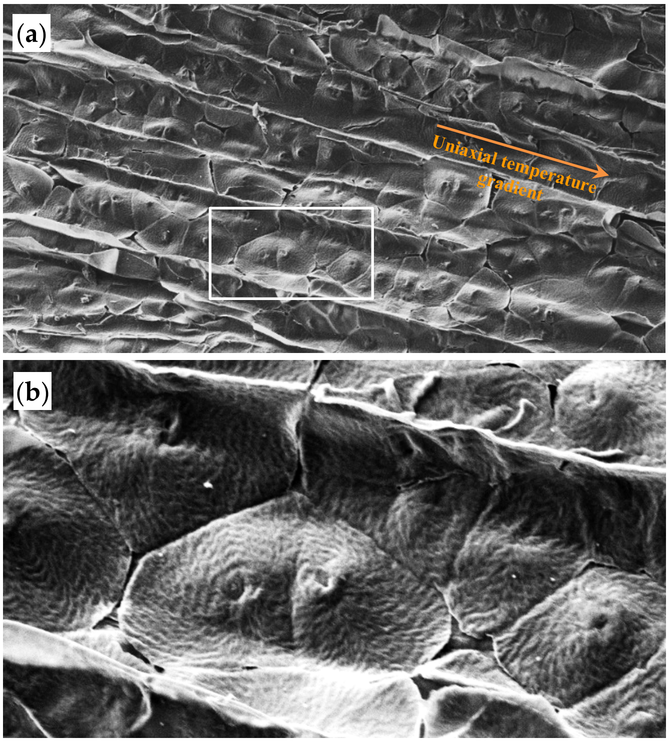

Figure 8. (**a**) SEM micrograph showing the cross-section of the PBS scaffold having oriented pores and prepared from a DXN solution under the thermal gradient provided by LN_2. (**b**) Higher magnification of the white rectangle in (**a**). Note the formation of planar spherulites in the thin walls of the scaffold.

It is known that crystallization of PBS from quiescent melt can led to different spherulitic morphologies. In general, ringed or banded textures have been obtained and have been interpreted as consequence of a twisting of radial lamellar crystals. Nevertheless, solution crystallization in thin films is more complicated and two different underlying origins have been proposed for the 2D ring-banded structure: a periodic lamellar twisting with change of the crystal orientation and a rhythmic variation of the radial thickness (i.e., changes on the packing mode of flat lamellae). In general, crystal morphologies obtained from solution are more variable than those attained from the melt and a rhythmic origin caused by the periodic presence of depletion zones in the crystal growth front (i.e. diffusion rate of the polymer in the rich phase solution lower than the rate at which chains are consumed to form the crystalline lamellae) cannot be discarded [59-61].

DSC heating runs of scaffolds prepared from the uniaxial LN_2 gradient showed a single melting peak with a lower enthalpy than that determined for samples with randomly oriented pores prepared at -20 °C cooling bath. (Figure 5b). This feature is in agreement with a hindered crystallization and formation of PBS spherulites after the development of oriented DXN crystals. The absence of the low temperature peak is indicative of a deficient crystallization that led to less stable thin crystals since they immediately experience the thickening process during heating.

4.3.4. Scaffolds from Liquid-Liquid Phase Separation with Random Pore Distribution from THF Solutions

Considering the relatively high cloud point of PBS/THF solutions (about 50 °C) in the studied concentration for preparation of polymer scaffolds (i.e., 2.5% (*w/v*)), the locus of binodal curve which is the boundary of liquid-liquid demixing in the polymer-solvent phase diagram shifts to higher temperatures compared to PBS/DXN samples. As explained earlier, there is less compatibility between PBS and THF (greater differences in their solubility parameters), compared to PBS-DXN system. Thus, a lower strength of interaction between the solution components for the former system is expected (larger Flory-Huggins interaction parameter).

In this situation the homogenous solution easily separates to a two-phase system under cooling. On the other hand, due to the very low crystallization temperature of THF (-108 °C), the occurrence of solid-liquid phase separation in such solutions is unattainable in the studied conditions (disregarding the line corresponding to crystallization of the solvent in the schematic phase diagram (Figure 3). Hence, the liquid-liquid phase separation will be the dominant mechanism and control the morphology of such foams. Although in PBS/DXN systems the morphological trace of liquid-liquid phase separation -especially upon slow cooling- was detected, this mechanism was not predominant. In case of DXN, the effect of solvent crystallization even in slow cooling must be regarded, while it is negligible in THF case.

Liquid-liquid phase separation below the binodal curve happens through NG and/or SD mechanism. Since NG is a slow mechanism and SD is a fast one [54], changes in the cooling rate result in changes in the contribution of the morphologies arisen from these mechanisms (i.e., polymer beads were produced from NG mechanism and open pores between several to tens of microns were produced from SD). The morphology of these scaffolds (Figure 9) confirms that upon slow cooling, the morphological effect of slow NG mechanisms is more evident. Accordingly, in Figure 9a, more contribution of bead-like morphologies (from NG of polymer-rich phase via liquid-liquid phase separation) and also leafy structures (from NG of polymer crystals) is detectable. Since polymer beads and leaves are suspended in a matrix of polymer-lean phase (i.e., no/poor connectivity between them), the porosities collapse to some extent after removing the solvent. In higher magnification (inset of Figure 9a), a beady-leafy structure is clearly observed, while thicker polymer leaves (compared with those formed from the PBS-DXN solutions in the same condition) indicates that a more complete crystallization process has led to the establishment of lamellar stacks in a larger scale.

Under higher cooling rate condition (Figures 9b and 9c), the contribution of fast SD mechanism during liquid-liquid phase separation process is more than the slow NG mechanism. Accordingly, polymer-rich and polymer-lean phase areas with perfect interconnectivies are formed through SD mechanism, having more opportunity for each phase to join/merge and increase their dimensions/size. By developing the process, the system start to minimize the free energy through decreasing the interfacial energy via coalescence of the separated phases, resulting in formation of a thicker bicontinuous network (i.e., thicker pore walls and also larger pores). Such behavior is more dramatic in the surface than in the cross section, due to the previously explained surface-to-center cooling rate gradient. The higher local cooling rate in the surface results in the formation of more interconnected parts derived from the fast SD mechanism, and therefore there is a higher possibility for both phases to be merged and increase their dimensions.

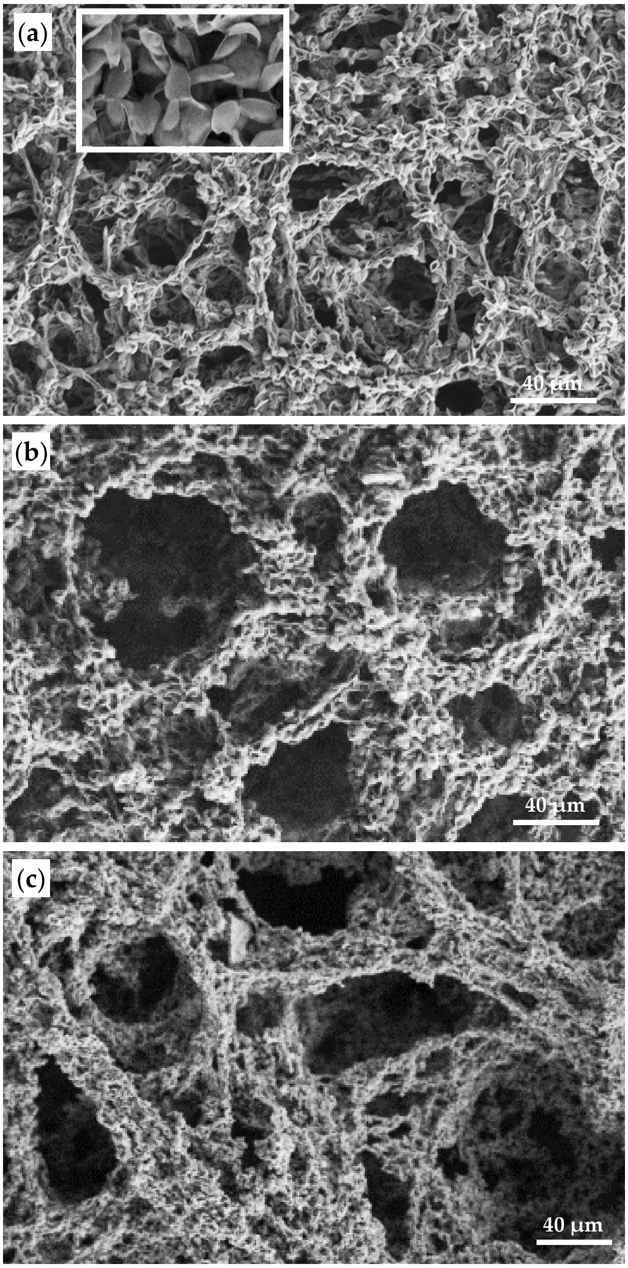

Figure 9. SEM micrographs showing the top surface (**a**,**b**) and the cross-section (**c**) of porous PBS scaffolds prepared through liquid-liquid phase separation using THF, by applying a random temperature gradient in baths at -20 °C (**a**) or at -74 °C (**b**,**c**).

4.3.5. Morphology of Drug-Loaded Scaffolds from Solid-Liquid Phase Separation

Incorporation of 5 wt% of CUR or PIP had no influence on the morphology (not shown) of the PBS scaffolds independently of the preparation method. This feature is logical considering the low drug loading and even the possible good interaction of CUR and even PIP with the polymer matrix. Obviously, results were clearly different for high loads (e.g., 100 wt%) as shown in Figure 10 for some representative scaffolds. This way, rounded agglomerates (CUR) and prismatic crystals (PIP) could be observed in the micrographs of top surfaces. High drug loading led to a decrease of voids caused by solvent sublimation and smoother surfaces as then will be evaluated. Such high loadings is speculated to affect the phase separation process and to some extent impede the formation of a well separated polymer-lean phase which later forms the porosities.

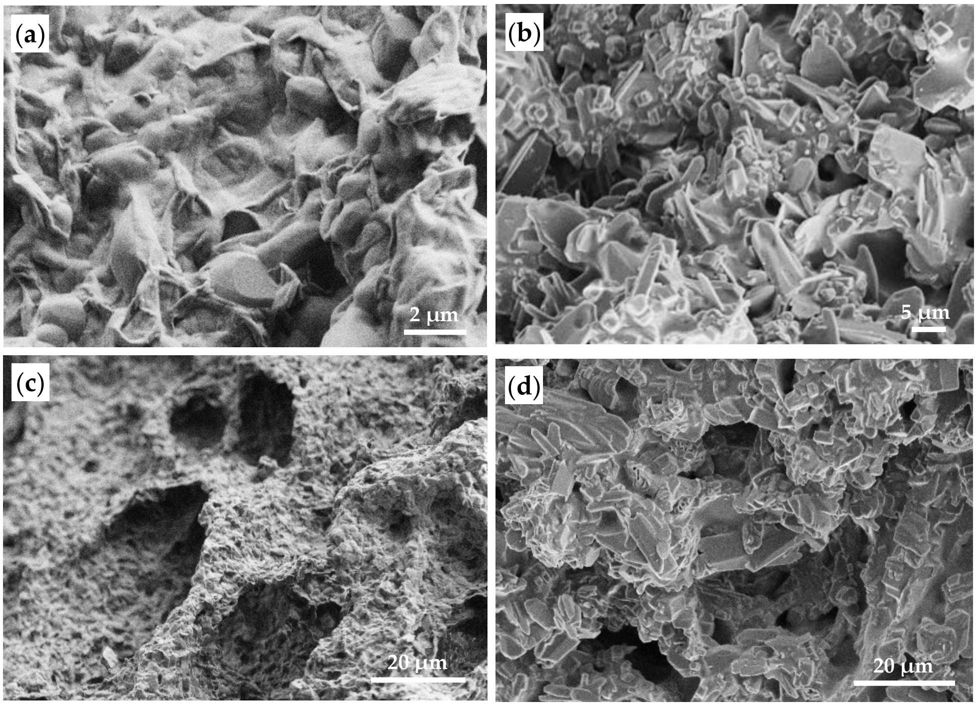

Figure 10. SEM micrographs showing the top surface (**a**,**b**) and the cross section (**c**,**d**) of PBS scaffolds loaded with 100 wt% of CUR (**a**,**c**) and PIP (**b**,**d**), which were prepared from DXN solutions at -20 °C cooling bath.

It is important to point out that CUR agglomerates appear well integrated in the PBS matrix (i.e., note the thin film that usually surrounded the particles). In this way, a typical Burst effect during release experiments could be precluded as well it could also be hindered for PIP as consequence of the well-developed crystalline phase. Morphologies corresponding to cross-sections (Figures 10c and 10d) revealed a homogeneous distribution of the drug particles within the scaffold skeleton.

4.3.6. Physicochemical Characterization of TIPS-Obtained Scaffolds

Contact angle measurements allowed getting conclusions about hydrophilicity and the surface roughness of the samples. Comparison between the contact angles determined for the smooth solvent casting films (prepared from PBS-chloroform solutions) and the rough TIPS-obtained scaffolds showed an increase from 83° to 117°/141° (oriented/random). Higher angles were determined for scaffolds with randomly oriented pores (e.g., those obtained from a bath at -20 °C, Figure 11). Incorporation of low concentration of CUR or PIP had a small influence on the contact angle values.

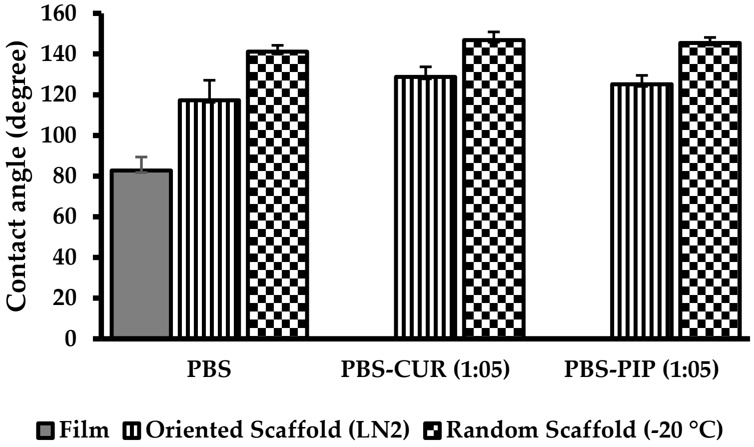

Figure 11. Contact angle measurements for a PBS film, scaffolds with oriented pored obtained from a LN$_2$ bath, scaffolds with random pores coming from a -20 °C bath, and the corresponding scaffolds incorporating 5 wt% of CUR or PIP.

Basically, the variation reflects the higher hydrophobicity of CUR or PIP with respect to the PBS polymer matrix. Thus, a slight increase in contact angle values with respect to the unloaded scaffolds was detected, being the effect slightly more significant for CUR (i.e., 125°/145° and 129°/147° for the oriented/random PBS scaffolds loaded with PIP and CUR, respectively). It can be postulated that he polar hydroxyl functional groups in the PIP structure somewhat increase the hydrophilicity compared to CUR-loaded samples. Accordingly, the formation of hydrogen bonding interactions with aqueous media is more expected for PIP, as it is confirmed by the release experiment results. The hydrophobic effect of drug incorporation was gentler at very high drug contents (i.e., 100 wt%) due to the lower porosity and therefore the decreased surface roughness, as revealed in the corresponding micrographs (Figure 10). Thus, values of 124°/127° and 128°/134° (oriented/random) were determined for the scaffolds loaded with 100 wt% of PIP and CUR, respectively.

Infrared spectra of 100 wt% loaded samples were basically a superposition of the spectrum of the pure polymer (strong bands at 1712 and 1152 cm^{-1}) and those corresponding to the added CUR or PIP drugs (Figure 12).

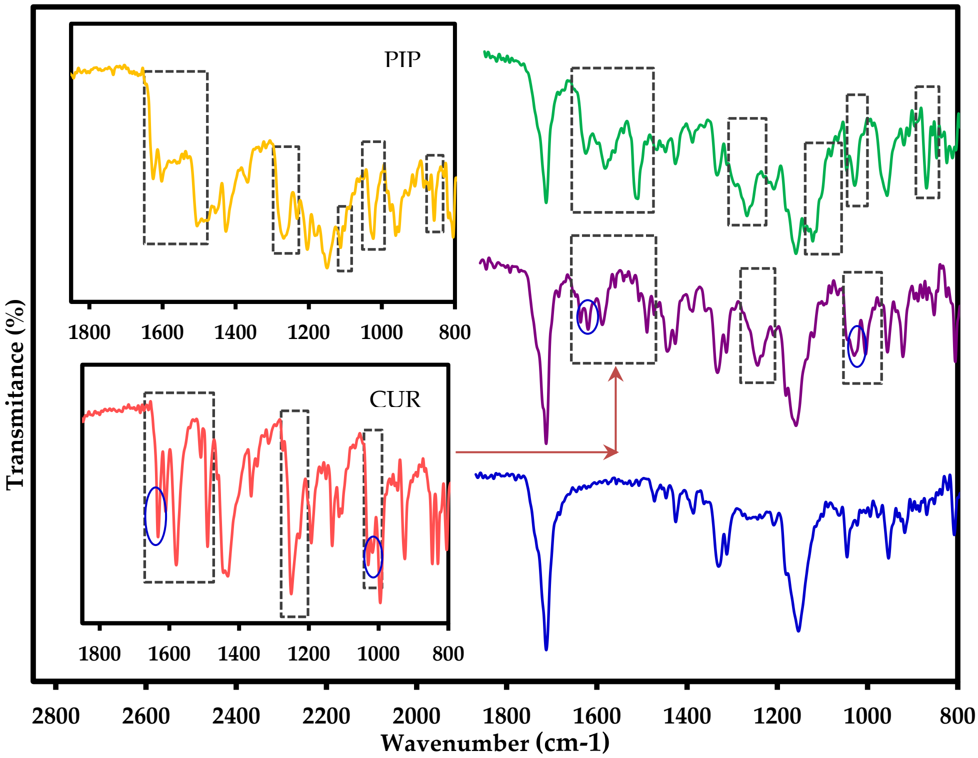

Figure 12. FTIR spectra of unloaded (blue) PBS scaffolds and loaded with 100 wt% of CUR (violet) and PIP (green). Insets show the spectra of pure drugs.

Nevertheless, the CUR absorption bands in the region between 1663 and 1478 cm^{-1} (left rectangle), 1294 and 1214 cm^{-1} (middle rectangle), 1064 and 976 cm^{-1} (right rectangle) showed slight changes in the loaded PBS scaffold (see blue ellipsoids in Figure 12), a feature that may be indicative of some drug-polymer interactions. Note that the spectrum of PIP loaded samples did not reveal any change associated to new potential interactions. Obviously, the presence of the drug was undetectable for the scaffolds with the 5 wt% drug content.

DSC heating runs of loaded scaffolds showed a clear influence of CUR on the melting behaviour of PBS despite the drug has a higher melting point (i.e., 169 °C in front of 115 °C) and the hypothetic CUR domains should remain in the solid state during fusion of PBS. Therefore, small amounts of CUR were incorporated during the phase separation process into PBS crystals and even in the amorphous phase. Figure 13 shows that the phase separation process (i.e., temperature and type of gradient) had also a clear influence on the final crystallinity and perfection of CUR-loaded samples (i.e., note the different curves for oriented and random pore structures). By contrast, the incorporation of PIP had a negligible effect on the melting behaviour, suggesting that no specific interactions between the drug and the PBS polymer were in this case established during the phase separation process.

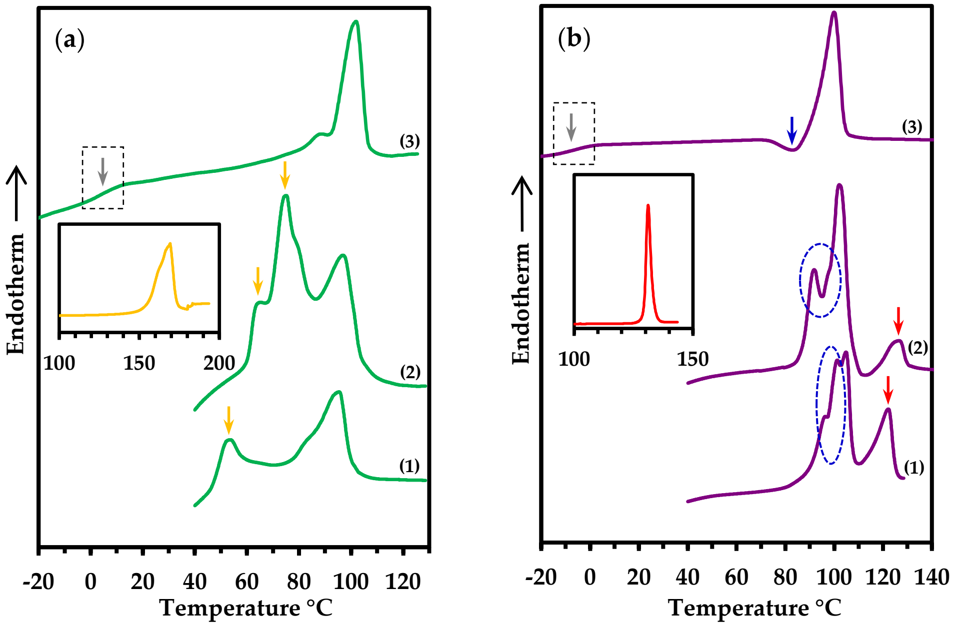

Figure 13. DSC heating runs of PBS scaffolds loaded with 100 wt% of CUR (**a**) and PIP (**b**). First heating run of oriented-pore (1) and random-pore (2) loaded scaffolds, and second heating run of random-pore loaded scaffolds after being crystallized from the melt (3). Inset corresponds to the heating runs of pure CUR (yellow) and PIP (red) drugs. Glass transition temperatures are indicated by grey arrows. Yellow arrows indicate minor melting peaks/shoulders derived from the presence of CUR. Blue arrow indicate the hot crystallization of PBS. Dashed ellipsoids point out differences on the relative intensities of PBS melting peaks. Red arrows indicate PIP melting peaks.

Table 1 summarizes the main calorimetric data from representative scaffolds, being reflected a clear decrease of both melting temperature and enthalpy for CUR-loaded samples. It is noticeable the presence of additional peaks and shoulders in the first heating run of CUR loaded scaffolds (Yellow arrows), which should be associated to the melting of PBS crystalline domains incorporating the drug. A complex fusion is characteristics of PBS and therefore some peaks have not been labelled.

Table 1. DSC calorimetric data of unloaded and drug loaded PBS scaffolds.

Sample	1st Heating		Cooling		2nd Heating		
	T_m (°C)	ΔH_m (J/g)	T_c (°C)	ΔH_c (J/g)	T_m (°C)	ΔH_m (J/g)	T_g (°C)
CUR	169.2	83.6					70.7
PIP	129.5	105.4			115.3	11.7	11.9
PBS (-20 °C)	109.9	108.7	84.8	69.4	112.0	65.5	-31.7
PBS (LN$_2$)	113.1	76.9	83.7	63.7	112.4	60.8	-29.5
PBS:CUR; 1:0.05 (-20 °C)	111.4	93.3	87.0	72.8	112.4	64.7	-22.8
PBS:CUR; 1:0.05 (LN$_2$)	110.7	75.0	80.7	69.4	110.4	65.7	-19.7
PBS:CUR; 1:1 (-20 °C)[1]	75.0	90.5	67.8	31.8	102.0	26.5	4.3
PBS:CUR; 1:1 (LN$_2$)[2]	95.3	47.6	45.8	20.3	94.8	23.9	8.6
PBS:PIP; 1:0.05 (-20 °C)	109.5	103.6	83.4	69.0	110.7	66.9	-26.0
PBS:PIP; 1:0.05 (LN$_2$)	110.9	83.9	81.6	66.5	110.5	63.9	-25.0
PBS:PIP; 1:1 (-20 °C)[3]	102.2	88.6	55.3	47.7	100.0	47.9	-7.2
PBS:PIP; 1:1 (LN$_2$)[4]	104.7	48.6	50.7	43.8	99.0	45.2	-8.4

[1] Minor peaks at 65.2 and 96.9 °C and a shoulder at 79 °C were observed in the first heating run. A shoulder at 88.7 °C was detected in the second heating run. All peaks correspond to PBS; [2] A minor peak at 53.5 °C and a shoulder at 84 °C were observed in the first heating run; [3] A minor peak at 91.7 °C and a shoulder at 97 °C correspond to PBS and a peak at 126.6 °C corresponds to PIP were observed in the first heating run. In the second heating run a hot crystallization exothermic peak at 82.9 °C was observed; [4] Minor peaks at 96.4 and 101.3 °C (associated to PBS) and a peak at 122.1 °C (associated to PIP) were observed in the first heating run.

Probably PIP crystallized in a deficient manner from the melt as deduced from the second heating run of the neat drug. Thus, melting enthalpies of 11,7 J/g and 105.4 J/g were determined for the second and first heating runs, respectively (Table 1). In addition, the melting temperature slightly shifted to the lower temperatures.

Scaffolds loaded with 100 wt% of PIP, exhibited in the first heating run a minor PIP melting peak (Figure 13b, red arrows) just after fusion of PBS and at temperatures quite lower than the melting temperature of the neat drug. This peak was not detected in the second heating run in agreement with the indicated behaviour of the neat PIP. The complex fusion of PBS was also detected in the heating run of PIP loaded scaffolds, being scarce the change corresponding to the melting temperatures. Note however that relative intensities of the minor peaks were clearly dependent on the method of preparation (see dashed ellipsoids in Figure 13b).

The glass transition temperature of CUR and PIP loaded scaffolds became intermediate between those corresponding to the neat polymer and the corresponding drug. Therefore, a mixing of the two components in the amorphous state could be speculated.

X-ray diffraction profiles (Figure 15) of CUR loaded scaffolds showed only PBS reflections as a consequence of the amorphous state of the drug or its effective incorporation into the crystalline PBS domains.

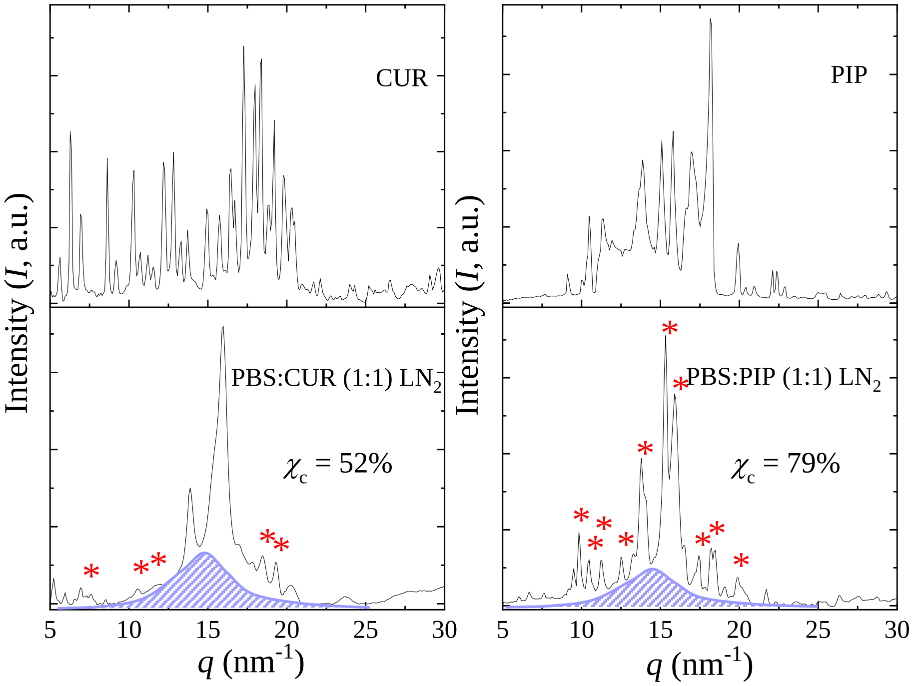

Figure 15. Representative X-ray diffraction profiles of CUR, PBS:CUR 1:1; PIP and PBS:PIP (1:1). The asterisks correspond to the Bragg peaks derived from the incorporated drugs.

By contrast, new reflections associated to PIP crystals were detected in the profiles of PIP loaded scaffolds. In the first case, the crystallinity of the sample decreased with respect to the neat PBS scaffolds, while in the second case the total crystallinity increased since due to the contribution of PIP crystals.

Thermogravimetric measurements allow also discerning between interactions that could be established in the melt state between PBS and each drug (Figure 14).

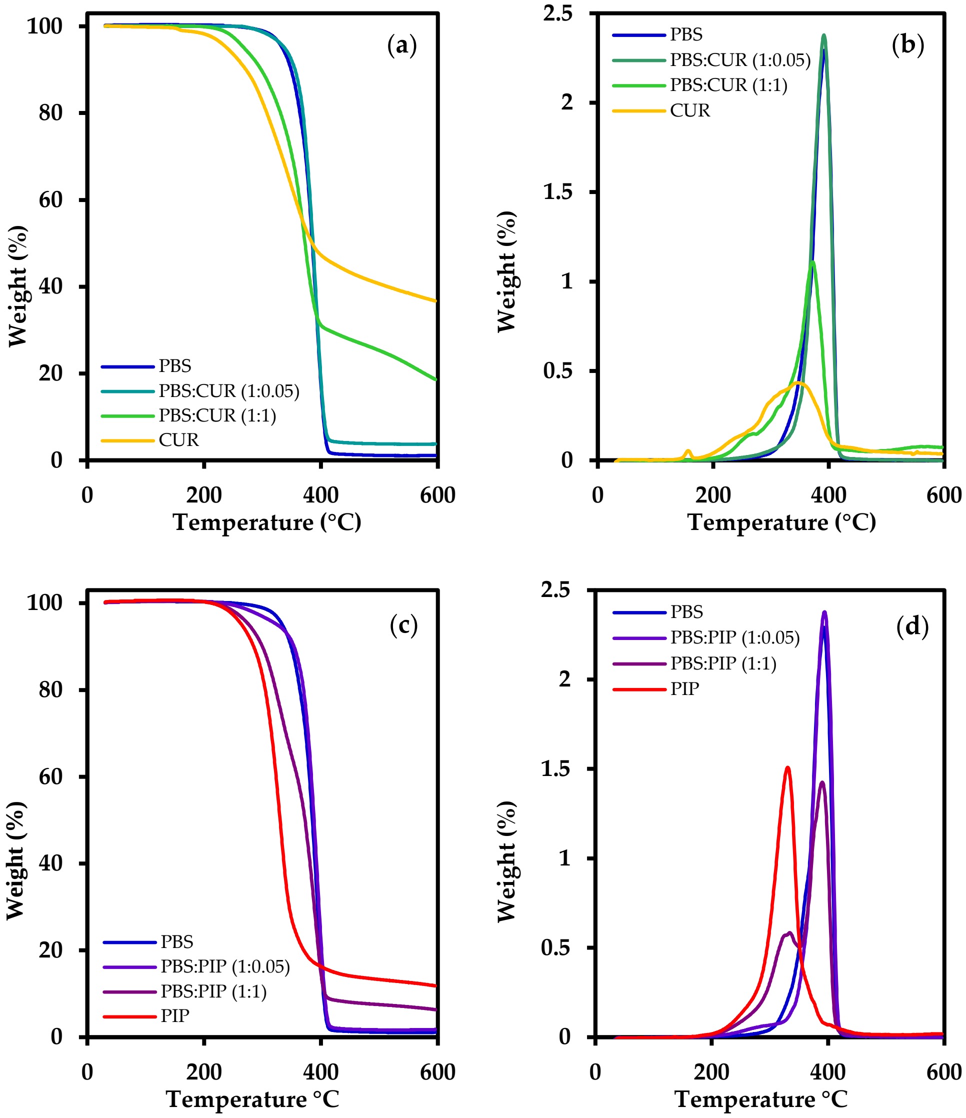

Figure 14. TGA (**a**,**c**) and DTGA (**b**,**d**) curves of PBS scaffolds loaded with 100 wt% of CUR (**a**,**b**) or PIP (**c**,**d**) and prepared using a LN_2 bath. Curves for neat PBS scaffolds are also given for comparison purposes.

Although each drug can individually affect the degradation behaviour of the polymer in the compound, the effect of a low concentration of the drug is negligible (i.e., the behaviour is very similar to pure PBS scaffold). By contrast, note that at high load (i.e., 1:1), the CUR-loaded sample showed complex TGA and DTGA curves that were not merely a superposition of the degradation curves of the two individual components (i.e., some interactions may be established between the two melted components). By contrast, a two-step process was characteristic of PIP-loaded scaffolds. In this case, the two steps had a perfect agreement with the decomposition process of pure PIP and PBS, being consequently discarded any effect associated to the mixture of both components. Note also that CUR degradation was slightly delayed in the mixture (i.e., onset degradation temperature of 372 °C and 347 °C for the 100 wt% loaded sample and the pure drug, respectively), while the degradation of PBS was preceded (i.e., maximum DTGA peak temperatures at 372 °C and 393 °C for the 100 wt% loaded sample and the neat polymer, respectively).

4.3.7. Drug Release of TIPS Scaffolds

Release of CUR and PIP drugs from representative scaffolds was evaluated in a relatively hydrophilic PBS aqueous medium as shown in Figure 15. In all cases, release profiles can be fitted with a combined Higuchi-1st order model. Corresponding k_H (release < 40%) and k_1 (release > 40%) for the 5 wt% loaded scaffolds are summarized in Table 2. Some points are significant and deserve further comments:

a) PIP was always delivered faster than CUR as consequence of its lower affinity with the PBS matrix and greater solubility in the release medium.

b) A complete release was not detected for scaffolds with the higher pay load (i.e., 100 wt-%) as consequence of both limited drug solubility and absence of a periodical renovation of the medium. Saturation levels were around 18-20% and 10-8% for PIP and CUR, respectively.

c) CUR and PIP were effectively incorporated into the polymer matrices independently of the processing conditions. Note that a Burst effect associated to the release of surface attached drug was not detected for the 5 wt% (and even for 100 wt%) loaded samples.

d) Release profiles were clearly dependent on the drug (i.e., CUR or PIP), but more interestingly on the structure of the scaffold (i.e., the way as the scaffold was prepared). Thus, release was faster when the scaffold was obtained from a 3D homogeneous temperature gradient. These scaffolds had randomly-oriented macropores delimited by thin polymer walls constituted by leafy crystals. These walls had an intrinsic small SD-formed porosities (several microns) and allowed an easy diffusion of drug molecules. By contrast, the structures of scaffolds prepared with a uniaxial and high temperature gradient had oriented pores delimited by dense and compact walls constituted by planar spherulites that restricted drug diffusion.

e) A sustained release of both CUR and PIP drugs could be achieved by appropriate selection of the scaffold preparation method. Specifically, a release of only 60% or 50% was attained for PIP and CUR loaded samples (5 wt%) after170 h of exposure to the PBS medium when scaffolds were obtained under the uniaxial high temperature gradient

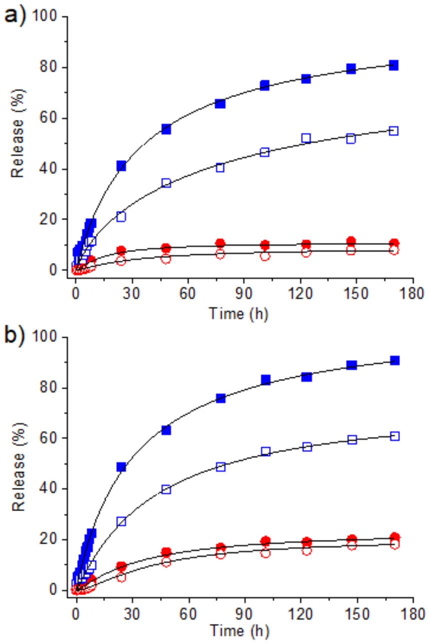

Figure 15. Drug release percentages on a PBS medium of selected scaffolds loaded with 5 wt% (square symbols, blue colour) and 100 wt% (circle symbols, red colour) of CUR (a) and PIP (b). Release from the scaffolds with randomly- and uniaxially-oriented pores prepared at quenching temperatures of -20 °C and -196 °C have been plotted with full symbols and empty symbols, respectively.

Table 2 summarizes the values of k_H and k_1 determined for representative scaffolds, where k_1 reflect ability to reach the final equilibrium condition whereas k_H values appear more interesting because they quantify and allow comparing drugs release speeds in the initial phase of delivery. This constant was higher for the 5 wt% loaded scaffolds obtained with a random pore distribution (i.e., 0.71 and 1.15 $h^{-0.5}$ for CUR and PIP, respectively).

Table 2. Higuchi and 1st order release constants using the combined model for representative scaffolds loaded with 5 wt% of CUR or PIP.

PBS:Drug	PBS-CUR				PBS-PIP			
	k_H ($h^{-0.5}$)	r	k_1 (h^{-1})	r	k_H ($h^{-0.5}$)	r	k_1 (h^{-1})	r
1:0.05 random (-20 °C)	0.71	0.996	0.24	0.978	1.15	0.973	0.22	0.997
1:1 random (-20°C)	0.20	0.968	0.20	0.996	0.31	0.958	0.23	0.997
1:0.05 oriented (LN_2)	0.60	0.988	0.24	0.985	0.92	0.971	0.22	0.989
1:1 oriented (LN_2)	0.11	0.990	0.26	0.976	0.29	0.924	0.20	0.988

A slight decrease was detected for scaffolds with an oriented pore distribution (i.e., 0.60 and 0.92 $h^{-0.5}$ for CUR and PIP, respectively). Release of CUR and PIP proceeded at a slower rate when the scaffolds had a high drug content (i.e., values of 0.11-0.20 $h^{-0.5}$ and 0.29-0.31 $h^{-0.5}$ for CUR and PIP, respectively).

4.3.8. Biocompatibility of TIPS Scaffolds

Adhesion and proliferation studies have been performed with different representative unloaded and CUR or PIP loaded scaffolds prepared by TIPS as shown in Figure 16 for MDCK and NRK cell lines. Main results can be summarized as follows:

a) Biocompatibility of PBS scaffolds was similar to the control. Thus, 90% of adhesion and proliferation was determined for TIPS scaffolds independently of the preparation method and the cell line. Therefore, no toxicity related to occluded solvent was found.

b) CUR was more problematic and showed clear toxic effects in the proliferation assays, even at the lowest load. Viability was only 70-45% for the adhesion assay with samples having the minimum load (i.e., 5 wt%). Note that viability decreased to 10% for the proliferation assays. Results attained with PIP were clearly different, being significant that a viability around 60-45% was determined for the worse conditions (i.e., maximum pay load of 100 wt%, and maximum exposure time for the proliferation assay). Scaffolds loaded with 5 wt% of PIP could be considered fully biocompatible since viability was around 80% for the proliferation test.

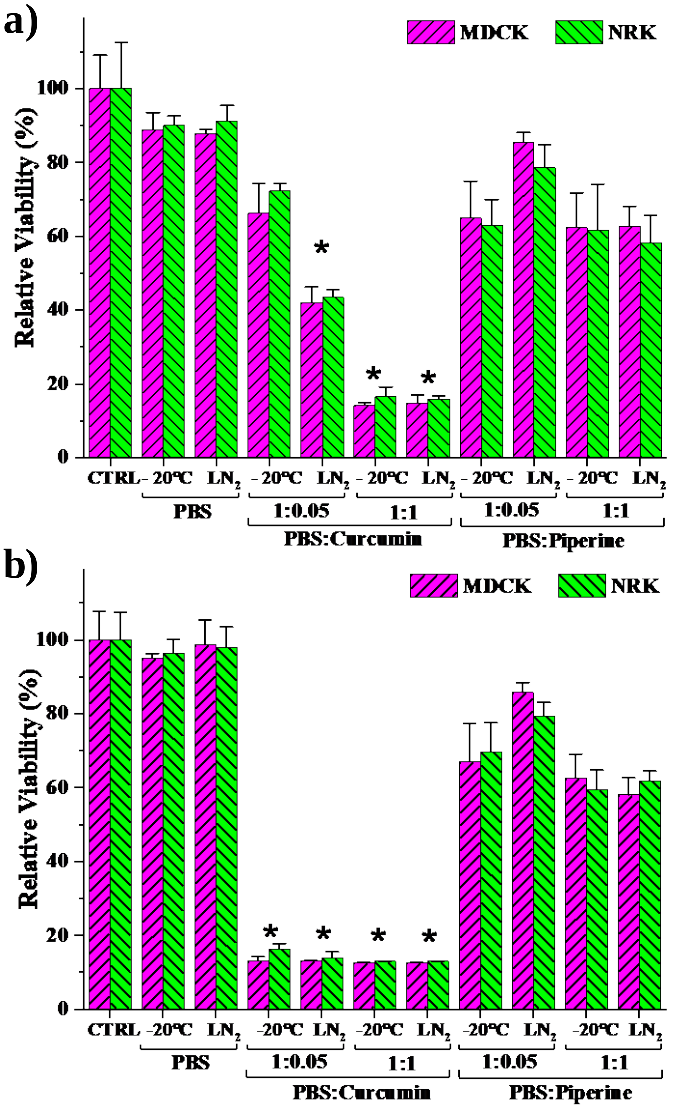

Figure 16. Adhesion (a) and proliferation (b) of MDCK (epithelial-like) and NRK (fibroblast-like) cells in the control, unloaded scaffolds and CUR and PIP loaded scaffolds at the indicated concentration. Scaffolds with randomly and oriented pores were prepared from -20 °C and LN_2 baths as explained in the text. * $p < 0.05$ vs control.

c) The scaffold structure influenced on the biocompatibility and specifically samples obtained from the uniaxial and high temperature gradient rendered the higher viability percentages in both adhesion and proliferation tests. Note for example that adhesion viability of PIP loaded samples (5 wt%) decreased from 80% to 65%

depending on the oriented or random pore structure. This result is in full agreement with the previously indicated slower release of the uniaxially oriented samples.

d) There are no differences between the sensitivity of the two cell types to drugs, and both drugs have the same mechanism of cytotoxic damage. The stability of the scaffolds incorporated piperine (e.g., better mechanical properties) allows better adhesion and cell proliferation. Curcumin-loaded scaffolds can produce small particles (e.g., micro and/or nanoparticles) that could be internalized by the cells (via endocytosis), leading to generation of free radicals or oxidative stress inside the cells and finally to cell death.

4.4. Conclusions

In this study, fabrication of PBS scaffolds and drug incorporation (i.e., CUR and PIP at different levels) have successfully been performed in one step via thermally-induced phase separation. Changes in the TIPS parameters such as solvent system, thermal gradient and cooling direction affected the process and the resulting architecture. Pore morphology and architecture of the scaffolds prepared using DXN and THF solvents were dominated to a greater extent by solid-liquid and liquid-liquid phase separation mechanisms, respectively. Morphologies formed through crystallization of the polymer were also detectable using both solvents, especially upon slower cooling. Applying uniaxial cooling, allowed controlling the crystallization direction of DXN and achieving structural orientation.

Although incorporation of drugs in small quantities did not affect the morphology, scaffolds with lower porosity and smoother surfaces were obtained as a result of great-quantity drug loading. The uniform distribution of drugs throughout the scaffolds confirmed the effectiveness of one-step TIPS process for both fabrication and drug incorporation. CUR appeared to be better integrated into the PBS matrix, as in the superficial images the rounded drug agglomerations were unified with the matrix through a surrounding thin film. This integration can be attributed to the higher affinity and possible interaction of CUR with PBS which was confirmed by calorimetric and thermogravimetric data and also infrared spectroscopy.

Regarding the effective incorporation of the both drugs into the polymer matrix, no burst effect associated with superficial release was observed. However, a faster release in PIP-loaded samples was attributed to the lower affinity of this drug with the polymer and its higher solubility in the release medium. Since the dense spherulitic pore walls of the microtubular oriented matrices impede the drug diffusion, such matrices exhibited a slower release profile compared to those having randomly-oriented pore structure. Accordingly, an ideal sustained release of both drugs from the oriented substrates was achieved. In accordance with the release study results, the matrices with uniaxial pore orientation presented greater biocompatibility (i.e., higher cell viability in both adhesion and proliferation tests). In addition, the full biocompatibility of neat PBS matrices (disregarding the porosity structure) proved that the lyophilization protocol was highly effective in removing the organic solvent. Our findings suggest that the oriented PBS matrices prepared via uniaxial and high temperature gradient TIPS are potential bio-substrates for cell/drug delivery purposes.

4.5. References

1. Liu, X.; Ma, P.X. Polymeric Scaffolds for Bone Tissue Engineering. *Ann. Biomed. Eng.* **2004**, *32*, 477-486.
2. Lu, J.X.; Flautre, B.; Anselme, K.; Hardouin, P.; Gallur, A.; Descamps, M.; Thierry, B. Role of interconnections in porous bioceramics on bone recolonization in vitro and in vivo. *J. Mater. Sci. Mater. Med.* **1999**, *10*, 111-120.
3. Pellis, A.; Silvestrini, L.; Scaini, D.; Coburn, J.M.; Gardossi, L.; Kaplan, D.L.; Herrero Acero, E.; Guebitz, G.M. Enzyme-catalyzed functionalization of poly(L-lactic acid) for drug delivery applications. *Process Biochem.* **2017**, *59*, 77-83.
4. Dorati, R.; DeTrizio, A.; Modena, T.; Conti, B.; Benazzo, F.; Gastaldi, G.; Genta, I. Biodegradable Scaffolds for Bone Regeneration Combined with Drug-Delivery Systems in Osteomyelitis Therapy. *Pharmaceuticals (Basel)* **2017**, *10*, 96.
5. Carfì Pavia, F.; Palumbo, F.S.; La Carrubba, V.; Bongiovì, F.; Brucato, V.; Pitarresi, G.; Giammona, G. Modulation of physical and biological properties of a composite PLLA and polyaspartamide derivative obtained via thermally induced phase separation (TIPS) technique. *Mater. Sci. Eng.* C **2016**, *67*, 561–569.
6. Hutmacher, D.W. Scaffolds in tissue engineering bone and cartilage. *Biomaterials* **2000**, *21*, 2529–2543.
7. Hutmacher, D.W. Scaffold design and fabrication technologies for engineering tissues-state of the art and future perspectives. *J. Biomater. Sci. Polymer Edn.* **2001**, *12*, 107–124.
8. Gaikwad, V.; Patil, A.; Gaikwad, M. Scaffolds for Drug Delivery in Tissue Engineering. *Int. J. Pharm. Sci.* **2008**, *1*, 113-122.
9. Van de Witte, P.; Dijkstra, P.J.; van den Berg, J.W.A.; Feijen, J. Phase separation processes in polymer solutions in relation to membrane formation. *J. Membr. Sci.* **1996**, *117*, 1–31.
10. Puppi, D.; Chiellini, F.; Piras, A.M.; Chiellini, E. Polymeric materials for bone and cartilage repair. *Prog. Polym. Sci.* **2010**, *35*, 403–440.
11. Mikos, A.G.; Temenoff, J.S. Formation of highly porous biodegradable scaffolds for tissue engineering. *Electron. J. Biotech.* **2000**, *3*, 1–6.
12. Chen, V.J.; Ma, P.X. Polymer phase separation. In *Scaffolding in Tissue Engineering*; Williams, C.G., Elisseeff, J.H., Eds.; Taylor & Francis: Boca Raton, FL, USA, 2006; pp. 125–137.
13. Gay, S.; Lefebvre, G.; Bonnin, M.; Nottelet, B.; Boury, F.; Gibaud, A.; Calvignac, B. PLA scaffolds production from Thermally Induced Phase Separation: Effect of process parameters and development of an environmentally improved route assisted by supercritical carbon dioxide. *J. Supercrit. Fluids* **2018**, *136*, 123–135.
14. Zeinali, R.; Khorasani, M.T.; Behnamghader, A.; Atai, M.; Valle, L.; Puiggalí, J. Poly(hydroxybutyrate-co-hydroxyvalerate) Porous Matrices from Thermally Induced Phase Separation. *Polymers* **2020**, *12*, 2787.
15. Dai, Y.; Shen, T.; Ma, L.; Wang, D.; Gao, C. Regeneration of osteochondral defects in vivo by a cell-free cylindrical poly(lactide-co-glycolide) scaffold with a radially oriented microstructure. *J. Tissue Eng. Regen. Med.* **2018**, *12*, e1647–e1661.

16. Feng, X.; Xu, P.; Shen, T.; Zhang, Y.; Ye, J.; Gao, C. Influence of pore architectures of silk fibroin/collagen composite scaffolds on the regeneration of osteochondral defects in vivo. *J. Mater. Chem. B* **2020**, *8*, 391–405.

17. Zeinali, R.; del Valle, L.J.; Torras, J.; Puiggalí, J. Recent Progress on Biodegradable Tissue Engineering Scaffolds Prepared by Thermally-Induced Phase Separation (TIPS). *International Journal of Molecular Sciences* **2021**, *22*, 3504.

18. Biomaterials: Silk gland mimic spins strong fibres. *Nature* **2017**, *541*, 137.

19. Gumede, T.P.; Luyt, A.S.; Müller, A. Review on PCL, PBS, and PCL/PBS blends containing carbon nanotubes. *Express Polym. Lett.* **2018**, *12*, 505–529.

20. Visscher, G.E.; Robison, R.L.; Maulding, H.V.; Fong J.W.; Pearson J.E.; Argentieri G.J. Biodegradation of and tissue reaction to 50:50 poly(DL-lactide-co-glycolide) microcapsules. *J. Biomed. Mater. Res.* **1985**, *19*, 349-365

21. Guo, R.; Chen, S.; Xiao, X. Fabrication and characterization of poly (ethylenimine) modified poly (l-lactic acid) nanofibrous scaffolds. *J. Biomater. Sci. Polym. Ed.* **2019**, *30*, 1523–1541.

22. Onder, O.C.; Yilgor, E.; Yilgor, I. Critical parameters controlling the properties of monolithic poly(lactic acid) foams prepared by thermally induced phase separation. *J. Polym. Sci. Part B Polym. Phys.* **2019**, *57*, 98–108.

23. McKenna, E.; Klein, T.J.; Doran, M.R.; Futrega, K. Integration of an ultra-strong poly(lactic-co-glycolic acid) (PLGA) knitted mesh into a thermally induced phase separation (TIPS) PLGA porous structure to yield a thin biphasic scaffold suitable for dermal tissue engineering. *Biofabrication* **2019**, *12*, 015015.

24. Liu, J.; Zhang, J.; James, P.F.; Yousefi, A.-M. I-Optimal design of poly(lactic-co-glycolic) acid/hydroxyapatite three-dimensional scaffolds produced by thermally induced phase separation. *Polym. Eng. Sci.* **2019**, *59*, 1146–1157.

25. Kumawat, V.S.; Ghosh, S.B.; Bandyopadhyay-Ghosh, S. Microporous biocomposite scaffolds with tunable degradation and interconnected microarchitecture-A synergistic integration of bioactive chain silicate glass-ceramic and poly(ε-caprolactone). *Polym. Degrad. Stab.* **2019**, *165*, 20–26.

26. Yao, Q.; Liu, Y.; Pan, Y.; Miszuk, J.M.; Sun, H. One-pot porogen free method fabricated porous microsphere-aggregated 3D PCL scaffolds for bone tissue engineering. *J. Biomed. Mater. Res. B Appl. Biomater.* **2020**, *108*, 2699–2710.

27. Díaz, A.; Katsarava, R.; Puiggalí, J. Synthesis, properties and applications of biodegradable polymers derived from diols and dicarboxylic acids: from polyesters to poly(ester amide)s. *Int. J. Mol. Sci.* **2014**, *15*, 7064-7123.

28. Fujimaki, T. Processability and properties of aliphatic polyesters, 'BIONOLLE', synthesized by polycondensation reaction. *Polym. Degrad. Stab.* **1998**, *59*, 209-214.

29. ai, S.M.; Huang, C.K.; Shen, H.F. Preparation and properties of biodegradable poly(butylene succinate)/starch blends. *J. Appl. Polym. Sci.* **2005**, *97*, 257-264.

30. Gigli, M.; Fabbri, M.; Lotti, N.; Gamberini, R.; Rimini, B.; Munari, A. Poly(butylene succinate)-based polyesters for biomedical applications: A review. *Eur. Polym. J.* **2016**, 75, 431-460.

31. Wu, F.; Huang, C.-L.; Zeng, J.-B.; Li, S.-L.; Wang, Y.-Z. Synthesis and characterization of segmented poly(butylene succinate) urethane ionenes containing secondary amine cation. *Polymer* **2014**, *55*, 4358-4368.

32. Wang, H.; Ji, J.; Zhang, W.; Wang, W.; Zhang, Y.; Wu, Z.; Zhang, Y.; Chu, P.K. Rat calvaria osteoblast behavior and antibacterial properties of O2 and N2 plasma-implanted biodegradable poly(butylene succinate). *Acta Biomater.* **2010**, *6*, 154-159.

33. Gigli, M.; Lotti, N.; Gazzano, M.; Finelli, L.; Munari, A. Synthesis and characterization of novel poly(butylene succinate)-based copolyesters designed as potential candidates for soft tissue engineering. *Polym. Eng. Sci.* **2013**, *53*, 491-501.

34. Oliveira, J.T.; Correlo, V.M.; Sol, P.C.; Costa-Pinto, A.R.; Malafaya, P.B.; Salgado, A.J.; Bhattacharya, M.; Charbord, P.; Neves, N.M.; Reis, R.L. Assessment of the Suitability of Chitosan/PolyButylene Succinate Scaffolds Seeded with Mouse Mesenchymal Progenitor Cells for a Cartilage Tissue Engineering Approach. *Tissue Eng. A* **2008**, *14*, 1651-1661.

35. Costa-Pinto, A.R.; Correlo, V.M.; Sol, P.C.; Bhattacharya, M.; Srouji, S.; Livne, E.; Reis, R.L.; Neves, N.M. Chitosan–poly(butylene succinate) scaffolds and human bone marrow stromal cells induce bone repair in a mouse calvaria model. *J. Tissue Eng. Regen. Med.* **2012**, *6*, 21-28.

36. Costa-Pinto, A.R.; Vargel, I.; Tuzlakoglu, K.; Correlo, V.M.; Sol, P.C.; Faria, S.; Piskin, E.; Reis, R.L.; Neves, N.M. Influence of scaffold composition over in vitro osteogenic differentiation of hBMSCs and in vivo inflammatory response. *J. Biomater. Appl.* **2013**, *28*, 1430-1442.

37. Pinho, E.D.; Martins, A.; Araújo, J.V.; Reis, R.L.; Neves, N.M. Degradable particulate composite reinforced with nanofibres for biomedical applications. *Acta Biomater.* **2009**, *5*, 1104-1114.

38. Sutthiphong, S.; Pavasant, P.; Supaphol, P. Electrospun 1,6-diisocyanatohexane-extended poly(1,4-butylene succinate) fiber mats and their potential for use as bone scaffolds. *Polymer* **2009**, *50*, 1548-1558.

39. Gualandi, C.; Soccio, M.; Govoni, M.; Valente, S.; Lotti, N.; Munari, A.; Giordano, E.; Pasquinelli, G.; Focarete, M.L. Poly(butylene/diethylene glycol succinate) multiblock copolyester as a candidate biomaterial for soft tissue engineering: Solid-state properties, degradability, and biocompatibility. *J. Bioact. Compat. Polym.* **2012**, *27*, 244-264.

40. Stoyanova, N.; Paneva, D.; Mincheva, R.; Toncheva, A.; Manolova, N.; Dubois, P.; Rashkov, I. Poly(l-lactide) and poly(butylene succinate) immiscible blends: From electrospinning to biologically active materials. *Mater. Sci. Eng. C* **2014**, *41*, 119-126.

41. Ribeiro, V.P.; Ribeiro, A.S.; Silva, C.; Durães, N.F.; Bonifácio, G.; Correlo, V.; Marques, A.P.; Sousa, R.A.; Oliveira, A.; Reis, R. Evaluation of Novel 3D Architectures Based on Knitting Technologies for Engineering Biological Tissues. *J. Donghua Univ.* **2013**, *5*, 421-426.

42. Liu, J.; Jiang, Z.; Zhang, S.; Saltzman, W.M. Poly(ω-pentadecalactone-co-butylene-co-succinate) nanoparticles as biodegradable carriers for camptothecin delivery. *Biomaterials* **2009**, *30*, 5707-5719.

43. Jäger, A.; Gromadzki, D.; Jäger, E.; Giacomelli, F.C.; Kozlowska, A.; Kobera, L.; Brus, J.; Říhová, B.; El Fray, M.; Ulbrich, K., et al. Novel "soft" biodegradable nanoparticles prepared from aliphatic based monomers as a potential drug delivery system. *Soft. Matter.* **2012**, *8*, 4343-4354.

44. Jäger, E.; Jäger, A.; Chytil, P.; Etrych, T.; Říhová, B.; Giacomelli, F.C.; Štěpánek, P.; Ulbrich, K. Combination chemotherapy using core-shell nanoparticles through the self-assembly of HPMA-based copolymers and degradable polyester. *J. Control. Release* **2013**, *165*, 153-161.

45. Tanaka, T.; Takahashi, M.; Kawaguchi, S.; Hashimoto, T.; Saitoh, H.; Kouya, T.; Taniguchi, M.; Lloyd, D.R. Formation of microporous membranes of poly(1,4-butylene succinate) via nonsolvent and thermally induced phase separation. *Desalin. Water Treat.* **2010**, *17*, 176-182.

46. Ebrahimpour, M.; Safekordi, A.A.; Mousavi, S.M.; Heydarinasab, A. Modification strategy of biodegradable poly(butylene succinate) (PBS) membrane by introducing Al2O3 nanoparticles: preparation, characterization and wastewater treatment. *Desalin. Water Treat.* **2017**, *79*, 19-29.

47. Imaizumi, M.; Nagata, T.; Goto, Y.; Okino, Y.; Takahashi, T.; Koyama, K. Solubility Parameters of Biodegradable Polymers from Turbidimetric Titrations. *Kobunshi Ronbunshu* **2005**, *62*, 438-440.

48. Hansen, C.M. *Hansen Solubility Parameters. A User's Handbook*, 2nd ed.; CRC Press: Boca Raton, FL, USA, 2007; ISBN 0849372488.

49. Van Krevelen, D.W.; Nijenhuis, K.T. *Properties of Polymers. Their Correlation with Chemical Structure Their Numerical Estimation and Prediction from Additive Group Contributions, 4th completely rev. ed.*; Elsevier: Amsterdam, The Netherlands, 2009; ISBN 9780080548197.

50. Valerio, O.; Misra, M.; Mohanty, A.K. Statistical design of sustainable thermoplastic blends of poly(glycerol succinate-co-maleate) (PGSMA), poly(lactic acid) (PLA) and poly(butylene succinate) (PBS). *Polym. Test.* **2018**, *65*, 420–428.

51. Abbott, S. Chemical compatibility of poly(lactic acid): A practical framework using Hansen Solubility Parameters. In *Poly(Lactic Acid): Synthesis, Structures, Properties, Processing, and Applications*; Auras, R., Lim, L.-T., Selke, S.E.M., Tsuji, H., Eds.; John Wiley & Sons, Inc.: Hoboken, NJ, USA, 2010; ISBN 9780470649848.

52. Yang, F.; Murugan, R.; Ramakrishna, S.; Wang, X.; Ma, Y.X.; Wang, S. Fabrication of nano-structured porous PLLA scaffold intended for nerve tissue engineering. *Biomaterials* **2004**, *25*, 1891–1900.

53. Buschmann, J.; Muller, E.; Luger, P. X-ray structure analysis of 1,4-dioxane, phase I at 279 K and phase II at 153 K. *Acta. Cryst.* **1986**, *42*, 873–876.

54. Conoscenti, G.; Carrubba, V.; Brucato, V. A Versatile Technique to Produce Porous Polymeric Scaffolds: The Thermally Induced Phase Separation (TIPS) Method. *Arch. Chem. Res.* **2017**, *1*, 1–3.

55. Önder, Ö.C.; Yilgör, E.; Yilgör, I. Fabrication of rigid poly(lactic acid) foams via thermally induced phase separation. *Polymer* **2016**, *107*, 240–248.

56. Lloyd, D.R.; Kinzer, K.E.; Tseng, H.S. Microporous membrane formation via thermally induced phase separation. I. Solid-liquid phase separation. *J. Membr. Sci.* **1990**, *52*, 239–261.

57. Zhang, R.; Ma, P.X. Poly(α-hydroxyl acids)/hydroxyapatite porous composites for bone-tissue engineering. I. Preparation and morphology. *J. Biomed. Mater. Res.* **1999**, *44*, 446-455.

58. Whinnery, L.L.; Even, W.R.; Beach, J.V.; Loy, D.A. Engineering the macrostructure of thermally induced phase separated polysilane foams. *J. Polym. Sci., Part A: Polym. Chem.* **1996**, *34*, 1623-1627.

59. Kyu, T.; Chiu, H.W.; Guenthner, A.J.; Okabe, Y.; Saito, H.; Inoue, T. Rhythmic Growth of Target and Spiral Spherulites of Crystalline Polymer Blends. *Phys. Rev. Lett.* **1999**, *83*, 2749-2752.

60. Jungnickel BJ. Crystallization Kinetical Peculiarities in Polymer Blends. In *Polymer Crystallization*. Reiter G., Sommer JU., Eds.; Springer: Berlin, Heidelberg, 2003; from Lecture Notes in Physics, Volume 606, pp. 208–237.

61. r. 61. Ding, G.; Liu, J. Morphological varieties and kinetic behaviors of poly(3-hydroxybutyrate) (PHB) spherulites crystallized isothermally from thin melt film. *Colloid Polym. Sci.* **2013**, *291*, 1547–1554.

Chapter 5

Biobased Terpene Derivatives: Stiff and Biocompatible Compounds to Tune Biodegradability and Properties of Poly(butyelene succinate)

Abstract

Different copolymers incorporating terpene oxide units (e.g., limonene oxide) have been evaluated considering thermal properties, degradability, and biocompatibility. Thus, polycarbonates and polyesters derived from aromatic, and monocyclic and bicyclic anhydrides have been considered. Furthermore, ring substitution with the myrcene terpene has been evaluated. All polymers were amorphous when evaluated dirctly from synthesis, although spherulites could be observed after slow evaporation of diluted chloroform solutions of the pure enantiomeric polylimonene carbonate. This feature was surprising considering the reported information that pointed out that only the racemic polymer was able to crystallize. All polymers were thermally stable and showed a dependence of the maximum degradation rate temperature with the type of terpene oxide. A graduation of glass transition temperatures was also observed, being higher those corresponding to the unsubstituted polymers. The chain stiffness of the studied polymers hindered both hydrolytic and enzymatic degradation while a higher rate was detected when an oxidative medium was assayed. All samples were biocompatible according to adhesion and proliferation tests performed with fibroblast cells.

Hydrophobic and mechanically consistent films were prepared by evaporation of chloroform solutions of different ratios of the studied biobased polyterpenes and poly(butylene succinate) (PBS). Films could show comparable tensile modulus and even similar tensile strength than pure PBS. Blends were degradable, biocompatible and useful to get scaffolds with an oriented or a random pore structure. These were successfully prepared by means of the thermal induced phase separation method and using 1,4-dioxane as solvent. Best results were attained with the blend constituted by PBS (30%) and the copolyester derived from limonene oxide and phthalic anhydride (70%).

5.1. Introduction

The use of partially or fully biobased materials is receiving an increasing attention to attain a gradual/complete substitution of petroleum-based resources [1-3]. Microorganisms, plants or algae can provide different biobased polymers (e.g., lignin, cellulose, sugar, starch and polyhydroxyalkanoates) but the majority of them is *ex vivo* produced from biological-based monomers (e.g., natural oils, fatty acids, glycols) [4].

Probably, chemistry of functional terpenes provides an interesting option to get new biopolymers (e.g., polyterpenes [5] and polycarbonates [6,7]). Ring opening copolymerization can also be employed to prepare related polyesters from aliphatic cyclic esters/anhydrides and epoxides [8,9]. Great interest is focused in the use of limonene, a commercial monoterpene that can easily be isolated from citrus fruits [10]. Epoxidation of the double bond belonging to the cycle gives rise to the reactive limonene oxide (LO) which can be used as a platform molecule to get polycarbonates, polyesters, polyurethanes and even polyamides [11]. Terpene oxide monomers (e.g., limonene oxide (LO) and menthene oxide (MO)) can be applied for the synthesis of cicloaliphatic (e.g., *cis*-4-cyclohexene-1,2-dicarboxylic anhydride (MA)) and aromatic (e.g., phthalic anhydride (PA)) anhydrides. The incorporation of rigid cycles appears a promising strategy for the development of high-T_g biobased polymers [12,13].

Polybutylene succinate (PBS) is an aliphatic polyester with excellent mechanical and thermal properties [14,15]. In fact, PBS is considered nowadays an interesting substitution for polyolefins in some applications due to both its good performance and its easy processing characteristics. PBS is produced by condensation of succinic acid and 1,4-butanediol monomers, which can either be derived from fossil fuels or bacterial fermentation. Several companies around the world are precisely developing technologies for the production of the biobased polymer [16,17]. PBS has been employed as mulch films, flushable hygiene products, foaming, packaging and even biomedical applications [18,19]. The polymer has also been blended with different polymers (e.g., polylactide and starch) to improve some properties (e.g., softness and barrier properties) [20,21]. Thus, PBS blended with furfural as a natural component showed a clear improvement on mechanical properties while the biobased content was increased [22].

Biocompatible and biodegradable scaffolds are continuously being developed to satisfy the different requirements that are needed in the field of tissue engineering.

In this sense, efforts are involved to expand the range of suitable polymers, including blends and composites, and the applied methodology. Thermally induced phase separation (TIPS) has widely been used in the recent years to fabricate three dimensional (3D) and porous scaffolds. Main advantages are their low production cost, its capacity to control the final architecture and its experimental simplicity [23]. Preparation of PBS scaffolds from TIPS has recently studied in detail, being demonstrated the ability to produce both random and oriented pore structures using 1,4-dioxane as a solvent [24].

The present work is focused to prepare new PBS blends with biobased terpene derivatives and explore the application of the selected composition to get scaffolds by the TIPS technique. To this end low molecular weight polylimonene carbonate and different copolyesters will be considered (Figure 1).

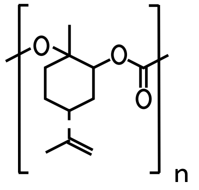

Poly(limonene carbonate) (PLC)

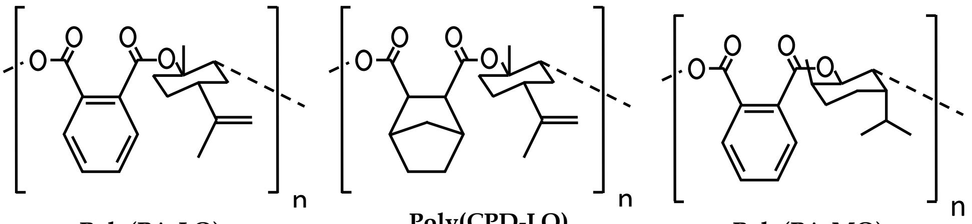

Poly(PA-LO) **Poly(CPD-LO)** **Poly(PA-MO)**

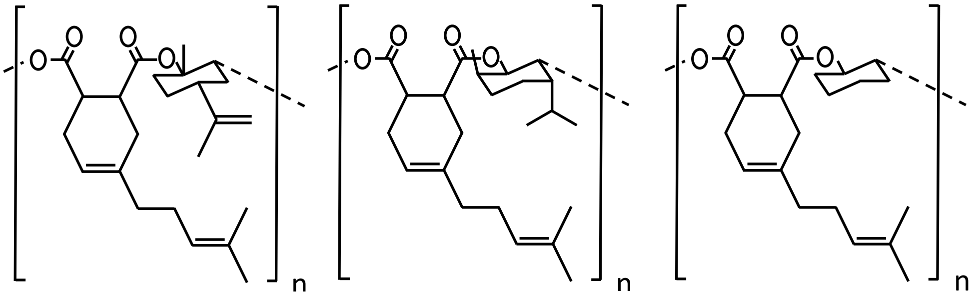

Poly(Myr/MA-LO) **Poly(Myr/MA-MO)** **Poly(Myr/MA-CHO)**

Figure 1. Chemical structure and abbreviations of the different studied terpene derivatives.

These copolymers will be prepared from two terpene oxide monomers (i.e., LO and MO) and different highly rigid anhydrides based on the aromatic phthalic unit, and also on monocyclic or bicyclic aliphatic units having internal double bonds. Furthermore, the terpene myrcene will be incorporated in some cases as a lateral group of the corresponding cycle to expand the range of properties. It is expected that the selected terpene biobased components will increase the rigidity of the final scaffold, will reduce the crystallinity due their amorphous character, will deaccelerate degradation due to their reduced chain mobility, and finally could be absorbed after the implantation period.

5.2. Experimental

5.2.1. Materials

Polybutylene succinate (PBS) used in this study was a commercial product (Bionolle® 1001 MD) supplied by Showa Denko K.K. (Germany). This polymer has a melt flow index of 1.6 g/10 min, measured at 190 °C under a load of 2.16 Kg according to ASTM-D1238. 1Copolymers having terpene units were synthesized in the Institute of Chemical Research of Catalonia (ICIQ).

4-Dioxane with the purity of 99.5% was purchased from Acros Organics and used as received. Lipase enzyme (L3126) from porcine pancreas and esterase (E-3019) from porcine liver crude were purchased from Sigma-Aldrich as well as boric acid.

5.2.2. Measurements

Molecular weight was estimated by size exclusion chromatography (GPC) using a liquid chromatograph (Shimadzu, model LC-8A) equipped with an Empower computer program (Waters). A PL HFIP gel column (Polymer Lab) and a refractive index detector (Shimadzu RID-10A) were employed. The polymer was dissolved and eluted in 1,1,1,3,3,3-hexafluoroisopropanol (HFIP) containing CF_3COONa (0.05 M) at a flow rate of 0.5 mL/min (injected volume 100 μL, sample concentration 2.0 mg/mL). Number and weight average molecular weights were calculated using polymethyl methacrylate standards.

Calorimetric data were obtained by differential scanning calorimetry with a TA Instruments Q100 series equipped with a refrigerated cooling system (RCS) operating at temperatures from -80 °C to 400 °C. Calibration was performed with indium. Experiments were conducted under a flow of dry nitrogen with a sample weight of approximately 5 mg. Calorimetric data were obtained from runs performed at a heating rate of 10 °C/min.

The thermal stability of the terpene derivatve was studied by thermogravimetric analysis (TGA) at a heating rate of 10 °C/min (sample weight *ca.* 5 mg) with a Q50 thermogravimetric analyzer of TA Instruments and under a flow of dry nitrogen. Test temperatures ranged from 30 to 600 °C.

Contact angle (CA) measurements were conducted using the sessile drop method. 0.5 μL of milliQ water drops were deposited onto the surface of the appropriate melt pressed samples or alternatively of solvent casting films. Rectangular pieces (3 cm x 1 cm) were fixed on a holder, and recorded after stabilization with the equipment OCA 15EC (DataPhysics Instruments GmbH, Filderstadt). The SCA20 software was used to measure the CA, which is shown as the average of at least 40 measures for each condition.

Mechanical properties were determined with a Zwick Z2.5/TN1S (Zwick/Roell; Ulm, Germany) testing machine in stress-strain tests carried out at a deformation rate of 10 mm/min. The load cell capacity was 100 N. Mechanical parameters were evaluated by means of the testXpert software of Zwick. In the case of the elastic modulus calculation, force values were delimited to the lineal part of the representation. Measurements were performed on rectangular samples of 3 cm × 0.4 cm and a width of 0.40 mm that were cut from the corresponding films. The mechanical parameters were averaged from a minimum of six measurements for each polymer sample.

The porous structure of the polymer matrices was evaluated using a scanning electron microscope (SEM) (Focus IonBeam Zeiss Neon 40 instrument, Carl Zeiss, Germany) at 5 kV, and controlling by Smart Tiff software (Carl Zeiss SMT Ltd., Germany). To obtain the original cross-sectional parts, the samples were fractured in liquid nitrogen after being soaked for several minutes. The top surfaces and cross-sections of the samples were coated with carbon for 700 s using a sputter coater (Mitec K950 Sputter Coater, England) before microscopy.

X-ray powder diffraction patterns were obtained with a PANanalytical X'Pert diffractometer with CuK_α radiation (λ = 0.1542 nm) and a Silicon monocrystalline sample holder. Deconvolution of WAXD peaks was performed using the PeakFit 4.0 program.

Synchrotron-based infrared microspectroscopy measurements (transmission mode) were performed at the infrared beamline MIRAS of ALBA synchrotron using the Hyperion 3000 microscope coupled to Vertex 70 spectrometer (Bruker, Germany) at 4 cm^{-1} resolution with 256 co-added scans per spectrum. In this case, the spherulites were grown from films prepared directly over infrared transparent windows of CaF_2 of 13 mm diameter and 0.5 thickness. All spectra were obtained using a single masking aperture size of 8 μm × 8 μm. In addition to the intrinsic quasi linear light polarization of synchrotron radiation, the synchrotron light was also polarized at 0° or 90° by a ZnSe holographic wire grid polarizer (Acal BFi Germany GmbH).

5.2.3. Degradation Studies

The degradation study was performed using different media at 37 °C, including hydrolytic media with pH 3, 7 or 10, lipase or esterase enzymatic media and oxidative media containing 30% of H_2O_2. The degradation in basic media with pH 10 was also performed at 70 °C.

The samples for degradation studies were prepared in the form of polymeric tablets by using a pressing machine. After preparation, the samples were exactly weighed. For statistical calculations, at least 3 samples were prepared for each degradation condition/period. The universal Britton–Robinson buffer was used to get different pH media following the procedure described in the literature [25]. A 10 mM borate buffer was prepared using boric acid and deionized water by adjusting the solution to pH 8.0 with 1M NaOH.

For enzymatic media, lipase was dissolved in phosphate buffer saline at the concentration of 1% (*w*/*v*), while esterase was dissolved in the borate buffer at the concentration of 50 units/mL. 2mL from each degradation media was added to the pre-weighed polymeric tablets and the samples were placed in the incubator at 37 °C.

In case of universal buffer media with pH 10, the samples were also placed in a 70 °C oven. During the degradation study, the samples were sealed to prevent evaporation and the media were changed with the fresh one 3 times a week (i.e., every 2-3 days). Every 7-days period, a group of samples were taken out from the incubator. They were washed first with distilled water, then the surface was well dried well with a paper and finally the sample was placed in the 37 °C desiccator until a constant weight was reached (usually 48 h). After drying, the samples were weighed in two consecutive days. If the weight difference was less than 5%, it was registered as the final weight of the sample, corresponding to its degradation period.

Weight loss (w_l) of the specimens was determined through equation 1 where w_d is the sample weight after degradation and w_0 is the initial simple weight, i.e., before exposure to the degradation medium:

$$w_l(\%) = \left(\frac{w_0 - w_d}{w_0}\right)100 \tag{1}$$

5.2.4. Cell Adhesion and Proliferation Assays

Studies were performed with fibroblast hFF cells (human foreskin fibroblasts, HFF-1 ATCC) and fibroblast MG-63 cells (derived from human osteosarcoma, CRL-1427, ATCC). In all cases, cells were cultured in Dulbecco's Modified Eagle Medium (DMEM) with 4500 mg/L of glucose, 110 mg/L of sodium pyruvate and 2 mM of L-glutamine supplemented with 10% fetal bovine serum (FBS), 50 U/mL penicillin, 50 mg/mL streptomycin and L-glutamine 2 mM at 37 °C in a 10% humidified atmosphere of 5% CO_2 and 95% air. Culture media were changed every two days. For sub-culture, cell monolayers were rinsed with phosphate buffered saline and detached by incubating them with 0.25% trypsin/EDTA for 2-5 min at 37 °C. The incubation was stopped by suspending in 5 mL of fresh medium. The cell concentration was determined by counting with Neubauer camera and using 4% trypan blue as dye vital.

Square pieces of films (1 cm x 1 cm) with a thickness of 0.1 cm were prepared by solvent-casting and fixed in each well of a 24-well culture plate with a small drop of silicone (Silbione® MED ADH 4300 RTV, Bluestar Silicones France SAS, Lyon, France). This plate was then sterilized by UV-radiation in a laminar flux cabinet for 15 min. For cell adhesion assays, aliquots of 50–100 μL containing 5×10^4 cells were seeded onto the scaffold samples in each well and incubated for 24 h (adhesion assay). For cell proliferation assays, the same aliquot volume but containing a lower cell concentration than that for adhesion experiments (i.e., 2×10^4 cells) was seeded and incubated for 96 h.

Adhesion and proliferation were evaluated to obtained quantitative data by the MTT method [26]. The procedure is based on a simple modification of the ISO10993–5:2009 standard test, which describes the appropriate methodology to assess *in vitro* cytotoxicity of medical devices. This test is designed to determine the *in vitro* biological response of mammalian cells using appropriate biological parameters. According to this ISO standard, devices fall into one of three categories based on expected contact with the patient: (a) Limited (≤24 h), (b) Prolonged (>24 h and ≤30 days) and (c) Permanent (>30 days). In our case, the assay was carried out according to the limited and prolonged categories. The viability results were averaged after doing four replicates. Samples with adhered and grown cells were fixed with 2.5% (*w/v*) formaldehyde at 4°C overnight. They were subsequently dehydrated and processed for observation of cell morphology using fluorescence microscopy, where the nucleus and actin cytoskeleton were stained with Hoescht and phalloidin, respectively.

5.2.5. Scaffold Preparation

Thermal induced phase separation (TIPS) fabrication process with a one-step cooling protocol was applied for preparation of PBS/Poly((Pa-Lo) scaffolds. The selected polymer mixture (70% of PBS) was dissolved in 1,4-dioxane at a concentrations of 2.5% (*w/v*) at a temperature of 70 °C. The initially homogeneous solution underwent a phase separation by decreasing temperature, which led to porous matrices after solvent removal. Specifically, the polymer solutions were poured into cylinder-shaped glass vials with a diameter of 14 mm and height of 40 mm and then carefully sealed to avoid evaporation. Samples were immediately incorporated to the corresponding cooling devices, that is, two freezers with pre-set temperatures of -20 °C and -74 °C and also a liquid nitrogen bath (-196 °C). Cooling process was performed under different thermal gradients, that is, from a relatively high temperature at which the solution is still clear and homogenous to the temperature of the selected baths. To apply multidirectional temperature gradient (i.e., a randomly-oriented cooling system), the glass molds were directly immersed in -20 °C or -74 °C baths. Whereas to apply uniaxial temperature gradient (i.e.. an uniaxially-oriented cooling system), the glass vials were inserted into a central hole of a polystyrene mold in order to insulate the perimeter walls of the vials and prevent the heat transfer through the side walls. In this case, only the bottom surface of the vials touched the -74 °C and -196 °C cooling baths. After remaining for 24 hours in the -20/-74 °C or 15 min in -196°C cooling baths, the samples were freeze-dried for a 120 h period using a Virtis® 6201-3120 lyophilizer (Gardiner, NY, USA). The obtained porous matrices were then dried in a vacuum desiccator at room temperature to reach a constant weight.

5.2.6. Statistical Analysis

Experimental values were averaged and graphically represented together with their respective standard deviations. Statistical analysis was performed by one-way ANOVA test to compare the means of all groups, and then Tukey's test was applied to determine a statistically significant difference between two groups. The test confidence level was set at 95% ($p < 0.05$).

5.3. Results and Discussion

5.3.1. Solubility, Molecular Weight and Hydrophobicity of the Biobased Terpene Derivatives

All synthesized biobased terpene derivatives were highly soluble in typical organic solvents (e.g., $CHCl_3$, 1,4-dioxane, THF, DMSO) and strong fluorinated acids such as trifluoroacetic acid. Main differences (Table 1) concerned to formic acid and alcohols such as ethanol and even methanol. Note that compounds having rings with lateral myrcene groups were the most soluble in alcohols probably as consequence of the difficult packing caused by these big groups. Note that all compounds were highly soluble in 1,4-dioxane, a solvent that was then selected for preparation of scaffolds by TIPS.

Table 1. Solubility of the selected terpene derivatives in common organic solvents.

Solvent [1]	**Poly (PA-LO)**	**PLC**	**Poly (PA-MO)**	**Poly (Myr/MA-LO)**	**Poly (Myr/MA-MO)**	**Poly (CPD-LO)**	**Poly (Myr/MA-CHO**
$CHCl_3$	++	++	++	++	++	++	++
TFA	++	++	++	++	++	++	++
HFIP	++	++	++	++	++	++	++
1,4 dioxane	++	++	++	++	++	++	++
THF	++	++	++	++	++	++	++
DMF	++	+	++	++	++	++	++
DMSO	+	+	-	++	-	+	--
Formic Acid	+	-	--	+	--	+	--
Formamide	-	-	-	-	-	-	-
Methanol	--	--	--	++	--	-	--
Ethanol	--	--	--	++	+	--	++

[1] Code: ++: Soluble in room temperature; +: Soluble in higher temperatures or high speed stirring/shaking; -: Insoluble; --: Very insoluble.

Table 2 shows the GPC data of polymers directly obtained from synthesis. In agreement with the synthesis procedure, the characteristic molecular weights were low (i.e., weight average molecular weights between 7,600 and 9,700 g/mol) and had a uniform distribution since polydispersity indices varied between 2.1 and 2.5. GPC curves for representative samples with the highest and lowest molecular weight are shown in Figure 2. Note that a significant mistake in the molecyular weight estimation is expected due to the use of the more flexible polymethyl methacrylate polymer as a calibrant.

Table 2. GPC data of the selected terpene derivatives.

	Poly (PA-LO)	PLC	Poly (PA-MO)	Poly (Myr/MA-LO)	Poly (Myr/MA-MO)	Poly (CPD –LO)	Poly (Myr/MA-CHO)
M_n	4,000	3,600	3,900	4,000	3,900	3,800	4,100
M_w	9,200	7,600	9,000	9,600	9,700	8,800	9,100
PDI	2.3	2.1	2.3	2.4	2.5	2.3	2.2

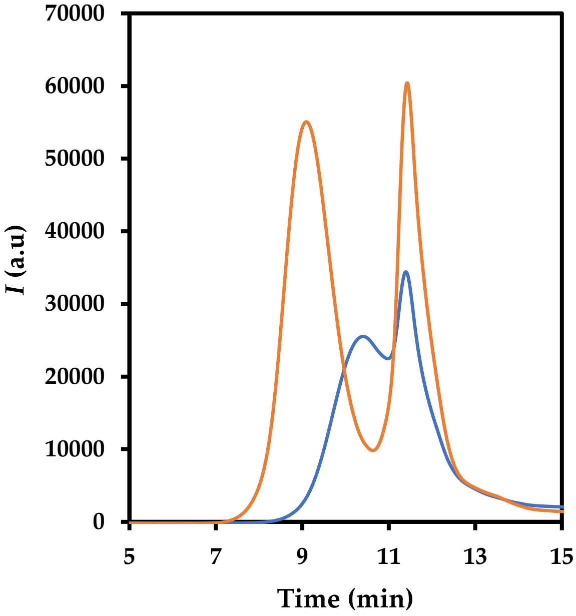

Figure 2. GPC curves for Poly(My/MA-LO) (orange) and PLC (blue) samples. Peaks at the high retention time (i.e., 12 min) corresponds to the salts of the elution medium.

Low molecular weights caused that only very brittle or powdered films were obtained from the different samples by solvent casting and specifically using chloroform as solvent. As then will be explained consistent films were only obtained after blending with PBS (Figure 3).

Figure 3. Solvent casting films obtained from PBS/Poly(PA-LO) 70:30 (**a**), PBS/Poly(PA-LO) 50:50 (**b**) and a pressed tablet of pure Poly(PA-LO) (**c**)

All samples could be considered slightly hydrophobic since contact angles were equal or higher than 90°. No significant variation was detected, being the greatest and lowest values 100° and 90° (Figure 4), respectively.

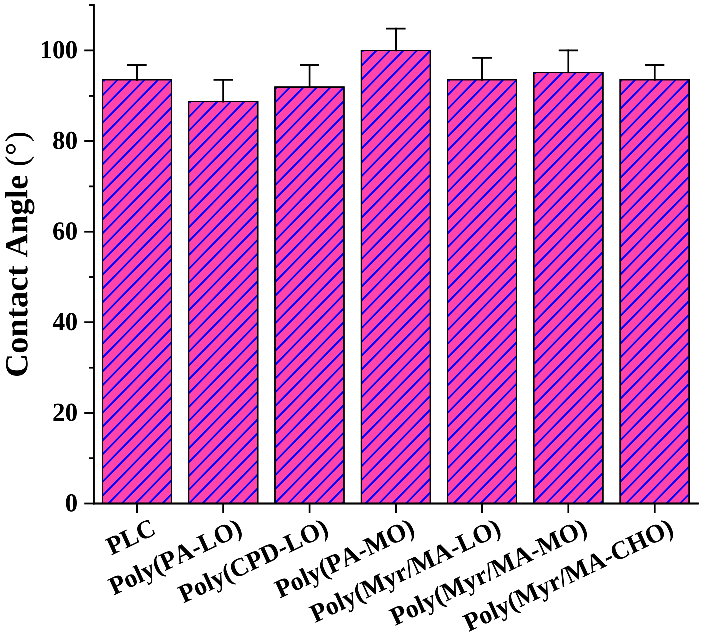

Figure 4. Contact angles determined from the different pressed tablets of the studied terpene derivative.

Note that contributions to hydrophilicity derived from terminal groups were practically identical for all samples due to their similar molecular weights. It should also be pointed out that the sample preparation method was identical and therefore the hydrophobic roughness contribution should also be similar. Therefore, the different modifications of the chemical repeat unit did not render an appreciable change on the surface hydrophobicity. Note that maximum and minimum contact angles correspond to highly similar samples derived from phthalic anhydride and a terpene oxide, while intermediate values were determined for the rest of the samples.

5.3.2. Thermal Properties of Studied Biobased Polymers

DSC heating runs of the studied biobased terpene derivatives were indicative of fully amorphous samples. Thus, only a well-defined glass transition was detected, and no evidences of a minor melting peak were observed even for PLC, which theoretically is the more crystalline sample as then will be explained. Figure 5 shows as the T_g varies in a wide temperature range (i.e., from 44 °C to 127 °C), corresponding the lower values to those polymers having myrcene lateral groups.

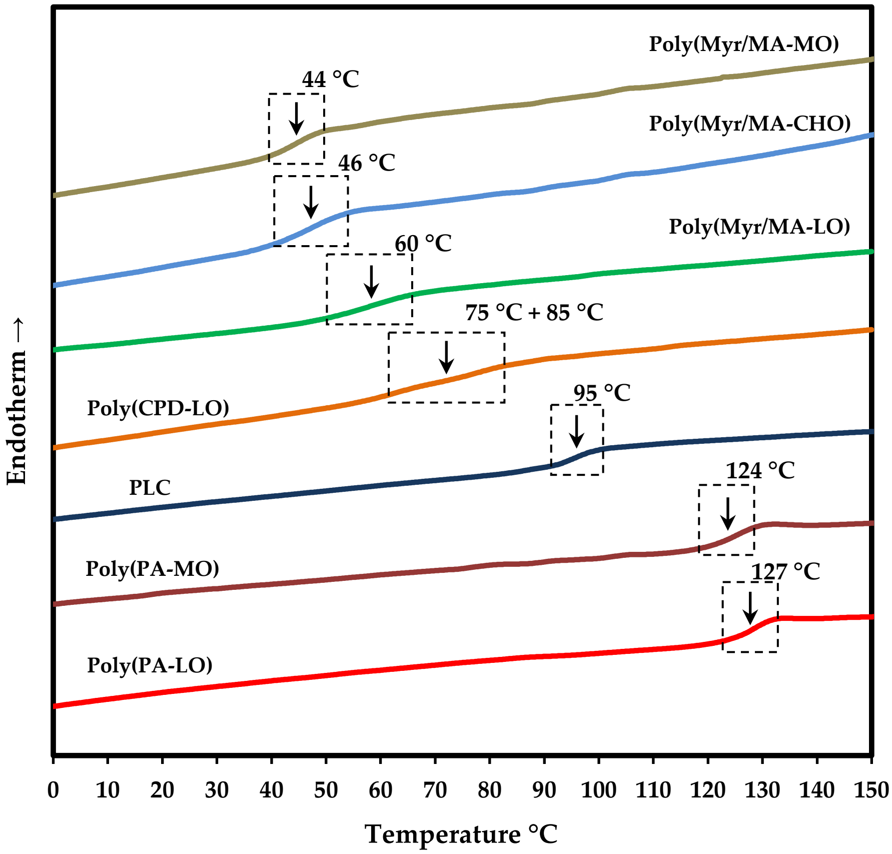

Figure 5. DSC heating runs of the synthesized terpene derivatives.

These are responsible of a certain mobility and will be discarded for further applications according to the proposed goals. The higher T_g values (i.e., 127 °C and 124 °C) were attained with the copolymers derived from phthalic anhydride, being the more rigid structure that incorporating LO units. It should also be indicated that PLC showed an interesting high value (95 °C), whereas the copolymer having the bicyclic unit seems to have two close T_gs at 75 °C and 85 °C.

All the studied polyterpene derivatives had a high thermal stability as demonstrated by the corresponding TGA and DTGA curves (Figure 6). PLC was the less stable sample with an onset of degradation lower than 200°C and a DTGA peak at 242 °C.

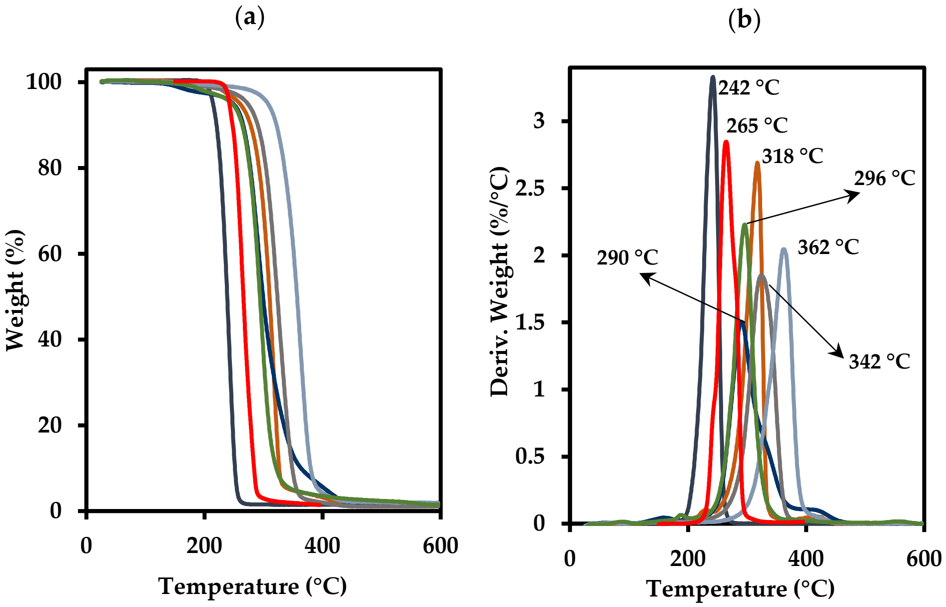

Figure 6. TGA (**a**) and DTGA (**b**) curves for the different studied terpene derivatives. Peak temperature for DTGA curves increased in the order: PLC, Poly(PA-LO), Poly(Myr/MA-LO), Poly(CPD-LO), Poly(PA-MO), Poly(Myr/MA-MO), Poly(Myr/MA-CHO). Same colour code is applied for TGA curves.

The onset temperature was higher than 200 °C for the different studied copolyesters, being the decomposition peak mainly related to the nature of the oxide unit (i.e., CHO, MO or LO). Thus, the peak temperature decreased in the order CHO > MO > LO (i.e., 362 °C, 324-318 °C and 296 °C, respectively).

Respect to the nature of the dicarboxylic unit (i.e., aromatic, aliphatic bicycle/monocycle, myrcene substituted cycles) a minor effect was detected. Note for example that peak temperatures of 290 °C and 296 °C were determined for polymers having highly different repeat units, but coming from the same terpene oxide (e.g., Poly(Myr/MA-LO) and poly(CPD-LO)). Degradation curves suggest a single step thermal decomposition process with the exception of the Poly(Myr/MA-LO) sample characterized by at least three different decomposition steps. PLC, the polymer with the simple repeat unit, had the narrowest DTGA curve. Probably degradation could be described in this caseby a single mechanism. Degradation was completed for all samples at 450 °C with a char yield lower than 5%.

5.3.3. Remarks on the Crystallization of Polylimonene Carbonate

Copolymers of limonene oxide and carbon dioxide have a chiral carbon atom (i.e., that linked to the isopropenyl substituent). Thus, two enantiomeric forms (poly(1S,2S,4R-limonene carbonate) and poly(1R,2R,4S-limonene carbonate) can be prepared using for example a β-diiminate zinc complex as catalyst [27]. It has been reported that both enantiomers are unable to crystallize despite having regular constitution and conformation. Interestingly, the racemic mixture gave rise to a stereocomplex and an interdigitate structure composed of sheets with an alternating disposition of chains with an opposite chirality [7]. A chain periodicity of 1.131 nm and a 2/1 helical conformation with nearly all-trans bonds in the backbone was postulated. Nevertheless, some conformational disorder was even observed for this favorable crystalline arrangement. Specifically, problems were related to the easy twisting of cyclohexane rings, the low conformational barrier of bonds connecting the isopropenyl groups to the ring and the statistical occupancy of up and down chains in the lattice [28]. Crystallization of the enantiopure form was problematic due to the weak interactions between molecular chains having an isochiral packing that led to a low crystallization kinetics. In fact it was reported that amorphous samples were always obtained despite exploring different precipitation and solution casting procedures and using polymers of very low molecular weight (e.g., 9000 g/mol) [28].

In the present work, we can report the possibility to get typical spherulitic morphologies by the slow evaporation of diluted chloroform solutions (i.e., 0.1 g/mL). This slow rate was achieved when drops of the solution were placed between a slip and a coverslip and led to evaporate at room temperature. The predominant morphology (Figure 7a) corresponded to ringed and ringed spherulites having diameters and interring spacings close to 80 μm and 5 μm, respectively. This negative birefringence is usually observed in polymers, including polyesters and polycarbonates. The maximum refractive index of the corresponding crystalline assemblies is associated to the chain molecular axis, which corresponds to the tangential direction of typical spherulites constituted by edge-on lamellae that radially growth from the crystalline nucleus.

A ringed texture is usually associated to the twisting of the constitutive edge-on lamellae [29], but other interpretations have also been postulated (e.g., development of interlamellar screw discolation [30] or the presence of different polymorphic structures [31]). However, the crystallization derived from the slow evaporation from dissolution and the low sample molecular weight could also be related to a rhythmic crystal growth derived from the presence of depletion zones in the growth front [32,33]. It has been postulated that the final spherulitic morphology is a consequence of a balance between the diffusion rate (v_d) of polymer chains and the crystallization rate (v_c) [33-35]. Ridge and valley topographic textures can therefore be observed depending of the special crystallization conditions [33].

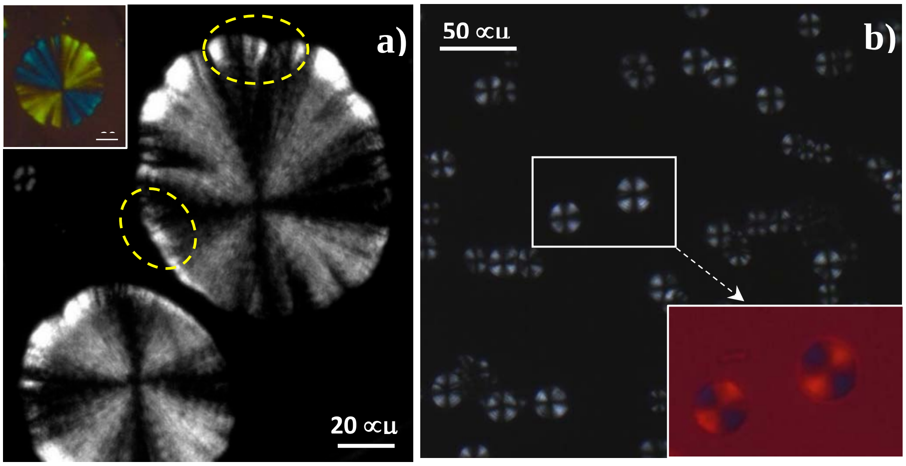

Figure 7. Spherulitic morphologies of PLC attained during slow evaporation of diluted chloroform solutions. Borders and sizes point out the crystallization of fractions with low (**a**) and medium (**b**) molecular weights.

It is highly interesting that all spherulites have also an umbrella-like geometry, which appear characteristic of the crystallization of low molecular weight polymers [36]. This umbrella-like or rose-like morphology has been discussed in detail by Okui et al. [37] for melt crystallization performed at high temperatures. Basically, the rosaceous growth was associated to the instability of the crystal growth front in molten thin film samples (a common feature for a crystallization performed from a diluted solution) [38]. Crystallization could begin with the growth of edge-on lamellae but before to attain the typical spherical envelop, a growth with flat-on lamellae is favoured. This can give rise to hedrites and rose-like crystals that contrast with the typical morphologies expected for the flat-on lamellae [39,40]. Note also in Figure 7a the high birefringence of the spherulite limits, appearing even brilliant some parts of the theoretically non-birefringent arms of the Maltese cross (see dashed ellipsoid).

A second but minority type of spherulites can also be detected (Figure 7b) during the evaporation process. In this case, the diameter is reduced to 20 μm, but both birefringence and ringed texture can be detected. The main difference corresponds to the rounded morphology, which together with the indicated small size of spherulites point out to the crystallization of a fraction of molecules with a bigger molecular weight. Nevertheless, this hypothesis is not supported by GPC data. In any case, the perfect spherical envelop and the clear rings (spacing close to 2 μm) suggest a twisting of edge-on lamellae.

Chemical images of the spherulites were obtained from the integration of the different infrared peaks (Figure 8a). In general, spherulitic sectorization was not observed in the chemical images derived from the most intense bands associated to the cyclohexane rings, as for example the asymmetric and symmetric stretching of the CH_2 group. In this case, the intensity of the peaks was practically constant. However, a detailed analysis was successful and a clear sectorization was observed by considering some minor intensity peaks as the high wavenumber shoulder at 2980 cm^{-1} and the bands around 3080 cm^{-1}. Interpretation of such peak is in progress but they are probably related to the $=CH_2$ and CH_3 groups belonging to the isopropenyl unit.

These result points out a specific orientation of this unit inside the lamellar crystals. Maltese crosses with two sectors with higher intensity (red) and two sectors with the lower intensity (blue) are derived as consequence of the distinct lamellar orientation in the spherulite (i.e., +45° and -45° with respect to the polarizer). Sectorization was clear in the imaging of the large spherulites associated to the low molecular weight fraction (left and middle images of Figure 8c). Puzzling results (see right image of Figure 8c) were achieved when the smaller spherulites were analysed. Nevertheless, the successful imaging results are interesting since reveal the role of attaining a proper and regular packing of isopropenyl groups for developing PLC crystals.

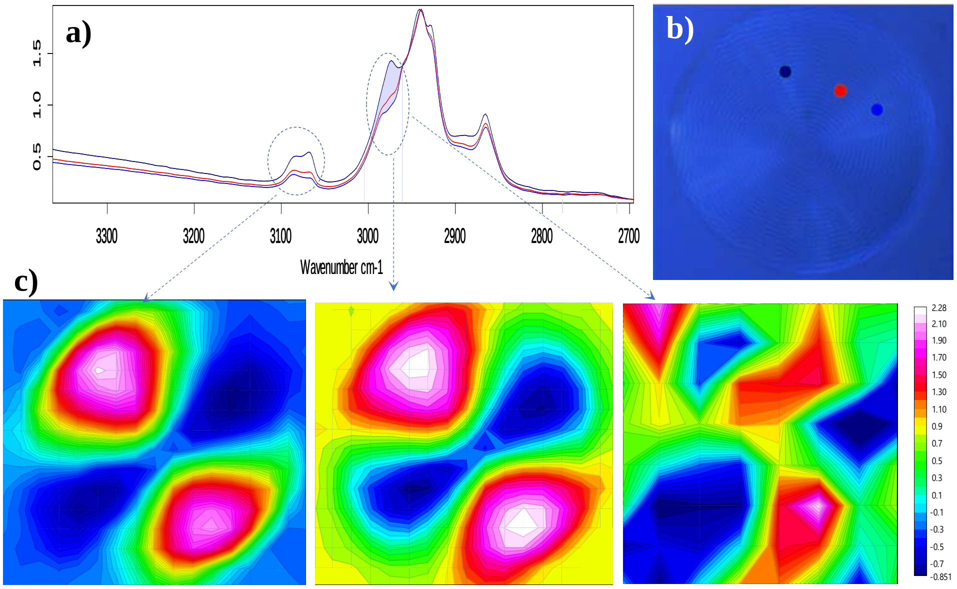

Figure 8. (**a**) FTIR spectra showing the C-H stretching region for PLC and taken from three representative microdomains of the spherulite. (**b**) Micrographs showing a representative banded spherulite and the specific microdomains were FTIR spectra were recorded. Colours are in agreement with those of the FTIR spectra. (**c**) Chemical images obtained from the FTIR bands pointed out by the circle and the ellipsoid. Left and middle images correspond to the bigger spherulites while the right image is derived from the smaller spherulites.

Figure 9 shows the X-ray diffraction profiles obtained with the different synthesized samples. In all cases, even for the regular PLC copolymer, broad peaks associated to an amorphous phase were observed. These usually low intense and broad humps are indicative of characteristic distances associated to a low-range order. Basically, all the studied samples showed three peaks (at approximately 0.754 nm, 0.505nm and 0.211 nm) with different relative intensities (note for example the different intensity ratio between the two first halos of poly(CPD-LO) and poly(PA-MO) samples More crystalline patterns could only be observed) in the case of PLC when the sample was obtained by slow evaporation of the chloroform solution.

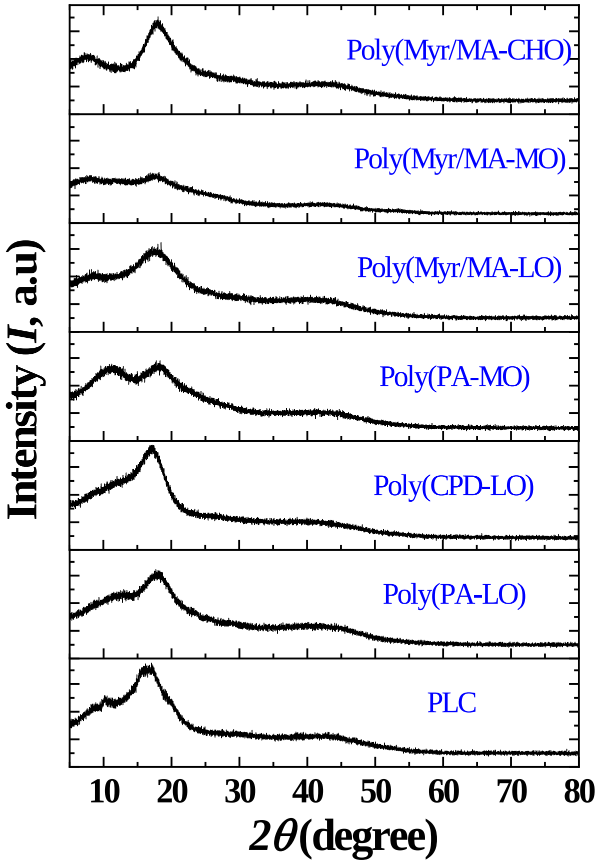

Figure 9. X-ray diffraction profiles of the as synthesized powdered samples of the different synthesized terpene derivatives.

Figure 10 clearly shows the splitting of the indicated halos into different Bragg reflections. Those more intense correspond to spacings of 0.880 nm, 0.852 nm, 0.572 nm and 0.520 nm. Note that these values are clearly different to those reported for stereocomplex sample, wich correspond to the spacings of 0.915-0.907 nm and 0.483-0.477 nm, and logically a different packing arrangement should be derived. A monoclinic or triclinic unit cell seems necessary if the molecular chain conformation is kept.

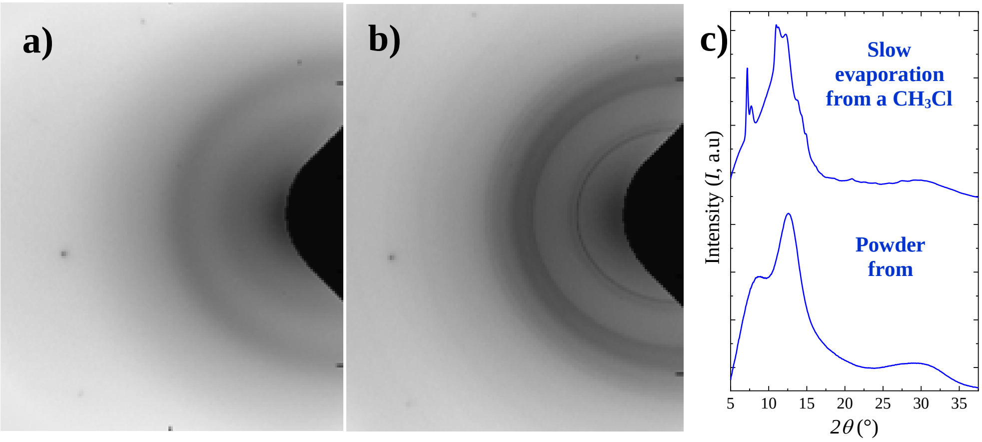

Figure 10. Bidimensional X-ray diffraction patterns of PLC as obtained from synthesis (**a**) and after slow evaporation of a chloroform solution (**b**). The corresponding linear X-ray profiles are given in (**c**).

5.3.4. Degradability of the Selected Terpene Derivatives

All the studied polycarbonates and copolyesters were stable after exposure for 21 days to both hydrolytic and enzymatic media according to weight loss measurements. Figure 11a shows the plot of the time evolution of the remaining weight for poly(PA-LO) as a representative sample, being also minimum the observed changes for the other studied sample. Hydrolytic degradation was similar for acidic, neutral and basic pHs at 37 °C, and only the increase of temperature to 70 °C caused a small evidence of degradation under the more aggressive basic conditions. Lipase and esterase enzymatic media did not cause any significant degradation, although esterase was slightly more effective. Addition of H_2O_2 gave rise to an oxidative medium that was relatively effective since at least a weight loss higher than 10% was observed after 21 days of exposure. Nevertheless, GPC curves of exposed samples showed a slight shift to higher retention times as an evidence of a certain degradation. Note the evolution of GPC curves (Figure 11b) for the representative poly(PA-Lo) sample during exposure to the esterase enzymatic medium. Thus, initial M_n and M_w values of 3,900 and 9,000 g/mol changed to 3,060 and 7,340 g/mol, respectively after only 7 days of exposure. Molecular weights of 2,300 and 6,100 g/mol were measured after 21 days, a feature that indicates an increase of the polydispersity index from 2.3 to 2.7. Therefore, it can be concluded that weight loss measurements did not report a clear evidence of degradation due to the small solubility of fragments in the degradation medium.

The performed studies demonstrated that although samples could be considered degradable, the rate was slow and consequently the integrity of the polymer was kept during at least one month of exposure under both hydrolytic and enzymatic media.

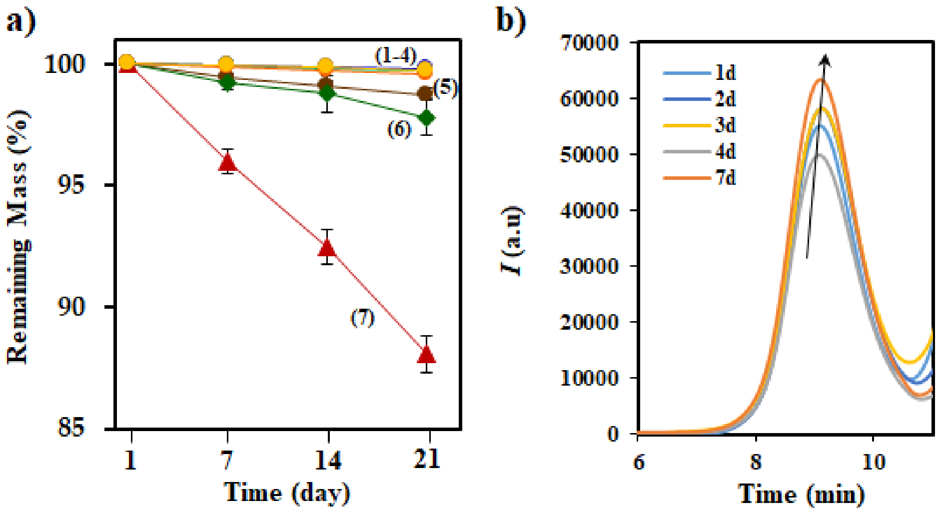

Figure 11. (**a**) Degradation of poly(PA-LO) as a function of time at different conditions: Hydrolytic degradation at pHs 3, 7 and 10 (curves 1-3), lipase enzymatic degradation at 37 °C (curve 4), esterase enzymatic degradation at 37 °C (curve 5), degradation in the basic pH 10 medium at 70 °C (curve 6) and degradation in oxidative media of H_2O_2 at 37 °C (curve 7) up to 12%. Weight losses were close to 0.5%, 1.5%, 2,7% and 12% for curves 1, curve 5, curve 6 and curve 7, respectively. (**b**) GPC curves taken for Poly(PA-LO) during exposure to the esterase enzymatic medium.

Surface degradation could also be detected through contact angles measurements although interpretation is again difficult as consequence of two opposite effects: a) The presence of more hydrophilic groups (e.g., carboxylic groups derived from the hydrolysis of ester groups) and b) the increase of surface roughness. Thus, a continuous increase was observed when the pH of the medium was increased, a feature that we associated to an enhanced degradation that affected the surface roughness. By contrast the angle significantly decreased to 60° after exposure to the oxidative medium as consequence of the significant increase of terminal groups.

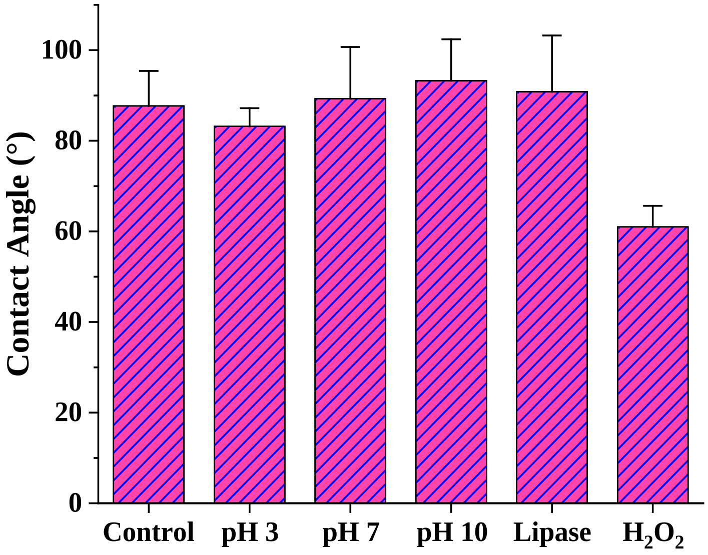

Figure 12. Contact angle measurements over the surface of poly(PA-LO) tablets after exposure to the indicated media for 21 days.

5.3.5. Biocompatibility of the Studied Biobased Polymers

The cytotoxicity of these new polymers was determined with the MTT assay. Fibroblast-type cells (hFF) and osteoblast-like cells (MG-63) seeded on the surface of the polymers derived from terpenoids and formed as films were evaluated at 24 h and 96 h after exposure to determine the cytotoxic effect on cell adhesion and proliferation. Figure 13 shows that the polymers derived from PLC and Poly(PA-LO) have no cytotoxic effect for cell adhesion and proliferation of the fibroblasts hFF and MG-63. However, those polymers that incorporate myrcene units showed a slight but non-significant decrease in cell adhesion and proliferation.

Terpenes and oxygenated derivatives of terpenes, commonly termed terpenoids, are the primary constituents of the essential oils of many types of medicinal plants and flowers. Synthetic variations and derivatives of natural terpenes and terpenoids greatly expand the variety of aromas used in perfumery and flavors used as food additives. Similarly, terpenes play a role in traditional and alternative medicines, such as aromatherapy, and are under investigation for antibacterial, antineoplastic, and other pharmaceutical functions [41]. Due to the uses of terpenoids by humans, its neoplastic activity and genotoxicity have been evaluated in some cases. Thus, it has been demonstrated that d-limonene induced neoplasms in the kidneys of male rats in association with hyaline droplet nephropathy; and beta-myrcene produced kidney and liver cancers in rats and mice after *in vivo* exposure [42], but no mutagenic activity was found [43,44].

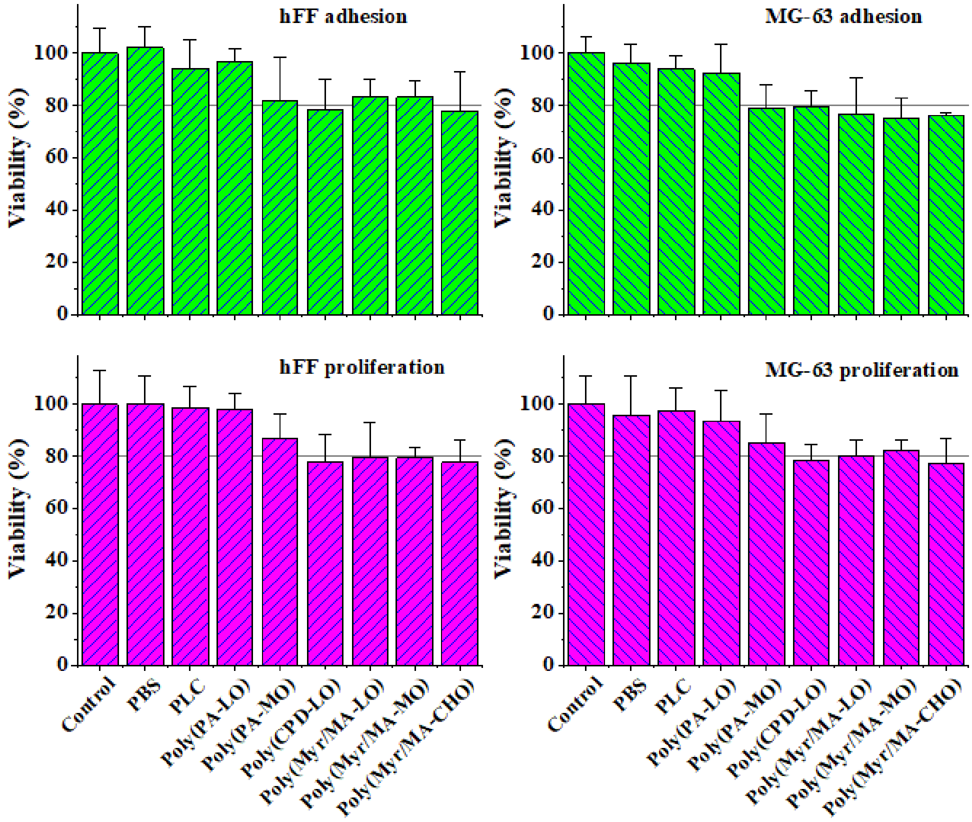

Figure 13. Cell adhesion and proliferation onto the surface of the polymers derived from terpenoids and formed as films. MTT assay was performed at 24 h (adhesion test) and 96 h (proliferation test) of culture.

Recently, the cytotoxicity of beta-myrcene was evaluated *in-vitro* using non-metabolizing cells such as the human peripheral blood mononuclear and metabolizing cells such as the human hepatoma cell line HepG2 / C3A. Regarding the MTT assay, the results showed cytotoxic effects for leukocytes at 250 µg/ml and higher concentrations, while for HepG2/C3A cells, absence of cytotoxicity was noted relative to all tested concentrations (after 24 hr exposure). However, under these experimental conditions, caution is recommended in the use of beta-myrcene, since this compound produced genotoxic effects especially after metabolic activation using human HepG2/C3A cells, which may be associated with carcinogenic and teratogenic effects previously reported in the literature [45].

In this way, the polymerization of terpenoids and considering their very low biodegradation seems to be an adequate strategy to avoid the metabolism of terpenoids in metabolizing cells and consequently their cytotoxicity and potential genotoxic damage.

5.3.6. Blending of PBS with Poly(PA-LO)

Poly(PA-LO) has been selected to be blended with PBS due to its higher glass transition temperature, presence of ester groups and good biocompatibility. Thermal properties of three blends varying its composition (i.e., 30%, 50% and 70% of PBS) were compared with those of the neat PBS (Figure 14). The first heating run was characterized by two melting peaks associated to PBS and no evidences of a polyterpene phase since the corresponding glass transition should be overlapped with the indicated melting peaks (Figure 14a). The DSC curves showed differences on the temperature of the former peak which appeared around 103 °C and consequently at lower temperature than observed for the neat PBS (107 °C). Differences suggest the formation of thinner lamellae in the blends. Note that the second and predominant peak corresponds to the lamellar reorganization/recrystallization that occurs during the heating process (i.e., a constant temperature around 113 °C was reached.

The second distinctive feature corresponds to the clear decrease of the melting enthalpy with samples having a poly(PA-LO) contents of 30% and 50%. In fact, correction of enthalpies considering the real PBS content gave values of 90 kJ/g, 92 kJ/mol and 103 kJ/mol for samples having 30%, 50% and 70% of PBS, respectively. Note than only in the third case the enthalpy was similar and even higher than observed for the neat PBS (i.e., 101 kJ/mol) as consequence of a nucleation effect. In any case, the global crystallinity of blends decreased as a consequence of the amorphous character of the polyterpene compound. Second heating runs (Figure 14b) pointed out the major difficulty to crystallize from the melt with respect to solvent casting (i.e., enthalpies were always lower for the melt crystallized samples). The lamellar population with lower thickness was not thermally stable in the case of blends, and even thinner lamellar were obtained from the neat polymer with respect those coming from solvent casting. Crystallinity of melt crystallized blends were in this case always lower than determined for the neat polyester since corrected enthalpies were 68 kJ/mol, 55 kJ/mol and 77 kJ/mol for blends having 70%, 50% and 30% of PBS, respectively. Note that again certain nucleation effect was found with the sample having a high poly(PA-LO) content and consequently the enthalpy approached to the 85 kJ/mol found for the neat polyester. Only the glass transition temperature of the PBS phase could be hardly observed around -33 °C and -42 °C. It should be pointed that any peak indicative of a miscibility between the two polymeric components was detected.

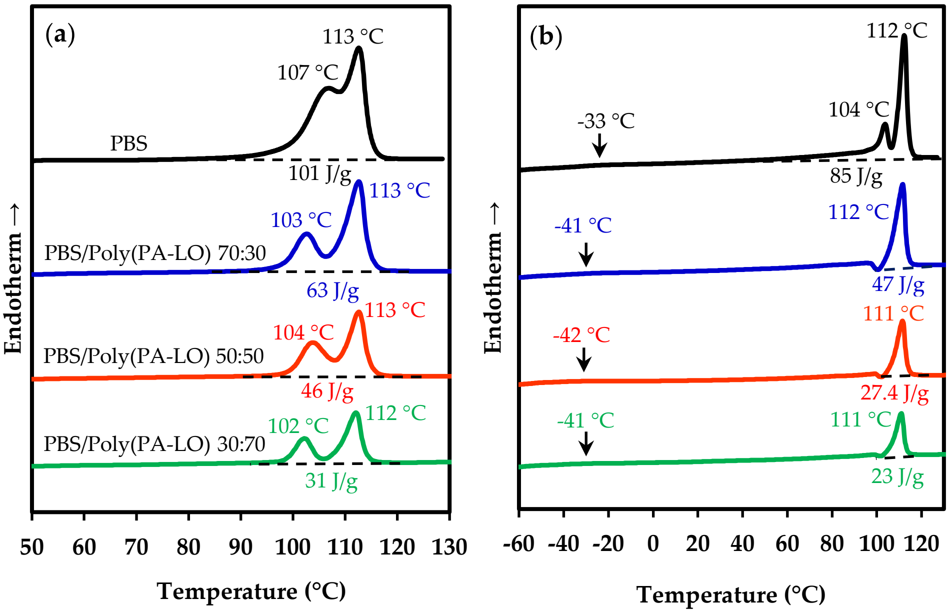

Figure 14. DSC first (**a**) and second (**b**) heating runs of PBS/Poly(PA-LO) blends with the indicated weight ratios.

Mechanical properties of the PBS/Poly(PA-LO) melt pressed films showed that the increase on the poly(PA-LO) content led to a decrease of the Young modulus. Thus, values of 330 MPa, 305 MPa and 265 MPa were determined for blends having a PBS content of 70%, 50% and 30%, respectively. The high decrease on the total crystallinity of the last sample justifies the lowest Young modulus. However the blend with 70% of PBS had similar modulus than the neat polymer (360 MPa) since in this case the stiffness of poly(PA-LO) could counterbalance the decrease of global crystallinity. A similar trend was observed when ultimate strength values (UST) were compared, although in this case differences were more evident (i.e., values of 14 MPa, 10 MPa and 7 MPa were obtained with blends having 70%, 50% and 30% of PBS, while 18 MPa was measured with the neat polymer). Basically, the observed decrease was consequence of the reduction of the elongation at break caused by a low compatibility between the two studied polymers.

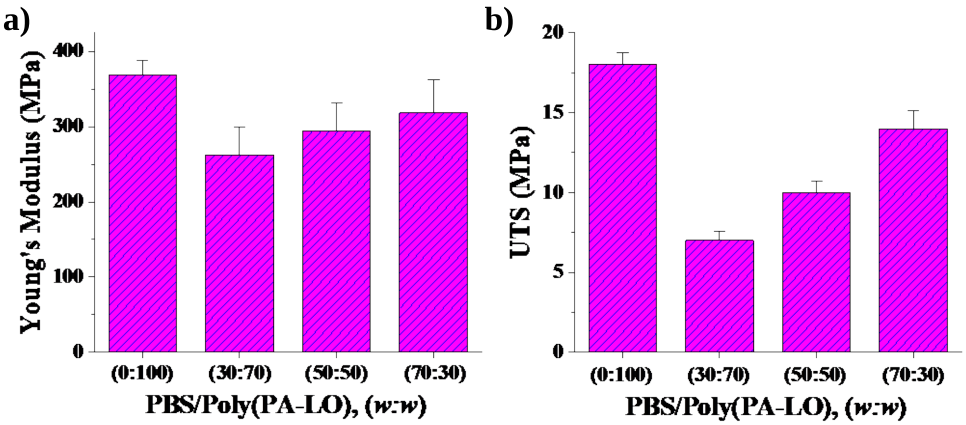

Figure 15. Comparison of the Young modulus (**a**) and the maximum strength (**b**) of neat PBS and the three studied PBS/Poly(PA-LO) blends.

All blends were hydrophobic since the contact angle of the neat PBS sample was 90° (solvent casting film) and after blending a gradual increase of the angle with the copolymer content was observed. Thus, angles of 98°, 105° and 108° were found with blends having a PBS content of 70%, 50% and 30%, respectively.

Obviously, degradability of blends increased with the increase of the biodegradable PBS fraction. Thus for example, the weight loss detected after 21 days of exposure to the esterase medium at 37 °C was 5%, 8% and 12% for the blends having 30%, 50% and 70% of PBS, respectively.

Figure 17 shows the results of the cell viability assay for the cell adhesion and proliferation at the control endpoints. The fibroblasts hFF and MG-63 cells were cultured on the films of the blends of PBS/PLC and PBS/Poly(PA-LO) prepared by solvent-casting with different proportions of the polymers. In all cases, no cytotoxic effect was observed, demonstrating that the surfaces of these blends allow adequate cell adhesion and then these cells maintain their proliferative capacity on the surface without evidence of cytotoxicity.

It is also interesting to point out that results obtained for the different blends were similar to those found for pure polymers such as PBS, PLC and poly(PA-LO). Figure 18 shows fluorescence images of proliferation cells on the different surfaces of the blend. In this case, the hFF fibroblasts adhered to the surface of the blends, being possible to observe their well-extended fusiform shape.

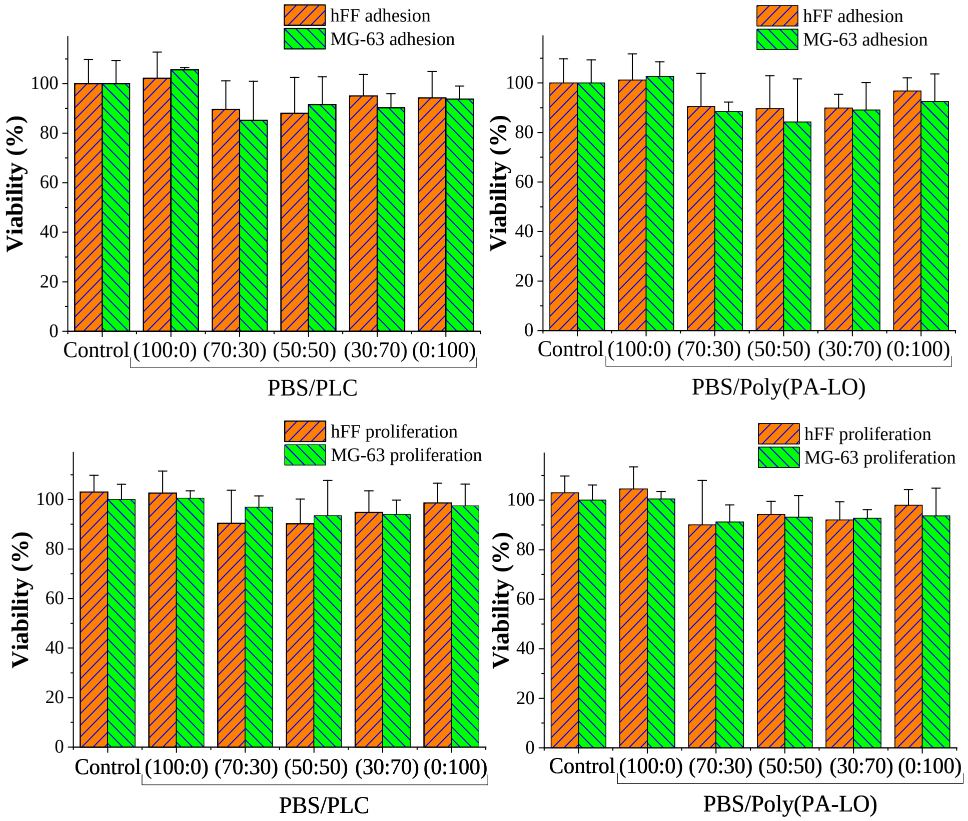

Figure 17. Cell adhesion and proliferation onto the surface of the PBS/PLC and PBS/Poly(PA-LO) blends formed as films. MTT assay was performed at 24 h (adhesion test) and 96 h (proliferation test) of culture.

Blends of PBS/PLC and PBS/Poly(PA-LO) have been characterized by the restriction of the mobility of terpene oxide and aromatic unit of phthalic, respectively. These restrictions in the mobility of the chains can favour the insolubility of the polymers and reduce their biodegradation. In this sense, this fact may favour biocompatibility because it is less likely that the terpene units were cleaved and solubilized. Therefore, the capacity of such unit to enter in the cellular metabolism producing cytotoxic effects was dramatically decreased.

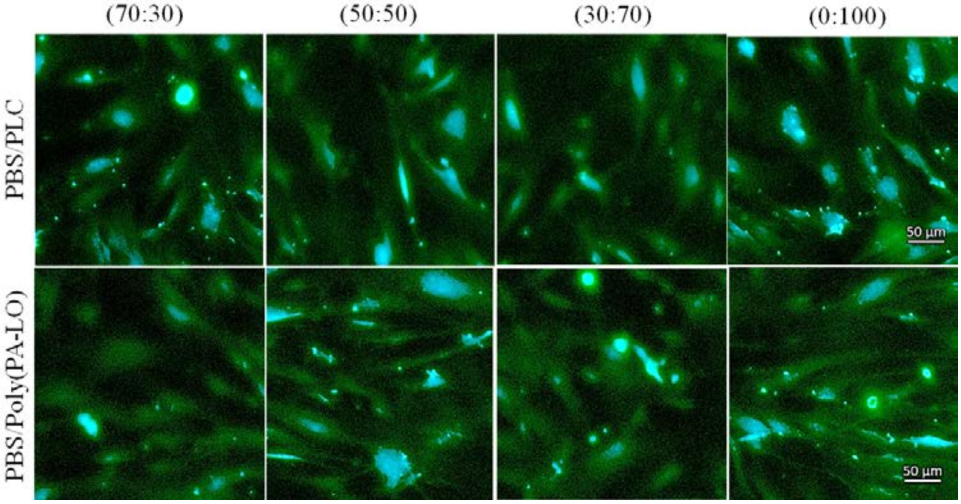

Figure 18. Fluorescence images of the proliferated hFF fibroblasts on the different surfaces of the PBS/PLC and PBS/Poly(PA-LO) blends. The cytoplasm was stained with phalloidin (green) and the nucleus with Hoechst (blue).

5.3.7. Poly(PA-LO) Blend Scaffolds from TIPS

The preparation of scaffolds constituted by the mixture of 70% of PBS and 30% of poly(PA-LO) was evaluated due to the interesting characteristic of the selected terpene derivative. In the present study, due to utilizing the 1,4 dioxane solvent with high crystallization temperature (i.e. 11.8 °C) a solid-liquid phase separation through crystallization of the solvent was expected during cooling. Nevertheless, in this system there is a natural tendency for the semi-crystalline PBS polymer to be crystallized (i.e. solid-liquid phase separation through crystallization of the polymer) and also a tendency for the polymer solution to be separated into polymer-rich and polymer-lean phases during the cooling process (i.e. liquid-liquid phase separation). Hence, the studied system includes driving forces for three different mechanisms of phase separation. In this situation, each phase separation mechanism produces its own typical structure and affects the final morphology of the polymer matrix.

Crystallization of the solvent generally leads to large isotropic solid-walled pores with well-defined pore walls when a multidirectional cooling system is applied to the solution [46]. The pores formed through this mechanism had a geometry similar to the solvent crystallites. By applying a uniaxial cooling system, the solvent crystals grew along the cooling direction and produced an anisotropic microtubular structure in which the porosities formed by solvent crystals have been oriented towards the heat transfer direction [47,48]. The surface of such matrices typically has a ladder-like architecture in which repeating units of channels and partitioning walls are respectively parallel and perpendicular to the temperature gradient [49]. Crystallization of the solvent rapidly advanced throughout the structure by expelling the polymer from the solvent crystallization front [47].

Liquid-liquid phase separation through the fast spinodal decomposition mechanism [50], produced a bicontinuous isotropic structure with the several-micron pores that may gradually coarsen to tens of microns if enough time was available [47,51]. Meanwhile, the polymer was able to crystallize slowly from the solution during or after the phase separation process in the polymer-rich phase, stabilizing the structure which has previously been formed by the phase separation. Crystallization or precipitation of the polymer from the solution may create different morphologies. By increasing the polymer concentration, these structures may vary from leafy structures characterized by randomly oriented and connected polymer leaves to spherulitic structures as an interconnected network of crystallites [52,53].

When the polymer solution involved driving forces for different phase separation mechanisms, the kinetics of phase separation specified whether the thermodynamically favored transition happens or not, and also to what extent the transition occurred [53]. Accordingly, by increasing the temperature gradient (i.e., faster cooling), the kinetically fast separation mechanisms, that is, solvent crystallization and spinodal decomposition, can affect the structure. Therefore, the large pores formed through solvent crystallization and smaller porosities generated by spinodal decomposition mechanism are expected to be observed at higher cooling rates.

As it is discernible in SEM micrographs, the scaffold prepared at the -74 °C bath, includes large pores originated from crystallization of 1,4 dioxane. Moreover, the small pores formed by spinodal decomposition mechanism that did not have enough time to grow, are observed as several-micron orifices in the pore walls, and play a role as interconnectivities (Figure 19a). The domination of large pores from solvent crystallization was obviously decreased in the polymer matrix prepared at the slower cooling condition in -20 °C bath (Figures 19b and 19c), while the spinodal-originated porosities were slightly coarsened. In this case, the texture of the pore walls was composed in a great extent of polymer leaves formed by crystallization of the polymer, a feature that is more detectable at higher magnification (inset of Figure 19b). Concerning their dimensions, these polymer leaves are supposed to be stacked lamellae that have developed with a significant curvature [52].

The surface image of the foam prepared using uniaxial temperature gradient in liquid nitrogen (Figure 20a, and the higher magnification image shown in the inset) exhibits the typical ladder-like structures with the repeating units and partitioning walls. The cross-section of this matrix demonstrates the microtubular architecture with the well-oriented porosities towards the heat transfer direction (Figure 20b).

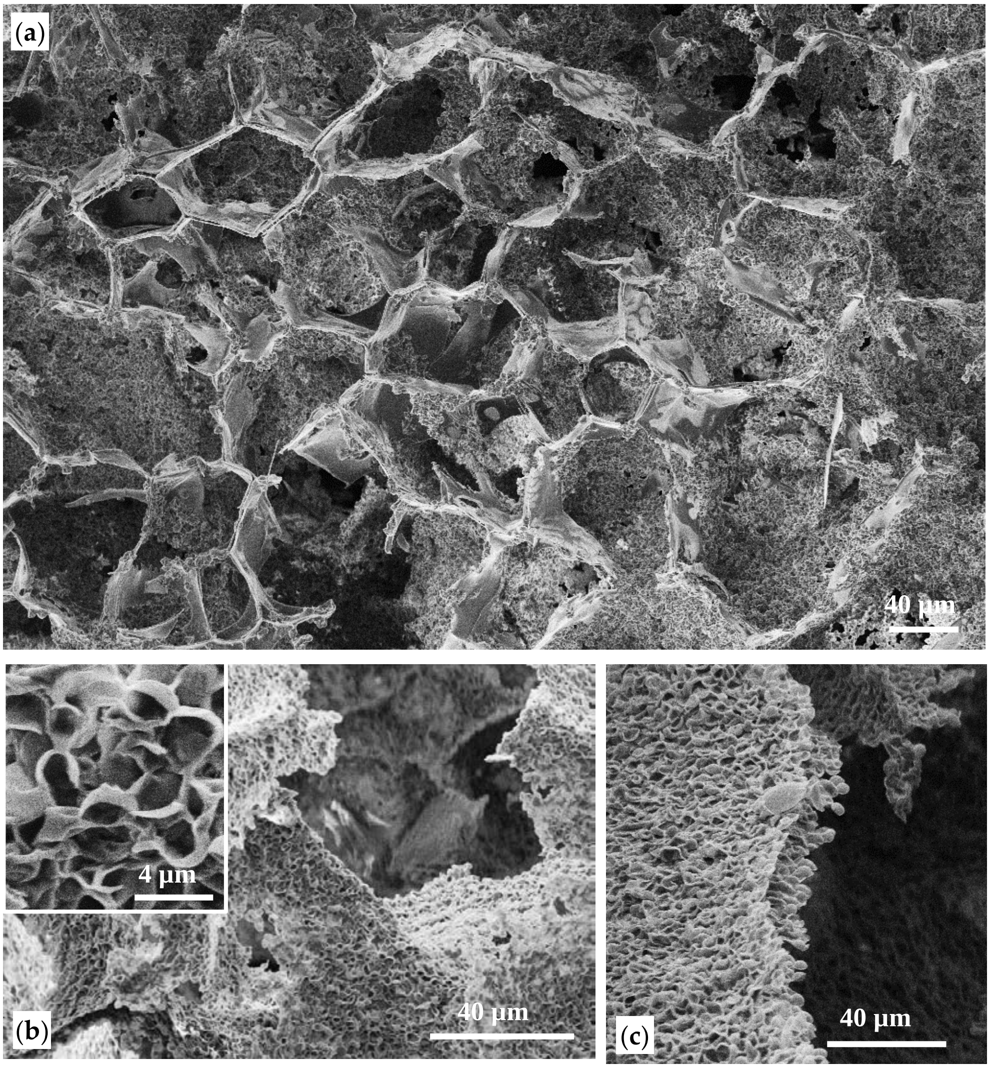

Figure 19. SEM micrograph of the PBS/poly(PA-LO) scaffold prepared using different cooling baths at: -74 °C (a), -20 °C (b,c). Inset shows the leafy structure of the corresponding scaffold at higher magnification.

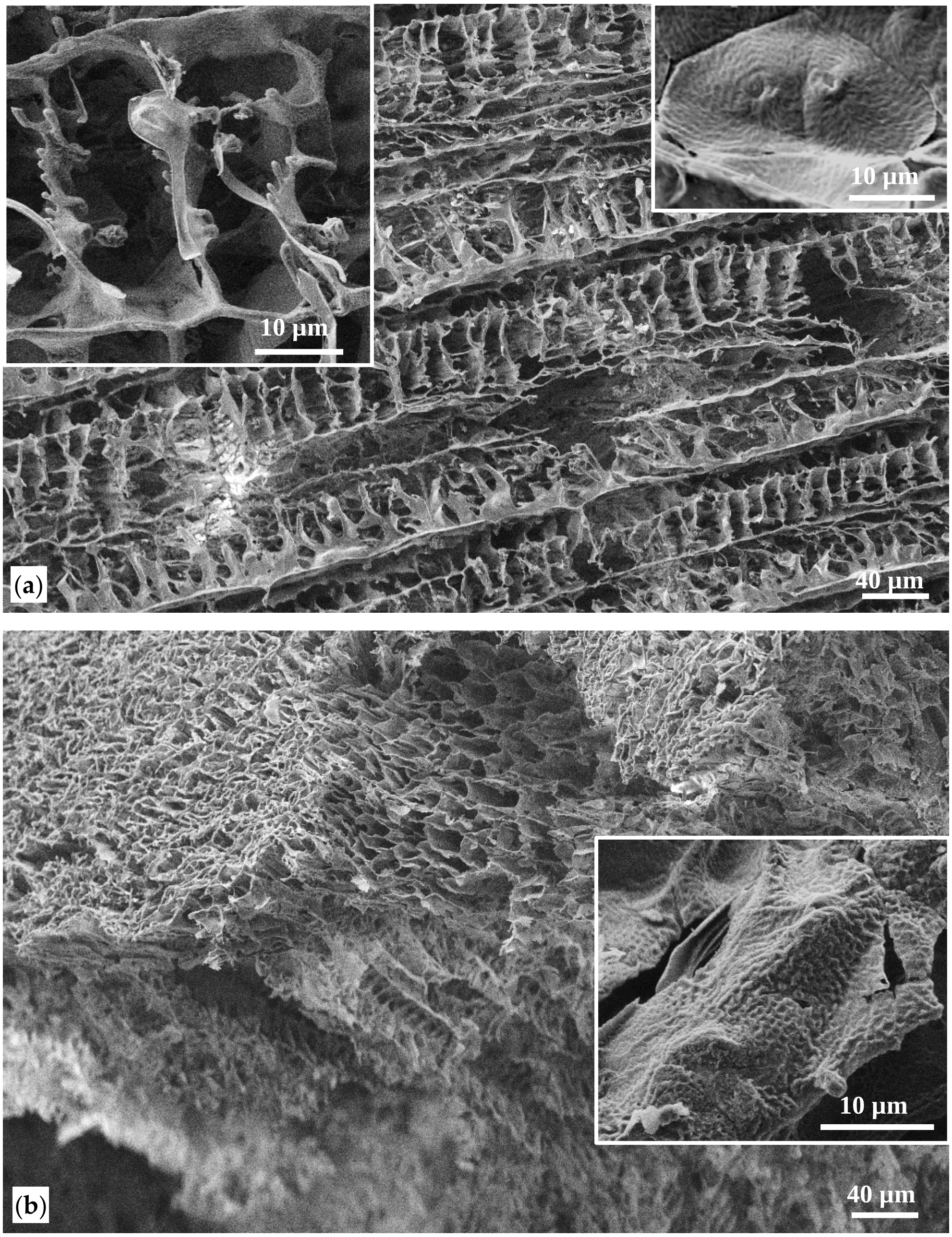

Figure 20. SEM micrograph of the PBS/poly(Pa-Lo) scaffold prepared under uniaxial temperature gradient condition at -196 °C: top surface (**a**), cross-section (**b**). Left inset of (**a**) shows a higher magnification of the corresponding surface. Right insets show spherulites with high magnification from the cross-section of oriented scaffolds made of neat PBS (**a**) [24] and PBS/Poly(Pa-LO) (**b**).

It is interesting to note that the polymer has been crystallized in the form of polymer leaves at the lower temperature gradient but has formed a spherulitic structure using the uniaxial high temperature gradient. It can be speculated that the fast and orientational crystallization of 1,4 dioxane strongly avoids the polymer from the crystallization front and results in the formation of a more concentrated polymer-rich phase compared to that formed through liquid-liquid phase separation. The higher polymer concentration allows forming supermolecular spherulitic structures.

The spherulitic structure observed in the walls of the oriented pores of PBS/poly(PA-LO) scaffold (right inset of Figure 20b) is not as planar as the spherulites observed in the neat PBS matrix (right inset of Figure 20a) [24], and has a smaller size, slightly rougher texture and less integrity with the adjacent spherulites. These features indicate the imperfection of spherulite formation during the crystallization of the polymer in the polymer-rich separated phase. Furthermore, this result is in agreement with the previous calorimetric study of the studied blend that indicated a more difficult crystallization compared to that observed with the neat PBS. on the Regarding the relatively low molecular weight of poly(PA-LO), it seems reasonable to assume that the small chains of this polymer can entangle between the PBS lamellae and cause structural disarrangement in the crystalline regions, limiting to some extent the ideal structures where the thickness of polymer leaves has been reduced (i.e., smaller lamella stacks) due to the presence of poly(PA-LO) in the polymer-rich phase. In addition, the presence of poly(PA-LO) somewhat has decreased the size and well-partitioning of large pores formed by solvent crystallization upon fast and multidirectional cooling.

5.4. Conclusions

Stiff biobased molecular chains can be obtained from the copolymerization of terpene oxides with either carbon dioxide or different dicarboxylic anhydrides having aromatic rings or aliphatic mono or bicycles. Copolymers offered a graduation of T_gs from 75 °C to 127 °C. In addition, rings having a myrcene substitution showed a relatively low T_g as consequence of the flexibility given by this lateral group.

The studied biobased polycarbonates and polyesters were thermally stable and specifically the type of terpene oxide was determinant. Copolymers were completely amorphous when directly obtained from synthesis, although poly(limonene carbonate) rendered spherulites by slow evaporation of diluted chloroform solutions. The capacity to crystallize of this enantiomeric copolymer was surprising and gave rise to a different structure than the orthorhombic packing previously reported for the racemic copolymer. The studied terpene based copolymers were degraded with difficulty when typical hydrolytic and enzymatic media were considered. Nevertheless, GPC measurements demonstrated the progress of degradation in contrast with the low weight loss measurements, which basically reflect the low solubility of degraded fragments. Copolymers were fully biocompatible according to adhesion and proliferation assays performed with fibroblast cells. Only the presence of myrcene lateral groups caused a certain toxicity.

Biobased terpene derivatives could be blended with poly(butylene succinate giving rise to biocompatible and degradable materials. PBS/poly(PA-LO) blends with a maximum content of the terpene derivative of 30% showed similar mechanical properties than the neat polyester as consequence of two opposite effects: the stiffness of the terpene compound and the decrease of the crystallinity of the sample.

Scaffolds with a random or an oriented pore distribution could successfully be prepared from 1,4-dioxane solutions by the temperature induced phase separation method. The control of the cooling process of the initial homogenous solution was fundamental to vary the type of pore distribution, the size of pores and even the development of crystalline entities.

5.5 References

1. Jasinska, L.; Koning, C. E. J. Waterborne Polyesters Partially based on Renewable Resources. *J. Polym. Sci., A: Polym. Chem.* **2010**, *48*, 5907−5915.
2. Engels, H.-W.; Pirkl, H.-G.; Albers, R.; Albach, R. W.; Krause, J.; Hoffmann, A.; Casselmann, H.; Dormish, J. Polyurethanes: Versatile Materials and Sustainable Problem Solvers for Today's Challenges. *Angew. Chem., Int. Ed.* **2013**, *52*, 9422−9441.
3. Darensbourg, D. J. Making Plastics from Carbon Dioxide: Salen Metal Complexes as Catalysts for the Production of Polycarbonates from Epoxides and CO_2. *Chem. Rev.* **2007**, *107*, 2388−2410.
4. Ye, J.; Ma, S.; Wang, B.; Chen, Q.; Huang, K.; Xu, X.; Li, Q.; Wang, S.; Lu, N.; Zhu, J. High-Performance Biobased Epoxies from Ferulic Acid and Furfuryl Alcohol: Synthesis and Properties. *Green Chem.* **2021**, *23*, 1772–1781.
5. Wilbon, P. A.; Chu, F.; Tang, C. Progress in Renewable Polymers from Natural Terpenes, Terpenoids, and Rosin. *Macromol. Rapid Commun.* **2013**, *34*, 8−37.
6. Martín, C.; Kleij, A. W. Terpolymers derived from Limonene Oxide and Carbon Dioxide: Access to Cross-Linked Polycarbonates with Improved Thermal Properties. *Macromolecules* **2016**, *49*, 6285− 6295.
7. Auriemma, F.; De Rosa, C.; Di Caprio, M. R.; Di Girolamo, R.; Ellis, W. C.; Coates, G. W. Stereocomplexed Poly(Limonene Carbonate): A Unique Example of the Cocrystallization of Amorphous Enantiomeric Polymers. *Angew. Chem., Int. Ed.* **2015**, *54*, 1215−1218.
8. Darensbourg, D. J.; Poland, R. R.; Escobedo, C. Kinetic Studies of the Alternating Copolymerization of Cyclic Acid Anhydrides and Epoxides, and the Terpolymerization of Cyclic Acid Anhydrides, Epoxides, and CO2 Catalyzed by (Salen)CrIIICl. *Macromolecules* **2012**, *45*, 2242−2248.
9. Si, G.; Zhang, L.; Han, B.; Duan, Z.; Li, B.; Dong, J.; Li, X.; Liu, B. Novel Chromium Complexes with a [OSSO]-Type Bis(Phenolato) Dianionic Ligand Mediate the Alternating Ring-Opening Copolymerization of Epoxides and Phthalic Anhydride. *Polym. Chem.* **2015**, *6*, 6372−6377.
10. Paggiola, G.; Stempvoort, S.V.; Bustamante, J.; Barbero, J.M.V.; Hunt, A.J.; Clark, J.H. Can bio-based chemicals meet demand? Global and regional case-study around citrus waste-derived limonene as a solvent for cleaning applications. *Biofuel. Bioprod. Biorefin.* **2016**, *10*, 686-698.
11. Della Monica, F.; Kleij, A.W. From terpenes to sustainable and functional polymers. *Polym. Chem.* **2020**, *11*, 5109-5127.
12. Robert, C.; de Montigny, F.; Thomas, C. M. Tandem Synthesis of Alternating Polyesters from Renewable Resources. *Nat. Commun.* **2011**, *2*, 586.
13. Nejad, E. H.; Paoniasari, A.; van Melis, C. G. W.; Koning, C. E.; Duchateau, R. Catalytic Ring-Opening Copolymerization of Limonene Oxide and Phthalic Anhydride: Toward Partially Renewable Polyesters. *Macromolecules* **2013**, *46*, 631−637.

14. Jacquel, N.; Freyermouth, F.; Fenouillot, F.; Rousseau, A.; Pascault, J.P.; Fuertes, P.; Saint-Loup, R. Synthesis and properties of poly(butylene succinate): Efficiency of different transesterification catalysts. *J. Polym. Sci. A Polym. Chem.* **2011**, *49*, 5301-5312.

15. Rafiqah, S.A.; Khalina, A.; Harmaen, A.S.; Tawakkal, I.A.; Zaman, K.; Asim, M.; Nurrazi, M.N.; Lee, C.H. A Review on Properties and Application of Biobased Poly(Butylene Succinate). *Polymers* **2021**, *13*, 1436.

16. Doug S. *BCC research reports PLS050A.* 2010. Bioplastics: technologies and global markets.

17. Ravenstijn, J.T.J. *The State-of-the-art on Bioplastics: Products, Markets, Trends, and Technologies*, Ravenstijn: Lüdenscheid, Germany, 2010.

18. Babu, R.P.; O'Connor, K.; Seeram, R. Current progress on biobased polymers and their future trends. *Prog. Biomater.* **2013**, *2*, 8.

19. Gigli, M.; Fabbri, M.; Lotti,N.; Gamberini, R.; Rimini, B.; Munari, A. Poly(butylene succinate)-based polyesters for biomedical applications: A review. *Eur. Polym. J.* **2016**, *75*, 431-460.

20. Weraporn, P.A.; Sorapong P.; Narongchai O.C.; Ubon I.; Puritud J.; Sommai P.A. Preparation of polymer blends between poly (L-lactic acid), poly (butylene succinate-*co*-adipate) and poly (butylene adipate-*co*-terephthalate) for blown film industrial application. *Energy Procedia.* **2011**, *9*, 581–588.

21. Bian, J.; Han, L.; Wang, X.; Wen, X.; Han, C.; Wang, S.; Dong, L. Nonisothermal crystallization behavior and mechanical properties of poly(butylene succinate)/silica nanocomposites. *J. Appl. Polym. Sci.* **2010**, *116*, 902-912.

22. Flores, E.D.; Funabashi, M.; Kunioka, M. Mechanical properties and biomass carbon ratios of poly(butylene succinate) composites filled with starch and cellulose filler using furfural as plasticizer. *J. Appl. Polym. Sci.* **2009**, *112*, 3410-3417.

23. Zeinali, R; del Valle, L.; Torras, J.; Puiggalí, J. Recent Progress on Biodegradable Tissue Engineering Scaffolds Prepared by Thermally-Induced Phase Separation (TIPS). *Int. J. Mol. Sci.* **2021**, *22*, 3504.

24. Zeinali, R; del Valle, L.; Franco, L.; Puiggalí, J. Poly(butylene succinate) Matrices Obtained by Thermally-Induced Phase Separation: Structural Modifications Affect Drug Release. *Molecules*, **2021**, In preparation.

25. Mongay, C., Cerdà, V. A Britton-Robinson buffer of known ionic strength. *Ann. Chim.* **1974**, *64*, 409-412.

26. Llorens, E.; del Valle, L. J.; Díaz, A.; Casas, M. C.; Puiggalí, J. Polylactide nanofibers loaded with vitamin B6 and polyphenols as bioactive platform for tissue engineering. *Macromol. Res.* **2013**, *21*, 775-787.

27. Byrne, C. M.; Allen, S. D.; Lobkovsky, E. B.; Coates, G. W. Alternating copolymerization of limonene oxide and carbon dioxide. *J. Am. Chem. Soc.* **2004**, *126*, 11404.

28. F. Auriemma, C. De Rosa, M. R. Di Caprio, R. Di Girolamo, G. W. Coates Crystallization of alternating limonene oxide/carbon dioxide copolymers: determination of the crystal structure of stereocomplex poly (limonene carbonate). *Macromolecules* **2015**, *48*, 2534−2550.

29. Barham, P.J.; Keller, A.; Otun, E.L.; Holmes, P.A. Crystallization and morphology of a bacterial thermoplastic: Poly-3-hydroxybutyrate. *J. Mater. Sci.* **1984**, *19*, 2781–2794.

30. Schultz, J.M.; Kinloch, D.R. Transverse screw dislocations: A source of twist in crystalline polymer ribbons. *Polymer* **1969**, *10*, 271–278.

31. Zhao, L.; Wang, X.; Li, L.; Gan, Z. Structural analysis of poly(butylene adipate) banded spherulites from their biodegradation behavior. *Polymer* **2007**, *48*, 6152–6161.

32. Kyu, T.; Chiu, H.W.; Guenthner, A.J.; Okabe, Y.; Saito, H.; Inoue, T. Rhythmic growth of target and spiral spherulites of crystalline polymer blends. *Phys. Rev. Lett.* **1999**, *83*, 2749–2752.

33. Ding, G.; Liu, J. Morphological varieties and kinetic behaviors of poly(3-hydroxybutyrate) (PHB) spherulites crystallized isothermally from thin melt film. *Colloid Polym. Sci.* **2013**, *291*, 1547–1554.

34. Duan, Y.; Jiang, Y.; Jiang, S.; Li, L.; Yan, S. Depletion-Induced Nonbirefringent Banding in Thin Isotactic Polystyrene Thin Films. *Macromolecules* **2004**, *37*, 9283–9286.

35. Keith, H.D.; Padden, F.J. Jr. A phenomenological theory of spherulitic crystallization. *J. Appl. Phys* **1963**, *34*, 2409–2421.

36. Planellas, M.; Puiggalí, J. Synthesis and properties of poly(L-lactide)-*b*-poly(L-phenylalanine) hybrid copolymers. *Int. J. Mol. Sci.* **2014**, *15*, 13247-13266.

37. Kawashima, K.; Kawano, R.; Miyagi, T.; Umemoto, S.; Okui, N. Morphological Changes in Flat-on and Edge-on Lamellae of Poly(Ethylene Succinate) Crystallized from Molten Thin Films. *J. Macromol. Sci. B* **2003**, *42*, 889-899.

38. Keith, H.D. On the relation between different morphological forms in high polymers. *J. Polym. Sci. A, Gen. Pap.* **1964**, *2*, 4339-4360.

39. Geil, P.H. *Polymer Single Crystals*, Wiley-Interscience: New York, USA, 1963.

40. Bassett, D.C. *Principles of Polymer Morphology*, Cambridge University Press: London, 1981.

41. Zwenger, S.; Basu, C. Plant terpenoids: Applications and future potentials. *Biotechnol. Mol. Biol. Rev.* **2008**, *3*, 1-7.

42. Kim, Y.W.; Kim, M.J.; Chung, B.Y.; Bang, D.Y.; Lim, S.K.; Choi, S.M.; Lim, D.S.; Cho, M.C.; Yoon, K.; Kim, H.S., et al. Safety Evaluation And Risk Assessment Of d-Limonene. *J. Toxicol. Environ. Health B* **2013**, *16*, 17-38.

43. NTP (National Toxicology Program). *Toxicology and carcinogenesis studies of d-limonene (CAS No. 5989-27-5) in F344/N rats and B6C3F1 mice (Gavage studies).* Natl. Toxicol. Program Tech. Rep. Ser. 347, 1990, 1–165.

44. NTP (National Toxicology Program). *Toxicology and carcinogenesis studies of β-myrcene (CAS No. 123-35-3) in F344/N rats and B6C3F1 mice (Gavage studies).* Natl. Toxicol. Program Tech. Rep. Ser. 557, 2010, 1–169.

45. Orlando, J.B.; Silva, B.O.; Pires-Cunha, C.L.; Hiruma-Lima, C.A.; Gaivão, I.O.N.d.M.; Maistro, E.L. Genotoxic effects induced by beta-myrcene following metabolism by liver HepG2/C3A human cells. *J. Toxicol. Environ. Health A* **2019**, *82*, 176-185.

46. Zeinali, R.; Khorasani, M.T.; Behnamghader, A.; Atai, M.; Valle, L.; Puiggalí, J. Poly(hydroxybutyrate-co-hydroxyvalerate) Porous Matrices from Thermally Induced Phase Separation. *Polymers* **2020**, *12*, 2787.

47. Chen, V.J.; Ma, P.X. Polymer phase separation. In *Scaffolding in Tissue Engineering*; Williams, C.G., Elisseeff, J.H., Eds.; Taylor & Francis: Boca Raton, FL, USA, 2006; pp. 125–137.

48. Zeinali, R.; del Valle, L.J.; Torras, J.; Puiggalí, J. Recent Progress on Biodegradable Tissue Engineering Scaffolds Prepared by Thermally-Induced Phase Separation (TIPS). *Int. J. Mol. Sci.* **2021**, *22*, 3504.

49. Zhang, R.; Ma, P.X. Poly(α-hydroxyl acids)/hydroxyapatite porous composites for bone-tissue engineering. I. Preparation and morphology. *J. Biomed. Mater. Res.* **1999**, *44*, 446-455.

50. Conoscenti, G.; Carrubba, V.; Brucato, V. A Versatile Technique to Produce Porous Polymeric Scaffolds: The Thermally Induced Phase Separation (TIPS) Method. *Arch. Chem. Res.* **2017**, *1*, 1–3.

51. Pavia, F.C.; La Carrubba, V.; Piccarolo, S.; Brucato, V. Polymeric scaffolds prepared via thermally induced phase separation: Tuning of structure and morphology. *J. Biomed. Mater. Res. A* **2008**, *86A*, 459–466.

52. Lloyd, D.R.; Kinzer, K.E.; Tseng, H.S. Microporous membrane formation via thermally induced phase separation. I. Solid-liquid phase separation. *J. Membr. Sci.* **1990**, *52*, 239–261.

53. Van de Witte, P.; Dijkstra, P.J.; van den Berg, J.W.A.; Feijen, J. Phase separation processes in polymer solutions in relation to membrane formation. *J. Membr. Sci.* **1996**, *117*, 1–31.

Chapter 6

Conclusions

In this investigation, the 3D microporous inter-connective matrices based on PHBV and PBS biodegradable polymers were manufactured by thermally-induced phase separation. The drug-loaded and blend scaffolds were prepared through a one-step fabrication/loading or fabrication/blending process via TIPS technique. Variation in TIPS process parameters such as polymer, solvent and cooling systems affected the phase separation process, resulting in different scaffold properties. Various TIPS-originated architectures with regular porosities ranging from several to hundred microns, or elongated/oriented-pore structures were obtained through solid-liquid and liquid-liquid phase separations. Various morphologies such as platelet-like, beady, leafy and spherulitic structures were also formed through crystallization of the polymers from the solutions during the fabrication process.

- *PHBV matrices*

With respect to the preparation of PHBV matrices, due to utilization of DXN solvent, the TIPS process generally was controlled by solid-liquid phase separation through crystallization of the solvent. Nevertheless, due to the existence of driving forces for liquid-liquid phase separation and polymer crystallization, the morphology was to a lesser or greater extent affected by these phenomena. Hence, there was a competition between the aforementioned mechanisms. The morphological effect of each mechanism was greatly dependent on its kinetics and the thermodynamic conditions. The process variables including material selection (i.e., PHBV with different HV molar ratios) and different cooling rates (caused by two different multidirectional thermal gradients) strongly affected the phase separation process. This led to differences in scaffold properties in terms of morphological features and mechanical properties. Specifically, under increased cooling rate/HV content conditions, the system tended to form large porosities with well-distinguished pore walls arising from solvent crystallization. Therefore, in these conditions the solid-liquid phase separation was recognized as the dominant mechanism and controlled the morphology. In addition, a uniform distribution of small several-micron pores, grown to tens of microns, formed by liquid-liquid phase separation were mostly observed in the pore walls, serving as structural interconnectivities. On the other hand, taking into account the slow kinetics of polymer crystallization, its corresponding platelet-like morphology with low structural continuity was observed to a greater extent upon slower cooling. The decreased rigidity of the scaffolds upon slower cooling can be ascribed to presence of more regions with this characteristics. The higher rigidity of the scaffolds with lower HV contents was attributed to the fact that the crystallinity degree of PHBV copolymers drops as their

HV units decrease. The MDCK and NRK cell culture studies revealed that the porous PHBV matrices were fully biocompatible throughout the whole culture period. This indicates that in addition to material safety, the TIPS fabrication process and lyophilization protocol used for extraction of the organic solvent perfectly fulfil to biocompatibility criteria for tissue engineering scaffolds.

- *PBS matrices*

With regard to the PBS polymer, scaffold fabrication and drug incorporation (i.e., different levels of CUR and PIP) were successfully performed in one step via TIPS technique. TIPS process variables in this case were extended to utilization of two different solvent (i.e., DXN and THF) and further cooling systems (i.e., further multidirectional thermal gradients and also a uniaxial one).

Roughly similar to PHBV scaffolds, pore morphology and architecture of the scaffolds prepared using DXN solvent to a great extent was controlled by solid-liquid phase separation, being more evident at higher rates. Compared to PHBV scaffolds, in this case the effect of liquid-liquid phase separation was more significant and crystallization of the polymer led to formation of a leafy structure (polymer leaves) rather than platelet-like regions. In addition to spinodal decomposition-derived small pores (which were also observed in PHBV scaffolds), polymer beads were also formed through liquid-liquid phase separation (i.e., nucleation and growth mechanism). This can be attributed to higher cloud point of PBS-DXN than PHBV/DXN system, resulting in remaining more time in two-phase region below the binodal curve until reaching the solvent freezing point. Logically these polymer beads and leaves were observed to a greater extent at slower cooling conditions. Since here the pore wall were composed of these beady-leafy morphologies, they were thicker with less definition compared to PHBV matrices.

Using THF solvent prevented the occurrence of solid-liquid phase separation in the system, resulting in formation of small to moderate-sized pores (depending on their growing stage) with roughly similar beady/leafy-textured pore walls.

Applying uniaxial high thermal gradient in liquid nitrogen, prevented the occurrence of liquid-liquid phase separation and its corresponding morphologies. Besides, such cooling system extremely limited the growth of DXN crystallites in all possible direction other than the uniaxial one. Thus, an anisotropic structure with highly elongated porosities, oriented towards the uniaxial heat transfer was formed. Interestingly, such cooling condition allowed the polymer to be crystallized form the polymer rich phase to form spherulites, leading to formation of dense spherulitic pore walls. Similar to PHBV scaffolds, the neat PBS matrices in all structural form displayed full biocompatibility, confirming the material/process safety.

- *Drug-loaded PBS matrices*

The incorporated drugs were uniformly dispersed all over the matrix structure indicating the one-step fabrication/drug loading process based on TIPS technique was an effective method. Although drug loading in low quantities did not influence the structure and morphology of PBS matrices, incorporation of drugs in high quantities led to decrease in porosity level and formation of smoother surfaces.

Upon high-level loading, the rounded CUR agglomerations seemed unified and integrated with the polymer network, being covered with a surrounding thin layer. Whereas aggregations of PIP prismatic crystals did not appear to be unified. Due to higher affinity of CUR, the integration was assumed to be as a result of a possible interaction with the polymer during the TIPS fabrication process, which was subsequently confirmed by physicochemical and thermal evaluations such as IR-spectroscopy and calorimetric and thermogravimetric analyses.

No burst effect associated with superficial release was observed in the release studies. However, the faster release of PIP from the microporous polymeric matrix could be attributed to its lower affinity with the polymer component and also higher solubility in the aqueous DMEM release medium.

Matrices with uniaxially-oriented pore structure exhibited a slower release profile compared to those having randomly-oriented porosities. It is speculated that the drug release is impeded by the dense spherulitic-textured framework of oriented matrices, resulting in a decelerated release rate and an ideal sustained release of both drugs. The oriented matrices also exhibited greater biocompatibility and cell viability all through the culture period. Our findings suggest that such TIPS-based structural modification/orientation can be presented as a state-of-the-art methodology for controlling the drug release and developing the cell/drug delivery potential of PBS matrices.

- *Blended PBS matrices*

The biobased terpene derived polymers with high rigidity were characterized in terms of thermal properties, degradability and biocompatibility. All materials exhibited good thermal stability, amorphous nature and high glass transition temperature, although the type of terpene oxide affect their properties. Unlike the previous reports describing that only racemic polymers are able to crystallize, the enantiomeric polylimonene carbonate could crystallize from a diluted solution in chloroform. Due to the chain stiffness they revealed an insignificant hydrolytic and enzymatic degradation. However, they showed satisfactory biocompatibility during adhesion and proliferation of fibroblast cells. Due to their bioresource, high rigidity and biocompatibility they can be considered as alternative materials to be blended with PBS. The blended materials displayed biodegradability and appropriate biocompatibility and mechanical strength. The sample with the highest mechanical strength, i.e., PBS/poly(PA-LO) with 30 wt% biobased terpene derivative was used for matrix fabrication via TIPS technique. The blended polymer solutions in 1,4-dioxane underwent phase separation using different cooling systems (i.e., thermal gradient with different intensity and direction). The blended materials could render microporous networks with various morphologies. The added terpene based polymer did not have a significant influence on the porosity structure (blended matrices with randomly/uniaxialy-oriented pore architecture similar to the neat PBS were obtained). However, the leafy structure obtained from multidirectional cooling in -20 °C bath consisted of thinner polymer leaves. The uniaxial temperature gradient in -196 °C resulted in formation oriented pore structures having spherulitic pore walls with less regularity and continuity. This feature can be attributed to the effect of terpene based polymer on the crystallization of PBS from the solution during the phase separation process.